Crystallography Reports, Vol. 46, No. 1, 2001, pp. 1–3. Translated from Kristallografiya, Vol. 46, No. 1, 2001, pp. 7–9.

CRYSTALLOGRAPHIC SYMMETRY

Information Patterns of Point Groups of Symmetry

N. S. Budnikov, A. V. Pitirimov, E. A. Soldatov, and E. V. Chuprunov

Nizhni Novgorod State University, Nizhni Novgorod, Russia

e-mail: krio@phys.unn.runnet.ru

Received March 22, 1999

Abstract—An algorithm for calculating information entropy of regular point systems in crystallographic point groups has been described. The information patterns visualizing the information properties of the groups are described. © *2001 MAIK "Nauka/Interperiodica".*

Traditionally, the structures of various materials are described by geometric images with the aid of various polyhedra, spheres, sets of points, etc. Such a description makes the basis of the geometric method for representing the atomic structures of condensed media. However, the geometric description is far from being complete and can be used as a basis for studying the relation between the structures of materials and their physical properties only in some cases. In most instances, the geometric characteristics of atomic structures should be combined with the energy, entropy, and other physical parameters of the respective atomic configurations.

Earlier [1], we suggested the method for calculating the volume of information contained in the simplest geometric objects modeling various atomic configurations. These objects were regular point systems of the crystallographic point groups, i.e., the finite sets of weighted points in a limited space region invariant with respect to a certain symmetry point group. Below, we qualitatively analyze the information properties of regular point systems of all crystallographic point groups.

The information entropy of the point systems can be calculated by the Shannon formula, which describes the information entropy of a certain distribution $\rho(x)$ [2]

$$S = -\int_{V} \rho(x)\ln\rho(x)dx. \qquad (1)$$

The system of weighted points can be well characterized by a set of point weights and a set of distances between these points. Therefore, the information properties of the spatial configuration of a system of weighted points can be characterized by a functional of the set of interpoint distances and point weights, i.e., by the information functional of the point system [1].

Using the Shannon formula, one can derive the following equation for the information functional of the system of weighted points [2, 3]:

$$S = -\sum_{i,j} f(R_{ij}, Z_i, Z_j)\ln f(R_{ij}, Z_i, Z_j). \qquad (2)$$

Here, $f(R_{ij}, Z_i, Z_j) = f_{ij}$ is a nonnegative monotonic function of interpoint distances and point weights. The values of this function can be interpreted as the probabilities of certain (generally speaking, quite abstract) transitions between the points i and j. The concrete form of this function depends on the physics of the problem to be solved. The simplest model of this kind was suggested by analogy with the Newton gravitation law formulated within the framework of the Darwin–Fowler method [1, 4].

$$f(R_{ij}, Z_i, Z_j) = \frac{kZ_iZ_j}{R_{ij}^2}. \qquad (3)$$

This method for calculating the information entropy received the name of the gravitation model.

Since the volume of information extracted from the point configuration within the gravitation model depends only on the weights of the points forming the set of interpoint distances, the information entropy of this configuration is determined by the vector system, which is a set of end points of the interpoint vectors with the weights equal to the product of the weights of the points of the main system.

In the X-ray analysis, the vector systems are used to represent the maxima of the interatomic (Patterson) function [5]. Thus, within the method based on this formula, the information potential is higher the more diverse the set of the weighted interpoint distances is. Isovector systems (i.e., the systems with the same vector) are equally informative. The fact (well known to all those engaged in X-ray diffraction studies) is that while singling out an isovector system from the main system, one usually obtains ambiguous/nonunique solutions reflecting the fact that the initial main systems and the corresponding crystal structures are equally informative.

1063-7745/01/4601-0001$21.00

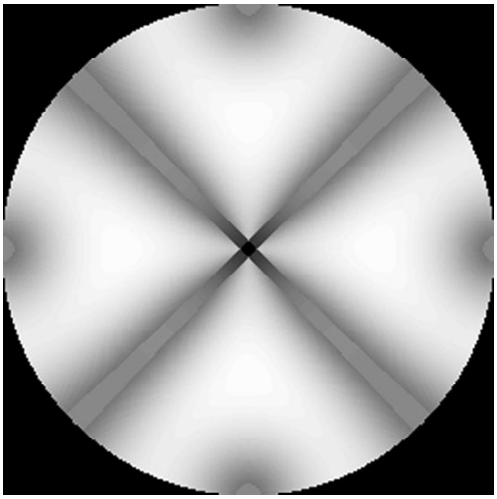

Fig. 1. Information pattern for the point group D_{2d}.

The configurations that can be transformed into one another by the similarity operation provide the same volume of information, which is equivalent to the normalization conditions imposed onto the distribution $f(R_{ij}, Z_i, Z_j)$

$$\sum_{i,j} f(R_{ij}, Z_i, Z_j) = 1. \quad (4)$$

It follows from the normalization condition that, within the gravitation model, the system consisting of two points contains the zero volume of information. To consider the volume of information provided by one point is absolutely senseless.

Geometric crystallography and crystal chemistry deal with the representations of crystal structure by sets of regular point systems occupied by the atoms in the symmetry groups. The regular point systems are characteristic of symmetry groups; however, different regular point systems of one group can be of different orders (have different numbers of points) and different symmetries [6, 7]. Therefore, the geometric properties of the symmetry group can fully be characterized only by the whole set of possible regular systems.

The information properties of point groups can be fully characterized on the basis of the information functional whose values should be calculated for all the regular point systems given by the initial positions of the initial point. In order to represent the functional in the clear graphic form for all the point groups, it is convenient to use a stereographic projection. The values of the information functional at the points of this projection can be reflected either by a half-tone pattern or by a three-dimensional graph.

To calculate the information functional, we wrote a special package of programs in the C^{++} language. These programs allow one to compute the information pattern of any point group as well as the minimum, the maximum, and the average functional values and the functional dispersion. It is also possible to examine in detail all the regions of the information pattern of interest and to store the pattern separately for further work. Using the above method, we obtained the stereographic projections of the information functionals for 32 crystallographic point groups. As an example, Fig. 1 shows the stereographic projection of the information functional for the regular point systems of the group D_{2d}.

Since within the framework of the gravitation model the entropy of the point system depends only on interpoint distances and point weights, the symmetry of the information pattern of a point group coincides with the symmetry of the corresponding vector system [5]. In particular, all the patterns are centrosymmetric.

Each point group can be characterized by a number of symmetrically different and consists of different numbers of the elements of regular systems (orbits). In particular, this determines the number of various simple forms which can form a polyhedron with the given point symmetry. It would be expedient to consider various regular point systems with the same symmetry but not invariant with respect to similarity. It is impossible to study such a difference within the framework of the traditional crystallographic symmetry. Information patterns provide the characterization of each group, e.g., by the minimum and the maximum information entropy, and, thus, the opportunity to study the possibility of obtaining topologically and symmetrically different regular systems within the given group.

Figure 2 represents the diagram showing the maximum and the minimum information functionals for all 32 crystallographic point groups. In this case, we neglected the regular systems consisting of only one point, because, as was indicated above, the volume of information within the gravitation model for such systems has no sense. The symmetry groups on the diagram are plotted along the abscissa in the order of an increase of the maximum information functionals. It is seen that the maximum amount of information is characteristic of the groups of the highest orders. The minimum functionals are zero for the groups of all the systems except for the cubic one. The most informative graph seems to be that of the maximum functional values. Thus, the maximum functional value can be considered as the objective characteristic of the complexity of the corresponding symmetry group.

Consider the volume information provided by individual regular point systems, All the regular point systems of the crystallographic point groups can be

Information functional for cubic simple forms

Indices	T	T_h	T_d	O	O_h
(100)	2.68	2.68	2.68	2.68	2.68
(110)	4.06	4.06	4.06	4.06	4.06
(111)	1.79	3.25	1.79	3.25	3.25

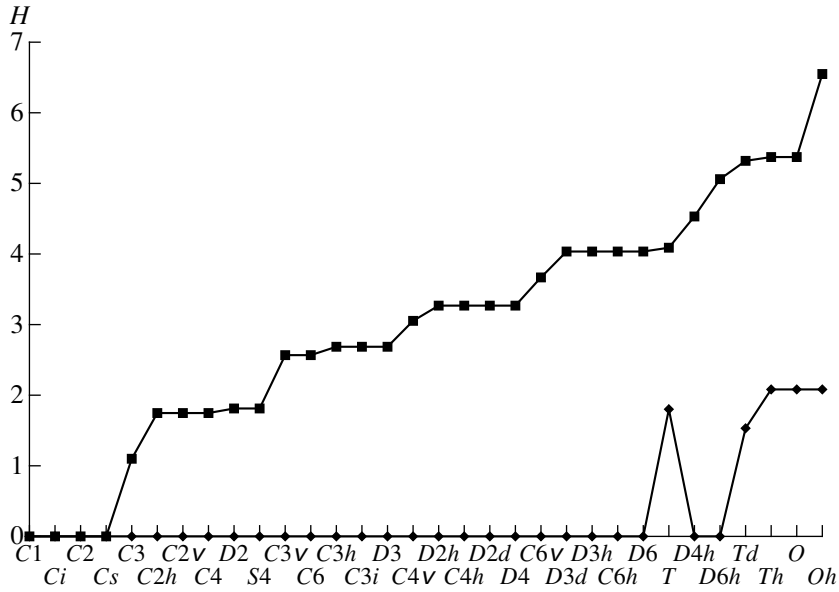

Fig. 2. Diagram showing the minimum (rhombuses) and the maximum (squares) values of the information functional for regular point systems of the crystallographic point groups. Point groups are plotted along the abscissa; entropy is plotted along the ordinate.

divided into general and special (lying on the symmetry elements). It follows from the general symmetry considerations, in particular, from the Neumann principle, that the vector of the gradient of the function S at the points coinciding with the points of the special regular point system coincides with the symmetry element on which this point is located. This signifies that the special regular point system corresponds to the conditional extremum of the function S. The reduction of the number of points in comparison with the number of points of the general regular point system should lead to a decrease of the information entropy. Thus, the information entropy has minima at the points corresponding to the special regular point systems. Moreover, the crystallographic groups have regular point systems with symmetries higher than the symmetry of the group which generated these systems. For such regular systems, the function S has the conditional maxima.

As an example, consider the function S for various regular point systems in the group D_{2d}. In addition to the general regular point systems (xyz) and the special ones (xxz) and ($x00$), the group also has the regular point systems ($xy0$) and ($x0z$) with the symmetry D_{4h}, ($00z$) with the cylindrical symmetry, and (000) with the spherical symmetry. At these points, the function S has local maxima. This function also has two maxima corresponding to the regular point system ($2xx0$) and ($x2x0$) having the noncrystallographic symmetry D_{8h}.

Information patterns allow one to study the information properties of regular point systems of other objects as well. Thus, bringing the faces of simple forms into correspondence with the points of the stereographic projections of face normals and calculating the informational functionals for the regular point systems, one can also study the informational properties of crystal polyhedra. The table shows the values of the information functional for the regular point systems corresponding to the most well known simple forms of the cubic system—a cube, a tetrahedron, and a rhombohedron.

REFERENCES

1. E. A. Soldatov and E. V. Chuprunov, Kristallografiya **41** (4), 746 (1996) [Crystallogr. Rep. **41**, 709 (1996)].
2. C. Shannon, *Works on the Information Theory and Cybernetics* (Inostrannaya Literatura, Moscow, 1963).
3. S. Kullback, *Information Theory and Statistics* (Wiley, New York, 1959; Nauka, Moscow, 1967).
4. A. D. Wilson, *Entropy in Urban and Regional Modelling* (Pion, London, 1970; Nauka, Moscow, 1978).
5. M. Buerger, *Vector Space and Its Application in Crystal-Structure Investigation* (Wiley, New York, 1959; Inostrannaya Literatura, Moscow, 1961).
6. A. V. Shubnikov, Kristallografiya **8** (6), 943 (1963) [Sov. Phys. Crystallogr. **8**, 760 (1963)].
7. E. V. Chuprunov, *Fedorov Pseudosymmetry of Crystals. Space Groups: On the Hundredth Anniversary of Their Derivation* (Nauka, Moscow, 1992).

Translated by L. Man

Crystallography Reports, Vol. 46, No. 1, 2001, pp. 100–102. Translated from Kristallografiya, Vol. 46, No. 1, 2001, pp. 108–111.

PHYSICAL PROPERTIES OF CRYSTALS

Study of Crystal Perfection in the KCl–KBr and KCl–RbCl Systems

E. A. Repnikova

Petrozavodsk State University, pr. Lenina 33, Petrozavodsk, 185640 Karelia, Russia

e-mail: erepn@mainpgu.karelia.ru

Received June 21, 1999

Abstract—The dislocation densities in the crystals of the KCl–KBr and KCl–RbCl systems with varying KCl concentration have been determined from the integrated reflection intensities. The results obtained lead to the conclusion about the formation of disordered solid solutions. It is shown that the dislocation density in the systems is higher than the dislocation density in the starting components and attains the maximum value for the compositions close to equimolar. The change of the dislocation and microstress densities depending on the KCl concentration are well correlated, which indicates the appearance of high stresses during the formation of a solid solution. © *2001 MAIK "Nauka/Interperiodica".*

INTRODUCTION

There are numerous publications to determine the degree of perfection of ionic crystals; however, there are almost no publications on the degree of perfection of the phases of variable composition.

We measured the microhardness and dislocation density of KCl–KBr and KCl–RbCl single crystals with the KCl concentration ranging from 0 to 100%. The lattice parameters of the pure KCl, KBr, and RbCl components were 6.283, 6.553, and 6.559 Å, respectively.

The microhardness was measured by a PMT-3 device under 50- and 70-g loads. The dimension d of the pyramid indentation was measured in an optical microscope. The experimental data were averaged over at least ten indentations obtained under the same load for the same time. We used as-cleaved surfaces.

The dislocation density was calculated from the integrated intensities of the (400), (600), and (800) reflections. The integrated intensities of the reflections were measured on a DRON-3.0 X-ray diffractometer (monochromatized Mo radiation, the scheme of a double-crystal spectrometer, the parallel specimen geometry reducing the possible dispersion). A monochromator was a Si (111) single crystal (the reflection angle 6.425°). To reduce the beam divergence, we used Soller slits. The primary beam was collimated to the cross section of 0.08×0.25 mm^2. The integrated reflection intensities were determined using the ω-scanning [1]. To take into account the error owing to a possible deviation of the reflection plane from the crystal surface, the X-ray reflections were recorded in the positions 0°, 180°, 90°, and 270° with respect to the goniometer axis with their subsequent averaging [2]. In order to provide the control of specimen homogeneity, the measurements were made on various parts of the specimens. The scanning intervals were chosen experimentally and varied from 3° to 6° for various Bragg angles.

It is well known that in Bragg geometry, the following inequality is valid for a real crystal: $R_{dyn} \le R_{exp} \le R_{id.\ mos.}$, where R_{dyn} is the integrated intensity for an ideal crystal (the dynamical limit) and $R_{id.\ mos.}$ is the integrated intensity for an ideal mosaic crystal. Then, we can write

$$y = R_{exp}/R_{id.\ mos.},$$

where y is the extinction parameter.

We compared the experimental integrated intensity R_{exp} with the theoretical values R_T calculated for a thick crystal within the kinematical approximation:

$$R_T = R_{id.\ mos.} = Q_v/2\mu, \quad (1)$$

$$R_{id.\ mos.} = (e^2/mc^2)^2 N^2 \lambda^3 |F|^2 e^{-2M} P(\theta) L(\theta) A(\mu), \quad (2)$$

where Q_v is the integrated intensity reflected by the volume unit;

$$Q_v = (e^2/mc^2)^2 N^2 \lambda^3 |F|^2 e^{-2M} P(\theta) L(\theta), \quad (3)$$

where N is the number of the unit cells in a volume unit ($N = 1/a^3$, a is the unit-cell parameter), λ is the radiation wavelength, $|F|^2$ is the structure factor, e^2/mc^2 is a classical radius of an electron, e^{-2M} is the temperature or the Debye-Waller factor, h is the Planck constant, $P(\theta) = (1 + \cos^2 2\alpha \cos^2 2\theta)/(1 + \cos^2 2\alpha)$, α is the Bragg angle of a monochromator, $L(\theta)$ is the Lorentz factor equal to $1/\sin 2\theta$, $A(\mu) = (1/2)\mu$ is the absorption factor (cm) for an infinitely thick crystal.

1063-7745/01/4601-0100$21.00

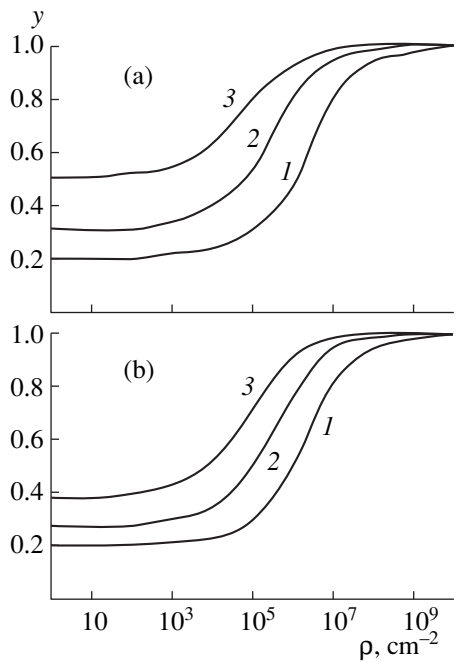

Fig. 1. Extinction parameter as a function of the dislocation density ρ for the (a) KCl (50%)–KBr (50%) and (b) KCl (50%)–RbCl (50%) systems; (*1*) (400) reflection, (*2*) (600) reflection, and (*3*) (800) reflections.

The experimental integrated reflection R_{exp} was determined from the following formula [3]:

$$R_{exp} = \frac{(E - I_b T)}{I_0}\omega, \qquad (4)$$

where E is the total energy dissipated along the main maxim (in pulses), I_b is the background intensity (pulse/s), T is the scanning time (s), ω is the angular velocity of the sample rotation (rad/s), and I_0 is the primary-beam intensity (pulse/s).

The dependence of the extinction parameter on the dislocation density for the Bragg's case of a "thick" crystal with due regard for the primary and secondary extinction has the form [4, 5]

$$y = \frac{1}{1+z}[(1+2x_0)^{-1/2} + z(1+2zx_0)^{-1/2}], \qquad (5)$$

where

$$z = \cos^2 2\alpha \cos^2 2\theta,$$

$$x_0 = \frac{Q_0 \sin 2\theta}{3\mu^2\lambda}\frac{(1+\beta\rho^{1/2}\sin\theta/\mu)}{(1+\sin\theta\rho^{1/2}/\mu)^2}, \quad \beta = \frac{\lambda}{a\sqrt{2\pi}}.$$

The errors in dislocation-density determination introduce the error into a measured energy of a primary beam and integrated intensity of the reflection. To determine the energy of the incident radiation, we used the absorbing filters with the experimentally obtained

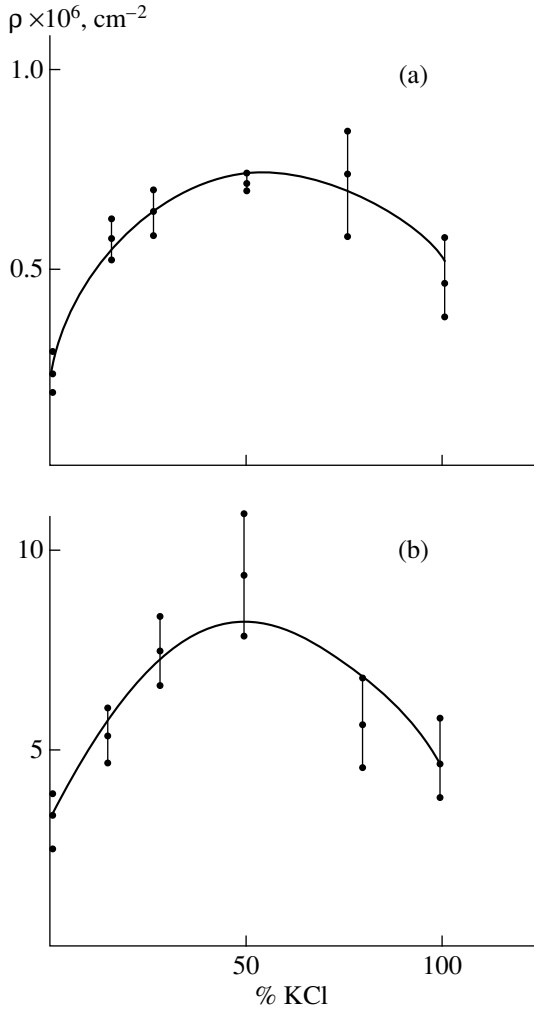

Fig. 2. Dislocation density as a function of the KCl concentration for the (a) KCl–KBr and (b) KCl–RbCl systems.

attenuation coefficient. The error in the determination of the primary-beam intensity did not exceed 3%, whereas the error in the determination of the integrated intensity was about 15%.

The experimental error in the determination of the diameter of a pyramid used to estimate microhardness exceeded the instrumental error and reached 5–10%.

RESULTS AND DISCUSSION

Two limiting variants are possible in the formation of the KCl–KBr and KCl–RbCl crystals. The first one is the mixture of KCl and KBr (RbCl) crystals as is the case of the eutectics formation. The second one is the variant in which the Cl^- and Br^+ (Rb^+) ions occupy their positions with equal probabilities (with due regard of their concentration), as is the case in the formation of a disordered solid solution.

The experimental results favor the second variant: one observes the (*h*00) reflections, which allow the

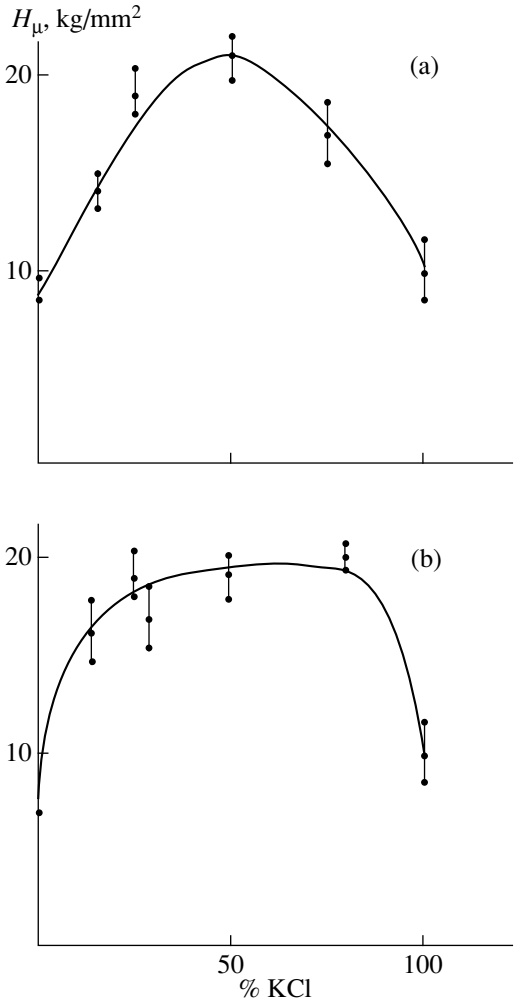

Fig. 3. Microhardness as a function of KCl concentration for (a) KCl–KBr and (b) KCl–RbCl systems.

determination of the lattice parameters in full accord with Vegard's law [6]. However, the different ions dimensions, Cl^- (1.81 Å), Br (1.95 Å), Rb (1.49 Å), and K (1.33 Å), result in high stresses in the structure.

Figure 1 shows the theoretically calculated $y = f(\rho)$ curves for KCl (50%), KBr (50%), KCl (50%), and RbCl (50%). Figure 2 shows ρ versus the KCl concentration. It is seen that the curves have a parabolic shape with the maximum corresponding to 50–60% of KCl in the KCl–RbCl system and to 50–75% KCl in the KCl–KBr system. The dislocation densities in pure components agree with data [7], whereas in the mixtures, the dislocation densities are considerably higher than in pure components. The dislocation densities were additionally measured by the selective-etching method. As-cleaved surfaces of single crystals were etched by 70% acetic acid. The etch pits had a regular rectangular shape. The dislocation densities determined by both independent methods were considered within the experimental error. Thus, the values of ρ obtained by the etching and the X-ray methods are $(5.5 \pm 0.8) \times 10^6$ and $(4.5 \pm 0.8) \times 10^6$ cm^{-2} for KCl (100%); $(9.4 \pm 1.7) \times 10^6$ and $(8.5 \pm 1.6) \times 10^6$ cm^{-2} for KCl (50%)–RbCl (50%); $(7.2 \pm 1.0) \times 10^6$ and $(7.0 \pm 0.1) \times 10^6$ cm^{-2} for KCl (50%)–KBr (50%), respectively.

The microhardness in both systems depends on the KCl concentration in a similar way; the hardness curves are similar to the curves of dislocation density (Fig. 3). The microhardness values of the KCl, KBr, and RbCl components are much lower than for their mixtures. High elastic stresses arising in the lattices of the KCl–KBr and KCl–RbCl solid solutions at the compositions close to equimolar result in considerable increase of dislocation density, which, in turn, provide an increase in system microhardness.

CONCLUSIONS

It has been established that the single crystals in the KCl–KBr and KCl–RbCl systems form disordered solid solutions.

The formation of the solid solutions is accompanied by the appearance of high static stresses caused by considerably different ionic radii.

The variations of microhardness and dislocation density depending on the KCl concentration correlate with each other and have the shape of a parabolic curve.

ACKNOWLEDGMENTS

The author is grateful to A. V. Kuznetsov for discussion of the results and to Professor P. Ketolainen from the University of Joensuun Yliopisto, Finland, for providing us single crystals.

REFERENCES

1. D. M. Kheĭker, *X-Ray Diffractometry of Monocrystals* (Mashinostroenie, Leningrad, 1973).
2. R. W. James, *The Optical Principles of the Diffraction of X-Rays* (Bell, London, 1950; Inostrannaya Literatura, Moscow, 1950).
3. A. A. Rusakov, *Radiography of Metals* (Atomizdat, Moscow, 1977).
4. A. V. Kuznetsov, X-Ray Determination of Dislocation Density in Crystals and Allowance for Extinction Effects (Petrozavodskiĭ Gos. Univ., Petrozavodsk, 1981).
5. A. V. Kuznetsov, Kristallografiya **18** (5), 944 (1973) [Sov. Phys. Crystallogr. **18**, 592 (1973)].
6. A. V. Kuznetsov and E. A. Repnikova, in *Proceedings of the IV All-Russia Scientific and Technical Conference "Physics of Oxide Films"* (Petrozavodskiĭ Gos. Univ., Petrozavodsk, 1994), p. 45.
7. E. I. Raĭkheĭl's, I. V. Smushkov, and V. M. Trembach, Fiz. Tverd. Tela (Leningrad) **10** (6), 1684 (1968) [Sov. Phys. Solid State **10**, 1330 (1968)].

Translated by A. Zalesskiĭ

Crystallography Reports, Vol. 46, No. 1, 2001, pp. 103–110. Translated from Kristallografiya, Vol. 46, No. 1, 2001, pp. 112–120.

Dedicated to the Memory of Professor A. P. Kapustin

High-Frequency Acoustic Domains in Liquid Crystals

O. A. Kapustina and O. V. Romanova

Andreev Acoustics Institute, Russian Academy of Sciences, ul. Shvernika 4, Moscow, 117036 Russia

e-mail: bvp@akin.ru

Received February 17, 1999; in final form, December 9, 1999

Abstract—A mechanism for the formation of one- and two-dimensional domains in planar nematic and cholesteric liquid crystal samples in an ultrasonic field is discussed. A new approach to the analysis of this phenomenon based on the concepts of nonequilibrium hydrodynamics and taking into account the relaxation properties of the mesophase is experimentally substantiated. © *2001 MAIK "Nauka/Interperiodica".*

The orientational behavior of liquid crystals (LC) in external fields specified by their effect and the type of a mesophase is one of the most remarkable physical phenomena of anisotropic liquids. A classic example is the ordered spatially modulated structures formed on various scales and having various configurations. The condition for the existence of such structures is of a threshold nature and determined by the balance of the volume and dissipative forces dependent on the effect of external factors.

As far back as the 1960s, Kapustin [1] in the Soviet Union and Williams [2] in the United States discovered the formation of textures in nematic liquid crystals (NLCs) in electric fields in the form of alternating bright and dark stripes (Fig. 1a), which received the name Kapustin–Williams domains [3]. These domains are formed upon the attainment of a certain threshold voltage and are not static formations (inside the domains, the vortices of the substance are formed with the maximum velocity observed at their centers) and the axes being always perpendicular to the NLC director **n**. At the same time, Kapustin also established that the use of a new (acoustic) external factor gives rise to a number of analogous phenomena in orientational behavior of NLCs including the formation of acoustically induced ordered structures. He also observed a system of linear (one-dimensional) domains in an NLC layer under the effect of compression waves of the ultrasonic range of (0.8–1.2 MHz) [4]. A higher level of this effect resulted in the transformation of domains into a dynamic system of "cells" formed by acoustic vortex microflows (Fig. 1b). Later, Guyon showed that in oscillating flows of nematic liquids caused by shear [5] or elliptical [6] oscillations, the system of acoustic domains is formed in a NLC layer also at the audio frequencies. A number of major directions of the studies in present-day acoustooptics of liquid crystals were indicated in [4–6], the results of which were generalized in the monograph [7] and some reviews [8, 9].

In the present paper, we restrict ourselves to only one of the problems related to acoustooptics of LCs—the structural transformations in planar LC layers in a field of longitudinal ultrasonic waves and the mechanism of formation of domains analogous to the Kapustin–Williams ones. Figures 2a and 2b show the micrographs of typical high-frequency acoustic domains in planar layers of NLC and cholesteric liquid crystal layers (NLC and CLC), observed in flat and wedgelike cells, respectively, under the conditions schematically illustrated by Figs. 2c and 2d, where *1* is a liquid crystal, *2* is a glass plate, *3* is a sound-transparent film, *4* is light-reflecting coating, *5* is a plane ultrasonic wave, and *6* is light probe. The micrograph of a NLC consists of a system of bright and dark stripes (so-called striped structure) perpendicular to the unperturbed director of the liquid crystal with the spatial period $\Lambda = 2\pi/q$ along the x axis, where q is the wave number of the periodic structure. In a CLC, the optical pattern of orientational distortion at the effect threshold is a two-dimensional system of equidistant bright lines parallel and perpendicular to the unperturbed director **n** (so-called "square grid") with the spatial period $\Lambda_1 = 2\pi/q_1$ along the x-axis and the period $\Lambda_2 = 2\pi/q_2$ along the y-axis, where q_1 and q_2 are the wave numbers.

In the corresponding experiments, we increased the level of external factor, i.e., the intensity I of an ultrasonic wave incident onto a LC layer up to the threshold intensity I_0 providing the domain formation and measured the spatial periods Λ in a NLC or Λ_1 and Λ_2 in a CLC. Figure 2e shows a typical dependence of the period of striped structure in NLC with an increase of the external-factor level expressed in terms of the vibration velocity V in the ultrasonic wave. It is seen that in the vicinity of the threshold, the period Λ of the structures slightly exceeds its value in the above-threshold

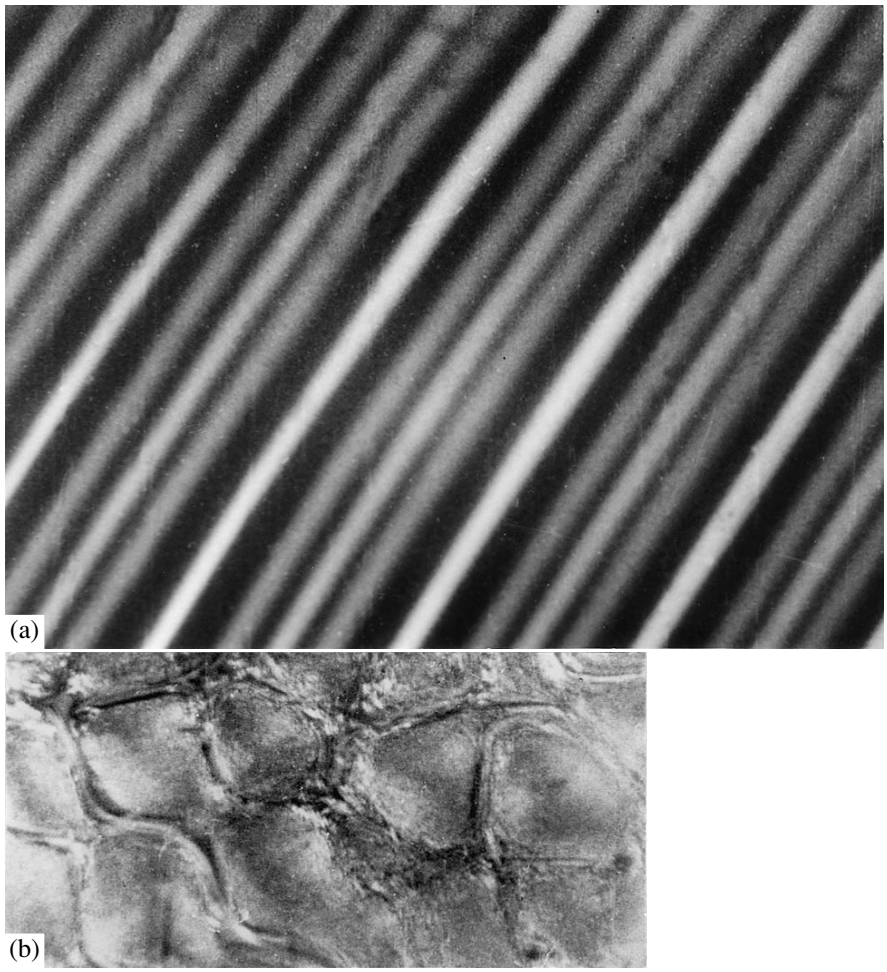

Fig. 1. Distortion of a director field in a nematic: (a) electric-field-induced Kapustin–Williams domains in a planar layer and (b) dynamic system of the "cells" formed in a layer of *p*-azoxyphenetole by acoustic vortex microflows in an ultrasonic field at the frequency 0.72 MHz (magnification ×450).

mode and, at $V = 1.5V_0$, approaches a steady-state value of about $0.5d$, where d is the thickness of a NLC layer and V and V_0 are the current and the threshold vibration velocities in the ultrasonic wave. Such variations in the structure period in the transition to the above-threshold mode take place for all the structures studied in nematics and cholesterics irrespectively of the layer thickness and the acting-factor frequency.

To describe quantitatively the domain formation in nematics and cholesterics, we varied the ultrasonic frequency f, the layer thickness, the helicoid pitch P_0 in a CLC, and liquid-crystal temperature within the range of the mesophase existence. The experiments were carried out on a NLC N-8 (the MBBA and EBBA mixture) and on a CLC with large helix pitch (cholesteryl chloride and caprate mixed with an LC-404 nematic).

Figures 3 and 4 show the experimental data obtained on NLC flat cells with the thickness ranging from 10 to 360 μm in the frequency range of 0.3–3 MHz and the temperature range of 20–45°C. It was found that the spatial domain period correlates with the thickness of the NLC layer (Fig. 3a, $f = 3.2$ MHz and $T = 30.2$°C). The threshold amplitude of the vibration velocity V_0 is almost independent of the layer thickness within a rather narrow thickness range (Fig. 3b: dashed curves show the experimental data at the frequencies of (○) 1 or (●) 3 MHz at the temperature of 30.2°C; *1–4* are theoretical curves). With an increase of the ultrasound frequency, the threshold vibration velocity showed a tendency to decrease. (This is seen from the position of the experimental points corresponding to the two frequencies (Fig. 3b)). The spatial period of the domains has a constant value (Fig. 3c). Varying the NLC temperature within the range of 22.8–35°C relating to the range of the mesophase existence does not affect the domain period Λ (Fig. 4a). It was also found that the vibration velocity V_0 at the threshold frequency has a tendency to decrease with the temperature T varying within the above interval. The experimental V_0 values in Fig. 4b are normalized to V_0^* corresponding to $T = 22.8$°C and

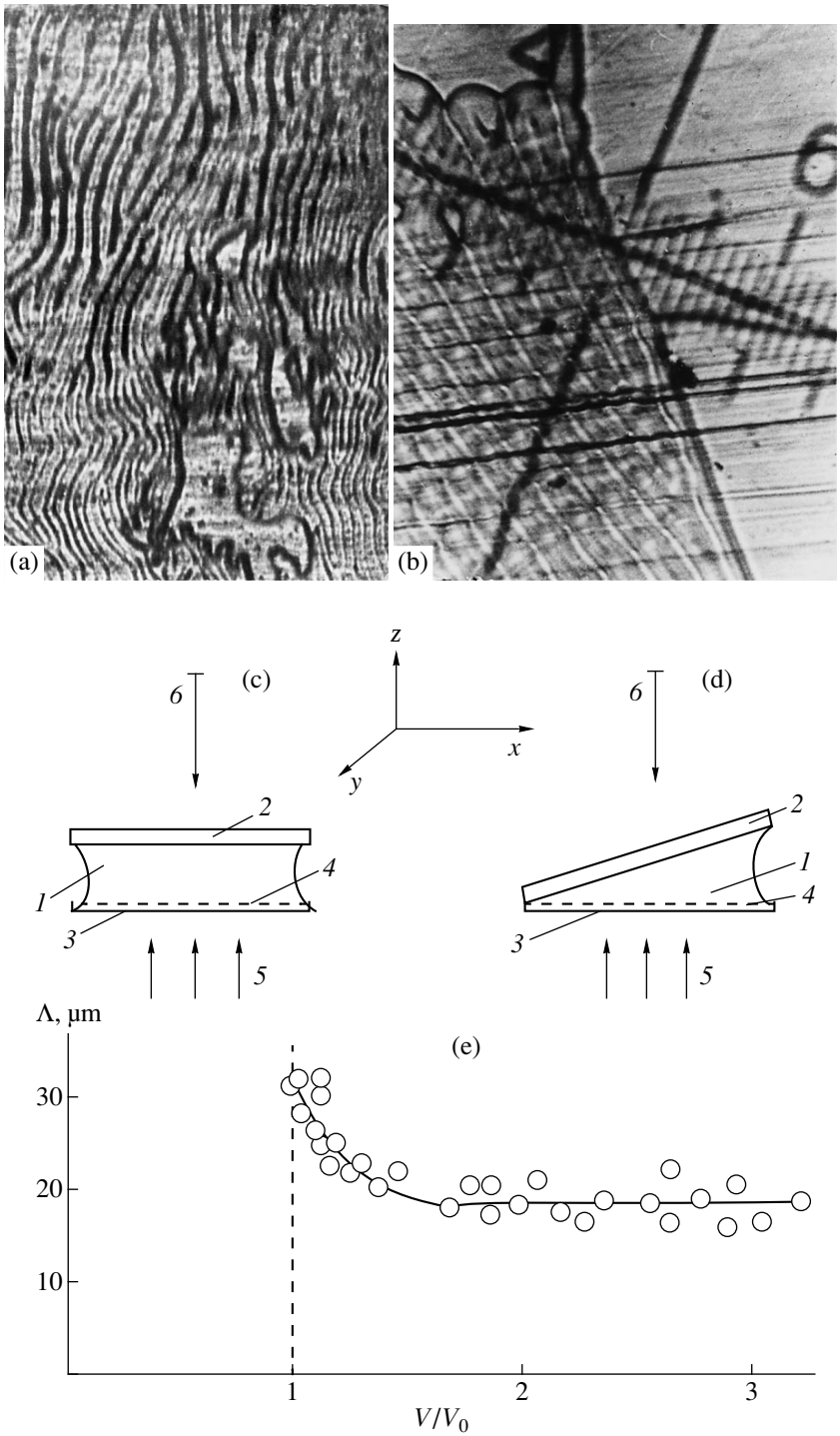

Fig. 2. High-frequency acoustic domains: distortions in (a) planar nematic layer (the frequency is 3.2 MHz, magnification ×100) and (b) cholesteric layer (the frequency is 1.2 MHz, magnification ×250). The schematics of the experiments with (c) flat and (d) wedgelike cells (see the text). (e) Spatial period of the domains Λ in the above-threshold mode as a function of the acoustic-factor level expressed in vibration velocity in an ultrasonic wave (in arbitrary units) for a nematic (the layer thickness 40 μm, the frequency 3.2 MHz).

are represented as differences ΔT between the temperature T_{NI} of the nematic–isotropic phase transition and the current temperature (at the layer thickness 40 μm and the frequency 3.2 MHz).

The experimental behavior of the threshold characteristics of one-dimensional domains in NLCs also hold for chiral samples in the flat and wedgelike cells. However, a new structural parameter inherent in this type of

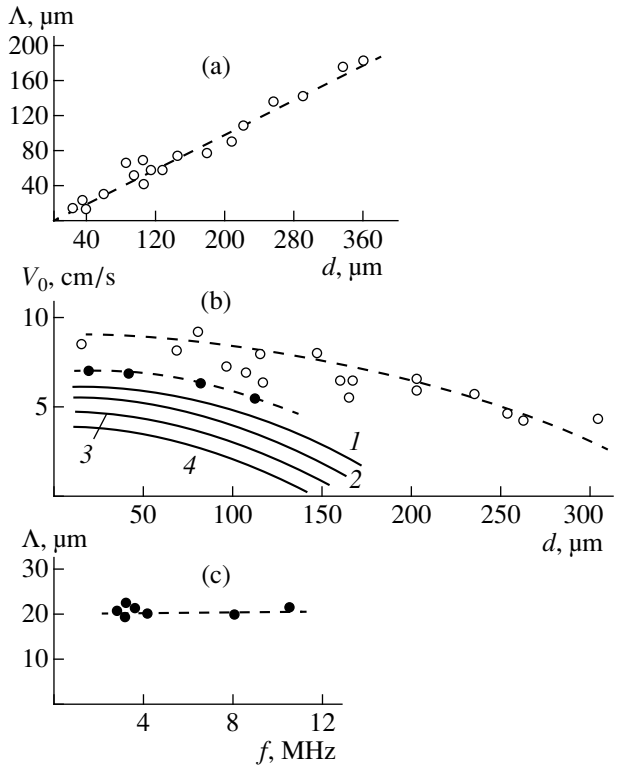

Fig. 3. Typical dependences, describing the behavior of planar layers of a nematic in an ultrasonic field: the effect of the layer thickness on (a) the spatial period of domains (at the frequency 3.2 MHz) and (b) the threshold vibration velocity at the frequencies (○) 1 and (●) 3 MHz, and (c) the spatial period of the structures in the frequency range 2.8–10 MHz.

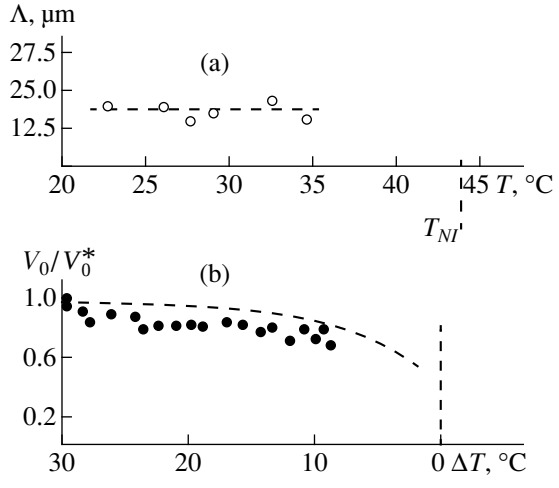

Fig. 4. Effect of the nematic temperature on (a) the spatial period of domains and (b) the threshold vibration velocity.

a mesophase—a helicoid pitch—not only affects the pattern of the distorted director field (formation of two-dimensional domains) but also the behavior of threshold characteristics of such distortions. Figure 5a indicates the spatial periods $\Lambda_1 = \Lambda_2$ for CLC samples (cholesteryl caprate mixed with LC-404) at the following d and P_0 values: (○) 10 and 4.5, (×) 40 and 2, (●) 10 and 10.5, (△) 40 and 4.5, (▲) 80 and 4.5, and (◮) 40 and 10.5 μm. Similar to NLCs, there is a correlation between the domain periods and layer thicknesses. However, in chiral liquid crystals, the layer thickness also depends on the helicoid pitch: Λ_1, $\Lambda_2 \sim (P_0 d)^{1/2}$. The effect of the ratio of P_0 and d on the threshold vibration velocity in the planar and wedgelike cells can be estimated from the data shown in Fig. 5b. Here, the notation is the same as in Fig. 5a and refers to the flat cell; the symbol "◑" represents the V_0 value for a sample in the wedgelike cell (the Grandjean zone X, the local layer thickness is 22.5 μm), P_0 = 4.5 μm, and f = 1.2 MHz. It is seen that the experimental dependence $V_0(P_0, d)$ is similar to the dependence $V_0 \sim (d/P_0)^{1/2}$. The change of the frequency within the range 0.33–3.65 MHz affects neither the threshold vibration velocity nor the domain period. Thus, the measurements performed on the wedgelike CLC sample (the Grandjean zone X) indicate that the threshold sound intensity is almost constant within the frequency range under consideration and comprises about 20 mW/cm^2, which corresponds to the threshold vibration velocity of ~1.8 cm/s. Figure 5c indicates the experimental values of the spatial period of the structures observed in the (●) plane (d = 40 μm) and the (○) wedgelike (22.5 μm) CLC cells for the frequency range studied; here, P_0 = 4.5 μm. It should be emphasized that the spatial period Λ_1 of the structure in a flat cell is equal to with the period Λ_0 = 14 μm of the square grid, observed in an independent experiment with cholesteric liquid freely flowing into a flat cell from side reservoir, when the connecting flexible tube is deformed. One more fact seems to be of importance: in a set of experiments with CLC, the formation of the steady-state periodic structures in the areas separated by the paird disclinations in the planar cell or by Cano-Grandjean disclinations in wedgelike cell, where the number of cholesteric layers is changed and helicoid pitch differs from the equilibrium P_0 value. We estimated the parameter σ of the helicoid structure extension in the planar cell at the portion limited by pairs of disclinations as 0.89 and 0.84, for the Grandjean zone X in wedgelike cell. The Grandjean zone X was chosen because the distortion pattern in wedgelike cell depends on the zone number: for zones I–IV, the patterns consist of a series of stripes, whereas for zones V–XV, the patterns are more or less regular grid with the extension parameter σ for zone X being the closest to the value of this parameter for the region limited by disclinations in the flat cell.

Let us interpret the experimental data. Traditionally, the orientational phenomena in LCs are analyzed in terms of Leslie–Ericksen hydrodynamics [10, 11], which takes into account only the anisotropy of viscous properties of liquid crystals. The appropriateness of such an approach to the low-frequency acoustic domains accompanying the sound-induced Gyuon–

Pieransky instability in an oscillating nematic-liquid flow was justified in [12] for the most general case of arbitrary angles between the flow velocity and the director. The studies of NLCs and CLCs with considerable helicoid pitch [13–15] showed that the traditional approach [14] of describing high-frequency acoustic domains cannot be applied to the phenomenon under study [13, 15], probably because the Leslie–Ericksen hydrodynamics ignores the relaxation character of the variation of the LC state due to ultrasonic waves.

The necessity of development of a physical concept based on nonequilibrium hydrodynamics can be justified as follows. It is necessary to consider two following relaxation processes in an LC: (1) the critical relaxation process associated with the relaxation of order parameter (τ_c) is the relaxation time and (2) the relaxation process associated with the rotation of the terminal groups of the molecules (τ_n is relaxation time). Now, we can write the following formula of the anisotropy of the dynamical elastic modulus ΔE and the anisotropy of bulk viscosity coefficient μ_3 of LC [16]:

$$\Delta E = \Delta E_c^{\infty}(\omega\tau_c)^2/[1+(\omega\tau_c)^2] + \Delta E_n^{\infty}(\omega\tau_n)^2/[1+(\omega\tau_n)^2], \quad (1)$$

$$\mu_3 = \Delta E_c^{\infty}\tau_c/[1+(\omega\tau_c)^2] + \Delta E_n^{\infty}\tau_n/[1+(\omega\tau_n)^2]. \quad (2)$$

Here, ΔE_c^{∞} and ΔE_n^{∞} are the components of the high-frequency elastic modulus corresponding to different relaxation processes. Kozhevnikov suggested a theoretical model [17] taking into account the above factors and the following physical interpretation of the phenomenon: at a random distortion inhomogeneous along the layer of the planar structure the molecules of a liquid crystal emerge from the layer plane and form with it a certain angle $\psi = \psi_0 f(x, z)$. Then, the compression of a liquid crystal due to an ultrasonic wave $u_{zz} \sim \exp(-i\omega t)$ gives rise to anisotropic shear stresses $\xi_{xz}(\psi, \mu_3, u_{zz}, \dot{u}_{zz}, \Delta E)$, which, in turn, give rise to oscillating vortex flows having a velocity $v_z' = \psi_0 \cos qx$. Interacting with the original ultrasonic field results in stationary shear stresses $\langle\xi_{xz}\rangle$ providing the stationary vortex flows and enhancing the initial distortion of the planar structure, with the most pronounced spatial harmonics of the form

$$\psi = \psi_0 \sin qx \sin pz;$$

for NLC,

and

$$\psi, \theta \cong \sin q_1 x \sin q_2 y \sin pz.$$

for CLC.

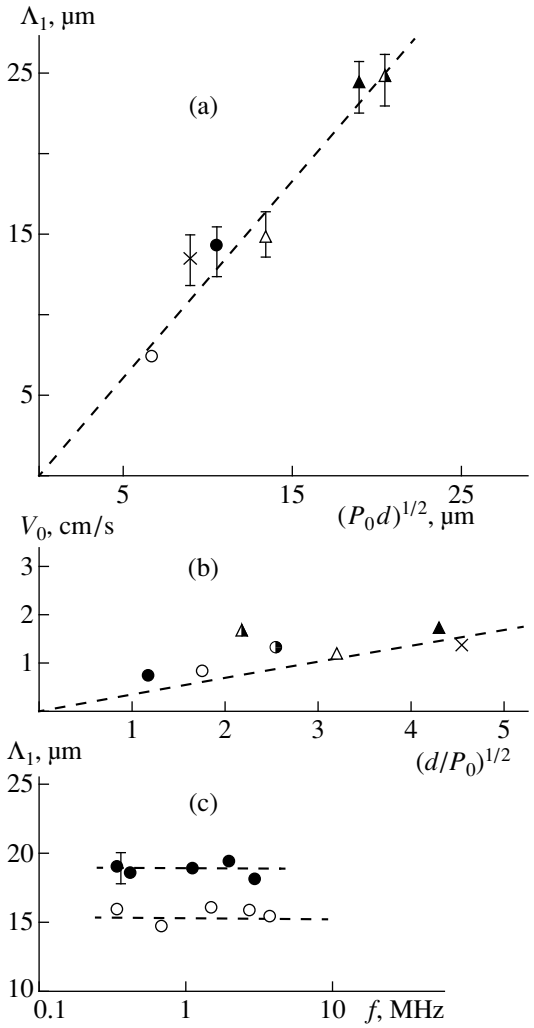

Fig. 5. Typical dependences describing the behavior of planar cholesteric layers in an ultrasonic field: (a) the effect of the layer thickness and helicoid pitch on the spatial period of the structures; (b) the threshold vibration velocity; and (c) the relation between the spatial period and the ultrasonic frequency for (●) flat and (○) wedgelike cells.

Here, $q_1 = \pi/\Lambda_1$, $q_2 = \pi/\Lambda_2$, $q = \pi/\Lambda$, $p = \pi/d$.[1] Upon the attainment of the threshold sound intensity, the destabilizing viscous torques proportional to the velocity gradients of the stationary flows exceed the Frank elastic torques, which results in a stationary spatially periodic misorientation seen as a system of one-dimensional domains (striped structure) in nematics and two-dimensional domains (square grid) in cholesterics.

The schematic illustrating the development of this phenomenon in an NLC, which follows from the model suggested in [17] is shown in Fig. 6.

[1] Analyzing distortion of the helicoidal structure of a cholesteric, one has to take into account not only the deviation of the molecules from the undistorted "cholesteric plane" (the angle ψ), but also their reorientation in the plane (the angle θ).

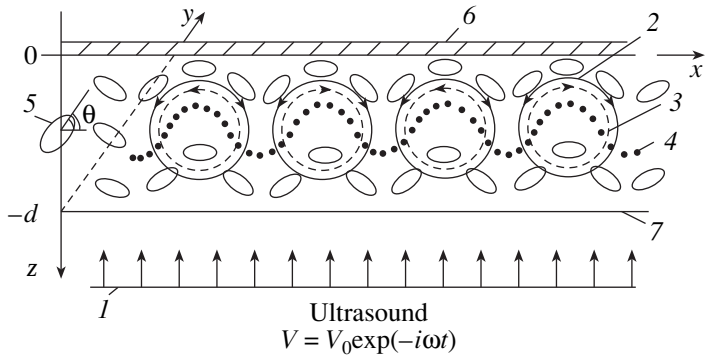

Fig. 6. Illustrating the model of the physical mechanism of the development of an orientational instability in a planar NLC under the effect of ultrasound: (*1*) ultrasound, (*2*) oscillating vortex flow, (*3*) steady-state flow, (*4*) distortion profile of a field of the director **n** in a nematic, (*5*) NLC molecule, (*6*) acoustically rigid boundary of a nematic, and (*7*) acoustically soft nematic boundary.

The calculation for the conditions adequate to the experimental ones (Fig. 2c, total reflection of the incident ultrasonic wave from the acoustically rigid cell boundary, the validity of the inequality $d\omega/c < 1$) leads to the following equations, which describe the main features of the threshold characteristics

$$\Lambda = d/s_0^2 \tag{3}$$

and

$$V_0 = 0.5c\pi[K\eta F(s_0)/\Delta E\gamma_1]^{1/2}/d \tag{4}$$

for a nematic and

$$\Lambda_1 = \Lambda_2 = [(1+m)/4m]^{1/4}(P_0 d)^{1/2}, \tag{5}$$

$$V_0 = c\pi\{K[m(1+m)]^{1/2}/P_0 \times d\Delta E(1+38\eta\pi^2/\rho\omega^2\tau d^2)\}^{1/2}(1-\sigma)^{1/2} \tag{6}$$

for a cholesteric.

Here $K = K_1, K_2$, and K_3 are the Frank elastic constants; $m = K_2/K_3$; s_0 is the value of the parameter $s = a^2/p^2$, which minimizes the function $F(s_0)$ in formula (4)[2]; $\eta = 0.5(\alpha_4 + 0.5\alpha_5)$, where α_i are the Leslie viscosity coefficients; γ_1 is the rotational viscosity; c is velocity of ultrasound propagation in an LC; P_0 is equilibrium value of the helicoid pitch; and σ is the relative extension of a cholesteric layer. By definition, $\sigma = \delta/\delta_c$, where δ is the change in cholesteric-layer thickness and δ_c is the critical value of δ at which a domain structure can be formed even in the absence of an ultrasonic field due to the extension of a cholesteric layer (the so-called "static domains") [14]. In the derivation of above formulas, we make allowance for only one relaxation process in an LC with the relaxation time τ. This allowed us to reduce Eqs. (1) and (2) to the form

$$\Delta E = \Delta E^{\infty}(\omega\tau)^2/[1+(\omega\tau)^2], \quad \mu_3 = \Delta E^{\infty}\tau/[1+(\omega\tau)^2], \tag{7}$$

which considerably simplified the subsequent analysis. In Eq. (6), the factor $(1-\sigma)^{1/2}$ takes into account the preliminary extension of cholesteric layers along the helicoid axis **h**. Experimentally, the extension was observed in the vicinity of the Grandjean lines in a wedgelike cell and pair disclinations in flat cell at which the number of the cholesteric layers changes.

Now, compare the above experimental data with the results following from model [17]. The form of the function $F(s_0)$ in Eq. (4), which predicts the behavior of the threshold vibration velocity V_0 for an NLC, depends on the ultrasonic frequency and the layer thickness. Introducing the parameter $B = \pi^2\mu_3\eta/\rho d^2\Delta E$, one can divide the entire frequency range into the subranges of low ($B \ll 1$) and high ($B \gg 1$) frequencies, in which the values of the parameter s_0, which minimizes the function $F(s_0)$, are 3.7 and 4.8, respectively. Then, the spatial period of domains in an NLC is $0.52d$ and $0.48d$, which is consistent with the value $\Lambda \cong 0.5d$ for the above-threshold mode (Fig. 3a). In fact, the variation of Λ with the frequency predicted by the theory is insignificant, which agrees with the experimentally established independence of the structure period of the ultrasonic frequency. The family of curves *1–4* in Fig. 3b calculated by Eq. (4) represents the dependence of the threshold amplitude of the vibration velocity V_0 on the thickness of an NLC layer at frequencies of 0.1, 1, 3.5, and 10 MHz. It is seen that the velocity V_0 weakly depends on the layer thickness d, which agrees with the experimental data in Fig. 3b. With an increase of the ultrasonic frequency, the velocity V_0 decreases. Qualitatively, this agrees with the experiment. A slight discrepancy between the absolute theoretical and the experimental V_0 values can be explained by the error in measuring of the level of the acting acoustic factor or

[2] The expression for the function $F(s_0)$ can be found in [17].

the inhomogeneity of the wave-parameter distribution over the cross section of the ultrasonic beam, which is characteristic of acoustic fields.

According to the model [17], the temperature dependence of the threshold amplitude of the vibration velocity V_0 depends on the parameter $\omega\tau_c$. At high frequencies ($\omega\tau_c \gg 1$), the threshold amplitude only slightly depends on the temperature and obeys the law $V_0 \sim T^{-1/8}$. At low frequencies ($\omega\tau_c \lesssim 1$), this temperature dependence for V_0 far from the transition temperature T_{NI}, where $\tau_c \ll \tau_n$ remains valid, while in the neighborhood of the nematic–isotropic transition ($\tau_c \gg \tau_n$), $V_0 \sim T^{-7/8}$. The dashed line in Fig. 4b represents the dependence $V_0(\Delta T)$ calculated for the model [17] at the frequency of 3.5 MHz and the layer thickness of 40 μm at the temperatures up to the phase-transition point. At the τ_c value 2.2×10^{-7} s typical of NLCs, we have $\omega\tau_c < 1$ within the experimental frequency range. At the temperatures far from T_{NI}, this results in a very weak temperature dependence of V_0. The latter fact agrees with the experimental data for the temperature range of 22.8–35°C (Fig. 4b).

Now, analyze the behavior of the threshold characteristics of a planar layer of a cholesteric. First of all, no comparison of the numerical calculated results with the experimental data is possible without the introduction of free parameters. Determine the m and σ values providing the best agreement of these data. It follows from the experimental curve in Fig. 5a that at a frequency of 1.2 MHz, $d = 40$ μm, and $P_0 = 4.5$ μm, the spatial period of domains is 14 ± 0.5 μm. Equating this value of Λ_1 to the theoretical value $\Lambda_1 = 13.42[(1 + m)/4m]^{1/4}$ obtained from Eq. (5), we obtain the elastic-moduli ratio, $m = K_2/K_3 = 0.268$. Then, using this Λ_1 value and Eq. (6), we obtain at $d = 40$ μm, $P_0 = 4.5$ μm, and $f = 1.2$ MHz that $V_0 = 11.9$ cm/s. (In calculations ΔE, K_3, c, τ, and η values typical of NLCs were used). Under the same conditions, the experimental V_0 value is ~1.4 cm/s. Introducing the correction for extension of the cholesteric layers along the helicoid axis determined by $(1 - \sigma)^{1/2}$ up to the theoretical value V_0 and equating the theoretical and the experimental velocities V_0, we can determine the value of the parameter σ which would provide the same V_0 values—0.98. This value is close to the σ value obtained experimentally on the layer regions limited by disclination pairs and in the vicinity of a Cano–Grandjean disclination in Grandjean zone X in flat and wedgelike cells, respectively.

Now, proceed to the relationship between the main theoretical and experimental dependences, which describe the system of the two-dimensional domains in a CLC. It follows from Eq. (6) that there exists a critical frequency f_c specified by the condition $38\pi^2\eta/\rho d^2\omega^2\tau = 1$, which divides the entire frequency range into low- and high-frequency subranges in which the threshold vibration velocities V_{0l} (low frequency) and V_{0h} (high frequency) are frequency-independent, whereas their relation to d and P_0 can be represented as

$$V_{0l} \sim (d/P_0)^{1/2} \tag{8}$$

and

$$V_{0h} \sim (P_0 d)^{-1/2}. \tag{9}$$

For experiments with wedgelike ($d = 22.5$ μm) and flat ($d = 40$ μm) cells, we estimated the critical frequencies as 5.3 and 3 MHz, respectively. This signifies that the corresponding experimental V_0 values should obey the dependence similar to Eq. (8), which is confirmed by Fig. 5b.

The above analysis justifies a new physical concept based on the ideas of the nonequilibrium hydrodynamics of the description of high-frequency acoustic domains (one-dimensional in NLCs and two-dimensional in CLCs). These domains are acoustic analogs of the Kapustin–Williams domains, whose behavior is described within the traditional equilibrium hydrodynamics. The acoustic domains observed at ultrasonic frequencies can be described only within a new approach taking into account the relaxation nature of anisotropic stresses with due regard for the mechanism of the formation of flows responsible for the distortion of initial planar macrostructure of an LC layer. This new approach provides a good agreement of the experimental and calculated threshold characteristics. In cholesterics, one has also to take into account the state of the helicoidal structure—equilibrium or deformed.

It is to be emphasized that the relationship between the changes in the LC structure and their acoustic and relaxation properties has long been known—for several decades. At larger thicknesses of greater LC layers, the optical measurements of the orientational phenomena are rather difficult. Here, the acoustic method of studying structural transitions in the mesophase is the most efficient. As early as the 1970s, a number of anomalies in the propagation of ultrasonic waves in liquid crystals associated with the relaxation phenomena were discovered. These are the dispersion of the phase velocity and deviation in the behavior of the ultrasound absorption coefficient β from the classical law $\beta/f^2 = \text{const}$. It was established that these anomalies are the most clearly observed in the vicinity of the phase transitions and within the megahertz frequency range. Kapustin was among the first who systematically studied these anomalies in various liquid crystals [18, 19]. It was established that anomalous absorption and dispersion of ultrasonic velocity were dependent on the nature of the relaxation process. The relaxation mechanisms in nematics were widely discussed in the literature and in a number of reviews [16, 20] and monographs [7, 21–24]. At present, the details of the dynamic behavior of nematics on a molecular scale are still unknown. However, the main groups of the relaxation processes have been identified. These are (a) the processes associated with order-parameter relaxation (the Landau–Khalatni-

kov mechanism) and the relaxation of the developed fluctuations of the order parameter (mainly in the disordered mesophase), (b) the processes caused by the rotation of molecules about their long and short axes and their translational motion, and (c) the processes related to the intramolecular motions, in which the end molecular groups move as a whole and undergo some conformational transformations.

In the model suggested in [17], which describes the structural transitions in thin nematic and cholesteric layers induced by ultrasound, which manifest themselves in the formation of domains having different configurations on different scales, the relaxation character of the changes in the orientational state of the mesophase in an ultrasonic field was taken into account. In this case, the anisotropic part of the elastic modulus of a liquid crystal was approximated by a sum of the terms, corresponding to only two of the above relaxation processes—the critical one (relaxation of orientational order parameter) and the normal one (rotation of the end molecular groups). The already mentioned correlation between the experimental data and the calculations performed for the model [17] justifies the new approach to the problem of the orientational instability of planar liquid-crystal layers in ultrasonic fields. The result obtained is important not only for the establishing the mechanism for this phenomenon, but also as one more step on the way of studying the role of relaxation processes in rearrangement of the macrostructure of mesophase layers in ultrasonic fields.

ACKNOWLEDGMENTS

The study was supported by the International Science Foundation, project no. J 70 100 and the Russian Foundation for Basic Research, project no. 00-02-17732.

REFERENCES

1. G. E. Zvereva and A. P. Kapustin, Primen. Ul'traakust. Issled. Veshchestva **15**, 69 (1961).
2. P. Williams, J. Chem. Phys. **39**, 384 (1963).
3. L. M. Blinov, *Electro-Optical and Magneto-Optical Properties of Liquid Crystals* (Nauka, Moscow, 1978; Wiley, New York, 1983).
4. A. P. Kapustin and L. M. Dmitriev, Kristallografiya **7** (2), 332 (1962) [Sov. Phys. Crystallogr. **7**, 263 (1962)].
5. E. Guyon and P. Pieranski, Phys. Rev. A **9**, 404 (1974).
6. E. Guyon, Phys. Rev. Lett. **39** (20), 1280 (1977).
7. A. P. Kapustin and O. A. Kapustina, *Acoustics of Liquid Crystals* (Nauka, Moscow, 1985).
8. O. Kapustina, Mol. Cryst. Liq. Cryst. **112** (1–2) (1984).
9. O. Kapustina, in *Handbook of Liquid Crystals*, Ed. by D. Demus *et al.* (Wiley-VCH, Veinheim, 1998), Vol. 1, Ch. 11, p. 549.
10. P. de Gennes, *The Physics of Liquid Crystals* (Clarendon, Oxford, 1974; Mir, Moscow, 1977).
11. S. A. Pikin, *Structural Transformations in Liquid Crystals* (Nauka, Moscow, 1981).
12. D. I. Anikeev and O. A. Kapustina, Zh. Éksp. Teor. Fiz. **110** (4), 1328 (1996) [JETP **83**, 731 (1996)].
13. D. I. Anikeev, O. A. Kapustina, and V. N. Lupanov, Zh. Éksp. Teor. Fiz. **100** (1), 194 (1995) [Sov. Phys. JETP **73**, 109 (1991)].
14. E. N. Kozhevnikov, Zh. Éksp. Teor. Fiz. **92** (4), 1306 (1987) [Sov. Phys. JETP **65**, 731 (1987)].
15. I. N. Gurova and O. A. Kapustina, Pis'ma Zh. Éksp. Teor. Fiz. **63** (11), 866 (1996) [JETP Lett. **63**, 907 (1996)].
16. K. Miyano and J. Ketterson, Phys. Rev. A **12**, 615 (1975).
17. E. N. Kozhevnikov, in *Proceedings of the VI All-Union Conference on Liquid Crystals, Chernigov, 1988*, Vol. 1, p. 121.
18. A. P. Kapustin and G. E. Zvereva, Kristallografiya **10** (5), 723 (1965) [Sov. Phys. Crystallogr. **10**, 603 (1965)].
19. A. P. Kapustin, Izv. Vyssh. Uchebn. Zaved., Fiz., No. 11, 55 (1967).
20. O. A. Kapustina, Akust. Zh. **20** (1), 1 (1974) [Sov. Phys. Acoust. **20**, 1 (1974)].
21. A. P. Kapustin, *Electro-optical and Acoustical Properties of Liquid Crystals* (Nauka, Moscow, 1973).
22. A. P. Kapustin, *Experimental Studies of Liquid Crystals* (Nauka, Moscow, 1978).
23. S. Candau and S. Letcher, in *Advances in Liquid Crystals*, Ed. by G. Brown (Jordon and Breach, New York, 1978), Vol. 3, p. 163.
24. P. Khabibullaev, E. Gevorkyan, and A. Lagunov, in *Reology of Liquid Crystals* (Allerton, New York, 1994), Chaps. 3.2, 6.3, 6.4.

Translated by A. Zolot'ko

Crystallography Reports, Vol. 46, No. 1, 2001, pp. 111–113. Translated from Kristallografiya, Vol. 46, No. 1, 2001, pp. 121–123.

LIQUID CRYSTALS

Effect of Magnetic Field on Lyotropic Nematic in the Vanadium Pentoxide (V_2O_5)–Water System

É. V. Generalova, A. V. Kaznacheev, and A. S. Sonin

Nesmeyanov Institute of Organoelement Compounds, Russian Academy of Sciences, ul. Vavilova 28, Moscow, 117813 Russia

Received July 6, 1999

Abstract—The optical textures of anisotropic phases of dispersed aqueous vanadium pentoxide solutions have been studied. It was established that the application of a magnetic field to these phases results in the formation of transient magnetohydrodynamic domains. The evaluation of the Freedericksz threshold field for the *S*-effect provided the determination of the elastic constant, $K_1 \approx 3.6 \times 10^{-7}$ dyn. It is concluded that the studied anisotropic phases can be related to nematics. © *2001 MAIK "Nauka/Interperiodica".*

As far back as 1912, Zocher [1] discovered that dispersed aqueous vanadium pentoxide solutions form optically anisotropic phases. The detailed studies performed in the period from 1920 to 1960 (see review [2]) showed that these phases are gradually formed from an isotropic 1% solution, which is accompanied by the gradual layering of the solution into sol and gel with the concentration boundary between them being located at 18 wt % V_2O_5.

Both sols and gels are optically anisotropic. In isotropic dispersed solutions, the sol formation is preceded by the formation of a two-phase region where the anisotropic domains of a spindlelike shape are formed (the so-called tactoids). In the anisotropic sol phase, layering results in the formation of isotropic domains having a shape similar to that of tactoids (the so-called atactoids).

All the above properties (and first and foremost, anisotropy) allowed Zocher to relate the phases formed in the dispersed aqueous vanadium pentoxide solutions to the liquid–crystals [3].

Recently, the interest in this system has been increased. However, no new reliable evidence for nematic ordering in these phases was obtained. The only exception is new X-ray data obtained on the flow-oriented samples which showed orientation ordering in the samples and allowed the calculation of the order parameter [4, 5]. However, the photographs of the optical textures of sols and gels bear no resemblance to the textures characteristic of nematic mesophases. The absence of any effect of electric and magnetic fields on these phases casts serious doubt on the nematic nature of these phases.

In this connection, we performed a detailed study of the optical textures of dispersed aqueous vanadium pentoxide solutions, including the effect of magnetic fields on these textures.

A dispersed aqueous vanadium pentoxide solution was prepared by the Biltz method [6] as follows: 1 g of ammonium vanadate was pulverized in a mortar together with 10 ml of 2*N* hydrochloric acid. The orange mixture thus obtained was washed with distilled water on a Büchner funnel. Light yellow waste water was removed prior to the formation of a red-brown liquid. The remained liquid was filtered separately. Then, 50 ml of distilled water was added to the filtrate obtained; the mixture was shaken. A dark red solution was poured into a high narrow cylinder with a ground stopper. As a result of the natural 5-month-long sedimentation at room temperature, we managed to isolate the dispersed phases of aqueous solutions with seven different V_2O_5 concentrations from 0.4 to 2.1 wt %. All these phases proved to be sols.

The samples studied were the dispersed phases packed into flat capillaries of a diameter ~ 100-μm due to natural flow and then were hermetically glued with picein. The optical textures of the samples obtained in crossed polarizers are shown in Fig. 1. The sols with the V_2O_5 concentration ranging from 0.4 to 0.75 wt % were two-phase systems. They had different values of the mesophase–isotropic phase volume ratios, with the fraction of the mesophase being higher the higher the V_2O_5 concentration. Figure 1a shows a two-phase domain of dispersed aqueous vanadium pentoxide solution at the V_2O_5 concentration of 0.7 wt %. In addition to the nematic mesophase, one can also see the droplets with the textures similar to those of the thermotropic nematics. At the V_2O_5 concentrations of 1.3 (Fig. 1b) and 1.4 wt % (Fig. 1c), a mesophase with the fine schlieren texture is observed. Finally, the sols with the V_2O_5 concentration 2.1 wt % had an unusual "spotted" texture (Fig. 1d).

Using the polarization-optical technique, we measured birefringence Δn in samples with planar orientation. Birefringence of dispersed aqueous vanadium

1063-7745/01/4601-0111$21.00

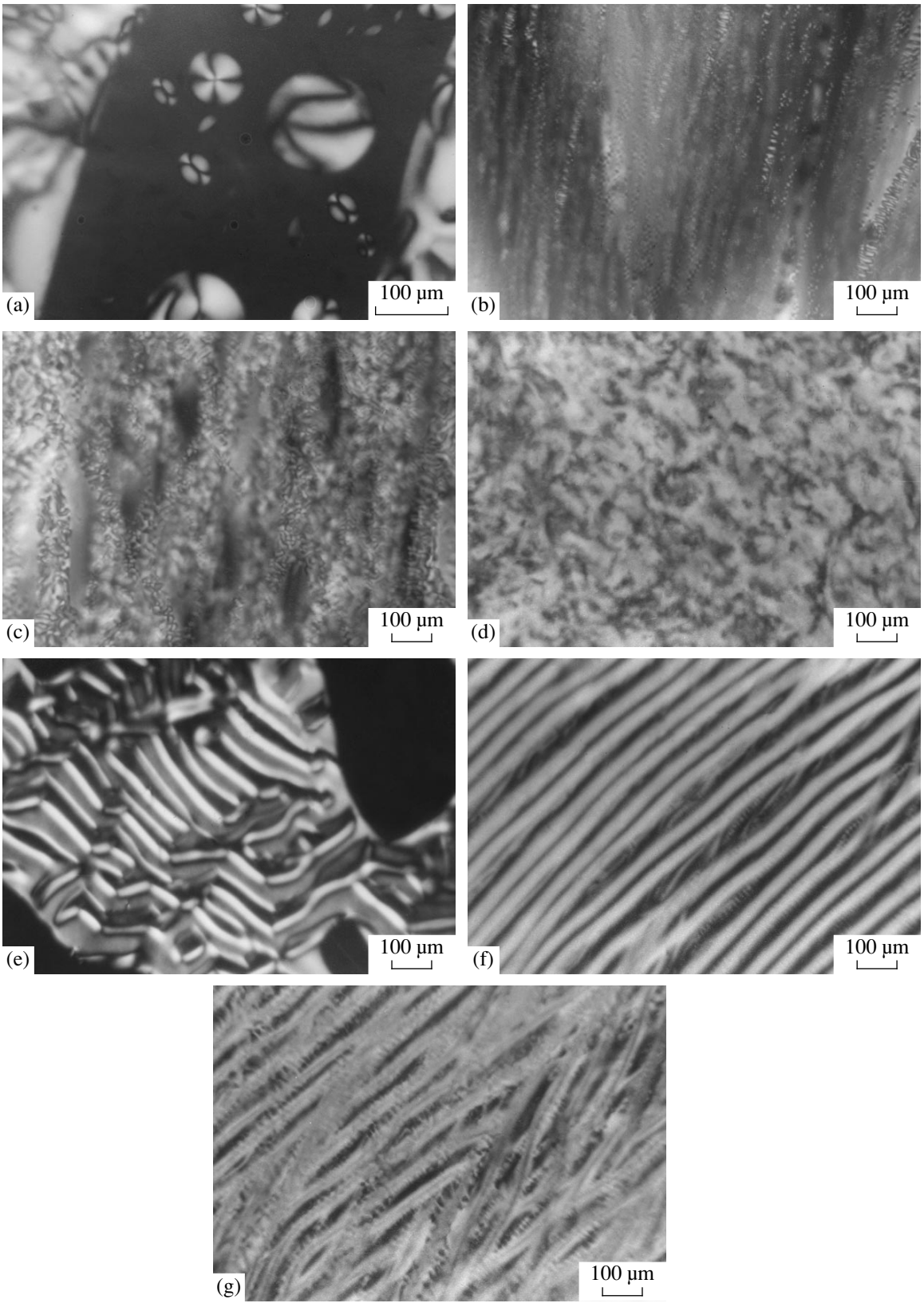

Fig. 1. (a–d) Textures of the nematic phase in the vanadium pentoxide–water system and the (e–g) transient domains formed due to application of the magnetic field H = 18 kOe at different vanadium pentoxide concentrations (a, e) 0.7; (b, f) 1.3; (c, g) 1.4, and (d) 2.1 wt %.

pentoxide solutions at the V_2O_5 concentrations of 0.75 and 1.3 wt % determined at 17°C was $\Delta n \approx 1.3 \times 10^{-3}$.

To confirm the nematic nature of ordering of the sols, the latter were placed for 15 min into an external magnetic field of the strength of H = 18 kOe. The field was applied normally to the cell plane. The textures formed due to the magnetic field effect are shown in Fig. 1 together with the initial textures described earlier. It is seen that the magnetic field gives rise to the formation of transient domains [7–9]. Depending on the V_2O_5 concentration in the samples, either a uniform (Fig. 1f) or a parquetlike (Fig. 1g) domain system is formed, which is similar to that observed in the tobacco–mosaic virus–water system [9]. Different types of domain patterns indicate a possible concentration dependence of the elastic and viscous coefficients of the nematic phase of the V_2O_5–water system. These results show that sols with the vanadium pentoxide concentrations ranging from 0.5 to 1.4 wt % are nematic phases. At the same time, the samples with the "spotted" texture (Fig. 1d) are not affected by magnetic fields with up to 20 kOe strength. Therefore, the question about their classification remains open and calls for further investigation.

We also evaluated the splay elastic constant K_1. It is well known [10] that

$$H_{F1} = \pi/d(K_1/\chi_a)^{1/2}, \quad (1)$$

where H_{F1} is the threshold Freedericksz field, χ_a is the anisotropy of magnetic susceptibility, and d is the layer thickness. To obtain the H_{F1} value, we applied magnetic fields of different strengths to a 100-μm-thick sample. The application of the field of $H \approx 6$ kOe did not provide any sample orientation. This field was taken to be the threshold Freedericksz field H_{F1}. Then, Eq. (1) yields K_1/χ_a = 360 dyn. The magnitude of χ_a was evaluated as follows. For a V_2O_5 crystal, we have $\chi_m = 1.1 \times 10^{-9}$ m^3/kg, $\rho = 3.36 \times 10^3$ kg/m^3 [11], where χ_m is the mass magnetic susceptibility and ρ is the density. With due regard for additivity of magnetic properties, the magnetic susceptibility of a V_2O_5 molecule is $\chi^{(1)} = 3.3 \times 10^{-28}$. In aqueous V_2O_5 solution with the concentration ~1 wt %, the number of V_2O_5 molecules is $N \approx 3.3 \times 10^{19}$. Then, the magnetic susceptibility of such a solution equals $\chi = N\chi^{(1)} \approx 10^{-8}$. Assuming that $\chi_a \sim 0.1\chi$, we have $\chi_a \sim 10^{-9}$. Using the above K_1/χ_a and χ_a values, we finally obtain $K_1 \approx 3.6 \times 10^{-7}$ dyn.

Thus, the observed phases of the V_2O_5–water system are really nematic ones. The obtained birefringence Δn and elastic constant K_1 values are in good agreement with the analogous values for the lyotropic liquid crystals [12, 13]. However, the range of V_2O_5 concentrations 0.5–1.4 wt %, in which the nematic phase was observed, is inconsistent with the range 2–18 wt % reported earlier [2]. Moreover, we found that the optical anisotropy can disappear under the effect of ultrasound. Furthermore, the as-prepared dispersed aqueous vanadium pentoxide solutions placed into flat capillaries respond fairly rapidly (within ~5 min) to the applied magnetic field. The response time of the same substance in a capillary measured a month later is ~15 h, but the appearance of the texture remained unaltered. The above facts can be associated with the change in elastic and viscous coefficients of the nematic phase dependent on the size of the structural units during the ageing process. Thus, it seems that the system is not in equilibrium and is characterized by a very slow growth of the structural units. In this case, the system parameters such as elastic constants and viscosity coefficients are determined not only by concentration and temperature but also by the dimensions of the structural units.

ACKNOWLEDGMENTS

The study was supported by the Russian Foundation for Basic Research, project no. 98-03-32810.

REFERENCES

1. H. Zocher, Z. Phys. Chem. **98**, 293 (1912).
2. A. S. Sonin, Kolloidn. Zh. **60**, 149 (1998).
3. H. Zocher, Mol. Cryst. Liq. Cryst. **7**, 751 (1969).
4. P. Davidson, A. Garreau, and J. Livage, Liq. Cryst. **16**, 905 (1994).
5. P. Davidson, C. Bourgaux, L. Shoutteten, *et al.*, J. Phys. II **5**, 1577 (1995).
6. W. Biltz, Ber. Deuh. Chem. Ges. **37**, 109 (1904).
7. E. Guyon, R. B. Meyer, and J. Salan, Mol. Cryst. Liq. Cryst. **54**, 261 (1979).
8. A. J. Hurd, S. Fraden, F. Lonberg, and R. B. Meyer, J. Phys. (Paris) **46**, 905 (1985).
9. S. Fraden, A. J. Hurd, R. B. Meyer, *et al.*, J. Phys. Colloq. **46** (3), C3-85 (1985).
10. P. de Gennes, *The Physics of Liquid Crystals* (Clarendon, Oxford, 1974; Mir, Moscow, 1977).
11. *Physical Quantities. Handbook*, Ed. by I. S. Grigor'ev and E. Z. Meĭlikhov (Énergoizdat, Moscow, 1991).
12. A. S. Sonin, Usp. Fiz. Nauk **153**, 273 (1987) [Sov. Phys. Usp. **30**, 875 (1987)].
13. A. V. Golovanov, A. V. Kaznacheev, and A. S. Sonin, Izv. Akad. Nauk, Ser. Fiz. **59** (3), 82 (1995).

Translated by A. Zolot'ko

Crystallography Reports, Vol. 46, No. 1, 2001, pp. 114–117. Translated from Kristallografiya, Vol. 46, No. 1, 2001, pp. 124–127.

Periodic-Shear-Induced Vortex Structures in Nematic Liquid Crystal

A. N. Chuvyrov and O. A. Skaldin

Institute for Physics of Molecules and Crystals, Ufa Research Center, Russian Academy of Sciences, pr. Oktyabrya 151, Ufa, 450075 Bashkortostan, Russia

Received March 15, 1999

Abstract—The effect of the periodic shear in the ultrasonic range on a homeotropically oriented layer in a nematic liquid crystal has been studied. The formation of a vortex lattice whose points are the centers of autowaves is established. The formation and stability of the vortex lattice are shown to be related to the processes of synchronization of spatial oscillators (autowave centers) and their interactions, as well as to the processes of self-organization. © *2001 MAIK "Nauka/Interperiodica".*

INTRODUCTION

Recently, considerable attention is given to self-organization processes in dissipative structures. One of the well-known examples of such processes is the Belousov–Zhabotinskiĭ reaction [1]. The possible existence of two-dimensional orientation autowaves in nematic liquid crystals (NLC) under simultaneous effect of periodic shear of the ultrasonic range and dc-field was shown in [2, 3].

In this study, we showed for the first time that a similar result can also be obtained without the application of a dc-field to an NLC layer, which is of great importance for better understanding the nature of this phenomenon. We also consider here the formation, stability, and spatial–temporal synchronization of two-dimensional oscillators (autowave centers) as well as their self-organization into a vortex lattice.

EXPERIMENTAL

The effect of periodic shear on an NLC was studied on the well-known compound—methoxybenzilidene-4'-*n*-butylaniline (MBBA) with the known parameters [4]. An NLC was placed into a sandwichlike cell (Fig. 1), one substrate of which was a glass coated with a semitransparent conducting chromium layer and the other, a 10 × 15-mm^2-large plate of piezoelectric $Bi_{12}SiO_{20}$ crystal, both surfaces of which were coated with semitransparent chromium films (electrodes). A plate cut out from a piezoelectric crystal along the (100) plane provided the generation of ultrasonic vibrations along the surface, whereas the chromium layers on the substrates provided the homeotropic alignment of the NLC and, at the same time, were the electrodes. The amplitude and the frequency of ac-voltage applied to the piezoelectric crystal ranged within 0–100 V and 10–100 kHz, respectively. Higher shear amplitudes (up to 10^{-6} cm) were obtained at the resonance frequency of the crystal vibrations. The NLC thickness (40 μm) was set by mica spacers. The cell was mounted on the objective table of an Amplival-Pol.U polarizing microscope. The polarization-optical measurements were made with the use of an SFN-10 LOMO spectrophotometric attachment supplied with a set of microprobes.

RESULTS AND DISCUSSION

The application of ac-voltage $U_1 = 30$ V ($f = 40$ kHz) to the electrodes made the homeotropic orientation of molecules in the NLC layer unstable (a bright NLC layer in crossed Nicols). At higher voltages, a tilt angle of an NLC director increases and, upon the attainment

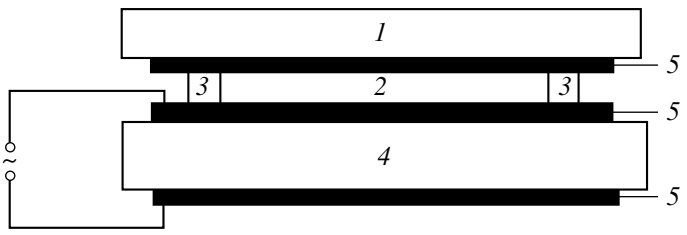

Fig. 1. Schematic of the experimental setup: (*1*) glass plate, (*2*) nematic liquid crystal, (*3*) mica spacer, (*4*) piezoelectric crystal, and (*5*) deposited semitransparent chromium films.

1063-7745/01/4601-0114$21.00 © 2001 MAIK "Nauka/Interperiodica"

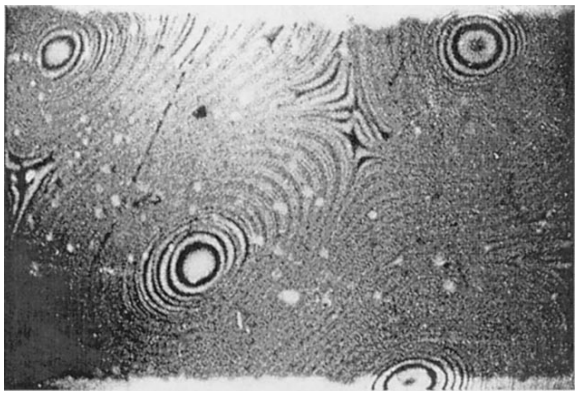

Fig. 2. Micrograph of a fragment of a vortex lattice (magnification ×10).

of the second threshold voltage, $U_2 = 40$ V, the director orientation becomes unstable [5], and a system of arbitrary shaped closed curves is formed, which propagate in the plane of the LC layer and, gradually, acquire the circular or elliptical shape. A fragment of such structure is shown in Fig. 2. The dynamics of curve motion indicate the existence of specific centers where these curves are periodically formed. Thus, these closed curves are, in fact, radial orientational waves. Usually, the director orientation at the wave front is constant; a 10 × 10-mm^2-large sample has from 6 to 8 such centers. Earlier, it was shown that this process had the autowave nature [3].

Consider the properties of an individual vortex in more detail. The director orientation varies periodically along any arbitrary direction (e.g., along the 0x axis of the x0y plane), which coincides with the plane of the NLC layer (Fig. 3a). In fact, Fig. 3a shows the distribution of the NLC director projected onto the NLC plane at a certain moment. The formation and the dynamics of the optical pattern (a system of bright and dark rings) is determined by the periodicity and the director rotation over a cone surface at each point of the x0y plane. In this case, the NLC director in crossed Nicols changes the orientation by an angle of $\pi/2$ in the transition from one ring to the other (e.g., from dark to bright one). Thus, the rotation of a director by the angle of 2π rad results in the formation of four dark and four bright rings, Topologically, this is equivalent to the formation of two disclinations with the Frank indices $m = \pm 1$ "pulled over" onto a singular point (center), which is the source of radial phase waves. Figure 3b shows the temporal evolution of the light flux $I(t)$ passed through the NLC area of far wave-center zones. The full revolution of the NLC director corresponds to the formation of a wave packet consisting of four fronts. It was shown that this structure is unstable. The orientation waves generated in the center of the ring "increase" their radii and propagate to the periphery, which is not accompanied by the transfer of centers of molecule mass. It was also established that there exist both right and left vortices, so that the structure is a square vortex lattice in which the right- and the left-hand vortices are staggered. The absolute value of the rotation frequency of an individual vortex is equal to the rotation frequency of the director, which linearly depends on the applied voltage up to saturation (Fig. 4). The saturation region is determined by the dynamics of the director reorientation (when the angle of its deviation from the homeotropic orientation becomes appreciable [4] and the torque induced by oscillating flows ceases to increase). It should also be emphasized that the total torque of the lattice equals zero.

Now, consider problems of the lattice formation by such centers (vortices), its stability, the spatial–temporal synchronization, and the effect of the boundary of the region of orientation-wave propagation. It was shown that the angular velocity of the director rotation is constant in the plane of the NLC layer, $\Omega(\mathbf{r}) = \text{const}$. However, in the space, the wave vector of this structure cannot be constant. As shown in [3], $R_n^2 \approx n$ (where n

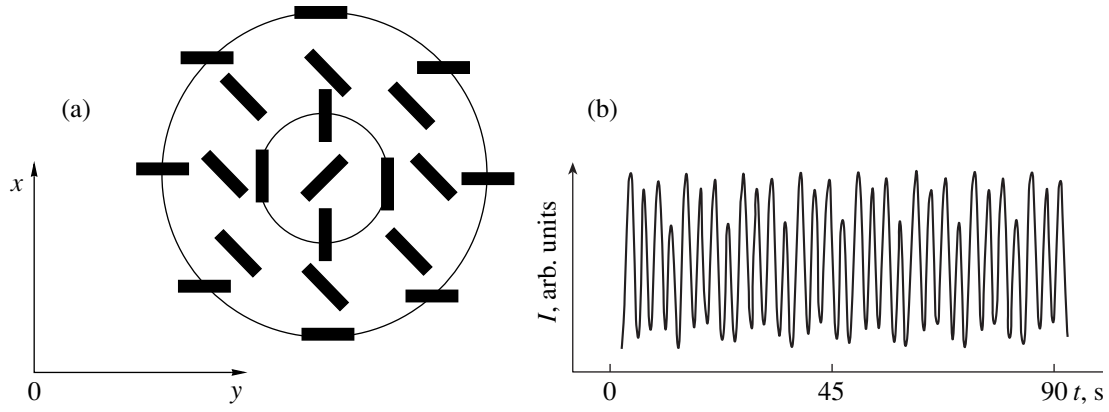

Fig. 3. (a) Spatial distribution of the director projected onto the plane of the NLC layer and (b) the intensity of the light transmitted by the cell in the far zones of an individual vortex versus time.

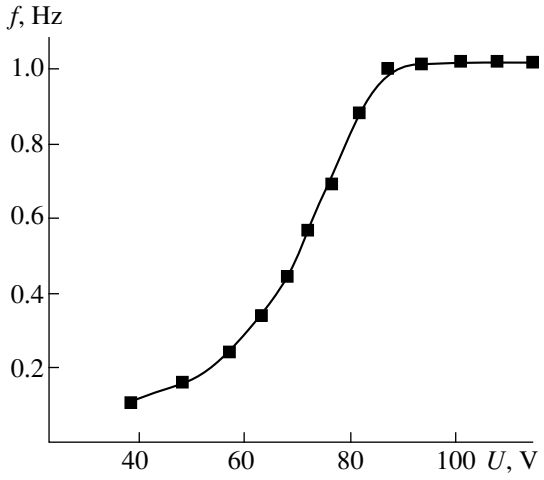

Fig. 4. The frequency f of the director rotation versus voltage U applied to the piezoelectric crystal.

is the number of the ring measured from the center). Performing some trivial transformations, one can determine the changes in the wave vector and establish the dependence of the phase velocity of the wave on the distance. Since $R_n^2 = An$, we have $(R_n^2)' = 2R_n\partial R_n/\partial n = A$, $2R_n\Delta R_n = A$, and $\Delta R_n = A/2R_n$. The wave vector equals $q = 2\pi/\Delta R_n = 4\pi R_n/A$, and, therefore, the modulus of q increases linearly with the distance from the center. Then, the phase velocity is

$$V = \Omega/q = A\Omega/4\pi R_n, \quad (1)$$

where Ω is the angular velocity of the director rotation and A is the proportionality factor. Hence, the wave velocity varies inversely proportional to the distance from the center. In other words, if the rotation velocity is constant, Eq. (1) shows that at large distances, the wave is decelerated. Then, the approximation to infinity, should lead to the halt of the wave packet and

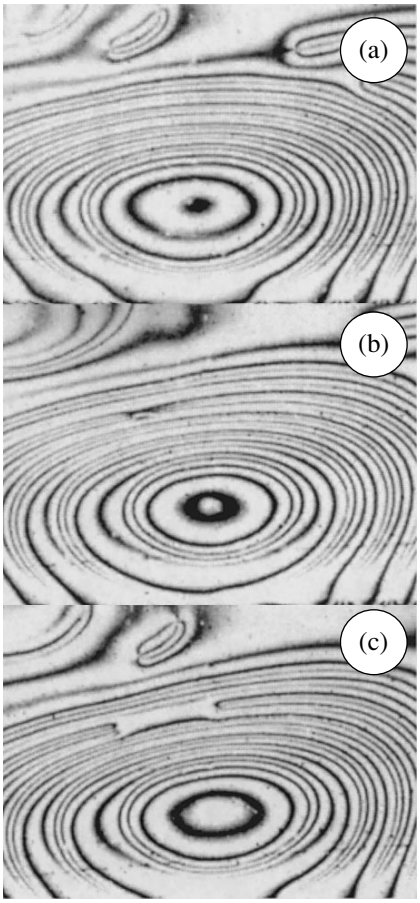

Fig. 5. Illustrating the formation of two disclinations in the far zones of an individual center: (a) of deformation of the wave packet and (b, c) break of the wave packet and spreading of disclinations (magnification ×50).

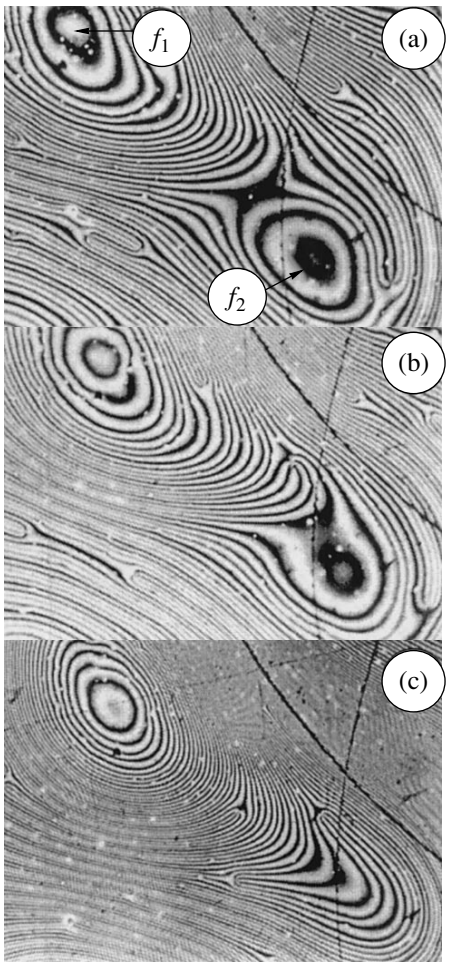

Fig. 6. Interaction of two centers with different frequencies of wave-packet generation ($f_1 > f_2$): (a) the initial stage of the process upon application of voltage U to the piezoelectric crystal and (b, c) suppression of the center with a lower frequency of generation of orientation waves (magnification ×50).

formation of a stationary "concentric structure." However, this situation is not implemented, because an increasing wave-vector modulus q would increase the density of the Frank elastic energy. On the other hand, there are some natural limitation imposed onto the existence of the spatial deformation of the director field associated with the spatial dimensions admitting the definition of the NLC proper [6]. Thus, the formation of the so-called wave-field "coat" should have stabilized the structure. However, the real situation is different. In far wave zones the wave packet becomes unstable (Figs. 5a, 5b) and can be broken, which results in the formation of a pair of disclinations with opposite signs (Fig. 5c), which annihilate along the path around the singular point (center). Considering the process in the reverse time direction, we see that the wave packet consisting of four fronts is equivalent to a pair of disclinations with the Frank indices $m = \pm 1$ pulled over the singular point. However, the presence of both right- and left-hand centers provides the lattice stabilization according to the source–sink mechanism (with some centers playing the role of sources and some other, of sinks).

For a better understanding the process of the vortex-lattice formation, we have to consider synchronization and interaction of individual centers with different rotation frequencies. The lattice formation is impossible without competition between different centers. In particular, it is reasonable to assume that centers with different frequencies of director rotation can be formed (Fig. 6a). This raises the question about the lattice formation or, in other words, about the "survival" of different centers. The study of the interactions between centers shows that the higher the rotation frequency ($f_1 > f_2$) of a center, the higher the probability of its survival. As is seen from Figs. 6b and 6c, the centers with low rotation frequencies are suppressed. All this leads to the following important conclusions: (1) A vortex lattice is stable if all the sources have the same frequencies of generation of orientation waves. (2) In such a system, only the spatial oscillators with the highest frequency [7] can "survive." However, unlike [7], the self-organization process in the case under study, gives rise to the formation of the vortex lattice by the centers having the identical properties.

Thus, we have established the formation of the vortex structure of the dissipative nature in rapidly oscillating nematic flows. We showed that this structure is stable only under the condition of the spatial-temporal synchronization of the lattice points (vortices) based on equal frequencies of spatial oscillators ($f_i = f_k$).

ACKNOWLEDGMENTS

The study was supported by the Program Integration Mathematical Modeling and Physics of Nonlinear Processes in Condensed Matter, project no. A0002.

REFERENCES

1. B. P. Belousov, in *Collection of Papers on Radiation Medicine Published in 1958* (Medgiz, Moscow, 1959), p. 145.
2. A. N. Chuvyrov, Zh. Éksp. Teor. Fiz. **82** (3), 761 (1982) [Sov. Phys. JETP **55**, 451 (1982)].
3. A. N. Chuvyrov, O. A. Scaldin, and V. A. Delev, Mol. Cryst. Liq. Cryst. **215**, 187 (1992).
4. L. M. Blinov, *Electro-Optical and Magneto-Optical Properties of Liquid Crystals* (Nauka, Moscow, 1978; Wiley, New York, 1983).
5. A. N. Chuvyrov, B. Kh. Mulyukov, and O. A. Skaldin, Kristallografiya **42** (1), 150 (1997) [Crystallogr. Rep. **42**, 138 (1997)].
6. P. de Gennes, *The Physics of Liquid Crystals* (Clarendon, Oxford, 1974; Mir, Moscow, 1977).
7. P. Schuster, Physica D (Amsterdam) **22**, 110 (1986).

Translated by A. Zolot'ko

Crystallography Reports, Vol. 46, No. 1, 2001, pp. 118–125. Translated from Kristallografiya, Vol. 46, No. 1, 2001, pp. 128–135.

LIQUID CRYSTALS

New Chiral Imines Based on *S*-α-Phenylethylamine and *S*-α-Benzylethylamine in Induced Cholesteric and Smectic Mesophases: II. Behavior of Chiral Dopants in Ester Liquid-Crystal Systems

G. P. Semenkova*, L. A. Kutulya*, N. I. Shkol'nikova*, and T. V. Khandrimaĭlova**

** Institute of Single Crystals, National Academy of Sciences of Ukraine, pr. Lenina 60, Kharkov, 310141 Ukraine*

*** Kharkov State University, pl. Svobody 4, Kharkov, 310077 Ukraine*

e-mail: kutulya@isc.kharkov.com

Received February 22, 1999

Abstract—The temperature dependences of the pitch of induced helical structures in the ester liquid-crystal systems containing hydroxyphenyl benzoate derivatives and chiral *N*-aroyloxybenzylidene-*S*-α-phenylethylamines or *N*-aroyloxybenzylidene-*S*-α-benzylethylamines have been measured. The twisting power of chiral dopants is calculated and the temperature dependence of the helical pitch in the induced cholesteric (*N**) and smectic *C** mesophases is quantitatively characterized. The parameters $A = dT_{is}/dC$ that characterize the effect of dopants on the thermal stability of the *N** phases are determined from the concentration dependences of the cholesteric–isotropic transition temperature T_{is} for the *n*-hexyloxyphenyl-*n*-butylbenzoate–chiral dopant systems. The results obtained are compared with the data for the 4-*n*-pentyl-4'-cyanobiphenyl (5CB)-based cholesteric systems induced by the chiral dopants under consideration. © *2001 MAIK "Nauka/Interperiodica".*

1. INTRODUCTION

Earlier [1, 2], we investigated the regularities of changes in the efficiency of inducing the helical ordering (twisting power β) for systematic series of nonmesogenic chiral dopants (α,β-unsaturated ketones with a fixed molecular conformation) and their influence on the thermal stability of induced cholesteric (*N**) phases. We formulated the general requirements for the molecular structure of strongly twisting chiral dopants: the presence of a sufficiently extended π-electron or other highly polarizable fragment in the molecule, anisometry and a high degree of molecular chirality (the chiral–anisotropic form), and conformational homogeneity. For the most part, these requirements were confirmed in the investigations of chiral dopants with conformationally labile chain molecules (*N*-arylidene-*S*-α-phenylethylamines and *N*-arylidene-*S*-α-benzylethylamines) in liquid-crystal systems based on 4-*n*-pentyl-4'-cyanobiphenyl (5CB) [3, 4]. It was found that a high degree of molecular chirality is reached when the substituents at the chiral center considerably differ in their bulk and polarization properties [3]. For the conformationally labile compounds, the high twisting power in the *N** mesophases becomes possible only in the case when the coexisting conformers are characterized by the same sign of twisting power [4].

In the analysis of the efficiency of inducing the helical ordering in achiral mesogen–chiral dopant systems, Gottarelli *et al.* [5–8] attached much importance to the structural similarity of components. In this respect, we examined the behavior of *N*-aroyloxybenzylidene derivatives of *S*-α-phenylethylamine (**I**) and *S*-α-benzylethylamine (**II**) in structurally similar liquid-crystal solvents of the phenyl benzoate class

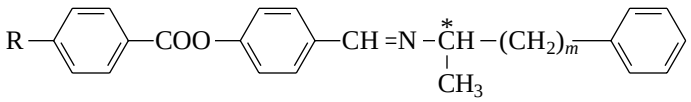

$m = 0$; R = H (**Ia**), R = CH_3 (**Ib**), R = CH_3O (**Ic**), R = $C_{10}H_{21}O$ (**Id**), R = C_6H_5 (**Ie**), and

R = $C_nH_{2n+1}C_6H_4$ at n = 1, 4–9 (**If**–**Il**);

$m = 1$; R = $C_nH_{2n+1}O$ at n = 7, 9, and 10 (**IIa**–**IIc**) and R = $C_nH_{2n+1}C_6H_4$ at n = 5–9, 11 (**IId**–**IIi**).

Here, the chiral center is labeled by the asterisk. The results obtained were discussed and compared with the data for systems based on 5CB.

1063-7745/01/4601-0118$21.00 © 2001 MAIK "Nauka/Interperiodica"

2. EXPERIMENTAL

The synthesis of chiral dopants **I** and **II** was described in [4]. Compounds **Ib** and **Ic** were first obtained by the interaction of 4-formylphenyl-4'-methylbenzoate and 4-formylphenyl-4'-methoxybenzoate with *S*-α-phenylethylamine according to the procedure similar to that used in [4] and were purified by crystallization from petroleum ether. The yields of **Ib** and **Ic** were equal to 65 and 62%, respectively. The IR spectra of the compounds prepared as solutions in carbon tetrachloride were recorded on a Specord-75. IR (ν, cm^{-1}): ν(C=O) 1742 (**Ib**) and 1739 (**Ic**); ν(C=N) 1650 (**Ib** and **Ic**). Chiral dopants **Ia**–**Ig** and **IIa**–**IIc** are nonmesogenic, and compounds **Ih**–**Il** and **IId**–**IIi** form smectic mesophases, as a rule, of the *SmA* type [4].

As achiral liquid-crystal solvents, we used esters **II**–**V**[1]

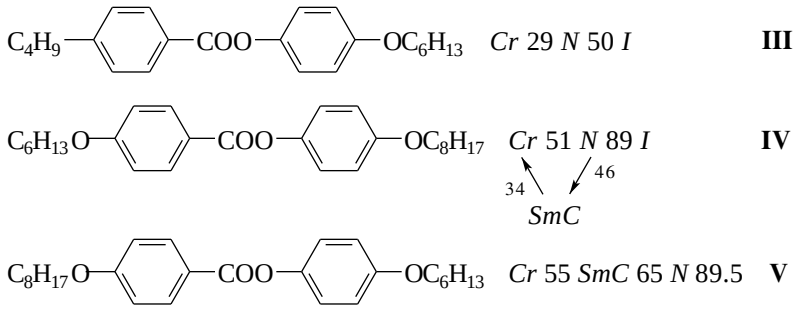

where *Cr* is the crystalline phase, *SmC* is the smectic *C* phase, *N* is the nematic phase, and *I* is the isotropic phases. Hereafter, the transition temperatures are given in Celsius degrees.

The helical pitch *P* in the induced *N** and smectic *SmC** phases of liquid-crystal systems were measured by the Grandjean–Cano method in a similar way as described in [10]. The temperature gradients of the helical pitch $dP/d(T_{is} - T)$ (where T_{is} is the cholesteric–isotropic transition temperature) were calculated within a linear approximation (the correlation coefficient r = 0.90–0.99; in most cases, r = 0.98–0.99). In calculations, the experimental data that corresponded to the temperatures differing from T_{is} by less than 4 K were ignored, because a rather sharp decrease in *P* is usually observed in the pretranstion range.

The twisting power β was calculated by the formula

$$\beta = 1/PC,$$

where *C* is the chiral dopant concentration in mole fractions and *P* is the helical pitch in microns. The chiral dopant concentration in liquid-crystal solutions in measurements of *P* and β varied from 0.01 to 0.02 mole fractions.

The temperatures T_{is} for the studied *N** systems were measured on an instrument for determination of melting temperatures with an accuracy of no worse than 0.1 K [2]. The slope of a linear portion in the concentration dependences of the T_{is} temperature (parameter *A*) at chiral dopant concentrations ranging from 0.5 to 10 mol % was used as a quantitative characteristic of the effect of chiral dopants on the thermal stability of *N** phases. The *A* parameter was calculated in a linear approximation (r = 0.98–0.99).

The phase transition temperature of the liquid-crystal solvents and the changes in enthalpy Δ*H* of the transition from the nematic to isotropic phase ($N \longrightarrow I$) for liquid crystals **III** and 5CB were measured by the differential scanning calorimetry on a Mettler TA 3000 thermoanalytical system. The measurements were carried out upon heating and cooling at a rate of 2 K/min.[2]

3. RESULTS AND DISCUSSION

3.1. Twisting power of chiral dopants. As can be seen from the β values listed in Table 1, the twisting power of chiral dopants **I** and **II** in the induced *N** mesophases of ester mesogens **III**–**V** is less than that in similar liquid-crystal systems based on 5CB. This regularity can be explained by the structural similarity between molecules of liquid crystals **III**–**V** and studied chiral dopants **I** and **II**: all these compounds contain the phenyl benzoate fragment. This assumption is supported by almost identical values of β in eutectic liquid-crystal systems based on phenyl benzoates and cyanobiphenyls for certain 2-arylidene-*n*-menthan-3-ones containing no ester groups [11]. The data reported in [11] also indirectly indicate that, for the given liquid crystals, the elastic constants K_{22} specifying the difference in twisting powers of chiral dopants in the induced cholesterics based on different nematics [8, 12, 13] do not differ considerably. Analysis of the available data on K_{22} for 5CB ($(3.2–3.4) \times 10^{-7}$ [14, 15], $\sim 5 \times 10^{-7}$

[1] The temperatures and types of phase transitions, which were determined in our experiments, agree closely with the data reported in [9].

[2] We are grateful to L.N. Lisetskiĭ for his assistance in performing the measurements.

Table 1. Twisting powers $|\beta|$ (μm^{-1} mole fraction^{-1}) of chiral dopants **I** and **II** in different liquid-crystal solvents

Chiral dopant	R	**III**	**IV**	**V**				5CB
		*N**	*N**	*N**	*SmC**			*N**
		at T^*_{red}	at T^*_{red}	at $T = T_{is} - 5$, °C	47°C	57°C	65°C	at T^*_{red}
Ia	H	19.9 ± 0.6	–	–	–	–	–	34.4 ± 1.5
Ib	CH_3	22.7 ± 3.6	14.9 ± 0.9	–	–	–	–	34.9 ± 1.6
Ic	CH_3O	21.4 ± 1.6	14.9 ± 0.4	–	–	–	–	35.7 ± 1.8
Id	$C_{10}H_{21}O$	20.5 ± 0.8	14.3 ± 0.6	15.5 ± 0.8	12.5 ± 1.9	10.4 ± 0.3	8.6 ± 1.7	40.4 ± 1.0
Ig	$C_4H_9C_6H_4$	–	17.6 ± 1.5	–	–	–	–	41.1 ± 2.0
Il	$C_9H_{19}C_6H_4$	21.9 ± 1.0	17.1 ± 0.4	17.3 ± 0.3	13.4 ± 1.5	11.0 ± 1.3	8.8 ± 1.5	43.2 ± 2.2
IIa	$C_7H_{15}O$	20.4 ± 0.1	–	–	–	–	–	27.3 ± 1.1
IIb	$C_9H_{19}O$	21.3 ± 0.4	–	–	–	–	–	27.7 ± 0.8
IIc	$C_{10}H_{21}O$	21.9 ± 0.8	14.6 ± 0.8	14.4 ± 0.7	–	–	–	26.4 ± 0.8
Id	$C_5H_{11}C_6H_4$	–	–	15.1 ± 2.9	7.1 ± 2.3	6.6 ± 1.9	6.1 ± 1.7	32.5 ± 1.3
IIe	$C_6H_{13}C_6H_4$	–	–	16.4 ± 3.6	6.7 ± 2.2	5.8 ± 0.9	5.1 ± 0.9	33.6 ± 1.8
IIf	$C_7H_{15}C_6H_4$	–	–	14.0 ± 2.0	8.5 ± 0.2	7.3 ± 0.8	6.5 ± 0.7	33.4 ± 1.1
IIh	$C_9H_{19}C_6H_4$	21.0 ± 1.4	13.4 ± 0.3	15.4 ± 2.3	8.4 ± 0.7	6.9 ± 0.6	5.7 ± 0.3	32.8 ± 1.0
IIi	$C_{11}H_{23}C_6H_4$	–	–	14.0 ± 1.7	–	6.5 ± 2.5	5.7 ± 2.5	34.6 ± 2.2

* T_{red} is the reduced temperature.

[16], and 7.2×10^{-7} dyn [17] at the reduced temperature $T_{red} = 0.98$ in all the cases) and some derivatives of hydroxyphenyl benzoate (2.8×10^{-7} dyn at $T_{red} = 0.98$ for 4-(*n*-pentyl)oxyphenyl-4-methoxybenzoate [18]), despite their scatter, suggests the higher elastic properties of 5CB as compared to ester nematics. This agrees with the fact that the degree of ordering of 5CB (the order parameter $S = 0.6$ at $T_{red} = 0.98$ [19]) is higher than that of ester nematic **III** ($S = 0.47$ at $T_{red} = 0.98$ [20]). The difference in physical properties of the nematics used could lead to an increase in the twisting power of chiral dopants in the systems based on esters **III**–**V** as compared to 5CB; however, this is inconsistent with the experimental results (Table 1). Therefore, the difference between the physical parameters of the ester nematics and 5CB is not responsible for different twisting powers of ester chiral dopants in these systems.

The found effect of the nematic nature on the twisting power of ester chiral dopants **I** and **II** substantially differs from the data obtained by Gottarelli *et al.* [5–8]. These authors noted that the β magnitudes for a series of chiral compounds increase in the liquid-crystal systems in which molecules of mesogen and chiral dopant are similar in shape.

A specific feature of the ester *N** phases consists in equalizing the twisting powers, depending on the structure of chiral dopants in the 5CB nematic matrix. Actually, in the 5CB-based systems, there is a clear differentiation between the β values for compounds **I** and chiral dopants **II** with a similar substitution and also for the compounds with different lengths of the π electron *N*-arylidene fragment (i.e., with one and two benzene rings in the R–C_6H_4CO– aroyl grouping) in both series of chiral dopants **I** (**Ia**–**Id**, **Ig**, and **Il**) and **II** (**IIa**–**IIi**) (Table 1, see also [3]). At the same time, the β values for the above chiral dopants in ester nematic **III** are virtually identical. The twisting power magnitudes $|\beta|$ for the *N** phases in the smectogenic *C* nematics **IV** and **V** are considerably less than those in the systems based on nematic **III**, and, correspondingly, the difference between these values and β_{5CB} increases (Table 1).

By analyzing the origin of the regularities describing the behavior of chiral dopants **I** and **II** in ester liquid crystals and 5CB, we should take into account several important factors: characteristic features in the molecular structure of the conformationally labile chiral compounds, structure and physical properties of the liquid-crystal solvents, and specific features of intermolecular interactions between components. It was found [4] that, for derivatives of *S*-α-phenylethylamine **I**, the possible conformations of isolated molecules due to hindered rotation about the N–C* bond are characterized by virtually the same molecular anisometry (α = 3.0–3.3 for conformers of compound **Ie**) and also by similar orientations of the phenyl and methyl substituents at the chiral center with respect to the axis of the *N*-arylidene fragment (see, for example, Fig. 1a). Therefore, the conformational transitions in these compounds occur without appreciable changes in the molecular geometry. By contrast, the derivatives of *S*-α-benzylethy-

lamine **II** have conformers of two types. The common feature of conformations of the first type is a nearly orthogonal mutual orientation of the axes of two nonconjugate π electron groupings (*N*-arylideneamine and benzyl) and, as a consequence, a relatively low molecular anisometry [α = 2.4–2.9 for model compound **II** with R = C_6H_5 (Fig. 1b)]. Conformers of the second type with the benzyl and arylideneamine groupings in the *trans* position relative to the N–C* bond exhibit a higher molecular anisometry [α = 4.1–4.6 (Fig. 1c)].

In chiral dopants **II**, conformers of the first type are more energetically favorable [4]. According to the X-ray structure analysis [21], the low-anisometry conformation of this type with a *gauche* arrangement of the N–C* and C(H_2)–C(phenyl) bonds with respect to the C*–C(H_2) bond is realized, for example, in crystals of *N*-(4-phenylbenzylidene)-*S*-α-benzylethylamine, whose chiral fragment is similar to that in chiral dopants **II**. However, a small calculated difference in the energies of conformations of two possible types for compounds **II** [4] suggests that the content of their high-anisometry forms in the orientationally ordered liquid-crystal medium can increase, specifically with an increase in the temperature and in the presence of an extended terminal substituent in molecules.

For high-anisometry conformers of compounds **II**, the phenyl group of the benzyl fragment is almost completely "inscribed" in the cross-section of a cylinder formed by the π electron *N*-arylidene grouping (Fig. 1c). This distinguishes chiral dopants **II** from compounds **I**, in which the above phenyl group in any conformations produces a large lateral protuberance, most likely, responsible for a higher degree of their chirality. In [4], these conformational differences were treated as a cause of the higher twisting power of imines **I** as compared to similar compounds **II** in the liquid-crystal systems based on 5CB with a high dielectric anisotropy. The conformational equilibrium of the studied chiral dopants in ester solvents can be considerably shifted compared to that in 5CB, because the physical properties (the temperature range of the *N** phase and dielectric anisotropy) and the chemical nature of these liquid crystals differ considerably. This can account for the fact that the quantitative regularities of changes in the twisting power of chiral dopants **I** and **II** in the ester liquid-crystal systems differ from those in the *N** mesophases based on 5CB: as noted above, the |β| values for chiral dopants with different structural groups are virtually identical.

3.2. Temperature dependences of the helical pitch in the induced cholesteric and smectic *C phases.** The temperature dependence of the helical pitch is an important characteristic of the helical ordering in liquid crystals. It follows from calculated gradients $dP/d(T_{is} - T)$ (Table 2) and also from Figs. 2 and 3 that, for the majority of the studied systems based on ester mesogens, the helical pitch in the *N** phase decreases with an increase in the temperature [positive

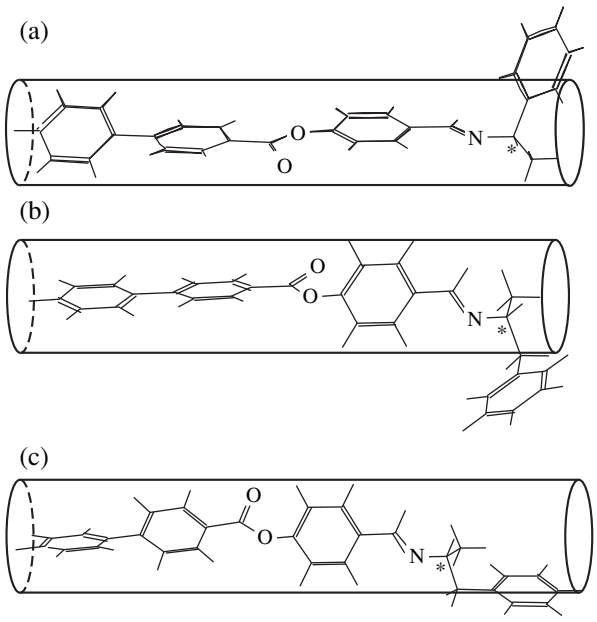

Fig. 1. Typical molecular conformations of imines (a) **I** and (b, c) **II** according to the molecular dynamics calculations for model compounds with R = C_6H_5. The chiral center is labeled by an asterisk.

values of $dP/d(T_{is} - T)$. By contrast, the dependence $dP/d(T_{is} - T)$ for mixtures of 5CB with chiral dopants **Ia**–**Ic** has the opposite character: the gradients $dP/d(T_{is} - T)$, even if small in magnitude, are negative. For the other chiral dopants of series **I** (**Id** and **Il**), the positive values of $dP/d(T_{is} - T)$ in the systems based on ester nematic **III** are substantially larger than those in 5CB. The opposite tendency is revealed in the systems containing chiral dopants **II**. The features observed in the dependences $P(T_{is} - T)$ for the used nematics reflect the differences both in their physical properties (the temperature range of the *N** phase, degree of ordering, and temperature dependence of K_{22}) and in the molecular structure of chiral dopants, specifically in their molecular anisometry. It should be noted that the temperature dependences of the order parameter *S* (and, probably, K_{22}) are virtually identical for 5CB and **III** [19, 20]. Consequently, the changes in $dP/d(T_{is} - T)$ are primarily determined by the structural features of chiral dopants and their interaction with the nematic medium.

It is characteristic that the dependences with the negative $dP/d(T_{is} - T)$ parameter are observed only in the 5CB-based systems containing chiral dopants with the least anisometric molecules **Ia**–**Ic** (according to the conformational analysis of **I** and **II** [4]). For the **III**–**Ia** system with nonmesogenic chiral dopant **Ia** that exhibits a relatively low molecular anisometry and contains no alkyl or alkoxy terminal groups, the *P* quantity virtually does not depend on the temperature (Fig. 2a, curve *1*; Table 2). A weak temperature dependence of *P* is also observed for nematic **III** upon introduction of

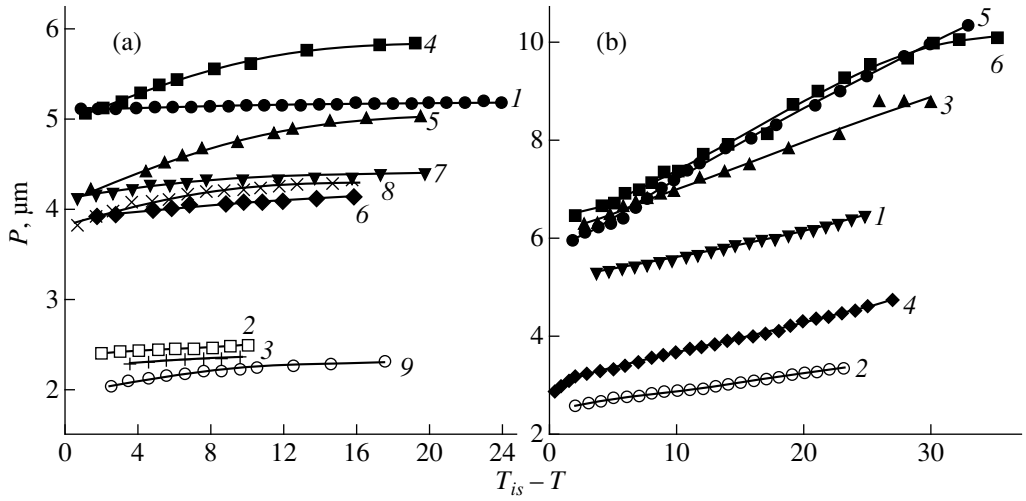

Fig. 2. Temperature dependences of the pitch of induced cholesteric helix in (a) the **III**–chiral dopant systems (concentration of the chiral dopand in mol % is given in parentheses): (*1*) **Ia** (0.97), (*2*) **Ib** (1.92), (*3*) **Ic** (2.11), (*4*) **Id** (0.89), (*5*) **Il** (0.95), (*6*) **IIa** (1.21), (*7*) **IIb** (1.10), (*8*) **IIc** (1.06), and (*9*) **IIh** (2.15) and (b) the **IV**–chiral dopant systems: (*1*) **Ib** (1.24), (*2*) **Ic** (2.41), (*3*) **Id** (1.01), (*4*) **Ig** (1.56), (*5*) **Il** (0.88), and (*6*) **Ih** (1.05).

chiral dopants **Ib** and **Ic** with terminal methyl and methoxy substituents (Fig. 2a, curves *2*, *3*). The dependences $P(T_{is} - T)$ considerably change in the case of the **III**-based liquid-crystal systems containing chiral dopants **I** with extended terminal groups (**Id** and **Il**): the pitch P substantially decreases as T_{is} is approached (Fig. 2a, curves *4*, *5*; Table 2). This is in agreement with the hypothesis that the molecular anisometry of chiral dopants affects the temperature dependence of P in the N^* phases [22]. Apparently, the chiral dopants with low-anisometry molecules can produce a disturbance of local orientational ordering that increases with temperature and leads to a certain untwisting of the helix. The introduction of alkyl or alkoxy terminal substituent into chiral dopant molecules can serve as a means of controlling the temperature dependence of the helical pitch in the induced N^* systems.

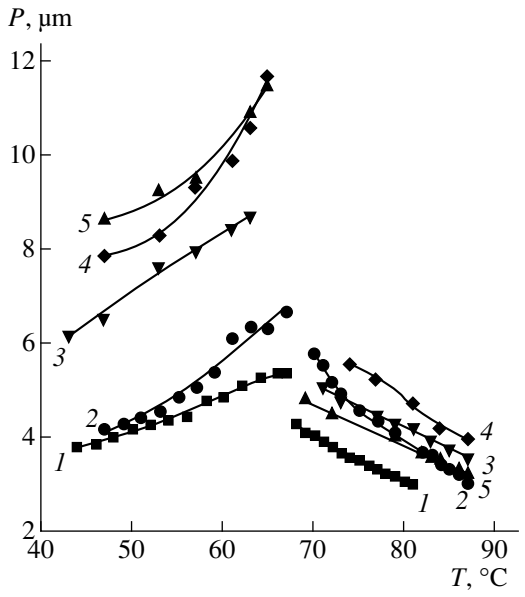

Fig. 3. Temperature dependences of the pitch of the induced cholesteric and smectic C* helices in the **V**–chiral dopant systems: (*1*) **Id** (1.99 mol %), (*2*) **Il** (1.79 mol %), (*3*) **IId** (1.78 mol %), (*4*) **IIe** (1.80 mol %), and (*5*) **IIh** (1.50 mol %).

It should be noted that the $dP/d(T_{is} - T)$ magnitudes for systems based on **III** with chiral dopants **I** are larger than those with chiral dopants **II** with the same length of the terminal substituent (Fig. 2a, Table 2; cf. data for **Id** and **IIc**, **Il** and **IIh**). A similar tendency is also observed for differences in the temperature dependences of the pitch of the helix induced by chiral dopants **I** and **II** in the case of liquid-crystal systems based on **IV** (Fig. 2b, Table 2). However, such a difference is not found for the 5CB-based systems (Table 2). A probable reason for the features observed in the behavior of chiral dopants is different conformational equilibria for compounds **II** in the ester and cyanobiphenyl systems. It seems likely that, compared to the cyanobiphenyl system, the ester system contains a larger amount of the low-anisometry and high-chirality forms of imine **II** (of the type shown in Fig. 1b) with a lower steric energy [4]. However, an increase in the temperature results in a certain increase in the fraction of their less energetically favorable high-anisometry conformers with a lower degree of chirality (Fig. 1c), which leads to a weaker increase in the helical twisting. These differences in the conformational dynamics of compounds **II** in different media are consistent with the fact that the differences observed in the twisting powers of chiral dopants **I** and **II** in 5CB-based systems are equalized in the ester liquid crystals (see Section 3.1).

Table 2. Parameter $dP/d(T_{is} - T)$ for the N^*-phases of liquid-crystal systems based on different nematics with chiral dopants **I** and **II**

Chiral dopand	R	$dP/d(T_{is} - T)$, μm/K			
		III	**IV**	**V**	5CB
Ia	H	0.003 ± 0.001	–	–	–0.012 ± 0.001
Ib	CH_3	0.010 ± 0.002	0.055 ± 0.002	–	–0.002 ± 0.001
Ic	OCH_3	0.010 ± 0.002	0.036 ± 0.001	–	–0.003 ± 0.001
Id	$OC_{10}H_{21}$	0.040 ± 0.011	0.099 ± 0.012	0.091 ± 0.008	0.013 ± 0.001
Ig	$C_4H_9C_6H_4$	–	0.062 ± 0.002	–	–
Il	$C_9H_{19}C_6H_4$	0.048 ± 0.008	0.145 ± 0.007	0.137 ± 0.017	0.032 ± 0.005
IIa	$C_7H_{15}O$	0.013 ± 0.003	–	–	0.018 ± 0.008
IIb	$C_9H_{19}O$	0.008 ± 0.004	–	–	0.019 ± 0.002
IIc	$C_{10}H_{21}O$	0.020 ± 0.004	0.057 ± 0.006	0.158 ± 0.010	0.021 ± 0.002
IId	$C_5H_{11}C_6H_4$	–	–	0.090 ± 0.023	–
IIe	$C_6H_{13}C_6H_4$	–	–	0.083 ± 0.006	0.031 ± 0.010
IIf	$C_7H_{15}C_6H_4$	–	–	0.089 ± 0.008	–
IIh	$C_9H_{19}C_6H_4$	0.015 ± 0.002	0.135 ± 0.009	0.130 ± 0.015	0.031 ± 0.009
IIi	$C_{11}H_{23}C_6H_4$	–	–	0.125 ± 0.039	–

The results obtained can also be interpreted under the assumption that, even at a relatively low content (1–2 mol %), chiral dopants **I** and **II** in the ester nematic liquid crystal affect its physical parameters (for example, the order parameter, elastic constants, and their temperature dependences), which indirectly reflects in the characteristics of helical twisting. Apparently, this effect differs for chiral dopants **I** and **II** with different chiral fragments. In turn, the manifestation of these effects in the ester liquid crystals, unlike the 5CB-based systems, can be supposedly explained by the possible formation of cybotaxic groups due to weak lateral dipole–dipole interactions between carbonyl groups or their interaction with π electrons of benzene rings (benzene complexes through carbonyl groups [23]). Undoubtedly, these cybotaxic groups also involve the chiral dopant molecules with the phenyl benzoate fragment. That is why the structural similarity of chiral dopants **I** and **II** to ester mesogens **III**–**V** is of importance. The intrinsic smectogenic properties of many chiral dopants [4] can also promote the formation of cybotaxic groups. This leads to a decrease in the twisting power of chiral dopants **I** and **II** in the ester liquid crystal as compared to that in 5CB and reflects in the temperature dependence of the helical pitch [11, 24].

It seems likely that both aforementioned factors—the features in the conformational dynamics of chiral dopants **I** and **II** in different media and the structural features of liquid-crystal solutions (the formation of cybotaxic groups involving the chiral dopant molecules)—simultaneously affect the microscopic characteristics of liquid-crystal systems in a symbate way.

Untwisting of the cholesteric helix with a decrease in the temperature can serve as a criterion for formation of cybotaxic groups in the ester N^* systems. This effect is especially pronounced in the presence of smectic mesophases: the monotropic (systems based on **IV**) or enantiotropic (systems based on **V**) smectic *SmC** phases (Figs. 2b, 3). In the systems based on liquid crystal **V**, the temperature dependence of the helical pitch P of the induced smectic *SmC** phase is the reverse of that for the N^* phase (Fig. 3).

3.3. Twisting power of chiral dopants in the smectic *SmC phase.** The helical smectic C^* phase in the systems based on liquid crystal **V** is induced by the introduction of small amounts (0.015–0.020 mole fractions) of anisometric chiral dopants **I** and **II** (Tables 1, 2), which, as a rule, are chiral mesogens [4]. In the binary **V**–chiral dopant systems, the twisting power of the studied chiral dopants in the smectic C^* phase is considerably less than that in the N^* phase (Table 1). At the same time, the $|\beta|$ values for all the studied dopants in the smectic C^* phase are of the same order of magnitude as those in the N^* phase in these liquid-crystal systems and differ by a factor of 1.5–2. This distinguishes the systems under consideration, for example, from *N*-salicylideneaniline derivatives [25], for which β_{N^*} and β_{SmC^*} differ by a factor of approximately 10. These differences can be associated with the structural features in the N^* phase of the ester systems, specifically with the presence of the cybotaxic groups, which are likely favorable for the efficient formation of the smectic C^* helix. As regards the structural features of the chiral dopant molecules, the twisting power of compounds **I** in the smectic C^* phase is higher than that of chiral dopants **II**, which is consistent with the relative degree of chirality of their molecules [4].

Table 3. Parameters *A* (K/mol %) for chiral dopants **I** and **II** in liquid-crystal systems **III**–chiral dopant

Chiral dopant	R	Parameter *A*	
		liquid crystal **III**	5CB
Ia	H	−1.53 ± 0.15	−1.88 ± 0.14 [4]
Ib	CH_3	−0.96 ± 0.03	−1.38 ± 0.03
Ic	CH_3O	−0.80 ± 0.02	−1.18 ± 0.04
Id	$C_{10}H_{21}O$	−0.54 ± 0.03	−0.71 ± 0.15 [4]
Ie	C_6H_5	−0.31 ± 0.04	−0.16 ± 0.10 [4]
If	$CH_3C_6H_4$	+0.37 ± 0.06	+0.48 ± 0.14 [4]
Ih	$C_5H_{11}C_6H_4$	+0.46 ± 0.04	–
Ii	$C_6H_{13}C_6H_4$	+0.47 ± 0.10	+0.66 ± 0.05
Ij	$C_7H_{15}C_6H_4$	+0.53 ± 0.06	+0.78 ± 0.06
Ik	$C_8H_{17}C_6H_4$	+0.48 ± 0.07	–
Il	$C_9H_{19}C_6H_4$	+0.52 ± 0.05	+0.66 ± 0.09 [4]
IIc	$C_{10}H_{21}O$	−0.17 ± 0.05	+0.07 ± 0.04
IId	$C_5H_{11}C_6H_4$	+1.02 ± 0.06	+1.73 ± 0.29 [4]
Ie	$C_6H_{13}C_6H_4$	+0.88 ± 0.06	+1.68 ± 0.12
IIf	$C_7H_{15}C_6H_4$	+0.97 ± 0.08	–
IIg	$C_8H_{17}C_6H_4$	+0.96 ± 0.06	–
IIh	$C_9H_{19}C_6H_4$	+1.02 ± 0.02	+2.02 ± 0.13

3.4. Effect of chiral *N*-arylideneamines on thermal stability of induced cholesteric phases. The parameters *A* for the studied chiral dopants in the ester liquid-crystal systems based on **III** are presented in Table 3. For comparison, the table lists the *A* parameters for 5CB. It is seen that the chiral dopants with R = H (**Ia**), CH_3 (**Ib**), OCH_3 (**Ic**), $OC_{10}H_{21}$ (**Id**), and C_6H_5 (**Ie**) in both liquid-crystal solvents show a disordering effect in the mesophase (the parameter *A* is negative [2, 4, 11]). This effect symbately weakens with an increase in the anisometry of dopant molecules upon introduction or elongation of alkyl or alkoxy substituent (compounds **Ia**–**Id**) and, especially, upon introduction of additional benzene ring (compounds **Ia** and **Id**). The chiral dopants containing terminal alkyl groups in the biphenylyl grouping (compounds **If**–**Il** and **IId**–**IIh**) exhibit a thermostabilizing effect in the mesophases (the *A* parameter is positive).

The parameter *A* depends on the nature of chiral dopants in the ester systems in much the same way as in the case of 5CB. It should be noted that the "sensitivity" of the T_{is} temperature to the presence of chiral dopants in the ester liquid crystals is somewhat less than that in the 5CB-based systems (Table 3; cf. parameters *A* in both nematics). Indeed, the disordering effect in the mixtures of **III** with chiral dopant **I**, as a rule, is weaker than that in the 5CB-based systems with the same dopants. A similar difference is observed for the thermostabilizing effect of chiral dopants **I** and **II** in the studied nematics. This difference is primarily associated with a stronger change in the enthalpy of the $N \longrightarrow I$ phase transition in the case of nematic **III** (ΔH = 1.19 and 0.84 kJ/mol upon cooling and heating, respectively), as compared to 5CB (according to our data, ΔH = 0.57 and 0.65 kJ/mol upon heating and cooling, respectively, and ΔH = 0.39 kJ/mol [26]).

It follows from Table 3 that, for chiral dopants **II**, the differences between the *A* parameters in two studied nematics are considerably larger than those for compounds **I**. Therefore, it can be assumed that these differences for the systems containing chiral dopants **II** are determined not only by the difference ΔH of the nematic–isotropic phase transition, but also by an additional essential factor. In [4], a profound stabilizing effect on the *N** mesophase in 5CB, and stronger intrinsic smectogenic properties of chiral compounds **II** as compared to dopants **I**, were explained by the ability of molecules **II** to adopt high-anisometry *trans* conformations (Fig. 1c) in the mesophases. It seems likely that a displacement of the conformational equilibrium of chiral dopants **II** in ester nematic **III** (in contrast with 5CB) toward the low-anisometry *gauche* forms (Fig. 1b) is the additional factor that is responsible for a substantial decrease in the thermostabilizing effect of chiral dopants **IId**–**IIh** in liquid crystal **III** as compared to 5CB. This interpretation is in agreement with the observed equalization of the differences in twisting powers of the studied chiral dopants in the ester nematic in comparison with 5CB (see Section 3.1). The regularities observed in variations of the parameter *A* can stem from the structural similarity of the studied chiral dopants to the ester mesogens and also from the corresponding structural features of the liquid-crystal solutions.

CONCLUSION

Compared to the liquid-crystal systems based on 4-pentyl-4'-cyanobiphenyl, the induced cholesteric systems that consist of achiral mesogenic hydroxyphenyl benzoate derivatives and structurally similar chiral dopants (*N*-aroyloxybenzylidene derivatives of *S*-α-phenylethylamine or *S*-α-benzylethylamine) are characterized by a considerable decrease in the efficiency of helical ordering and, in some cases, by a substantial change in the temperature dependence of the helical pitch.

The chiral dopants in the induced cholesteric *N** phases exhibit both disordering and stabilizing effects depending on the degree of anisometry of their molecules. The effect of dopants on the thermal stability of the *N** mesophases in the ester systems is less pronounced than that in the cyanobiphenyl systems.

The regularities revealed can be explained by the features in the molecular structure of chiral compounds [different equilibria between the low-anisometry (high-chirality) and high-anisometry (with a lower degree of chirality) conformers of the *S*-α-benzylethylamine

derivatives in liquid-crystal media of different nature and also by the specific microscopic structure of the liquid-crystal solutions (tendency toward formation of the cybotaxic groups in the case of ester mesogenic solvents and dissolved chiral dopants).

ACKNOWLEDGMENTS

This work was supported by the Ukrainian State Foundation for Basic Research, project no. 3.4 / 00399.

REFERENCES

1. L. A. Kutulya, I. B. Nemchenok, and T. V. Khandrimaĭlova, Kristallografiya **35** (5), 1234 (1990) [Sov. Phys. Crystallogr. **35**, 724 (1990)].
2. L. A. Kutulya, I. B. Nemchenok, and S. S. Oleĭnik, Kristallografiya **35** (5), 1242 (1990) [Sov. Phys. Crystallogr. **35**, 729 (1990)].
3. L. A. Kutulya, G. P. Semenkova, S. N. Yarmolenko, *et al.*, Kristallografiya **38** (1), 183 (1993) [Crystallogr. Rep. **38**, 97 (1993)].
4. L. A. Kutulya, G. P. Semenkova, N. L. Kramarenko, *et al.*, Funct. Mater. **1** (1), 128 (1994).
5. G. Gottarelli, M. Hibert, B. Samori, *et al.*, J. Am. Chem. Soc. **105** (25), 7318 (1983).
6. G. Gottarelli, G. P. Spada, R. Bartsch, *et al.*, J. Org. Chem. **51** (5), 589 (1986).
7. G. Gottarelli, P. Mariani, G. P. Spada, *et al.*, Tetrahedron **39** (8), 1337 (1983).
8. G. Gottarelli and G. P. Spada, Mol. Cryst. Liq. Cryst. **123** (1–4), 377 (1985).
9. *Liquid Crystal Database: Version 3.1* (Volkmar Vill, LCI, 1998).
10. N. L. Kramarenko, G. P. Semenkova, V. I. Kulishov, *et al.*, Kristallografiya **37** (5), 1266 (1992) [Sov. Phys. Crystallogr. **37**, 681 (1992)].
11. L. A. Kutulya, Doctoral Dissertation in Chemistry (Bogatskiĭ Physicochemical Institute, National Academy of Sciences of Ukraine, Odessa, 1992).
12. A. P. Fedoryako, Candidate's Dissertation in Physics and Mathematics (Institute of Single Crystals, National Academy of Sciences of Ukraine, Kharkov, 1990).
13. L. N. Lisetski and A. V. Tolmachev, Liq. Cryst. **5** (3), 877 (1989).
14. T. Toyooka, G.-P. Chen, H. Takezoe, and A. Fukuda, Jpn. J. Appl. Phys., Part 1 **26**, 1959 (1987).
15. H. J. Coles and M. S. Sefton, Mol. Cryst. Liq. Cryst., Lett. Sect. **4** (5), 123 (1987).
16. P. P. Karat and N. V. Madhusudana, Mol. Cryst. Liq. Cryst. **40** (1–4), 239 (1977).
17. H. Hakemi, E. F. Jagodzinski, and D. B. DuPre, J. Chem. Phys. **78** (3), 1513 (1983).
18. M. A. Osman, Hp. Schad, and H. R. Zeller, J. Chem. Phys. **78** (2), 906 (1983).
19. S. Sen, P. Brachma, S. K. Roy, *et al.*, Mol. Cryst. Liq. Cryst. **100** (3–4), 327 (1983).
20. V. V. Aleksandriĭskiĭ, V. V. Volkov, I. V. Novikov, *et al.*, Izv. Vyssh. Uchebn. Zaved., Khim. Khim. Tekhnol. **39** (3), 38 (1996).
21. L. A. Kutulya, V. P. Kuznetsov, L. D. Patsenker, *et al.*, Kristallografiya **40** (3), 269 (1995) [Crystallogr. Rep. **40**, 242 (1995)].
22. L. Kutulya, V. Vashchenko, G. Semenkova, and N. Shkolnikova, Mol. Cryst. Liq. Cryst. (1999).
23. C. K. Prout and S. C. Wallwork, Acta Crystallogr. **21** (3), 449 (1966).
24. A. V. Tolmachev, L. N. Lisetskiĭ, and V. G. Tishchenko, Kristallografiya **33** (3), 788 (1988) [Sov. Phys. Crystallogr. **33**, 466 (1988)].
25. K. D. Vinokur, D. G. Sikharulidze, G. S. Chilaya, and Z. M. Élashvili, *Liquid Crystals with Helical Structure and Their Applications to Information Display Systems* (Metsniereba, Tbilisi, 1988).
26. R. A. Orwoll, V. J. Sullivan, and G. C. Campbell, Mol. Cryst. Liq. Cryst. **149**, 121 (1987).

Translated by O. Borovik-Romanova

Crystallography Reports, Vol. 46, No. 1, 2001, pp. 126–132. Translated from Kristallografiya, Vol. 46, No. 1, 2001, pp. 136–143.

CRYSTAL GROWTH

Effect of Organic Impurities on the Surface Morphology and Growth Mechanism of KBP Crystals ($C_8H_5O_4K$)

V. A. Kuznetsov*, N. D. Samotoin, and T. M. Okhrimenko***

** Shubnikov Institute of Crystallography, Russian Academy of Sciences, Leninskiĭ pr. 59, Moscow, 117333 Russia*

*** Institute of Geology of Ore Deposits, Petrography, Mineralogy, and Geochemistry, Russian Academy of Sciences, Staromonetnyĭ per. 35, Moscow, 109017 Russia*

Received February 24, 1998

Abstract—The surface morphology of the (010) face of potassium biphthalate (KBP) crystals grown from aqueous solutions under the supersaturation ranging within 0.029–0.04 has been studied by the methods of optical and electron microscopies. It was revealed that the (010) surface has polygonal growth macrohills of the dislocation nature, small hillocks developing by the mechanism of successive two-dimensional nucleation, and numerous two-dimensional nuclei. The density of small hillocks (10^4–10^5 cm^{-2}) exceeds the dislocation density in KBP crystals by one to two orders of magnitude. It is shown that at low supersaturations, the (010) face grows simultaneously by the dislocation mechanism and the mechanism of successive two-dimensional nucleation. It is also established that the tangential velocity of growth-step motion on the (010) face increases in the presence of organic impurities. This effect can be used as one of the factors increasing the growth rates of crystal faces at low impurity concentrations (the so-called catalytic effect of impurities). © *2001 MAIK "Nauka/Interperiodica".*

Potassium biphthalate (KBP) crystals are convenient model objects for studying the mechanism of crystal growth from aqueous solutions. The surface of the (010) face of a KBP crystal is characterized by the well developed macrorelief with the well distinguishable 13.3-Å-high elementary growth steps (equal to the lattice parameter *b* of the KBP crystal). This provides the resolution of fine details of the surface relief even in an optical microscope and the study of various factors that can influence crystal growth, e.g., the effect of impurities on the morphology and the growth mechanism. The results obtained in [1–5] allowed the authors to draw the conclusion that KBP crystals grow by the dislocation or the Burton–Cabrera–Frank (BCF) mechanism. Later, the electron microscopy study of sodium and cesium biphthalate crystals [6] revealed two-dimensional islands on the (010) surface. It was assumed that the dislocation and the two-dimensional nucleation mechanisms can act simultaneously (the so-called *B* + *S* growth model). Recently, KBP crystals, along with KDP (KH_2PO_4) crystals, were also used as model objects for studying the effect of the organic impurities on the growth kinetics of various faces [7–10]. It was established that at low impurity concentrations, the growth rate of faces increases (the so-called catalytic effect of impurities). It was logical to associate this effect with the thermodynamic effect of a decrease in the free energy γ of the step end caused by impurity adsorption [11]. However, the estimates of a possible increase of the normal growth rate *R* for BCF crystals and for *B* + *S* growth models showed no satisfactory agreement between the experimental data and the theory [9, 10]. Therefore, the studies of fine changes in the morphology of growing faces at low impurity concentrations seem to be very important. These studies can provide an additional information about the mechanism of the effect of an impurity on the growth kinetics of the faces.

Below, we present the data on the surface relief of the (010) face of KBP crystals grown from a "pure" aqueous solution and from solutions with ethylene glycol, glycerin, acetone, benzene, and acetic acid obtained by the methods of optical and electron microscopies. The electron microscopy methods provided the study of details finer than those reported in our earlier studies. The study was made at two concentrations—the impurity concentration C_1 corresponded to the maximum *R* value on the $R(C_i)$ dependence and a higher concentration C_2 corresponding to the right-hand decreasing branch of this dependence. The concentrations of the impurities were as follows: ethylene glycol 0.03 and 0.3 mol %, glycerin 0.6 and 2.0 mol %; acetone 0.05 and 0.5 mol %; benzene, 0.001 and 0.01 mol %; and acetic acid 0.05 and 0.6 mol %.[1]

[1] Impurity concentrations were determined as the ratios of the number of moles of the additive introduced into the solution to the number of moles of the solution (in percent).

1063-7745/01/4601-0126$21.00 © 2001 MAIK "Nauka/Interperiodica"

EXPERIMENTAL

Potassium biphthalate (KBP) crystals were grown by evaporating the saturated solution at the temperature of 18–20°C. The evaporation rate was controlled by the degree of opening of the crystallization vessel containing the starting saturated solution and was chosen in such a way that a crystal of length ~1 cm would grow within 48 h. According to our estimates, the relative supersaturation in this case attained a value of 0.03–0.04. At the same time, we also grew KBP crystals in the kinetic growth mode at the fixed supersaturation (0.029). The surface morphologies of the (010) face for both types of crystals were identical.

The grown crystals were taken away from the solution within a short time (1–3 s), dried with the filter paper, and placed into an exciccator. We did not use *n*-hexane to facilitate the removal of the crystals from the solution, because it was established that it can change the surface and, thus, hinder the analysis of fine elements of the surface structure, because *n*-hexane is only partly desorbed from the crystal surface.

The grown crystals were studied in the reflected light in a Neophot optical microscope and by the method of vacuum decoration with gold in a JEM-100C microscope supplied with a goniometer providing the specimen tilt up to ±60°. The specimen was annealed for 90 min in a 10^{-6} mm Hg vacuum at the substrate temperature 120°C and then was decorated with gold. In some experiments, the decorated (010) face was compared with the cleavages parallel to the (010) face with the aim to prove that a 90-min annealing of the specimen in vacuum at 120°C "cleans" the surface of the adsorbed components without undesirable evaporation of the native material (which could distort the surface pattern reflecting the last stage of crystal growth). Upon specimen decoration with gold (the conditions were the same for all the specimens), the surface was coated with a 100- to 150-Å-thick carbon film, which was dissolved in distilled water prior to specimen study in an electron microscope.

EXPERIMENTAL RESULTS

Main Elements of the Surface Relief of the (010) Face

We revealed the following main elements of the (010) face relief: polygonal hillocks, small rounded hillocks, and two-dimensional nuclei. The polygonal hillocks in the shape of asymmetric rhombuses are formed by growth steps oriented along the [101] directions. Usually, we observed from one to three larger polygonal "macrohillocks" which could be seen even with a naked eye in the reflected light (these hillocks were described in detail in [1, 2]) and were identified either with the unit dislocations or dislocation bundles.

Small rounded hillocks have the shape of cones, often with flattened tops usually displaced with respect to the hillock center because of the anisotropy in the growth rate along the [001] direction. Sometimes, such small hillocks had strictly circular cross sections, with the diameter ranging from several tenths of a micron to 10–15 μm.

Figure 1 illustrates different morphologies of small hillocks. The slopes of some of these hillocks are formed by growth macrosteps (hundreds of angstroms in height, Fig. 1a) with the terraces between these steps

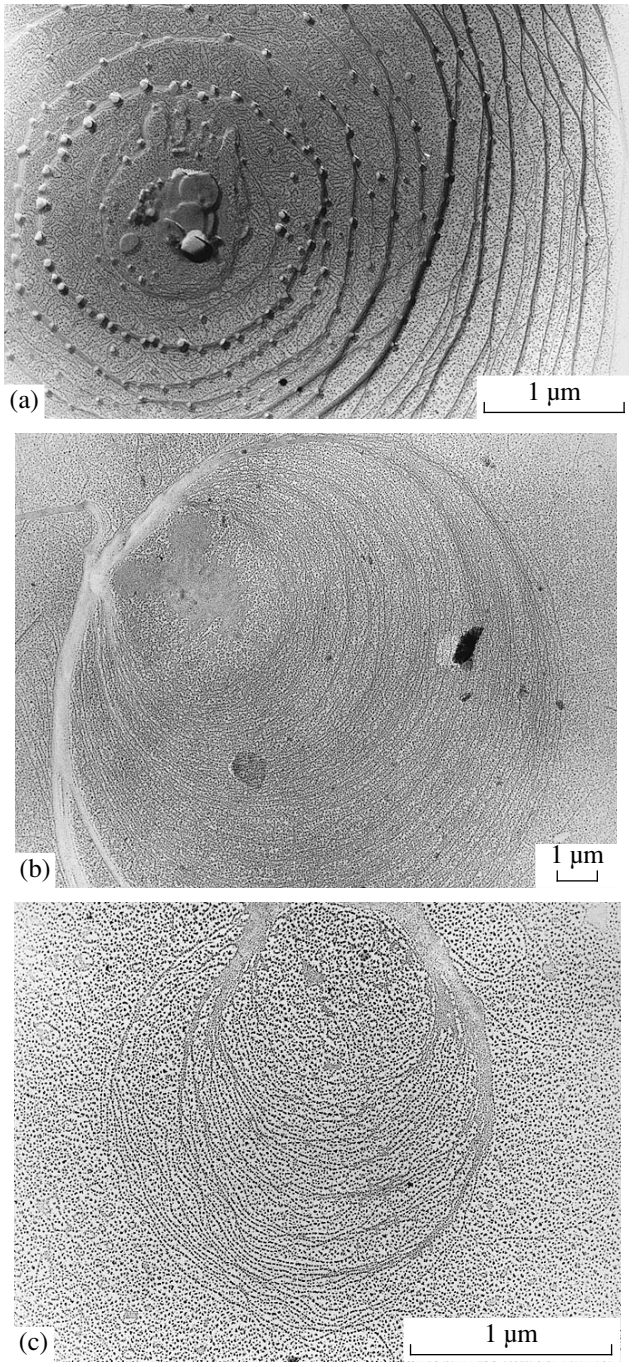

Fig. 1. Morphologies of small growth hillocks: (a) a hillock top with a rivet, (b) a rivet characterized by a high density of decorating particles, and (c) two-dimensional nuclei.

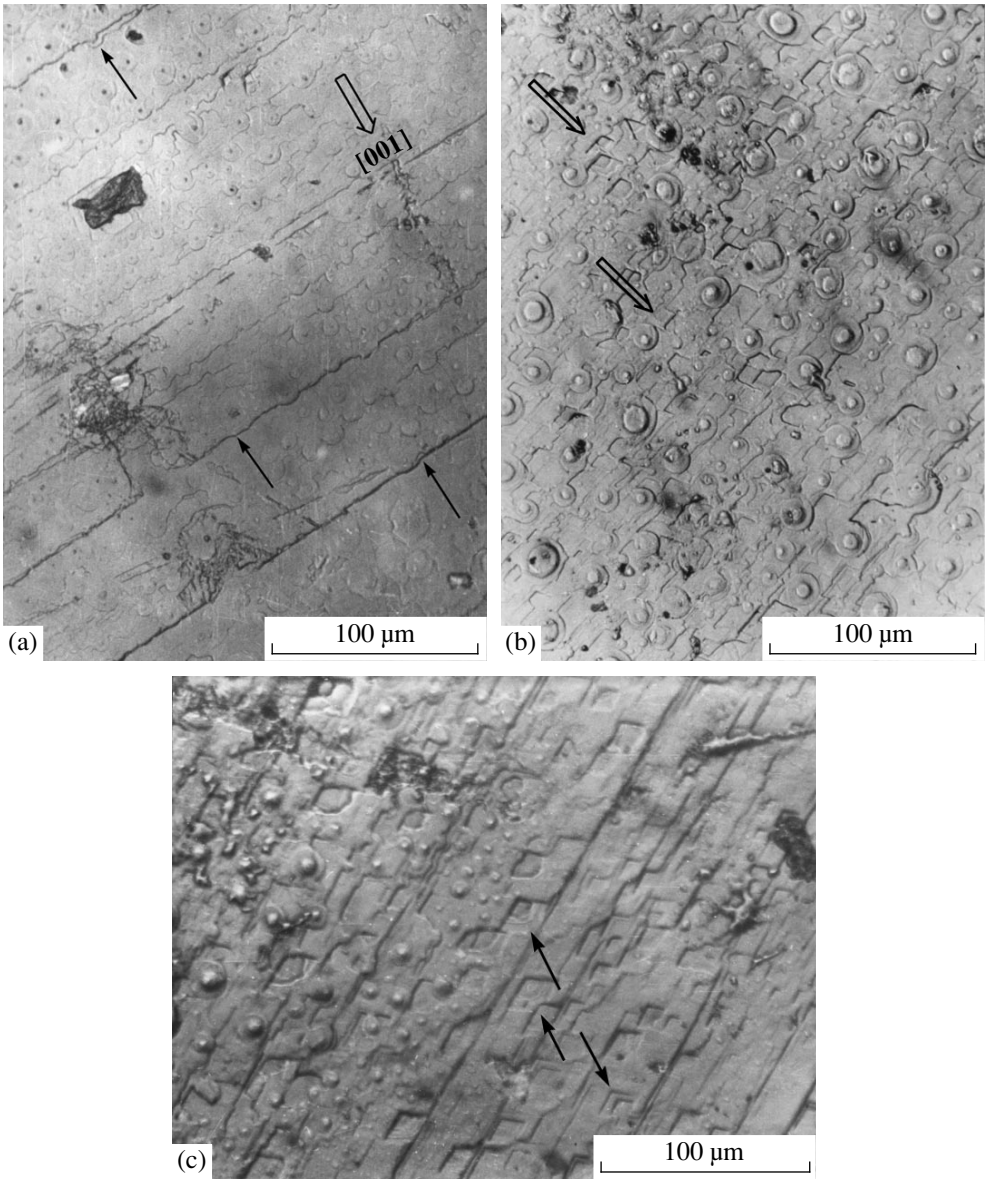

Fig. 2. (a) Small growth hillocks on the terraces between the macrosteps (indicated by an arrow). (a, b) A double arrow indicates the direction of the step motion. (c) Conventional arrows indicate growth caverns.

showing fine growth steps. We also observed the characteristic effect of alternating splitting and merging of the fine steps, which uniquely indicates that their heights correspond either to one (13.3 Å) or two (26.6 Å) unit-cell parameters along the *b*-axis of a KBP crystal [12]. In what follows, these steps will be referred to as elementary or monomolecular ones. The tops of such hillocks are covered with some formations ("rivets") characterized by high densities of decorating particles and nonresolvable fine structure (Fig. 1a). More often, small hillocks with slopes formed mainly by elementary steps and steps consisting of two to three monomolecular layers are observed (Figs. 1b, 1c). The average distances between the steps vary from 600 to 1000 Å. Sometimes, the tops of these hillocks are also covered with rivets with high densities of decorating particles having no fine relief (Fig. 1b). If the hillock tops have no rivets, it is possible to resolve elementary steps and rounded islands (200–300 Å) of monomolecular heights interpreted as two-dimensional nuclei (Fig. 1c). Sometimes, elementary steps in the vicinity of the hillock tops are so crowded that no regular fine relief can be revealed.

It should be emphasized that we never observed spiral growth steps with the heights equal to one or several molecular dimensions on the hillock tops, despite the fact that the method used allowed observation of such steps (which will be considered later). The average den-

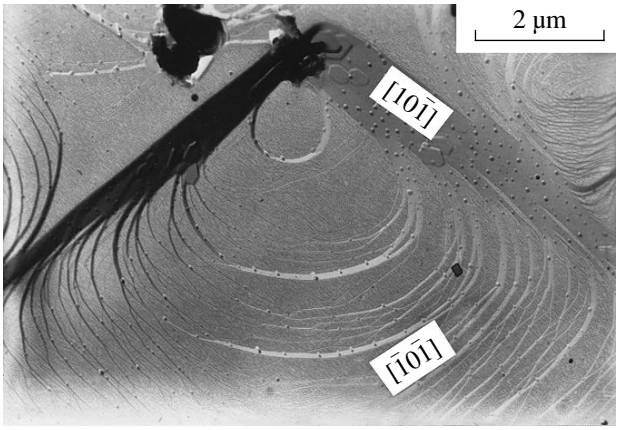

Fig. 3. Growth cavern. On the upper right: an asymmetric small growth hillock; the hillock and the cavern are rotated by 180° with respect to one another along the [001] direction.

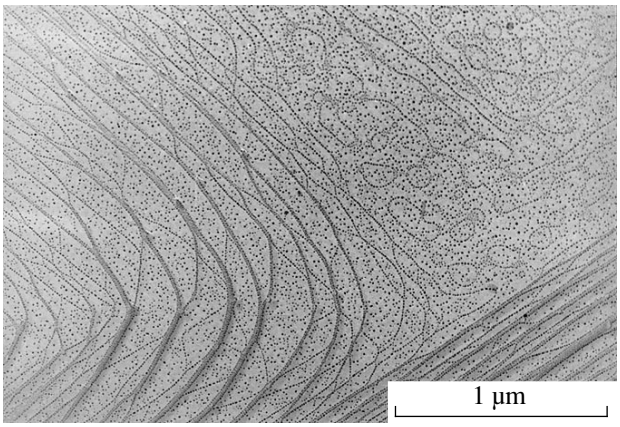

Fig. 4. Two-dimensional nuclei on the surface of the (010) face.

sity of small hillocks on the (010) face attains a value of 10^4–10^5 cm^{-2}, but the hillocks are distributed over the surface irregularly. As a rule, the hillock density at the narrow terraces in the vicinity of the centers of large polygonal hillocks is rather low. With an increase of the distance from the center of a polygonal hillock and the areas of the terraces, the density of small hillocks also increases (Fig. 2a). The elementary steps of neighboring hillocks merge together and form a common front oriented along the [101] direction. At still larger distances from the center of a polygonal hillock (Fig. 2b), the small hillocks form new macrosteps. The process is concluded with formation of surface regions with high densities of large closely located macrosteps (Fig. 2c) oriented along the [101] direction. The front of these steps is strongly cut; the surface has numerous deepenings ("growth caverns"), whose shape can hardly be distinguished from that of growth hillocks (Fig. 3) but which are rotated with respect to the latter by 180° about the *c*-axis.

Large terraces are covered with numerous two-dimensional nuclei formed by closed steps of the monomolecular height (Fig. 4). Less often, three-dimensional nuclei are formed by several concentric elementary steps. The density of two-dimensional nuclei attains a value of 10^8–10^9 cm^{-2}. No such nuclei are observed on narrow (less than ~0.2 μm in width) terraces (which reflect the width of the diffusion zone) and at the bottom of deep growth caverns, where supersaturation is lower than in the adjacent regions of the (010) surface.

Only some electron micrographs showed the spiral elementary steps, which were identified with dislocations.

Effect of Organic Impurities on Surface Morphology of the (010) Face

Impurity concentration C_1. The characteristic feature of the crystals grown at such impurity concentrations is a smoother relief of the (010) face. Large polygonal macrohillocks formed by high macrosteps either are seldom formed or not seen in the reflected light.

Among small growth hillocks, those with the slopes formed by the steps of the monomolecular height or the steps with a height multiple to the monomolecular height prevail (they are similar to hillocks shown in Figs. 1b, 1c). In rare occasions, macrosteps are formed at hillock slopes. In the presence of impurities, the hillock density slightly increases (up to 10^5–10^6 cm^{-2}), as does the hillock diameter. It is especially well seen in the presence of ethylene glycol and glycerin (the average hillock diameter is 60–70 μm, but there are some hillocks with the dimensions up to 300–400 μm and, in some occasions, even of 500 μm) and also in the presence of acetic acid (the hillock diameter attains a value of 200 μm). At the same time, the angle of a hillock slope decreases. To estimate the slope, we considered the symmetric hillock with a diameters of ~10 μm formed only by elementary steps. The slope angle was determined for a number of such hillocks and the average interhillock distance. In the control crystals, the hillock slope angles ranged within 4°–4.5°, whereas in the crystals grown in the presence of benzene, acetone, ethylene glycol, and acetic acid, the slope angle reduced to ~2°. A decrease of the slope angle of hillocks with the simultaneous increase of their diameter indicate a higher tangential velocity *V* of growth-layer motion in the presence of organic impurities. This seems to be the cause of somewhat larger two-dimensional nuclei and their coagulation on the (010) face for "doped crystals" in comparison with the nuclei dimensions in the control crystals.

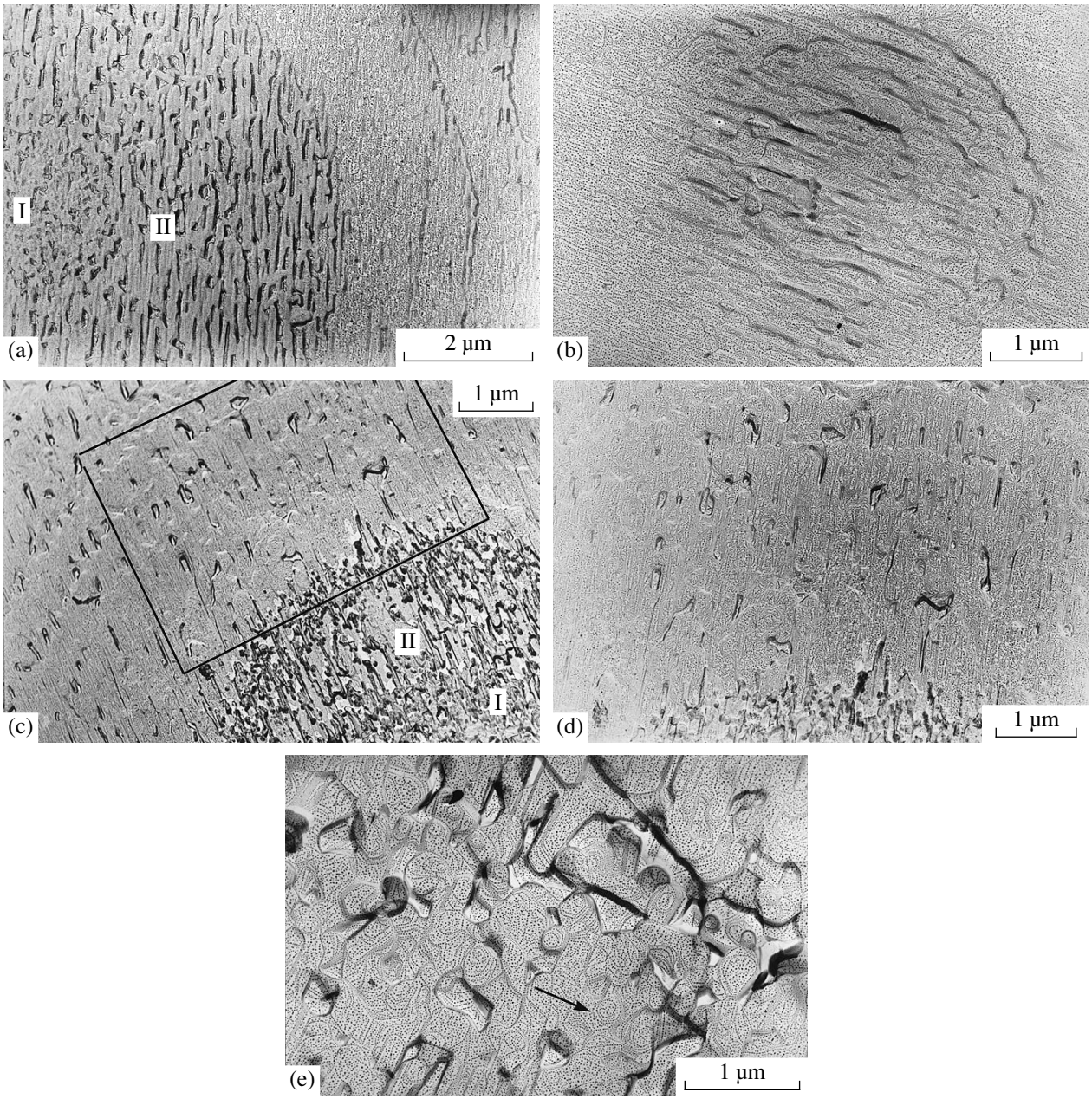

Fig. 5. Small growth hillocks at the impurity concentrations C_2: (a) ethylene glycol 0.3 mol %, (b) acetone 0.5 mol %, and (c, d, e) benzene 0.01 mol %, (d) a segment of the terrace framed in (c), and (e) the region between small growth hillocks on the surface of the (010) face. The arrow indicates the spiral step.

Impurity concentration C_2. The morphology of small growth hillocks at the organic-impurity concentration C_2 essentially differs from the morphology considered above (Fig. 5). The hillocks are similar to those in Fig. 1 only in the presence of the acetic acid impurity; however, the elementary steps on their slopes form mascrosteps with the cut ends. In the presence of other impurities, hillocks have the shape of truncated mildly sloping cones which seem to consist of superimposed circular "platforms." One can clearly distinguish a small central area (a center, zone I in Figs. 5a, 5c) of lumpy formations gradually transforming into high heaps along the [001] direction and cut by deep protrusions (zone II, Figs. 5a, 5c). Hillocks have steep slopes and flat surfaces. They are developed independently of neighboring hillocks from their centers in the upward direction. Figure 5b shows the central zone of a very mildly sloping hillock. One can also see a fine striated pattern formed by decorating particles and closed elementary steps repeating the hillock contours and concentric steps forming the hillock center. The latter "is indicated" by a circular two-dimensional nucleus. This

pattern is characteristic of growth by the mechanism of successive two-dimensional nucleation.

Outside zones I and II, one can see terraces on which decorating particles are located along the [001] direction, thus forming a dense system of parallel chains. It is possible to distinguish elementary steps located here with a very high density (with the interstep distances ranging within 100–150 Å) and numerous islands elongated in the [001] direction, which are formed by the system of closed elementary steps. The "center" of such islands is often "indicated" by a two-dimensional nucleus. Figure 5d shows a part of the terrace framed in Fig. 5c. It is seen that the whole terrace surface is formed by such elongated islands.

Figure 5e shows the part of the (010) face (growth in the presence of 0.01 mol % of benzene) located between two small growth hillocks. The surface is formed by merged large hillocks with steep slopes. Clearly seen systems of concentric elementary steps indicate that the hillocks are formed by the mechanism of successive two-dimensional nucleation. Only in some cases (Figs. 5b, 5d, and 5e) can one distinguish elementary spiral steps (one of such steps is indicated by an arrow in Fig. 5e). It should be emphasized that the hillocks formed due to screw dislocations have the diameters and heights equal to those of the hillocks which grew by the mechanism of successive nucleation. In other words, under the given growth conditions for the (010) face, screw dislocations provide no advantages for crystal growth.

Despite the essentially different morphologies, the small-hillock densities at the impurity concentrations C_1 and C_2 are approximately the same and are equal to $\sim 10^6$ cm^{-2}.

DISCUSSION OF RESULTS

The above results show that at low supersaturations (0.029–0.04) on the (010) face, growth of KBP crystals proceeds simultaneously by two mechanisms—the dislocation or Burton–Cabrera–Frank mechanism and the mechanism of successive nucleation. By several reasons, our results do not confirm the conclusion made in [1, 2]. Indeed, the density of small hillocks (10^4–10^5 cm^{-2}) exceeds the dislocation density in KBP crystals (10^3–10^4 cm^{-2}) [7]. Also, the decoration patterns show that a considerable number of small hillocks are not of the dislocation nature. The formation of two-dimensional nuclei at the hillock tops (Fig. 1c) indicates that they grow by the mechanism of successive two-dimensional nucleation (the $B + S$ or the *NAN* mechanisms [11, 13]). It should also be emphasized that the surface relief of the (010) face could not be formed due to postgrowth processes such as the separation of the material from the film of the solution remaining on the surface upon the removal of the crystal from the crystallizer. First, the density and the average diameter of small hillocks are such that the thickness of the solution layer remaining on the surface and necessary for their formation should be about 8 to 10 μm, which is hardly probable in our case of removal crystal removal from the solution and their fast drying. Second, we never observed the situation, where small hillocks with rivets completely covered the lower surface relief (e.g., growth steps), which should have necessarily taken place during fast separation of the material from drops. Of course, the postgrowth phenomena can produce a certain effect on the surface morphology of the (010) face, but they cannot drastically change it.

Thus, the formation of the dislocation-free small hillocks and numerous two-dimensional (2D) nuclei on the (010) face confirm the mechanism of two-dimensional nucleation at low (0.029–0.04) supersaturations, which is in good accord with a number of the known experimental data [14–18]. Growth of faces by the mechanism of two-dimensional nucleation under low supersaturations was also analyzed in [19]. Nevertheless, as is well known, the mechanism of this phenomenon is still not quite clear. The two-dimensional 2D nucleation under low supersaturations can be caused by defects of the crystalline surface as well as impurities, disturbances of the periodic structure of the surface different from the structure of lower crystalline layers [20], and the edge dislocations [21–24]. It is important that the generators of the concentric steps forming the dislocation-free hillocks can be more efficient than screw dislocations [25].

The effect of organic impurities (at concentrations C_1) in our experiments showed itself in a certain stimulation of 2*D*-nucleation, which should logically be associated with a decrease in the end energy γ of steps (confirmed in [26]) and an increase in the velocity V of step motion. The latter fact cannot be explained by the change in γ due to absorption of impurity, because in the mechanism of two-dimensional nucleation (in the $B + S$ growth model), the velocity V should be independent of γ [11]. There are no grounds to believe that this can be associated with two-dimensional nucleation on terraces, because the distances between the elementary steps at the slopes of small hillocks are so small that no nucleation was observed at these sites. The changes in the roughness of the step ends should also be excluded because of the high kink density at the circular steps. We believe that the main cause of an increase in velocity V is enhanced dehydration of the (010) surface in the presence of organic impurities [27]. We can also not exclude possible accelerated desorption of inorganic-ion impurities from the surface under the effect of organic molecules.

An increase of the step velocity V can be one of the possible causes of the catalytic effect of organic impurities. The latter effect is more pronounced in the presence of ethylene glycol and glycerin [8], which is in good accord with the maximum increase in V in the presence of these additives. Indeed, the normal growth rate of the face, R, is related to V by the equation $R =$

Vp, where p is the slope of the growth hillock. Although the presence of ethylene glycol and glycerin results in a double reduction of p, a more drastic increase in V (by seven to ten times) compensates this reduction and, on the whole, the normal growth rate R of the (010) face increases. The presence of the acetic acid increases V to a lesser degree than ethylene glycol and glycerin, and the catalytic effect due to this impurity is not so pronounced [8].

At high concentrations of organic impurities C_2, the important role of the mechanism of successive nucleation in growth of the (010) face is seen more clearly. In this case, the central zones of growth hillocks and terraces in the lower layer are formed by intergrown formations (heaps) developed by the mechanism of successive two-dimensional nucleation.

The rate of the tangential growth of these heaps is lower than the rate of their normal growth, which is seen from their steep slopes. As a result, the merge of these heaps is accompanied by the formation of numerous voids, which are preserved in the form of inclusions in the grown crystal. The causes of a high activity of the central zones of growth hillocks, which provide the formation of the largest and the highest heaps, are still unclear as well as the circular shape of the platforms forming growth hillocks, despite the drastically anisotropic shape of the constituent heaps.

CONCLUSIONS

It is established by the methods of optical and electron microscopies that under the supersaturation of 0.029–0.04 in aqueous solution, the (010) face of KBP crystals grows simultaneously by the dislocation growth mechanism and the mechanism of successive two-dimensional nucleation.

At a low concentration, organic impurities enhance the process of two-dimensional nucleation and increase the tangential velocity of step motion, which is one of the factor providing the catalytic effect of impurities described earlier.

At high impurity concentrations, the role of successive two-dimensional nucleation on growth of the (010) face becomes more important, whereas the contribution due to the Burton–Cabrera–Frank mechanism decreases.

ACKNOWLEDGMENTS

This study was supported by the Russian Foundation for Basic Research, project no. 97-03-33613.

REFERENCES

1. W. J. P. van Enckevort and L. A. M. Jetten, J. Cryst. Growth **60**, 275 (1982).
2. L. A. M. J. Jetten, B. van Der Hoek, and W. J. P. van Enckevort, J. Cryst. Growth **62**, 603 (1983).
3. M. H. J. Hottenhuis and C. B. Lucasius, J. Cryst. Growth **91**, 623 (1988).
4. M. H. J. Hottenhuis and A. Oudenampsen, J. Cryst. Growth **92**, 513 (1988).
5. M. H. J. Hottenhuis and C. B. Lucasius, J. Cryst. Growth **94**, 708 (1989).
6. E. I. Suvorova and G. I. Distler, Kristallografiya **35** (3), 792 (1990) [Sov. Phys. Crystallogr. **35**, 464 (1990)].
7. T. M. Okhrimenko, S. T. Kozhoeva, V. A. Kuznetsov, *et al.*, Kristallografiya **37** (5), 1309 (1992) [Sov. Phys. Crystallogr. **37**, 705 (1992)].
8. V. A. Kuznetsov, T. M. Okhrimenko, and Kh. S. Bagdasarov, Kristallografiya **41** (3), 557 (1996) [Crystallogr. Rep. **41**, 527 (1996)].
9. V. A. Kuznetsov, T. M. Okhrimenko, and M. Rak, Proc. SPIE **3178**, 100 (1997).
10. V. A. Kuznetsov, T. M. Okhrimenko, and M. Rak, J. Cryst. Growth **193**, 164 (1998).
11. R. J. Davey, *Industrial Crystallization 78* (Elsevier, Amsterdam, 1984), p. 97.
12. N. D. Samotoin, Izv. Akad. Nauk SSSR, Ser. Geol., No. 10, 114 (1971).
13. R. Janssen van Rosmalen, P. Bennetna, and J. Garside, J. Cryst. Growth **29**, 342 (1975).
14. K. Tsukamoto, H. Ohba, and I. Sunagawa, J. Cryst. Growth **63**, 18 (1983).
15. W. van Erk, HJ. G. J. van Hoek-Martens, and G. Bartels, J. Cryst. Growth **48**, 621 (1980).
16. K. Tsukamoto, Faraday Discuss. **183**, 95 (1993).
17. J. J. De Yoreo, T. A. Land, and B. Dair, Phys. Rev. Lett. **73** (6), 838 (1994).
18. Carlos M. Pina, Udo Becker, Petr Risthaus, *et al.*, Nature **395**, 483 (1998).
19. A. A. Chernov, V. F. Parvov, M. O. Kliya, *et al.*, Kristallografiya **26** (5), 1125 (1981) [Sov. Phys. Crystallogr. **26**, 640 (1981)].
20. A. A. Shternberg, in *Crystal Growth* (Nauka, Moscow, 1972), Vol. 9, p. 34.
21. A. A. Chernov, L. N. Rashkovich, I. L. Smol'skiĭ, *et al.*, in *Crystal Growth* (Nauka, Moscow, 1986), Vol. 15, p. 43.
22. K. V. Keller, in *Crystal Growth* (Yerevanskiĭ Gos. Univ., Yerevan, 1975), Vol. 11, p. 196.
23. E. Banser and M. Strunk, J. Cryst. Growth **51**, 362 (1981).
24. F. C. Frank, J. Cryst. Growth **51**, 367 (1981).
25. A. A. Chernov and G. F. Kopylova, Kristallografiya **22** (6), 1247 (1977) [Sov. Phys. Crystallogr. **22**, 709 (1977)].
26. S. P. Kuz'min, V. A. Kuznetsov, T. M. Okhrimenko, and Kh. S. Bagdasarov, Kristallografiya **39** (5), 914 (1994) [Crystallogr. Rep. **39**, 834 (1994)].
27. T. M. Okhrimenko, V. A. Kuznetsov, O. F. Pozdnyakov, and V. P. Redkov, Kristallografiya **42** (3), 541 (1997) [Crystallogr. Rep. **42**, 494 (1997)].

Translated by L. Man

Crystallography Reports, Vol. 46, No. 1, 2001, pp. 13–18. Translated from Kristallografiya, Vol. 46, No. 1, 2001, pp. 19–24.

Generation of Molecular Bravais Structures by the Method of Discrete Modeling of Packings

A. V. Maleev

Vladimir State Pedagogical University, Vladimir, Russia

e-mail: laemail@mail.ru

Received April 19, 1999; in final form, February 15, 2000

Abstract—An algorithm for the generation of possible crystal structures consisting of molecules with the known shapes in the symmetry classes with one translationally independent molecule (the so-called molecular Bravais structures) has been proposed within the framework of the method of discrete modeling of packings in molecular structures. The algorithm was used to write a special complex of computer programs. Some examples of testing this complex on molecules with the structures determined earlier by the methods of X-ray diffraction analysis are also considered. © *2001 MAIK "Nauka/Interperiodica".*

INTRODUCTION

Many physical properties of molecular crystals are determined mainly by their molecular packings, i.e., the mutual arrangement of molecules in the crystal. This makes it quite timely to develop the methods for modeling (generation and construction) all the possible crystalline modifications of chemical compounds. On the other hand, the modeling of molecular crystals is also used in the determination of crystal structures, especially in those cases, where the collection of complete set of X-ray diffraction data is impossible.

Below, we suggest an algorithm for constructing all the possible variants of packings of molecules with the known shape in the symmetry classes with one molecule in a primitive unit cell (i.e., with one translationally independent molecule). Among such classes there are, e.g., $P1$, $Z = 1(1)$; $P\bar{1}$, $Z = 1(\bar{1})$; $P2$, $Z = 1(2)$; Pm, $Z = 1(m)$; $P2/m$, $Z = 1(2/m)$; Cm, $Z = 2(m)$; $C2$, $Z = 2(2)$; $C2/m$, $Z = 2(2/m)$; $R3m$, $Z = 1(3m)$; etc. The algorithm is based on the method of discrete modeling of molecular packings [1, 2]. The structures described by the above symmetry classes are called molecular Bravais structures. Their number amounts up to 2% of the total number of homomolecular organic crystals [3].

The algorithm consists of four major programs for the following:

(1) Approximation of a molecule by a discrete model (a polycube);

(2) Exhaustive search for all the possible variants of the translation packings of polycubes with the given packing coefficient;

(3) Reduction of the unit-cell parameters to the standard form and calculation of the atomic coordinates corresponding to the obtained variants of polycube packings;

(4) Optimization of the translation-lattice parameters and molecule orientation aimed at minimizing of the energy of molecular interactions.

APPROXIMATION OF A MOLECULE BY A DISCRETE MODEL

The mutual arrangement of atoms of a molecule is uniquely set by the atomic coordinates $\{\mathbf{r}_j | j = 1, 2, \ldots, m\}$, where m is the number of atoms in the molecule. According to the close-packing principle, two atoms of the neighboring molecules in molecular crystals cannot be located closer than within a certain distance [4] determined by the types of the atoms forming this pair (e.g., in the absence of specific interactions, this distance cannot be considerably less than the sum of the van der Waals radii of these atoms). Proceeding from this requirement, the space part occupied by the given molecule can be considered as a geometric figure $M = \cup_{j=1}^{m} S_j$, where S_j is a sphere of the radius R_j (van der Waals radius of the jth atom) with the center at the point $\mathbf{r}_j$, the so-called geometric model of a molecule.

We define a polycube or a three-dimensional polyomino as a geometric figure consisting of a finite number of the equivalent cubes, each of which shares at least one face with another cube of a polycube. A polycube consisting of p cubes can be set by the integral coordinates of their centers $\{\mathbf{l}_i, i = 1, 2, \ldots, p\}$ in the basis whose vectors are parallel to three cube edges outcoming from one vertex and having the lengths equal to the cube edge. Then, a polycube is a geometric figure described as $P = \cup_{i=1}^{p} C_i$, where C_i is the cube with the center located at the point with coordinates $\mathbf{l}_i$.

The approximation of a molecule by a polycube is understood as the search for determining of such a polycube, in which the centers of the constituent cubes

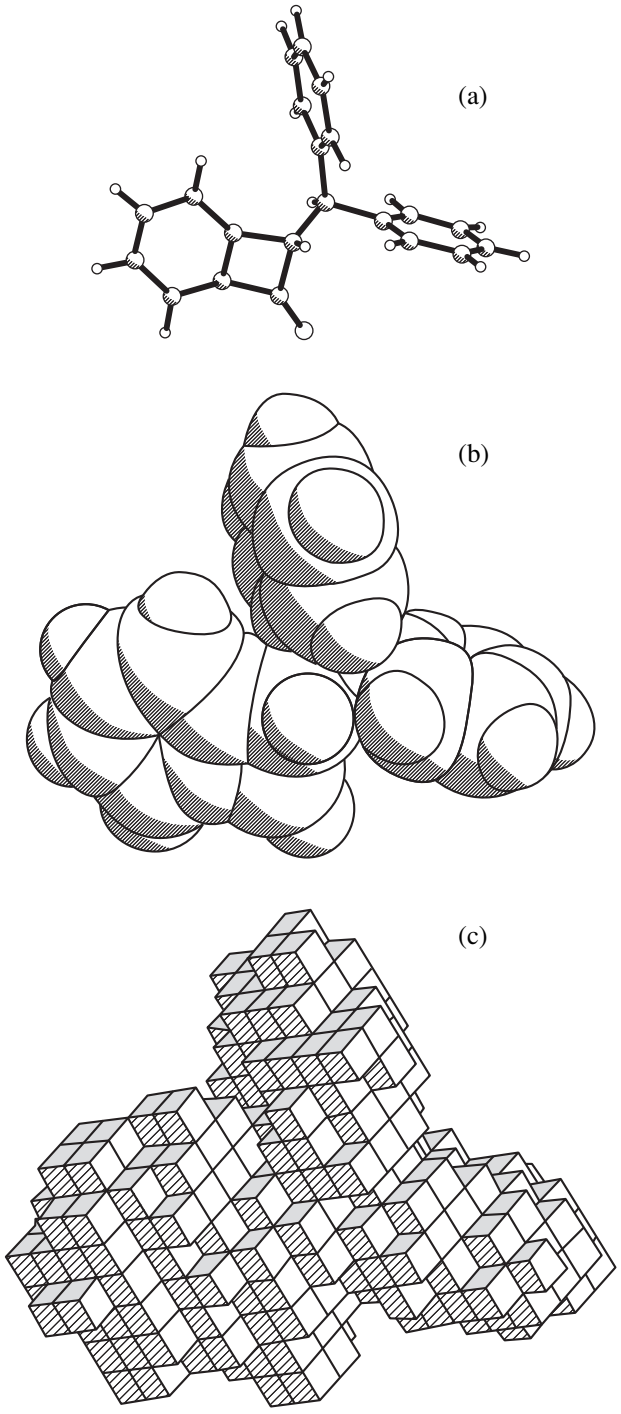

Fig. 1. (a) A model of spheres and rods, (b) the geometric model, and (c) a polycube of a 2-diphenylmethylbenzocyclobutenone molecule.

belong to the geometric model of the molecule. The approximation algorithm reduces to the calculation of the coordinates of the molecule atoms in an arbitrarily oriented orthonormalized basis with the vectors, whose magnitudes are equal to the approximation step, and the search for all the integral points in this basis that belong to the geometric model of the molecule. It is logical to suggest as the criterion of the approximation quality the ratio of the sum of the volumes of the figure part P not belonging to the figure M plus the figure part M not belonging to the figure P to the volume of the figure M, i.e.,

$$\delta = (V_{M-P} + V_{P-M})/V_M.$$

Figure 1 depicts (a) the traditional model consisting of spheres and rods, (b) the geometric model, and (c) the discrete model (i.e., a polycube) for an organic molecule 2-diphenylmethylbenzocyclobutenone [5].

EXHAUSTIVE SEARCH FOR ALL THE POSSIBLE VARIANTS OF THE TRANSLATION PACKINGS OF POLYCUBES WITH THE GIVEN PACKING COEFFICIENT

The necessary and sufficient criterion for the existence of a translation packing of polyominoes (in the three-dimensional case, of polycubes) consisting of p points with the packing coefficient $k = p/N$ is given elsewhere [2]. According to this criterion, if a polycube given by the set $\{\mathbf{l}_i, i = 1, 2, \ldots, p\}$ is to have a translation packing (a packing, in which any two polycubes are related by a translation) with the packing coefficient $k = p/N$, it is necessary and sufficient that there would exist a packing space of order N in which the pairs of the points with coordinates $\{\mathbf{l}_i, i = 1, 2, \ldots, p\}$ have different weights. The algorithm of the exhaustive search for all the possible ways of packing the given polycubes with the packing coefficient k reduces to checking the packing criterion for each packing space of order N. Each packing space satisfying this criterion defines one of the possible ways of polycube packing.

A packing space is a lattice in which each point (or unit cell) is attributed a certain weight so that any set of the lattice points with the same weights would form the same sublattice of the initial lattice (within an accuracy of a shear). The columns of vector coordinates (in the basis of the initial lattice) of a basis of this sublattice form the following integral matrix:

$$Y = \begin{bmatrix} x_1 & x_2 & x_3 \\ 0 & y_2 & y_3 \\ 0 & 0 & z_3 \end{bmatrix},$$

where $x_1 > 0$, $y_2 > 0$, $z_3 > 0$, $0 \le x_2 < x_1$, $0 \le x_3 < x_1$, $0 \le y_3 < y_2$. The Y matrix is called the matrix of the packing space. The order of the packing space coincides with the sublattice index and equals the product of the diagonal elements of the Y matrix: $N = x_1y_2z_3$. The weight of the point with the coordinates (u, v, w) is determined from the equation

$$g(u, v, w) = \{(u - [w/z_3]x_3 - [(v - [w/z_3]y_3)/y_2]x_2)/x_1\}x_1 + \{(v - [w/z_3]y_3)/y_2\}x_1y_2 + \{w/z_3\}N,$$

Table 1. Some data on crystal structures used for testing the algorithm of discrete modeling

Compound	Formula	Symmetry class	Reference to X-ray determination
2-Diphenylmethylbenzocyclobutenone	$C_{21}H_{16}O_1$	$P1$, $Z = 1(1)$	[5]
3-Iodo-1-trichloromethylbicyclo[1,1,1]pentane	$C_6H_6Cl_3I$	Cm, $Z = 2(m)$	[7]
3-Chloro-1-trichloromethylbicyclo[1,1,1]pentane	$C_6H_6Cl_4$	$R\,3m$, $Z = 1(3m)$	[7]
1,4-Bis(chloromethyl)-2,3,5,6-tetrachlorobenzene	$C_8H_4Cl_6$	$P\bar{1}$, $Z = 1(\bar{1})$	[8]
n-Hexane	C_6H_{14}	$P\bar{1}$, $Z = 1(\bar{1})$	[9]
p-Dichlorobenzene	$C_6H_4Cl_2$	$P\bar{1}$, $Z = 1(\bar{1})$	[10]
1,2,4,5-Tetrahydrodicyclobuta(*a*,*d*)benzene	$C_{10}H_{10}$	$P\bar{1}$, $Z = 1(\bar{1})$	[11]
Cubane	C_8H_8	$R\bar{3}$, $Z = 1(\bar{3})$	[12]
1,5-Dibromotetracyclo[4.2.2$^{2.5}$.O$^{2.6}$]dodecane	$C_{12}H_{16}Br_2$	$P\bar{1}$, $Z = 1(\bar{1})$	[13]

where $[r]$ is the integer closest to r such that $[r] \le r$, whereas $\{r\} = r - [r]$ is the fractional part of the number r.

The number of three-dimensional packing spaces of order N is determined as $\sum \Delta_1^2 \Delta_2$, where summation is performed over all the possible factorizations of the number N into $\Delta_1\Delta_2\Delta_3$ with due regard for the order of the factors [2, 6].

Obviously, the time of the search for all the possible ways of polycube packings is proportional to the number p of points in the polycube, the number of the packing spaces of order N, and the time necessary for computation of the weight of the packing-space point with coordinates $\mathbf{l}_i$. To reduce this time, it is expedient to choose the order N of the packing spaces to be a simple number. Then, first, the number of packing spaces is determined by the formula $N^2 + N + 1$ and, second, the weight of the point is calculated by a simpler (in terms of the computational time) formula $g(u, v, w) = \{(u - vx_2 - wx_3)/N\}N$. The number p of the points in a polycube (a discrete model of a molecule) is determined mainly by the approximation step s. The space order is determined by the number p and the packing coefficient k. Then, N is the simple number closest to the fraction p/k.

REDUCTION OF THE UNIT-CELL PARAMETERS TO A STANDARD FORM AND CALCULATION OF THE ATOMIC COORDINATES CORRESPONDING TO THE OBTAINED VARIANTS OF POLYOMINO PACKINGS

A packing space satisfying the packing criterion determines the lattice of translations of a variant of the polyomino packing. The basis of this lattice in the orthonormalized basis is set by the columns of the packing-space matrix Y

$$\mathbf{a} = s\begin{bmatrix} x_1 \\ 0 \\ 0 \end{bmatrix}; \quad \mathbf{b} = s\begin{bmatrix} x_2 \\ y_2 \\ 0 \end{bmatrix}; \quad \mathbf{c} = s\begin{bmatrix} x_3 \\ y_3 \\ z_3 \end{bmatrix},$$

where s is the approximation step. In the same orthonormalized basis, the atomic coordinates of a molecule are given by the set $\{r_j | j = 1, 2, \ldots, m\}$, where m is the number of atoms in the molecule. Any of the known reduction algorithms [e.g., the Delone (Delaunay) algorithm] can be used to transform the above basis **a**, **b**, **c** into a standard crystallographic basis $\mathbf{a}_n$, $\mathbf{b}_n$, $\mathbf{c}_n$, in which the atomic coordinates of the molecule are calculated in the unit cell fractions; i.e., $\mathbf{r}'_j = Y_n^{-1} \cdot \mathbf{r}_j$, where Y_n is the matrix of the column vectors $\mathbf{a}_n$, $\mathbf{b}_n$, $\mathbf{c}_n$ in the basis **a**, **b**, **c**.

OPTIMIZATION OF THE TRANSLATION-LATTICE PARAMETERS AND THE MOLECULE ORIENTATION IN ORDER TO MINIMIZE THE ENERGY OF MOLECULAR INTERACTIONS

If one assumes the molecules to be rigid, the energy of molecular interactions in a crystals with one translationally independent molecule in the unit cell is determined, first, by the geometric characteristics of the translation lattice and, second, by the orientation of the molecule with respect to this lattice. Nine varying parameters correspond to these factors, e.g., the unit-cell parameters of the translation lattice (a, b, c, α, β, and γ) and the Eulerian angles of the molecule (θ, φ, ψ). The minimization of the crystal-lattice energy function $U(a, b, c, \alpha, \beta, \gamma, \theta, \varphi, \psi)$ is performed by the least

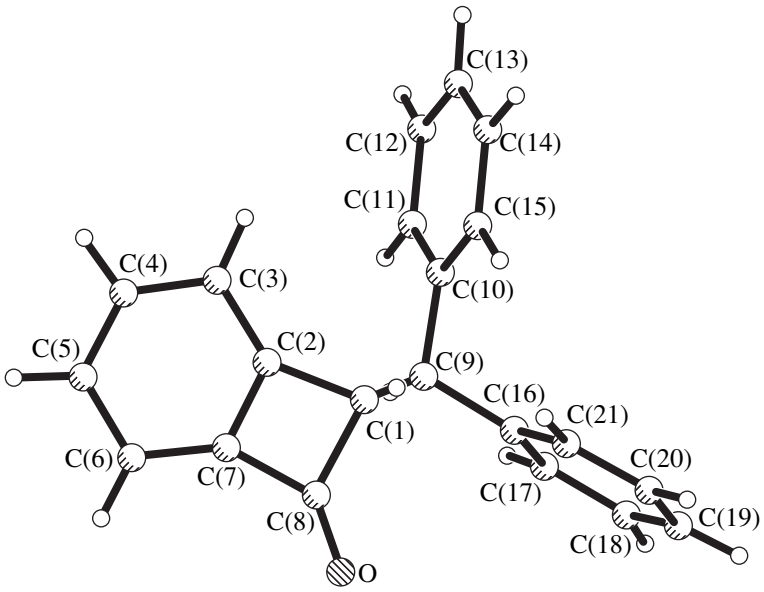

Fig. 2. View of a 2-diphenylmethylbenzocyclobutenone molecule.

squares method within the model of the atom–atom potential.

The above algorithm was used to write a complex of programs for an IBM-compatible personal computer. The complex was tested on a number of crystal structures determined earlier by the methods of the X-ray diffraction analysis. The materials, their brutto formulas, and the symmetry classes of some of these materials are listed in Table 1. For each molecule, the discrete models (polycubes) with different approximation step (ranging from 0.4 to 1.1 Å) were computed and then various crystal structures were generated at the packing coefficients ranging from 0.6 to 0.8. In each case, the number of different variants of molecular packings did not exceed five–seven. Upon optimization of the lattice parameters and molecule orientations, the "true" variant (i.e., the variant corresponding to the X-ray structure determination) was singled out from the variants with the "best energy" of molecular interaction.

As an example, consider modeling of the crystal structure of 2-diphenylmethylbenzocyclobutenone [5]. Schematically, the molecule with the numbered atoms is shown in Fig. 2. To avoid a possible distortion of the molecule shape by the crystal field during modeling, we constructed a discrete model (a polycube) without using the atomic coordinates determined by the X-ray diffraction method [5]. Instead, we computed these coordinates by the method of molecular mechanics using the MMX program [14]. At both stages—approximation and optimization of the translation-lattice parameters—the molecule was assumed to be rigid.

Table 2. Unit-cell parameters of the crystal structure determined by the method of the X-ray diffraction analysis and the corresponding structure model

Unit-cell parameter	*a*(Å)	*b*(Å)	*c*(Å)	α(deg)	β(deg)	γ(deg)
Crystal structure	5.953	7.459	9.409	69.11	82.09	89.74
Model	5.71	8.16	9.33	66.8	85.0	89.8

Polycubes were constructed for five random molecule orientations with the approximation steps 0.50, 0.51, 0.52, …, 1.10 Å. Applying the above criterion δ, we selected 15 polycubes variant. Then, for each of these polycubes, we performed the exhaustive search for all the possible packing variants with the packing coefficients ranging from 0.57 to 0.60. As a result, 150 variants of polycube packings were obtained. Upon the unit-cell reduction and the computation in the atomic coordinates in the crystal structures for each variant of polycube packing, we performed the comparative analysis of the obtained crystal structures to obtain 125 variants close to one another and to the structure determined earlier by the X-ray diffraction method [5]. These structures had close geometric characteristics (unit-cell parameters and molecule orientations in the lattice).

The optimization of the translation-lattice parameters and the molecule orientation by the method of atom–atom potentials confirmed this result. Upon optimization, these 125 variants had the same energy of molecular interaction (–28.0 kcal/mol), the same translation lattices (the differences in the lattice parameters did not exceed 0.1 Å, the differences in the lattice angles did not exceed 0.1°), and the same molecule orientations in the lattice (for nonhydrogen atoms, the differences did not exceed 0.001 in unit-cell fractions). In

Table 3. Coordinates of nonhydrogen atoms of the crystal structure and the corresponding structure model

Atom	*x*	*y*	*z*	Atom	*x*	*y*	*z*
O	0.2553	0.5829	0.8235	C(11)	0.4756	0.3721	0.3001
	0.332	0.578	0.825		0.480	0.363	0.307
C(1)	0.4650	0.6255	0.5598	C(12)	0.5785	0.3906	0.1535
	0.499	0.630	0.546		0.576	0.359	0.172
C(2)	0.3268	0.7712	0.4515	C(13)	0.7877	0.4720	0.0971
	0.338	0.772	0.450		0.785	0.442	0.108
C(3)	0.3106	0.8692	0.2935	C(14)	0.9108	0.5357	0.1873
	0.298	0.870	0.303		0.897	0.527	0.181
C(4)	0.1281	0.9876	0.2699	C(15)	0.8084	0.5149	0.3366
	0.117	0.981	0.287		0.800	0.529	0.317
C(5)	−0.0209	1.0134	0.3821	C(16)	0.5812	0.2781	0.6806
	−0.013	0.993	0.411		0.574	0.297	0.668
C(6)	−0.0064	0.9176	0.5365	C(17)	0.4829	0.0940	0.7524
	0.027	0.893	0.560		0.461	0.137	0.731
C(7)	0.1720	0.7950	0.5653	C(18)	0.5758	−0.0429	0.8710
	0.205	0.786	0.569		0.544	0.000	0.849
C(8)	0.2903	0.6561	0.6864	C(19)	0.7727	0.0071	0.9139
	0.339	0.649	0.684		0.744	0.022	0.906
C(9)	0.4758	0.4255	0.5502	C(20)	0.8729	0.1868	0.8453
	0.477	0.449	0.535		0.860	0.180	0.845
C(10)	0.5932	0.4373	0.3924	C(21)	0.7785	0.3287	0.7280
	0.589	0.448	0.382		0.776	0.316	0.727

other words, all these packing variants corresponded to the same crystal structure. The potential was calculated as

$$u_{ij} = -a_{ij}r_{ij}^{-6} + b_{ij}\exp(-c_{ij}r_{ij}),$$

where r_{ij} is the distance between the ith and jth atoms and the a_{ij}, b_{ij}, and c_{ij} parameters are taken from [15]. The potentials were summed up for all the pairs of atoms spaced by distances not exceeding 12 Å.

The remaining 25 variants of the generated crystal structures had "much worse" energies of molecular interaction (exceeding 25.2 kcal/mol). Table 2 lists the unit-call parameters for the crystal structure determined by the methods of X-ray diffraction analysis [5] as well as parameters for the crystal structure generated by the method of discrete modeling. Table 3 gives the coordinates of nonhydrogen atoms in fractions of the unit-cells of these structures.

The tests of the program showed that the time of the search for a variant of the polycube packing is proportional to cubed order N of the packing space (e.g., the computations on an IBM PC AT-486DX2-50-type computer, required 0.25 min for $N = 257$, and about 205 min for $N = 2677$).

It should be emphasized that, within the method of discrete modeling, the above algorithm can readily be extended to the symmetry classes with two translationally independent molecules related by a center of inversion (e.g., the structural classes $P\bar{1}$, $Z = 2(1)$; $P2/m$, $Z = 2(m)$; $P2/m$, $Z = 2(2)$; $C2/m$, $Z = 4(m)$; etc.). This will be the subject of our next article.

REFERENCES

1. A. V. Maleev, V. G. Rau, K. A. Potekhin, *et al.*, Dokl. Akad. Nauk SSSR **315** (6), 1382 (1990) [Sov. Phys. Dokl. **35**, 997 (1990)].
2. A. V. Maleev, Kristallografiya **40** (3), 394 (1995) [Crystallogr. Rep. **40**, 354 (1995)].
3. P. M. Zorky and O. N. Zorkaya, Zh. Strukt. Khim. **39** (1), 126 (1998).
4. A. A. Kitaigorodsky, *Molecular Crystals* (Nauka, Moscow, 1971).
5. R. M. Wilson, W. S. Patterson, S. C. Austen, *et al.*, J. Am. Chem. Soc. **117**, 7820 (1995).

6. B. N. Delone (Delaunay) and D. K. Faddeev, *Theory of Irrationalities of the Third Order* (Akad. Nauk SSSR, Moscow, 1940), Tr. Mat. Inst. im. V. A. Steklova Akad. Nauk SSSR, Vol. 11.
7. K. A. Potekhin, A. V. Maleev, A. Yu. Kosnikov, *et al.*, Dokl. Akad. Nauk SSSR **304** (2), 367 (1989).
8. R. Basaran, Dou Shi-qi, and A. Weiss, Ber. Bunsenges. Phys. Chem. **96**, 1688 (1992).
9. N. Norman and H. Mathisen, Acta Chem. Scand. **15**, 1755 (1961).
10. G. L. Wheeler and S. D. Colson, J. Chem. Phys. **65**, 1227 (1976).
11. R. Boese and D. Blaser, Angew. Chem. Int. Ed. Engl. **27**, 304 (1988).
12. E. B. Fleischer, J. Am. Chem. Soc. **86**, 3889 (1964).
13. M. G. Matturro, R. D. Adams, and K. B. Wiberg, J. Chem. Soc. Chem. Commun. **878** (1981).
14. U. Burkert and N. Allinger, *Molecular Mechanics* (American Chemical Society, Washington, 1982; Mir, Moscow, 1986).
15. D. E. Williams and D. J. Houpt, Acta Crystallogr., Sect. B: Struct. Sci. **42**, 286 (1986).

Translated by L. Man

Crystallography Reports, Vol. 46, No. 1, 2001, pp. 133–137. Translated from Kristallografiya, Vol. 46, No. 1, 2001, pp. 144–148.

CRYSTAL GROWTH

Growth and Study of Single Crystals of $Pb_{1-x}Ba_xSc_{0.5}Nb_{0.5}O_3$ Solid Solutions

I. P. Raevskiĭ, V. V. Eremkin, V. G. Smotrakov, E. S. Gagarina, and M. A. Malitskaya

Institute of Physics, Rostov State University, Rostov-on-Don, 344090 Russia

e-mail: smotr@iphys.rnd.runnet.ru

Received March 23, 1999

Abstract—Crystals of $Pb_{1-x}Ba_xSc_{0.5}Nb_{0.5}O_3$ solid solutions with $0 \le x \le 0.58$ have been grown by the method of mass crystallization from flux. It is established that, unlike the concentration dependence of the corresponding ceramic, the concentration dependence of the temperature T_m (the maximum dielectric constant ε in crystals) does not attain saturation. Cooling of crystals with $x \le 0.04$ resulted in a spontaneous transition from the relaxor to the macrodomain ferroelectric state. In crystals with a higher barium content, the relaxor state is "locked in." © *2001 MAIK "Nauka/Interperiodica".*

INTRODUCTION

Recently, the solid solutions of and the barium scandioniobate of the composition $Pb_{1-x}Ba_xSc_{0.5}Nb_{0.5}O_3$ (PBSN) attract ever growing attention, on the one hand, as model objects for studying ferroelectrics–relaxors [1, 2] and, on the other hand, as a promising basic component for creating new materials for electrooptics and capacitors [3, 4]. However, the data on the *T*–*x* phase diagram and diffusion of the phase transitions in PBSN [2–4] indicate a strong dependence of the ceramic sample properties of these solid solutions on conditions of the growth. In particular, it is still unclear why the concentration dependence of the temperature T_m on the maximum dielectric constant becomes rather weak at $x > 0.3$–0.4. The situation with the Ba-concentration at which the relaxor state is locked-in and the spontaneous transition from the microdomain (relaxor) to macrodomain ferroelectric state observed in the disordered ceramic of the composition $PbSc_{0.5}Nb_{0.5}O_3$ (PSN) is suppressed is also unclear. At the same time, it is rather difficult to make the precise measurements on ceramic specimens because of the different reactivities of PSN and $BaSc_{0.5}Nb_{0.5}O_3$ giving rise to concentration gradients of the components in ceramic grains [4]. The latter, in turn, hinders the synthesis of the ceramic of the equilibrium PBSN solid solutions. This fact provides the formation of additional anomalies in the dependence $\varepsilon(T)$ observed in numerous studies [2, 4]. The diffusion of the $\varepsilon(T)$ maximum (because of the inhomogeneous composition) masks the effects caused by ion substitutions [5, 6]. In order to attain the equilibrium state, one has to increase both temperature and time of annealing of the PBSN-ceramic, thus increasing the probability of formation of lead vacancies V_{Pb}, which also lock-in the relaxor phase [7, 8].

In this study, we made an attempt to grow single crystals of PBSN solid solutions and study the effect of lead substitution by barium on the spontaneous transition from the relaxor to the macrodomain ferroelectric state. We also compared the properties of the crystals grown with the properties of the PBSN ceramic specimens obtained by hot pressing at high temperatures [3] (in such specimens, the formation of V_{Pb} vacancies and composition inhomogeneities are much less probable than in the ceramic obtained due to conventional annealing).

EXPERIMENTAL RESULTS AND DISCUSSION

The $Pb_{1-x}Ba_xSc_{0.5}Nb_{0.5}O_3$ crystals were grown by the method of mass crystallization from flux. We used the standard lead borate solvent of the composition $PbO–O \cdot 26B_2O_3$, the crystallization temperature range was 1160–1050°C, the melt was cooled at a rate of the 5.5°C/h. The starting materials were PbO, BaO_2, and B_2O_3 of the analytical grade, Nb_2O_5 of the extrapure grade, Sc_2O_3 of the trademark E (TU VZ-649-88). The PSN compound was preliminarily synthesized for four hours at 800°C. The yellow transparent crystals usually had an isometric shape and were faceted with the {100} planes of the perovskite-type basis and had 2-mm-long edges. Some crystals had plateletlike habit and the thickness exceeding 100 μm.

Upon the preliminary mechanical treatment of the crystal surfaces, the composition of the crystals was studied in a Camebax-Micro scanning microscope–microanalyzer by the standard method of the introduction of ZAF corrections. The standards were $PbSc_{1/2}Nb_{1/2}O_3$ and $BaTiO_3$ single crystals. The error in

1063-7745/01/4601-0133$21.00

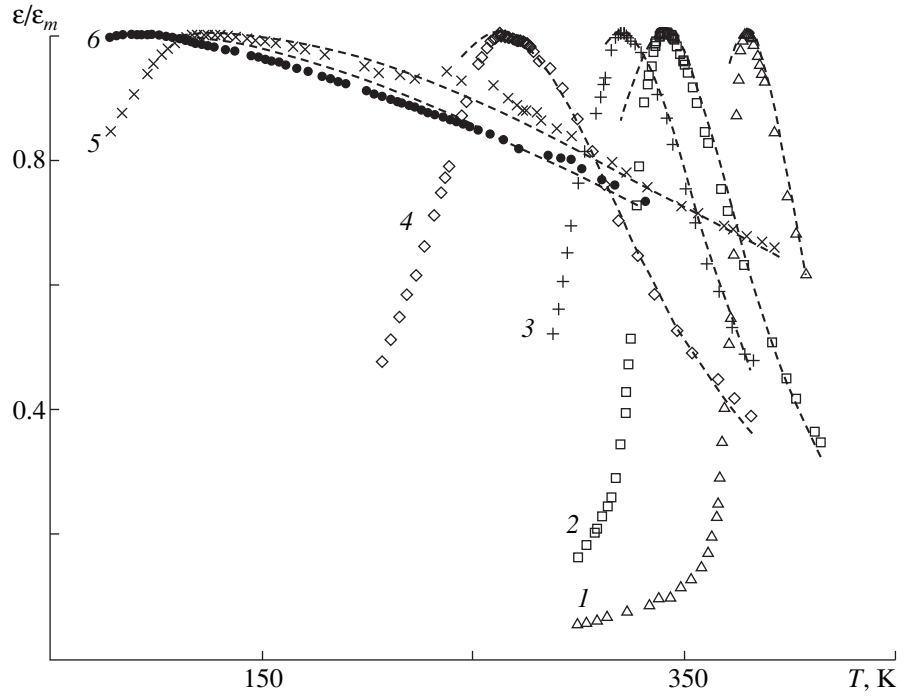

Fig. 1. Temperature dependences of $\varepsilon/\varepsilon_m$ recorded during heating of $Pb_{1-x}Ba_xSc_{0.5}Nb_{0.5}O_3$ crystals at a measuring-field frequency of 1 kHz; *x*: (*1*) 0, (*2*) 0.04, (*3*) 0.06, (*4*) 0.17, (*5*) 0.48, and (*6*) 0.58. Dots indicate the experimental data, dashed lines indicate the data calculated by Eq. (1) with the use of the $A = 1/2\varepsilon_m\sigma^{*2}$ values.

composition determination did not exceed 2%. The method of crystals studies were described elsewhere [6].

The X-ray diffraction analysis of the powders (ground crystals) showed that with an increase of *x*, the powders of the compositions $Pb_{1-x}Ba_xSc_{0.5}Nb_{0.5}O_3$ with $0 < x < 0.1$ showed an increase of the angular parameter α_R of the rhombohedrally distorted perovskite-like unit cell (determined from the 222 and $22\bar{2}$ diffraction reflections) from 89.89° to 89.97°. Within the experimental error, the unit cell of the crystals with $x \geq 0.1$ is cubic. The reduced parameter *a* of the perovskite-like unit cell calculated using the 400 reflection ($\Delta a = \pm 0.001$ Å) approximately linearly increases with *x* in the whole barium concentration range studied. Unlike the case of ceramic [4], we observed no line broadening on X-ray diffraction pattern in comparison the linewidth observed for PSN. Indirectly, this indicates that the solid solutions obtained are homogeneous. The corresponding X-ray diffraction patterns showed no superstructural reflections due to Sc- and Nb-ion ordering. This is consistent with our earlier data [6] indicating that the PSN crystals grown in the indicated temperature range are obviously disordered.

Dielectric measurements showed that, similar to the case of ceramic, an increase of Ba concentration results in a decrease of the temperature T_m of the maximum of $\varepsilon(T)$ for PBSN crystals, an increase in the diffusion maximum, and a decrease in the maximum value of ε_m. Figure 1 illustrates the change in the $\varepsilon(T)$ curve with the change in the Ba-concentration. Since the ε_m values of crystals show a considerable scatter, it is more convenient to compare the temperature dependences of $\varepsilon/\varepsilon_m$ ratio for the PBSN crystals. The concentration dependences of ε_m and T_m of the PBSN crystals are shown in Fig. 2. At low Ba-concentrations, these curves are close to the analogous curves for the ceramic calculated by the data [3]. At $x > 0.4$, the $T_m(x)$ curve for the ceramic attains saturation, whereas the T_m values for crystals continue decreasing with an increase in *x*. It should be indicated that, according to [3], ε for the PBSN ceramic specimens with $x > 0.5$ is almost temperature-independent. On the contrary, the $\varepsilon(T)$ dependences for crystals with $x \approx 0.6$ have a clearly pronounced maximum (Fig. 1, curve *6*). Different $T_m(x)$ dependences for crystals and ceramics at high Ba-concentrations seem to be caused by a nonequilibrium of the ceramic specimens, which is more probable the higher the *x* value.

The $\varepsilon(T)$ dependences for some crystals with high Ba-concentration show insignificant additional anomalies at $T > T_m$ (Fig. 1, curves *5*, *6*). These anomalies seem to be caused by the formation of a thin subsurface layer in the crystal during the pouring-out of the mother liquor with PSN concentration higher than in the crystal bulk. The formation of such subsurface layers were also observed in crystals of other solid solutions [6].

Above T_m, the temperature dependences of ε for most crystals are well described by the following equation [9]:

$$1/\varepsilon = 1/\varepsilon_m + A(T - T_m)^n, \quad (1)$$

where A is a constant and $1 < n \le 2$. If $n = 2$, the diffusion of the $\varepsilon(T)$ maximum is usually evaluated with the aid of the parameter σ [9]:

$$\sigma = (T - T_m)[2\varepsilon_m(1/\varepsilon - 1/\varepsilon_m)]^{-1/2}, \quad (2)$$

To compare the diffusion of the $\varepsilon(T)$ maxima in crystals and ceramic specimens, we used the effective value of the diffusion parameter σ* calculated by Eq. (2) for the point $\varepsilon = 0.75\varepsilon_m$ of the dependence $\varepsilon(T)$ at $T > T_m$. For the symmetric maximum of ε, the value of σ* thus determined is about 2.5 times higher than the value of the width of the ε maximum at the height of 3/4, which is often used as the characteristic of diffusion of the $\varepsilon(T)$ dependence [10]. The $\varepsilon(T)$ dependences calculated by Eq. (1) with the use of the σ*-values (dashed lines in Fig. 1) agree quite well with the experimental data at $T > T_m$, which justifies the use of σ* for the comparative analysis of the diffusion of $\varepsilon(T)$ maxima. As is seen from Fig. 2, the σ* values are close to the corresponding values for ceramic specimens [3].

All the crystals studied showed frequency dispersion in ε and an increase in T_m with the frequency f of the measuring field. Figure 3 shows the $\varepsilon(T)$ dependences for crystals with low and high Ba-concentration measured at various field frequencies. The change in the shape of $\varepsilon(T)$ with the field frequency in the crystals with $x \ge 0.08$ is characteristic of relaxors. The crystals with $0 \le x \le 0.04$ have a jump in the $\varepsilon(T)$ dependence slightly below the temperature T_m. Unlike T_m, the temperature position of this jump is almost frequency-independent; however, it is characterized by a considerable temperature hysteresis, which increases with x (Fig. 4). Earlier, similar anomaly was observed for the PSN ceramic and was interpreted as the spontaneous transition from the relaxor to the macrodomain ferroelectric state [7, 8].

Earlier, this transition was observed only for the ceramic, and, therefore, we decided to study its effect on the optical properties of PSN and PBSN crystals. At room temperature, the crystals with $0 \le x \le 0.04$ studied in the transmitted polarized light demonstrated the symmetric (at an angle of 45° with respect to the side faces) extinction during table rotation. This corresponded to the rhombohedral system of the low-temperature PSN and PBSN phases. Upon crystal heating, the transition to the relaxor phase was accompanied by a considerable reduction (almost to zero) in the birefringence in the central part of the crystal with the subsequent motion of the diffuse phase fronts toward external faces. During cooling, the spontaneous transition to the macrodomain ferroelectric phase was accompanied by the appearance of birefringence characteristic of rhombohedral crystals and showed a considerable hysteresis close to the hysteresis for $\varepsilon(T)$.

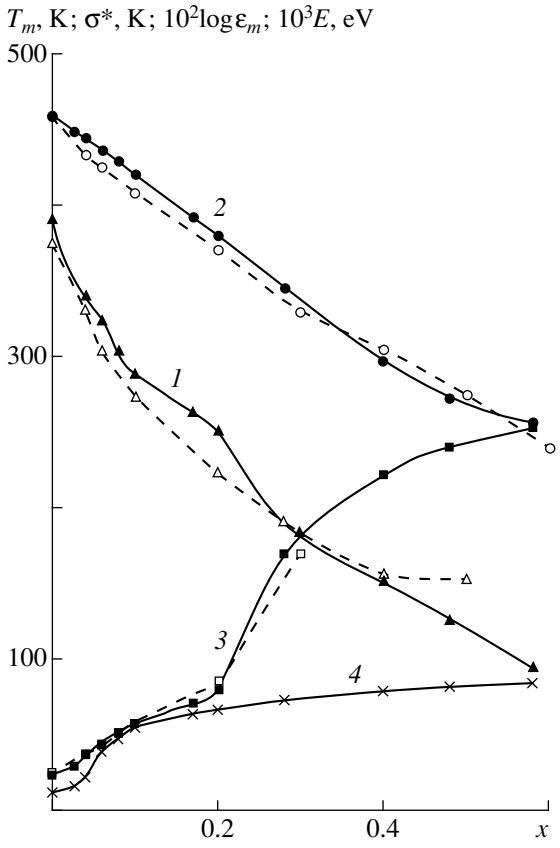

Fig. 2. Concentration dependences of the temperature T_m of (*1*) the maximum value of ε, (*2*) the maximum value of ε_m, (*3*) the effective parameter σ* of the phase-transition diffusion, and (*4*) the activation energy E in the Fogel–Foolcher law for the $Pb_{1-x}Ba_xSc_{0.5}Nb_{0.5}O_3$ solid solutions. Solid lines indicate the data for the crystals, dashed lines indicate the data for the ceramic specimens [3].

In all the crystals studied, the dependence of T_m on f is well described by the Fogel–Foolcher law:

$$f = f_0\exp[-E/k(T_m - T_0)], \quad (3)$$

where f_0 is the frequency of the attempts to overcome the potential barrier E, k is the Boltzmann constant, T_0 is the Fogel–Foolcher temperature (often interpreted as the temperature of static lock-in of electric dipoles or the temperature of the transition to the dipole-glass state [11]). For PBSN crystals, $f_0 = (0.5–1) \times 10^{11}$ Hz, which is close to the values known for other ferroelectrics–relaxors [7, 8, 11]. For crystals with $0 \le x \le 0.04$, the T_0 values are approximately equal to the temperature of the jump on the $\varepsilon(T)$ dependence, similar to the case of the PSN ceramic studied earlier [7, 8] (Fig. 4). The activation energy E in the Fogel–Foolcher law increases with an increase in x and attains a value of $E = (0.08 \pm 0.01)$ eV at $x \approx 0.4$. Then it remains approximately constant. It should be noted that almost the

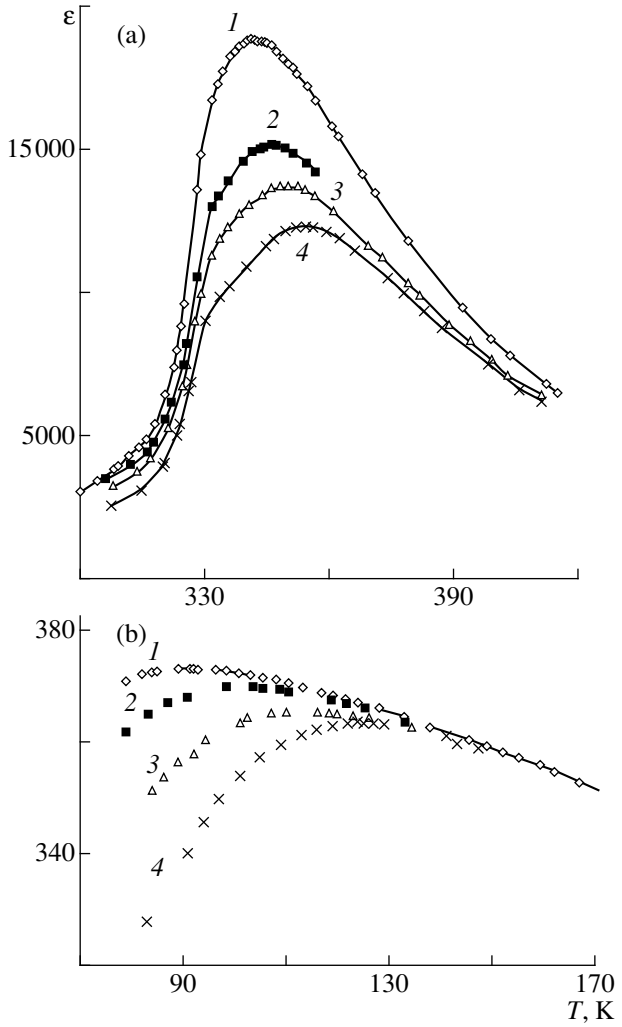

Fig. 3. Temperature dependences ε(*T*) for $Pb_{1-x}Ba_xSc_{0.5}Nb_{0.5}O_3$ crystals with the composition parameter (a) $x = 0.04$ and (b) $x = 0.58$. The measuring-field frequencies are: (*1*) 1, (*2*) 10, (*3*) 100, and (*4*) 1000 kHz.

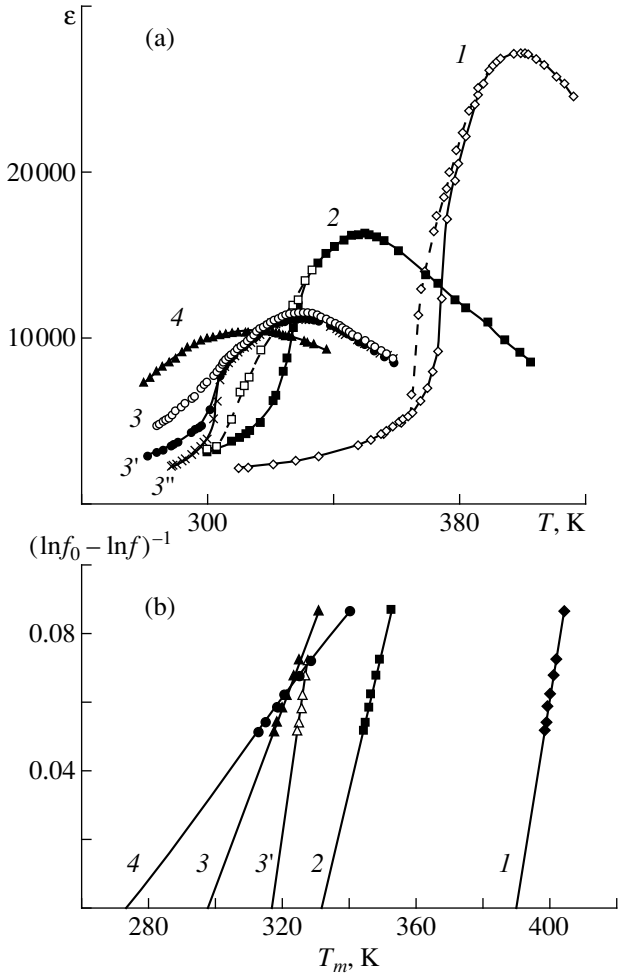

Fig. 4. (a) The ε(*T*) dependences recorded during heating (solid lines) and cooling (dashed lines) at a measuring-field frequency of 100 Hz and (b) the $(\ln f_0 - \ln f)^{-1}$ (T_m) dependences for $Pb_{1-x}Ba_xSc_{0.5}Nb_{0.5}O_3$ crystals with the composition parameter *x*: (*1*) 0, (*2*) 0.04, (*3*) 0.06, and (*4*) 0.08. Curve *3*' was recorded upon 80-day-storage of the crystal at room temperature and curve *3*" was recorded upon crystal cooling from 370 to 300 K in a 1.5 kV/cm constant field.

same *E* values were also observed in $PbMg_{1/3}Nb_{2/3}O_3$ crystals [7, 11]. In the Ba-concentration range corresponding to the lock-in of the relaxor state, $0.06 \le x \le 0.10$, the $E(x)$ curve has a kink (Fig. 2).

Some of the crystals studied earlier showed the so-called dielectric aging, i.e., a decrease in ε-values and dielectric losses with time. Earlier, similar phenomenon was also observed in conventional ferroelectrics and relaxors and seemed to be caused by pinning of the domain structure due to screening of domain walls and formation of internal electric fields [12–14]. In crystals with $x = 0.06$ (showing no spontaneous transition from the relaxor to the macrodomain ferroelectric state during cooling), aging for several days at room temperature resulted in the appearance of a jump in ε(*T*) during the subsequent heating (Fig. 4a, curve *3*'). Thus, the properties of the aged crystals with $x = 0.06$ are analogous to the properties of the PBSN crystals with a lower Ba-concentration (in which heating induces the transition from the macrodomain ferroelectric state to the relaxor one) and those of the classical relaxors, $PbMg_{1/3}Nb_{2/3}O_3$ and $PbZn_{1/3}Nb_{2/3}O_3$, exposed to a constant electric field with the intensity exceeding 2–2.5 and 10–20 kV/cm, respectively [15]. It seems that this behavior is provided by inducing a macrodomain ferroelectric phase due to internal electric fields formed in the process of dielectric aging. The intensity of such fields in the $PbMg_{1/3}Nb_{2/3}O_3$-based relaxor ceramic attains several kilovolts per centimeter [15], i.e., is comparable with the intensity of the external field necessary for inducing the macrodomain ferroelectric phase. To confirm this assumption, we obtained the ε(*T*) dependences for the PBSN crystals with $x = 0.06$ in (i) the heating mode without a field and (ii) upon

cooling from 370 to 300 K in a constant 1.5 kV/cm electric field. In this case, the $\varepsilon(T)$ curve really had a jump similar to that observed for the aged crystal (Fig. 4a, curve *3*"). Heating of the crystal up to 400–430 K completely removed all the residual effects, and the dependence $\varepsilon(T)$ (both during cooling and the subsequent heating) exactly repeats curve *3* in Fig. 4a. The results obtained indicate that an external electric field comparable with the internal fields formed in the process of dielectric aging induces a macrodomain ferroelectric phase in PBSN crystals with $x = 0.06$. It seems that the change in the properties of the PBSN crystals with $x = 0.06$ during dielectric aging is analogous to the phenomenon observed in a number of earlier studies [16]—the formation of macrodomain ferroelectric state in relaxors caused by an electron beam incident onto a specimen in electron microscopy studies. Indeed, the intensification of dielectric aging during the photoactive or the ionizing irradiation (facilitating the screening processes) was observed for numerous ferroelectrics [12, 13].

CONCLUSION

Thus, the saturation of the dependence $T_m(x)$ in ceramics of the PBSN solid solutions observed at $x > 0.4$ seems to be associated with the concentration inhomogeneities. At the same time, considerable diffusion of the phase transition taking place in both ceramics and crystals seems to be explained by the appearance of the properties characteristic of dipole glasses. This interpretation is also favored by the heat-conductivity data for ceramic PBSN specimens [1]. With an increase of Ba concentration, the relaxor state gradually becomes more stable and, at the critical concentration, $x \approx 0.05$, is "locked in." In the crystals with the Ba-concentration slightly considerably exceeding the critical value, the macrodomain ferroelectric phase can be induced by a relatively weak external electric field or by internal electric fields formed during dielectric aging.

ACKNOWLEDGMENTS

This study was supported by the Russian Foundation for Basic Research, project no. 96-02-17463.

REFERENCES

1. M. Fahland, G. Mattausch, and E. Hegenbarth, Ferroelectrics **168**, 9 (1995).
2. C. Malibert, B. Dkhil, J. M. Kiat, *et al.*, J. Phys.: Condens. Matter **9**, 7485 (1997).
3. M. Ya. Dambekalne, K. Ya. Borman, A. R. Shternberg, *et al.*, Izv. Akad. Nauk, Ser. Fiz. **57**, 78 (1993).
4. I. P. Pronin, T. Ayazbaev, N. V. Zaĭtseva, *et al.*, Neorg. Mater. **32**, 1528 (1996).
5. A. A. Bokov and I. P. Rayevsky, Ferroelectrics **144**, 147 (1993).
6. V. Eremkin, V. Smotrakov, E. Gagarina, and I. P. Raevskiĭ, J. Korean Phys. Soc. **32**, S1597 (1998).
7. F. Chu, I. M. Reaney, and N. Setter, Ferroelectrics **151**, 343 (1994).
8. F. Chu, I. M. Reaney, and N. Setter, J. Appl. Phys. **77**, 1671 (1995).
9. V. A. Isupov, Fiz. Tverd. Tela (Leningrad) **28**, 2235 (1986) [Sov. Phys. Solid State **28**, 1253 (1986)].
10. C. G. F. Stenger and A. J. Burggraaf, Phys. Status Solidi **61**, 653 (1980).
11. D. Viehland, S. Jang, L. E. Cross, *et al.*, Philos. Mag. B **64**, 335 (1991).
12. V. M. Fridkin, *Photoferroelectrics* (Nauka, Moscow, 1979).
13. I. P. Raevskiĭ, M. A. Malitskaya, P. F. Tarasenko, *et al.*, Zh. Tekh. Fiz. **54**, 1325 (1984) [Sov. Phys. Tech. Phys. **29**, 763 (1984)].
14. L. S. Kamzina and N. N. Kraĭnik, Fiz. Tverd. Tela (St. Petersburg) **40**, 527 (1998) [Phys. Solid State **40**, 485 (1998)].
15. L. E. Cross, Ferroelectrics **76**, 241 (1987).
16. L. E. Cross, Ferroelectrics **151**, 305 (1994).

Translated by L. Man

Crystallography Reports, Vol. 46, No. 1, 2001, pp. 138–143. Translated from Kristallografiya, Vol. 46, No. 1, 2001, pp. 149–154.

CRYSTAL GROWTH

Autodeformation Bending of Gypsum Crystals Grown under the Conditions of Counterdiffusion

Yu. O. Punin and O. I. Artamonova

St. Petersburg State University, Universitetskaya nab. 7/9, St. Petersburg, 199164 Russia

e-mail: valera@crysgen.geol.pu.ru

Received April 6, 1999

Abstract—The dynamics and kinetics of growth-induced bending of gypsum crystals grown from solution have been studied. Crystallization was performed by the method of chemical reaction under the conditions of component counterdiffusion. It is established that autodeformation bending occurs in the [001] direction at the growth front and is caused by cationic impurities. The crystal curvature depends on the anisotropy of growth rate and increases at lower supersaturations. The mechanism of growth-induced crystal bending is suggested which takes into account the heterometry stresses providing the appearance of a bending moment at the growth front. © *2001 MAIK "Nauka/Interperiodica".*

INTRODUCTION

Spontaneous macroscopic deformation of crystals occurring during their growth (autodeformation of the bending–twisting type) is a rather widespread phenomenon. It was observed in both natural crystals [1, 2] and numerous artificially synthesized compounds [3, 4]. However, the phenomenon is studied insufficiently and mainly on mineral crystals [5–12]. Only several experimental studies to this effect are known [3, 13]. The articles are devoted only to a particular aspect of the problem, the so-called Ashelby effect in filamentary crystals (whiskers).

The results of our previous studies of mostly natural twisted and bent crystals [10–12, 14, 15] and the analysis of the known data led to a conclusion that the determining role in growth-induced bending or twisting is played by intersectorial heterometry stresses. However, it is very difficult to establish the characteristics of this process on crystals grown, although some attempts along this line have been undertaken [10, 11]. The formation of synthesized bent gypsum ($CaSO_4 \cdot 2H_2O$) crystals was first observed elsewhere [16, 17]. Bent gypsum crystals are also known to be formed under natural conditions [1, 2].

Below, we describe the results of the experimental *in situ* growth of bent gypsum crystals.

EXPERIMENTAL

Gypsum was crystallized from aqueous solutions at room temperature under a microscope by the following exchange chemical reaction:

$$CaCl_2 + Me_2^{n+}(SO_4)_n + H_2O \longrightarrow CaSO_4 \cdot 2H_2O\downarrow + MeCl_n,$$

where n is the valence of an exchange cation. Quantitatively, the bending kinetics of gypsum crystals was studied in the systems with monovalent exchange Me^{n+} cations (Li^+, K^+, and Rb^+). We also performed a series of qualitative experiments with a large number of mono-, bi-, and trivalent cations.

The crystallization process was decelerated by the method of reagent counterdiffusion developed elsewhere [16]. The schematic of the experiment is shown in Fig. 1. A flat glass cell has two deepenings–reservoirs filled with dry regents. The gap between the cell base and its cover (i.e., the crystallization space) is filled with water, and then the cell is placed onto the microscope table. Upon certain time, a narrow dense "bridge" of a fine-crystalline precipitate is formed at the site where the diffusing components meet. On both sides of this bridge, gypsum crystals slowly grow up to the complete consumption of the reagents from the cell

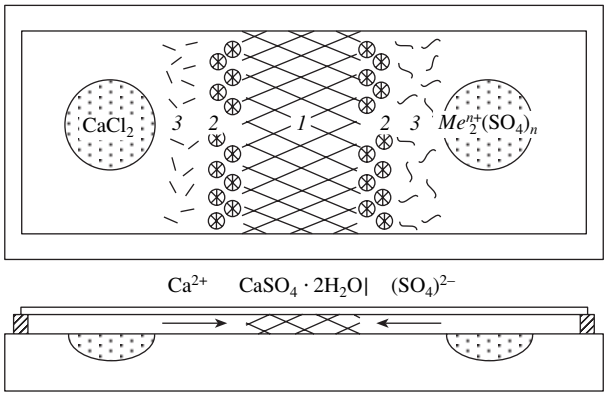

Fig. 1. Schematic of a cell and the crystallization space. (*1*) a partition from a dense fine crystalline gypsum precipitate, (*2*) spherulite zone, and (*3*) single crystal zone.

1063-7745/01/4601-0138$21.00 © 2001 MAIK "Nauka/Interperiodica"

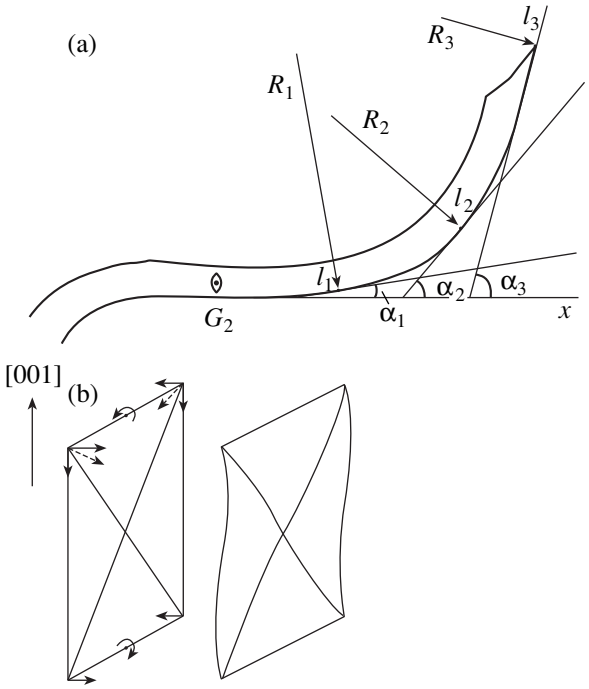

Fig. 2. Schematic of (a) gypsum-crystal bending and (b) system of forces acting at the growth front and caused by heterometry stresses.

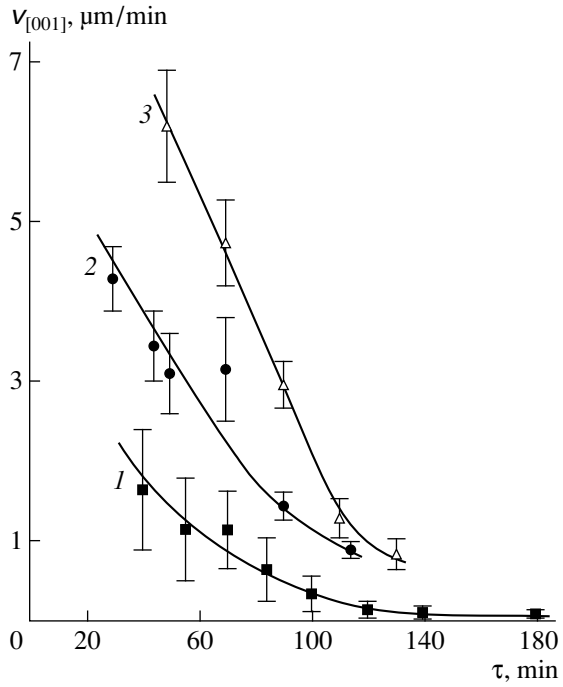

Fig. 3. Growth rates of gypsum crystals along the [001] direction versus crystallization time. Me^{n+}: (*1*) K^+, (*2*) Rb^+, and (*3*) Li^+.

reservoirs. At the end of the experiment, the crystals attained ~0.1–0.3 mm in length. In the crystallization zone space adjacent to the reservoir with exchange sulfate cations, the grown crystals were *S*-like bent. Choosing the fixed fields of view in the crystallization space and regularly taking the photographs of these fields, we managed to record the changes in the shape and size of the gypsum crystals in the course of crystallization. These data were used to calculate the growth rates of crystals at any time and determine the characteristics of bending deformation. In this case, growth rates were measured along curvilinear trajectories of the points moving on the surfaces of bent crystals along the [001] direction [i.e., the middle line of the (010) face] and along the transverse direction in the vicinity of the crystal center. Since the conditions in the crystallization space were inhomogeneous and the rigorous standardization of the experiments by this method is rather difficult, we had to perform from five to twenty experiments for each system, which included the investigation of from three to five fields of view for each system. The experimental kinetic curves of linear crystal dimensions along different directions and the bending angles versus time were obtained by averaging the data over about 200 points. This provided rather low root-mean square deviations and, to a large extent, compensated the inhomogeneous conditions existing in various experiments and at different points of the crystallization space.

CRYSTAL MORPHOLOGY AND BENDING DYNAMICS

The synthesized gypsum crystals (the 2/*m* symmetry) were faceted with the pinacoid {010} and prism {120} and {111} faces. They were elongated in the [001] direction and flattened along {010}. Crystals were bent in the (010) plane. In the perpendicular direction, [010], no considerable bending component was observed. This was concluded from the unvariable microscope focusing over the whole surface of the upper (010) face even at the maximum magnification. The occurrence of deformation and not the distortion of the external shape of the crystal due to inhomogeneous relief was proved by the change of the extinction position along the crystal length. The angular difference in the extinction positions at the crystal center and at its top corresponded to the total angle of morphological bending. Figure 2 shows the schematic of the *S*-like bending of a gypsum crystal lying on the (010) face. It is seen that the bending axis coincides with the [010] direction and that the curvature radius *R* decreases toward the crystal periphery (denoted by the emerging symmetry axis G_2 at the crystal vertices). The bending axis, being normal to the direction of preferable growth, [001], "moves" in the space. This deformation distribution over the crystal length leads to a conclusion that, at the end of the process, the bending becomes more intense. The characteristic feature of the method used is a decrease of the supersaturation during the experiment because of the reagent consumption from

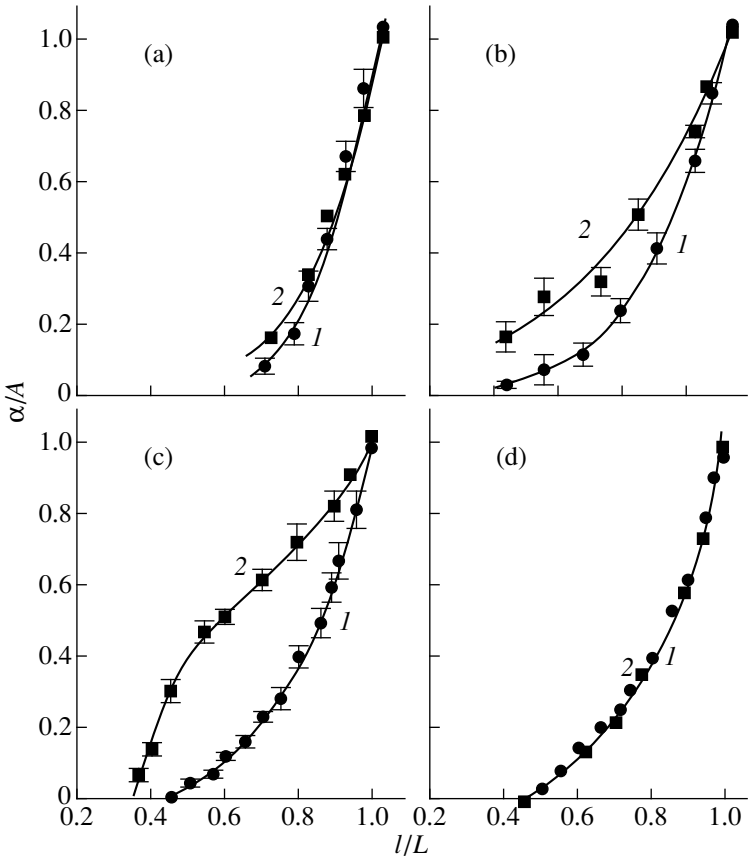

Fig. 4. Variation of the bending angle along the crystal length: (*1*) calculated from the final crystal shape, (*2*) determined from the frames taken for Me^{n+}: (a) K^+, (b) Rb^+, and (c) Li^+, and (d) Paris twins in the Rb-system.

the reservoirs. In other words, the process is nonstationary. This is clearly seen from the temporal growth-rate dependences (Fig. 3). Thus, the changes in the bending characteristics of crystals with time also reflects their dependence on supersaturation.

The bending geometry of gypsum crystals shows that bending occurs along the ±[001] directions at the growth front, i.e., on the {111} faces. No volume bending deformation, i.e., bending of a crystal as a whole, during growth takes place; otherwise, the accumulation of deformation would result in the "opposite curvature distribution" along the crystal irrespectively of the bending kinetics.

To confirm this very important conclusion, compare the dependences of the bending angle α at the given point of the crystal as a function of the distance *l* of the point along [001] from the crystal center (Fig. 2a) obtained by two different methods—from the final crystal shape and from the crystal photographs taken at successive moments of its growth. These dependences (curves *1* and *2*, respectively) are shown in Figs. 4a–4c for three different exchange cations, K^+, Rb^+, and Li^+. Each curve was constructed by the data averaged over seven to nine crystals. Along the coordinate axes, we plotted the reduced values of the angles α/*A* and length *l*/*L*, where α and *l* are the current values, whereas *A* and *L* are the total (final) values of the corresponding quantities. For *Me* = K, curves *1* and *2* coincide within the mean error. This uniquely proves the already bent crystal experiences no additional bending under the arising stresses during further growth of the crystal. The behavior of these curves for *Me* = Li is more interesting: curve *2* lies above curve *1*; in other words, during further growth of the already bent crystal, this crystal even unbends! The case *Me* = Rb is intermediate—at short growth times, the crystal behaves similar to the Li system, and at the end of the growth process, similar to the K system. Obviously, unbending of the already bent crystal in the process of its growth can proceed only due to the transverse growth in the directions normal to [001]. Indeed, overgrowth of the layer on a bent substrate results in the appearance of elastic stresses, which unbend the substrate. This phenomenon was first studied by Shaskol'skaya [18]. The existence of pronounced elastic stresses in growth pyramids of the [001] zone (i.e., {120} and {010}) is indicated by the intense cracking of the growing material. The crack planes are almost normal to the [001] direction.

Thus, the process of growth-induced bending (for the sake of brevity, hereafter called simply growth bending) of gypsum crystals can be divided into two

stages—(1) bending proper along the preferable [001] direction during crystal growth and (2) unbending during growth along the transverse direction. In this case, bending takes place at the growth front (in the surface layer of the "head" {111} faces), whereas unbending is of the volume character. The same two stages were also observed for bent lithium mica [11] and twisted quartz [10]. Growth-induced twisting was also observed in axalic acid crystals [14].

BENDING MECHANISM

When separating (cleaving) bent crystals into parts, no bending relaxation is observed. This indicates that we deal with plastic bending. It can be assumed that, similar to other known cases of growth bending–twisting [10–12, 14], autodeformation of gypsum occurs via formation of microblocks with the systematically unidirectionally misoriented at the growth front. Indirectly this fact is also confirmed by formation of macroblocks (splitting subindividuals) at the bent ends of gypsum crystals. As was showed [19, 20], these macroblocks arise due to geometric "selection" from ensembles of microblocks emerging at the growth front.

Formation of growth microblocks, in general, and bending–twisting, in particular, should be caused by stresses of the constitutional heterometry [19], i.e., inhomogeneous impurity distribution in crystals. The key part of impurities is emphasized in most studies to the effect [1–8, 13, 16, 17], and also in our earlier papers [10–12, 14]. The experiments on gypsum show that, in this case as well, crystal bending is caused by impurities, whose role is played by exchange cations. Indeed, under the conditions of counterdiffusion, bent crystals are always formed in the zone of the reaction space enriched with exchange cations, but never in the zone enriched with Ca (Fig. 1). During gypsum crystallization by the method of solvent evaporation from hemihydrate solution (i.e., from the impurity-free system), no bending crystals are formed. Thus, it is highly probable that growth-induced bending of gypsum crystals is caused by cationic impurities.

Earlier, it was shown that crystal twisting during growth is caused by a torque formed due to intersectorial stresses [10, 14]. In growth bending of gypsum crystals, the bending moment should be formed at the growth front of the "crystal head" ({111} faces with respect to the [010] direction). This moment can be represented as a system of forces (Fig. 2b) provided, e.g., by impurity-induced broadening of growth sectors of the {111} faces in the (010) plane, i.e., along the *a*- and *c*-directions. This is confirmed by mathematical modeling of gypsum-crystal bending [15]. Unfortunately, small crystal dimensions do not allow the direct measurement of the unit-cell parameters in various growth sectors of the gypsum crystal. The determination of the average unit-cell parameters of the crystals grown in systems with different exchange cations by the method of powder diffractometry is very inaccurate ($\sim 5 \times 10^{-3}$ Å) because there are no intense reflections on powder diffraction patterns of gypsum (in the range of large angles 2θ). Therefore, we failed to obtain reliable values of the differences in the unit-cell parameters of gypsum crystals grown in various systems. An indirect piece of evidence of the nonuniform capture of impurities by growth sectors of the {111} faces and the {120} zone is the sectorial extinction of gypsum crystals lying on the {010} faces. The growth sectors of the faces belonging to the same simple form were observed to extinguish simultaneously. The difference in the extinction positions for different simple forms attained up to five angular degrees. This indicates slightly different orientations of the optical indicatrix in different sectors and, thus, their different impurity compositions.

BENDING KINETICS

Above, we showed that there are two components of growth bending—plastic bending at the front of the preferential crystal growth and volume unbending in growth along the transverse directions. These processes occur in parallel and are relatively independent. The method used allowed us to analyze the kinetics of these two processes separately.

To characterize growth bending, we introduce a specific bending angle $\beta = \Delta\alpha/\Delta l$. In the limit (at $\Delta l \longrightarrow 0$), the angle β measured using the final growth shape tends to the angle of crystal curvature and, thus, reflects both processes—bending proper and unbending. Therefore, it is necessary to use the β-values calculated from the successive frames (curves *2* in Fig. 4), which provides the determination of the true bending angle per unit increment of the crystal along the [001] direction, i.e., the bending intensity. Figure 5a shows the change in the β-value with time for crystallization with *Me* = K, Li, and Rb. The bending intensity varies with the system composition, but, in all the three cases, it increases with an increase of growth time, although the rates of this increase are different. We have already indicated that at the end of the growth process, supersaturation in the reaction space decreases. Figure 5a reflects an increase of the autodeformation intensity of gypsum crystals with a decrease of supersaturation. This behavior is rather unusual. Indeed, for other types of autodeformation processes (such as splitting, twinning, and polytype transformations), the intensity of the process usually increases with an increase in supersaturation [19]. Scarce data on bending–twisting seem to confirm this tendency as well [3, 21]. However, the behavior of gypsum shows that this tendency is not universal.

Possibly, an increase of bending intensity with a decrease of supersaturation is caused by a more pronounced bending moment at the growth front. In accordance with the schematic in Fig. 2b, the bending moment increases with an increase of the tilt of growth-sector boundaries with respect to [001], i.e., with a decrease of the difference in the growth rates along

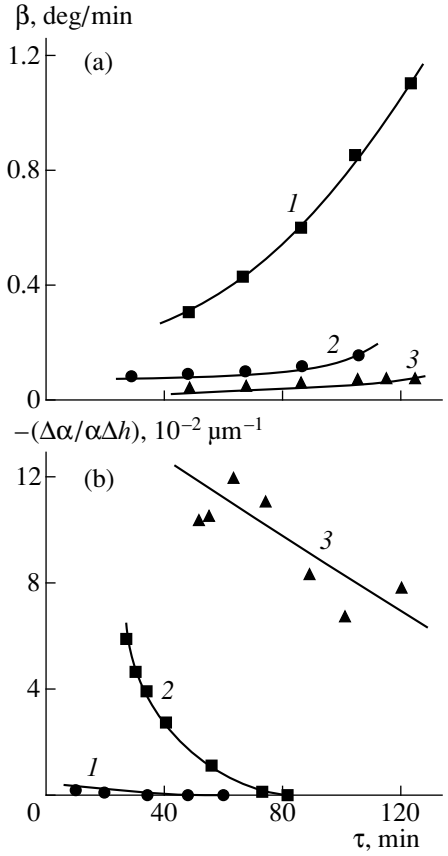

Fig. 5. (a) Bending and (b) unbending intensities in gypsum crystals as functions of crystallization time. Me^{n+}: (*1*) K^+, (*2*) Rb^+, and (*3*) Li^+.

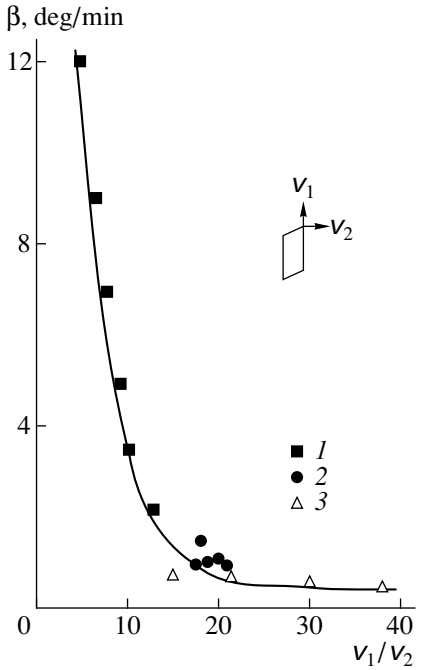

Fig. 6. Bending intensity as a function of growth-rate of gypsum crystals. Me^{n+}: (*1*) K^+, (*2*) Rb^+, and (*3*) Li^+.

[001] and in the transverse directions. On the other hand, the experimental data show that, for all the three systems with monovalent exchange cations, the anisotropy in growth rates decreases with a decrease of supersaturation (i.e., with an increase of the growth time). Figure 6 demonstrates the inverse relation between the bending intensity of crystals and the anisotropy of the growth rate. The points for different exchange cations satisfactorily fit the same hyperbolic-type curve. It should be noted that possible accumulation of impurities in the crystallization space is compensated by a decrease in the anisotropy of growth rates, which affects the difference between the impurity compositions in various growth sectors.

Now, consider the second process of the autodeformation—volume unbending of gypsum crystals. The intensity of this process can be characterized by the quantity $\Delta\alpha/\Delta h$. In other words, with a decrease of the initial bending angle $\Delta\alpha$ per unit increment in crystal growth Δh in the transverse direction. Since unbending is caused by elastic stresses in the layer growing on a bent substrate and the fact that these stresses are more pronounced the more pronounced the initial bending is, we have to consider the relative unbending intensity $\Delta\alpha/\alpha\Delta h$. Figure 5b shows the dependence of this quantity on growth time. In the case of unbending (Fig. 4), the process becomes less intense at the end of crystallization. Since unbending is a volume process, this behavior can readily be interpreted. With an increase of the growth time, the transverse cross section of the crystal also increases and, therefore, the bending stiffness must also increase. This is confirmed by the absence of any unbending for Paris twins in the Rb system (cf. Figs. 4b, 4d). Anomalously wide twin partners give rise to pronounced bending stiffness. The dynamics of the process drastically changes: the $\alpha/A = f(l/L)$ curves constructed using the current α values and the final crystal shape coincide. Thus, a decrease of the unbending intensity in the course of crystallization is associated not with the change in supersaturation, but only with an increase of the crystal width.

The influence of the system composition on crystal unbending is more complicated. Since the growth rates in the transverse directions in various systems are close, the transverse dimensions of crystals grown within the same times are also close. On the other hand, there is an obvious direct correlation between the unbending intensity and the anisotropy in growth rates, which decreases in the row from Li to K (because of a decrease of growth rates in the [001] direction, Fig. 3). Therefore, we assume that different unbending abilities of growing crystals in the systems with different compositions are associated mainly with different anisotropies in growth rates. Indeed, we have already pointed out that a decrease in the crystal anisometricity results in an increase of the bending moment at the growth front. In turn, this bending moment "suppresses" the elastic stresses in the layers growing along the normal

to the [001] direction and, thus, also hinders crystal unbending.

Thus, supersaturation affects both processes occurring during growth bending of gypsum crystals mainly via the change of crystal shape. This confirms once again the conclusion drawn in our earlier studies of bent and twisted crystals of other compounds [10–12, 14, 15] that crystal morphology, faceting, and habit determine both the kinetics of crystal bending–twisting of crystals during growth and autodeformation.

CONCLUSIONS

Spontaneous bending of gypsum crystals during their growth occurs under the conditions of enrichment of the solution with cationic impurities and seems to be caused by their capture.

Bending takes place along the direction of preferential growth [001] at the growth front and is intensified with a decrease of supersaturation.

The kinetics of autodeformation bending is controlled by the crystal shape, which is explained by the distribution of stresses of the intersectorial heterometry.

ACKNOWLEDGMENTS

The study was supported by the Russian Foundation for Basic Research, project no. 98-05-64151.

REFERENCES

1. L. J. Spencer, Miner. Mag. **19** (95), 263 (1921).
2. M. P. Maleev, *Properties and Genesis of Natural Filamentary Crystals and Their Aggregates* (Nauka, Moscow, 1971).
3. F. Bernauer, *Gedrillte Kristalle* (Gebruder Borntraeger, Berlin, 1929).
4. H. Buckley, *Crystal Growth* (Wiley, New York, 1951; Inostrannaya Literatura, Moscow, 1954).
5. G. G. Lemmleĭn, *Morphology and Genesis of Crystals* (Nauka, Moscow, 1973), p. 107.
6. S. A. Borodin, Zap. Vses. Mineral. O–va., No. 5, 578 (1961).
7. M. S. Pichugin, Yu. A. Kharitonov, and N. V. Belov, Zap. Vses. Mineral. O–va., No. 1, 55 (1969).
8. A. Searl, Miner. Mag. **53** (5–6), 547 (1989).
9. H.-G. Machel, Geology **15** (10), 963 (1987).
10. M. A. Kuz'mina, Yu. O. Punin, and I. E. Kamentsev, Zap. Vses. Mineral. O–va., No. 4, 445 (1987).
11. A. G. Shtukenberg, Yu. O. Punin, and E. N. Kotel'nikova, Zap. Vses. Mineral. O–va., No. 5, 53 (1993).
12. Yu. O. Punin, E. N. Kotel'nikova, Yu. E. Makagonova, and P. B. Sokolov, Zap. Vseross. Mineral. O–va., No. 2, 23 (1997).
13. J. Torgsen and J. Strasburger, Science **146** (3640), 53 (1964).
14. Yu. O. Punin and O. M. Boldyreva, in *Physics of Crystallization* (Kalinin. Gos. Univ., Kalinin, 1980), p. 46.
15. M. A. Kuz'mina, S. V. Moshkin, and Yu. O. Punin, in *Physics of Crystallization* (Tver Gos. Univ., Tver, 1991), p. 24.
16. A. V. Nardov, Candidate's Dissertation in Geology and Mineralogy (Leningrad State Univ., Leningrad, 1986).
17. C. Rinando, M. Franchini-Angela, and R. Boistelle, Miner. Mag. **53** (4), 479 (1989).
18. M. P. Shaskol'skaya and P. P. Pashkov, Kristallografiya **6** (3), 476 (1961) [Sov. Phys. Crystallogr. **6**, 381 (1961)].
19. Yu. O. Punin, Zh. Strukt. Khim. **35** (5), 50 (1994).
20. M. A. Kuz'mina, Yu. O. Punin, S. V. Moshkin, and T. A. Karyakina, Zap. Vseross. Mineral. O–va, No. 4, 30 (1997).
21. P. P. Yukhtanov, *Twisted Quartz Crystals* (Komi Nauchn. Tsentr, Ural. Otd. Akad. Nauk SSSR, Syktyvkar, 1989), p. 32.

Translated by L. Man

Crystallography Reports, Vol. 46, No. 1, 2001, pp. 144–147. Translated from Kristallografiya, Vol. 46, No. 1, 2001, pp. 155–158.

Pulsed Electromagnetic and Acoustic Emission Accompanying Fast Crystallization of Supercooled Water Droplets

A. A. Shibkov, Yu. I. Golovin, M. A. Zheltov, and A. A. Korolev

Tambov State University, ul. Internatsional'naya 33, Tambov, 392622 Russia

e-mail: golovin@inbox.ru

Received April 26, 1999

Abstract—Electromagnetic and acoustic emission was found to accompany crystallization of distilled-water droplets supercooled to –30°C. It was shown that the front of an electromagnetic pulse provides the information on growth kinetics of ice in a supercooled droplet. A mechanism of electromagnetic pulse generation based on the Workman–Reynolds effect is proposed. *© 2001 MAIK "Nauka/Interperiodica".*

INTRODUCTION

It is well known that under the conditions of nonequilibrium crystal growth from a supercooled melt, the phase boundary is a "source" not only of diffusion-induced physical (thermal and concentrational) fields [1, 2] but also of acoustic [3–6] and electromagnetic [7–14] fields. The latter fact is characteristic of many dielectric materials [8] and is associated with the difference between the potentials of the liquid and solid phases. Under certain conditions (for example, in crystallization of diluted aqueous solutions of electrolytes), this difference can be as high as tens or even hundreds of volts (the so-called Workman–Reynolds effect [7]). It was reported [11] that crystallization of distilled water at relatively low supercooling $\Delta T \sim 1$ K is accompanied by ultralong-wavelength electromagnetic radiation in the form of a series of unipolar pulses. By analogy with acoustic emission, this phenomenon is referred to as electromagnetic emission. It was shown [12–15] that the pulses of electromagnetic emission are associated with the evolution of individual grains (dendrites) of polycrystal ice and are caused by the morphological instability of the electrically active water–ice interface. Thus, such an emission is a direct indication of non-steady-state crystallization under such cooling conditions. The aim of this study was to follow the relation between the parameters of electromagnetic emission and crystallization kinetics under strongly nonequilibrium conditions: of fast crystallization of a droplet of distilled water supercooled to ΔT = 15–30 K.

EXPERIMENTAL TECHNIQUE

Distilled water *1* was introduced into mineral oil *2* in glass container *3* by an injector (Fig. 1). Depending on the introduced volume (up to $V \approx 1$ ml), a water droplet retained an almost spherical shape and was immobile in the course of it observation (~10^3 s). The droplet in the container was cooled in cryostat *4* at the temperature ranging from –15 to –30°C. The electric component of electromagnetic emission (ac electric voltage) was measures by capacitance probe *5* having the area 1 cm^2. The channel for recording electric signals included broadband preamplifier *6* ($R_0 = 10^{12}$ Ω, C_0 = 20 pF, bandpass 10^{-1}–10^6 Hz), commutator *7*, analog-to-digital converter *8*, and computer *9*. Simultaneously, the process of droplet crystallization was recorded in the transmitted polarized light with the use of a polariscope consisting of light source *10*, polarizers *11*, microscope *12*, and video camera *13*. The thermal control of phase transformations was made with the aid of thermocouple *14* (sensitivity 20 μV/K, the operation speed was determined by the time of its thermal relaxation $d^2/a \sim 10^{-4}$ s, where d = 100 μm is the diameter of the conductors and $a \sim 10^{-4}$ m^2/s is the thermal diffusivity).

RESULTS AND DISCUSSION

The thermogram (Fig. 2) and the corresponding video film show that the droplet crystallization proceeds in three stages:

(1) The stage preceding the formation of critical nuclei at $T < T_M$ (T_M = 0°C is the melting point of ice) (region I in Fig. 2); the duration of this stage ($\Delta t_1 = 10^2$–10^3 s) strongly depends on the supercooling $\Delta T = T_M - T$ and bears the information on the activation energy of the nucleation process [16];

(2) The stage of thermodynamically irreversible crystallization whose duration Δt_2 is about 10 ms (region II in Fig. 2). This stage corresponds to spontaneous nucleation and growth of an ice platelet in the plane of the diameter of the supercooled droplet;

(3) The stage of quasi-isothermal freezing of the remained water volume; the duration Δt_3 of this stage is ~10 s (region III in Fig. 2).

1063-7745/01/4601-0144$21.00 © 2001 MAIK "Nauka/Interperiodica"

Then, the ice granule formed cools down for about 10^2 s to the thermostat temperature (region IV in Fig. 2). In what follows, we consider the stage of fast spontaneous crystallization (stage II).

The oscillograms of electrical *1* and acoustical *2* signals accompanying spontaneous nucleation and growth of an ice disc in the droplet supercooled down to ΔT = 25 K are shown in Fig. 3. Usually, a typical acoustic signal is a packet of 4 to 6 short pulses of duration 5 ms. A typical electrical signal has an almost triangular shape with the average front duration $\bar{t}_j$ = 10 ms, average amplitude $\bar{\varphi}_m$ = 70 μV, and average decay time $\bar{\tau}$ = 30 ms. The latter is comparable with the Maxwell relaxation time τ_M (τ_M was measured by the method described in [13]). Thus, the front of electrical pulse depends mainly on dynamics of the electromotive force caused by the charge separation in the course of the fast growth of the platelet. The pulse fall-off is determined mainly by the electrical relaxation in the two-phase ice–water system. The front duration provides the information on the velocities of the motion of the tip $v_1 = 2R/\bar{t}_f = 60$ cm/s and the side surface $v_2 = 2h/\bar{t}_f =$ 10 cm/s of the ice platelet (region II in Fig. 2), where $2h$ is the platelet thickness.

In many respects, the kinetics and the geometry of the nonequilibrium growth of ice in a supercooled water droplet is similar to those for spontaneous crystallization of a supercooled distilled water film reported in [14, 15]. Following [15], we first calculated the thickness of the ice platelet which could spontaneously arise in a droplet supercooled by ΔT = 15–30 K. The estimates made show that the heat transferred by the droplet to the surrounding medium did not exceed several tenths of percent; i.e., the platelet grew under quasi-adiabatic conditions. Considering the energy balance, we obtain

$$L\rho_1 V_1 = C_v \rho_2 V_2 \Delta T, \quad (1)$$

where ρ_1 and ρ_2 are the ice and water densities, respectively; C_v = 4.19 J/(g K) is the specific heat of water; L = 334 J/g is the latent heat of crystallization; and V_1 and V_2 are the volumes of the solid and liquid phases, respectively. Introduce the following dimensionless parameters: relative supercooling $\Delta = \Delta T/(L/C_v)$, relative volume of the solid phase $\xi = V_1/V$ (V is the droplet volume), and $k = \rho_1/\rho_2$. Then Eq. (1) can be written in the form

$$\xi = \Delta/k(1 + \Delta). \quad (2)$$

At the end of the stage of fast crystallization, ice acquires the shape of a disc with the thickness $2h$. With due regard of this fact, we obtain

$$h = 2R\Delta/3\xi(1 + \Delta), \quad (3)$$

where R is the droplet radius. Substituting the values of the parameters characteristic of a typical experiment, ΔT = 25 K, Δ = 0.31, ξ = 0.92, and R = 3 mm, we have $2h$ = 1 mm, which agrees well with the data of optical observations. The releasing latent heat of crystallization increases the temperature. At the end of this stage, the water temperature attains the melting point $T \approx T_M$; the subsequent (final) stage of crystallization (stage III) proceeds at the expense of heat transfer to thermostat.

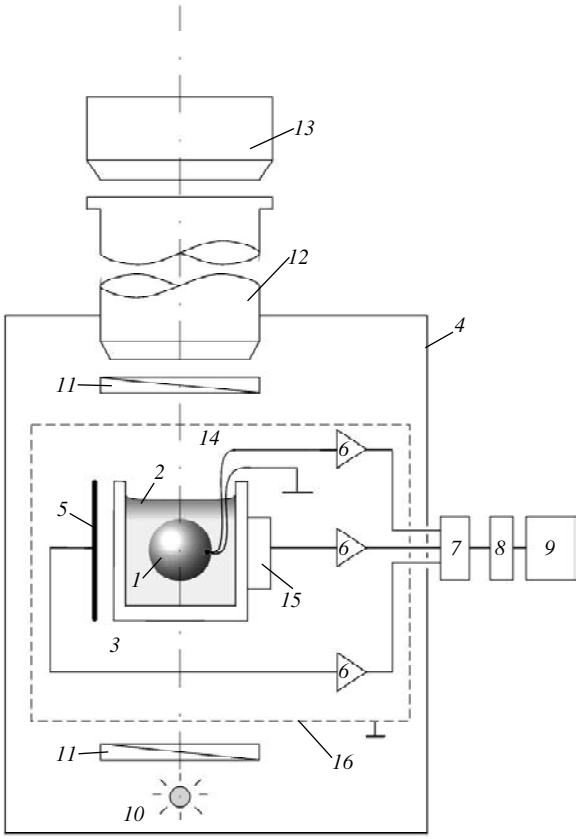

Fig. 1. Schematic of experimental setup for *in situ* studies of kinetics of spontaneous crystallization in water droplets by the thermal, optical, acoustic, and electrical methods: (*1*) water droplet; (*2*) immersion oil; (*3*) glass container; (*4*) freezing chamber; (*5*) flat capacitance probe; (*6*) preamplifier; (*7*) commutator; (*8*) analog-to-digital converter; (*9*) computer; (*10*) light source; (*11*) polarizers; (*12*) microscope; (*13*) video camera; (*14*) thermocouple; (*15*) piezoelectric probe; and (*16*) steel screen.

Now, discuss the mechanism underlying the generation of an ac electric field at the stage corresponding to the formation of an ice platelet. It is well known that at the crystallization front propagating in a diluted aqueous electrolyte solution a double electric layer is formed. This layer consists of impurity cations and anions nonuniformly trapped by the solid phase. The voltage arising across the "plates" of this layer (the freezing potential) can be as high as tens and even hundreds of Volts [17–19]. According to [19], the power of the double electric layer and the value of the freezing potential U are determined by the product of the initial impurity concentration $\tilde{C}_0$ ($\tilde{C}_0 = 10^{-5}$ mol/l in distilled

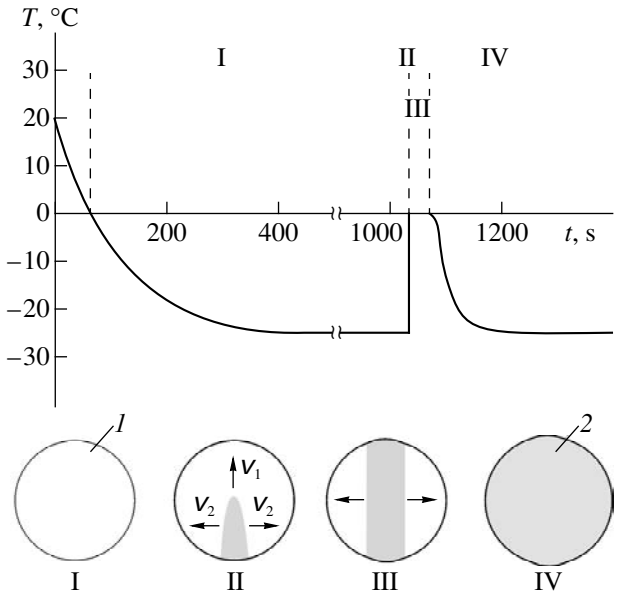

Fig. 2. Thermogram of cooling and crystallization of a supercooled water droplet of radius $R = 3$ mm with the indication of the characteristic stages of the process: I is the stage preceding the formation of the critical nuclei; II is the stage of quasi-adiabatic growth of an ice platelet; III is the stage of quasi-isothermal freezing of the remaining water volume; and IV is the stage of cooling down of a formed ice granule. (*1*) and (*2*) denote the liquid and solid phases, respectively; v_1 is the velocity of the platelet tip; and v_2 is the velocity of the side-surface of the platelet.

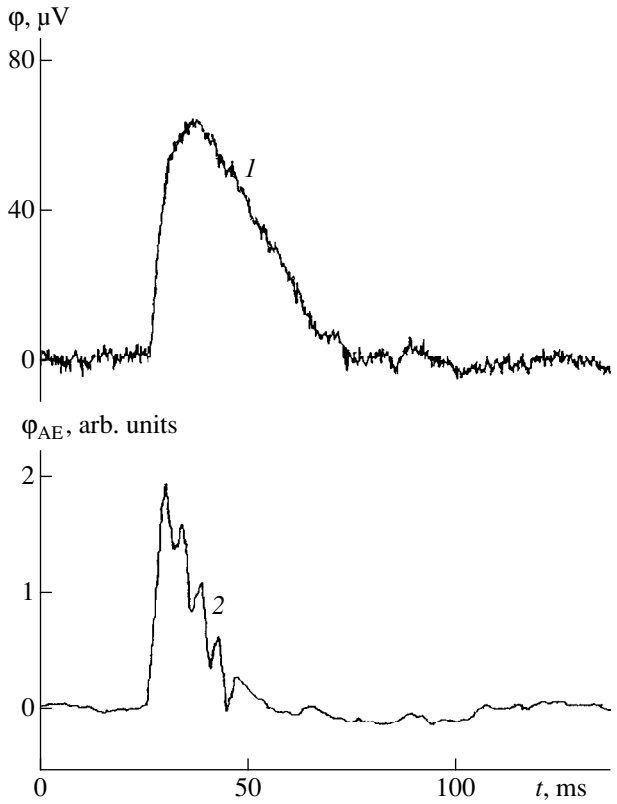

Fig. 3. Oscillograms of (*1*) electromagnetic and (*2*) acoustic emission pulses arising at the stage of growth of an ice platelet in a droplet of distilled water supercooled to –25°C.

water), the difference between the distribution coefficients of cations K^+ and anions K^- in the contacting phases and by the velocity v of the crystallization front. Therefore, we used an electrical model of the thin ice platelet growing in the water droplet in the form of a pair of antiparallel double layers by the distance $2h$ (a planar quadrupole). Thus, the electrically active ice–water interface with the area rapidly growing in the course of platelet growth can be source of electric signal. For the case of spontaneous crystallization of a water film an estimate similar to that discussed in [14] shows that in order to explain the experimental amplitude of the electric signal, we have to assume that the freezing potential is ~10 V. The later value is characteristic of aqueous electrolyte solutions with concentrations $\tilde{C}_0 \sim (10^{-6}–10^{-5})$ mol/l [8].

The proposed technique for measuring an ac electric field accompanying the spontaneous crystallization of a supercooled water droplet is essentially different from that discussed in [20]. Since no contacts are used, it is passive and does not influence the crystallization process. Thus, it is preferable for modeling electrical phenomena under the atmospheric conditions at the level of individual droplets. Moreover, this method provides the study of droplets at higher degrees of supercooling (to the glass-transition point). The results presented here open new possibilities for *in situ* studies of the competing processes of crystallization and electrization in individual water droplets and determination of the degree of correlation of occurring processes in an ensemble of droplets. As a result, it becomes possible to analyze the evolution of the total electric voltage arising in the droplet ensemble as a function of supercooling and impurity concentration with due regard for external fields of the nondiffusion nature, i.e., electric and acoustic fields.

ACKNOWLEDGMENTS

The study was supported by the Russian Foundation for Basic Research, project no. 98-02-17054.

REFERENCES

1. D. A. Kessler, Y. Koplik, and H. Levine, Adv. Phys. **37** (3), 255 (1998).
2. A. Karma and J. S. Langer, Phys. Rev. A **30** (6), 3147 (1984).
3. S. N. Zadumkin, Kh. B. Khononov, and Kh. B. Shokarov, Zh. Éksp. Teor. Fiz. **68** (4), 1315 (1975) [Sov. Phys. JETP **41**, 653 (1975)].

4. A. L. Lube, Kh. S. Bagdasarov, E. A. Fedorov, *et al.*, Kristallografiya **27** (3), 584 (1982) [Sov. Phys. Crystallogr. **27**, 353 (1982)].
5. A. T. Zlatkin, A. L. Lube, I. N. Tsigler, *et al.*, Kristallografiya **34** (6), 1579 (1989) [Sov. Phys. Crystallogr. **34**, 944 (1989)].
6. I. I. Sakharov, Inzh.-Fiz. Zh. **67** (1–2), 23 (1994).
7. E. Y. Workman and S. E. Reynolds, Phys. Rev. **78** (1), 254 (1950).
8. A. M. Mel'nikova, Kristallografiya **14** (3), 548 (1969) [Sov. Phys. Crystallogr. **14**, 464 (1969)].
9. L. G. Kachurin, S. N. Kolev, and V. F. Psalomshchikov, Dokl. Akad. Nauk SSSR **267** (2), 347 (1982).
10. O. I. Gudzenko, A. I. Lapshin, A. V. Kosoturov, *et al.*, Zh. Tekh. Fiz. **55** (3), 612 (1985) [Sov. Phys. Tech. Phys. **30**, 362 (1985)].
11. Yu. I. Golovin, A. A. Shibkov, M. A. Zheltov, *et al.*, Izv. Akad. Nauk, Ser. Fiz. **61** (5), 913 (1997).
12. Yu. I. Golovin, A. A. Shibkov, M. A. Zheltov, *et al.*, Kristallografiya **44** (4), 717 (1999) [Crystallogr. Rep. **44**, 667 (1999)].
13. A. A. Shibkov, Yu. I. Golovin, M. A. Zheltov, *et al.*, Kristallografiya **44** (5), 924 (1999) [Crystallogr. Rep. **44**, 863 (1999)].
14. A. A. Shibkov, Yu. I. Golovin, M. A. Zheltov, *et al.*, Kristallografiya **44** (6), 1139 (1999) [Crystallogr. Rep. **44**, 1067 (1999)].
15. A. A. Shibkov, M. A. Zheltov, M. A. Tatarko, *et al.*, Vestn. Tambov. Gos. Univ., Ser. Estestv. Tekh. Nauki **3** (4), 353 (1998).
16. D. Bertolini, Cassettari, and G. Salvetti, Phys. Scr. **38**, 404 (1988).
17. A. A. Chernov and A. M. Mel'nikova, Kristallografiya **16** (3), 477 (1971) [Sov. Phys. Crystallogr. **16**, 404 (1971)].
18. A. A. Chernov and A. M. Mel'nikova, Kristallografiya **16** (3), 488 (1971) [Sov. Phys. Crystallogr. **16**, 413 (1971)].
19. V. A. Bronshteyn and A. A. Chernov, J. Cryst. Growth **112**, 129 (1991).
20. L. G. Kachurin and V. I. Bekryaev, Dokl. Akad. Nauk SSSR **130**, 57 (1960) [Sov. Phys. Dokl. **5**, 137 (1960)].

Translated by K. Kugel

Crystallography Reports, Vol. 46, No. 1, 2001, pp. 148–153. Translated from Kristallografiya, Vol. 46, No. 1, 2001, pp. 159–164.

CRYSTAL GROWTH

Earth Optimization of Space Experiment on Growth of Germanium by Floating-Zone Technique with the Use of Rotating Magnetic Fields

A. V. Kartavykh, É. S. Kopeliovich, M. G. Mil'vidskiĭ, and V. V. Rakov

Institute of Chemical Problems for Microelectronics, Bol'shoĭ Tolmachevskiĭ per. 5, Moscow, 109017 Russia

Received July 6, 1999

Abstract—The results are considered of the earth experiments on growth of high-purity and Ga-doped germanium single crystals 15 mm in diameter and 60 mm in length, which were performed in a Zona-4 "space furnace" under the technological regimes close to those existing in space orbits. It is shown that the use of a magnetohydrodynamic (MHD) factor [weak (0.15–0.2 mT) rotational (400 Hz) magnetic fields] during crystallization of semiconductors by the floating-zone technique is a very promising method for control of dopant distributions and electrophysical properties in a growing crystal. It is shown that in such magnetic fields, the effective coefficient of Ga distribution in Ge decreases by 10%. The shift of the donor–acceptor balance of the residual dopants in a compensated semiconductor during growth with the MHD-stirring of the melt was first established in growth of undoped germanium single crystals. It was also established that magnetic fields produce different effects on the resistivity microinhomogeneity in undoped and doped crystals. The mechanisms of the MHD effect on the properties of the grown crystals are discussed as well as the perspectives of performing analogous experiments aboard spacecrafts. It is predicted that, under the microgravitation conditions, the effects revealed in terrestrial experiments would be more pronounced. © *2001 MAIK "Nauka/Interperiodica".*

INTRODUCTION

The analysis of doped semiconductor single crystals grown in space showed an extremely weak heat and mass transfer in the melts under the microgravitation conditions [1]. The thickness δ_c of the diffusion layer at the interface in the melt is much higher (~3–6 mm) than in the crystallization processes performed on earth (0.1–1.0 mm) [2, 3]. A high value of δ_c provides a high sensitivity of the crystallization process (and also nonuniform incorporation of a dopant into a crystal) to various factors in space flights—both of the fundamental (capillary forms of convection) and the technogenic (*g*-jitter) nature [4, 5].

In order to reduce the effect of such noncontrollable factors on the homogeneity of the dopant distribution in a crystal grown in space, we invoke the principle of the artificially created optimum hydrodynamic situation in the melt by using special external physical factors, which provide the specific stirring mode [1, 6]. The main idea of the use of these factors reduces to the attempts of controlling the δ_c parameter by creating controllable high-frequency vortex flows in the melt. In particular, we suggested to use an alternating rotating magnetic field with a low induction in combination with the floating-zone technique.

Earlier [6], our experiments performed on a Foton satellite showed that the use of a weak alternating magnetic fields provided the complete melting of undoped Ge specimens at the melting-zone width equal to the diameter of an ingot and the melt overheating not exceeding 10°C with respect to T_m. Melting of low-doped materials in such a "mild" thermal mode without the use of a magnetohydrodynamic factor is practically impossible.

The technical and methodological difficulties encountered in the attempts to attain such thermal modes with the minimum overheating under the conditions of space flights dictate the use of the preliminary detailed optimization of all the principles of applying the MHD factor. Below, we consider the method for preparing and conducting experiments on growth of Ge single crystals in rotating magnetic fields on a "space equipment" and analyze in detail the results obtained.

THE CHOICE OF THE MHD PARAMETERS

In order to analyze the effect produced by a MHD-rotor, we performed the parametric studies of the hydrodynamic processes in Ge melts. The parameters to be studied are the Hartmann number $\mathrm{Ha}_r = BR\sqrt{\sigma_e/\rho\nu}$, the Reynolds number $\mathrm{Re}_r = 2\pi fR^2/\nu$ calculated from the rotation velocity of a magnetic field, and the Grashoff number $\mathrm{Gr} = g\beta_T R^3\Delta T/\nu^2$, where R is the

1063-7745/01/4601-0148$21.00

melting-zone radius; ρ, ν β_T, and σ_e are the density, the viscosity, the volume expansion coefficient, and the electric conductivity of the melt, respectively; B and f are the induction and the frequency of magnetic-field rotation; and g is the acceleration in the crystallization system.

Depending on the values of the Ha_r and Re_r numbers in the melt, either the steady-state or vibrational mode of flow is implemented in the melt. The generalized stability diagram of the melt flow under the effect of the MHD-rotor is shown in Fig. 1, where *1* is the curve limiting the region of the steady-state flow constructed by the data calculated in [7] and the region on the right-hand side of this curve corresponds to the nonstationary (vibrational) flow modes and *2* is the curve limiting the region of the steady-state flow (according to [8]).

It was indicated [9] that the instability region for the Ge-melt lying on the right-hand side is limited by the value $\log Re_r = 22.4$. At $\log Re_r > 3.05$ ($Re_r > 1.12 \times 10^3$), the upper and the lower branches of curve *1* can be described by the equations $\log Ha_r = 0.5 \log Re_r$ and $\log Ha_r = -0.5 \log Re_r + 1.045$, whereas the lower branch of *2*, by the equation $\log Ha_r = -0.6 \log Re_r + 2.16$. Then, it follows from the calculations and the data in [8] that the melt motion during MHD-rotation occurs in the steady-state mode if $\log Ha_r > 0.5 \log Re_r$ and $\log Ha_r < -0.6 \log Re_r + 2.16$. In particular, in growth of crystals with a diameter of 15 mm, the steady-state flow takes place at $B > 3.1$ T, $B < 10^{-4}$ T, and the MHD-rotor frequency of 400 Hz.

Taking into account the energy limitations aboard a spacecraft, we studied the region A characterized by the vibrational mode at low induction values (in accordance with Fig. 1). The experiments were performed at the following parameters:

$$f = 400 \text{ Hz}, \quad Re_r = 1.04 \times 10^6, \quad \log Re_r = 6;$$

$$B = 0.15 \text{ mT}, \quad Ha_r = 0.045, \quad \log Ha_r = -1.35;$$

$$B = 0.2 \text{ mT}, \quad Ha_r = 0.06, \quad \log Ha_r = -1.2.$$

PRINCIPLES OF CONTROLLED DOPING OF A GROWING CRYSTAL DURING MHD-STIRRING OF THE MELT

During the crystallization of doped melts, the dopant concentration in the solid phase is related to the thickness of the diffusion boundary layer by the Burton–Prime–Slichter equation [10]

$$k = C_s/C_l = k_0/[k_0 + (1 - k_0)\exp(-v\delta_c/D)], \qquad (1)$$

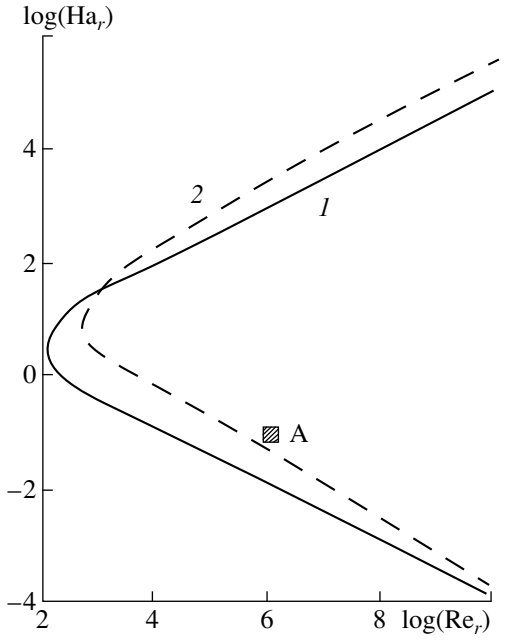

Fig. 1. Generalized stability diagram of germanium-melt flow under the MHD-effect.

where k and k_0 are the effective and the equilibrium coefficients of the dopant distribution, respectively; v is the crystallization rate; and D is the diffusion coefficient of the dopant in the melt. The crystallization rate can be varied by controlling the thermal conditions in the melt. The thickness of the δ-layer enriched with the dopant at $k_0 < 1$ can be varied by changing the stirring conditions by applying a magnetic field of strength H rotating in the interface plane. Such a field configuration in the zone-melting process [11] is described by the following empirical relationship:

$$\delta_c/D = (\delta_c/D)_0 \exp(-\gamma H^2), \qquad (2)$$

where $(\delta_c/D)_0$ is the conjugated parameter of the diffusion layer without the MHD factor and γ is the empirical coefficient of the MHD-sensitivity of the crystallization system. For metal melts in a field of frequency 400 Hz, γ is of the order of 10^{-8} m^2/A^2 [11].

The joint solution of Eqs. (2) and (1) provides the basis for the semiempirical analysis of the MHD effect on the averaged ("smoothened") pattern of the dopant distribution along the growth axis of a semiconductor crystal. However, it should be indicated that Eq. (2) yields no information on the dopant microinhomogeneity arising in crystals under the effect of the MHD-stirring.

It should also be noted that the MHD effects on the distribution of electrophysical properties in a growing crystal is essentially dependent on the nature of dopants introduced into the melt during crystallization (in accordance with the values of the parameters k_0, d, and

γ). These effects should be especially pronounced in the case, where the melt is simultaneously doped with two or more different dopants which behave differently in accordance with Eqs. (2) or (1).

EXPERIMENTAL

As is seen, at this stage of the study only some information necessary for optimizing the MHD parameters can be calculated. Therefore, we had to perform a series of growth experiments on a *Zona-4* apparatus used in space still under the terrestrial conditions [12]. The heating unit of the furnace was supplied with an in-built MHD-inductor whose design and technical characteristics were described elsewhere [13]. Within the framework of the program of such tests, we recrystallized two Ge specimens in a magnetic field. The starting material used for recrystallization was ⟨100⟩-oriented single-crystal Ge rods 15 mm in diameter and 110 mm in length. One of these rods was doped with Ga up to a level of 1×10^{18} at/cm^3, the second one having the *p*-type conductivity and the hole concentration of 10^{12} cm^{-3} (the resistivity of ρ = 58 Ω cm) was not doped at all. In addition, we also performed two control experiments on the identical starting materials without using of the MHD factor. Crystal growth proceeded along the horizontal axis. The existence of the free upper surface of the melt allowed partial simulation of the "space conditions" for the floating-zone technique with the aid of the method described in [14]. The initial unmelted part of the rod played the role of a seed. The recrystallized part was ~60 mm in length, the velocity of the melted-zone motion in various experiments was 7.0 ± 0.2 mm/h at the melt temperature 945°C (these technological parameters were close to those used in space experiments).

The single crystals thus grown were cut into halves along the growth axis. Their inhomogeneity was studied along the axial direction in the cut plane by the method of spreading-resistance R_s. The R_s-profiles obtained for doped crystals were recalculated into the resistivity profiles ρ. In order to characterize the most informative initial stage of the crystallization process, the crystals were scanned in the vicinity of the seeding front at a step of 25 μm.

To reveal the fine structure of the microinhomogeneity structure and its possible periodicity, we applied the Fourier transformation to the resistivity profiles as was described in [14]. A profile was considered as a set of discrete R_s or ρ values which were the functions either of the scanning coordinate *l* or the sequential number of the step, *t*. Then, it was assumed that the stationary component of this sequence (microinhomogeneity) can numerically be approximated by an algebraic sum (superposition) of the finite number *n* of harmonic functions

$$\rho(t) = \sum_{j=1}^{n} (a_j \cos\omega_j t + b_j \sin\omega_j t), \qquad (3)$$

where a_j and b_j ($j = 1, 2, \ldots, n$) are independent centered normally distributed quantities with the dispersion $M\{a_j^2\} = M\{b_j^2\} = \sigma_j^2$. The dispersion σ_j^2 is a function of the frequency ω_j and is called the spectral density. Applying the algorithm of the numerical Fourier transformation to the experimental sequence ρ(*t*), it is possible to describe the inhomogeneity by a series of the values $\sigma_1^2; \sigma_2^2; \ldots; \sigma_j^2$ for the sequence either of frequencies $\omega_1; \omega_2; \ldots; \omega_j$ or of periods of harmonics $T_1; T_2; \ldots; T_j$. The graphical representation of the function $\sigma_j^2 = f(T_j)$ has the form of a spectrum, where T_j is the period of the *j*th harmonic and σ_j^2 is its statistical contribution to the total distribution of ρ. Thus, we managed to reveal, separate, and evaluate the amplitudes of oscillations in R_s or ρ occurring with different periods along the growth direction.

We also calculated the total value of inhomogeneity for the R_s or ρ distribution in the form of the parameter of the relative root-mean-square (standard) deviation *StD*.

RESULTS AND DISCUSSION

Gallium-doped germanium. The results of the study of gallium-doped germanium single crystals are given in Figs. 2 and 3. It is seen that the application of a magnetic field to the melt results in a slight increase of the inhomogeneity index of the dopant distribution from 5.2 to 7.1% (Figs. 2a, 3a). This shows that the MHD modes used are still far from optimum. However, the application of a magnetic field considerably improves the inhomogeneity structure. The scatter in the experimentally measured individual ρ values in this case is described quite well by a random Gaussian distribution, and the Fourier-spectrum of the process is close to the "white noise" (Fig. 3b). The nonstructurized inhomogeneity, which under the MHD effect is observed over the whole crystal volume, indicates the complete melt homogenization under the conditions of forced convection, which is rather promising for the further use of MHD-effect in growth of doped semiconductors in space.

High-purity germanium. The recorded R_s distributions along the axes of the grown crystals *1* (control) and *2* (MHD) brought into coincidence are shown in Fig. 4a. These curves show an extremely high sensitivity of undoped Ge to MHD stirring of the melt. It is seen that the application of a field really intensifies melt stirring. Therefore, the initial transient part of R_s is

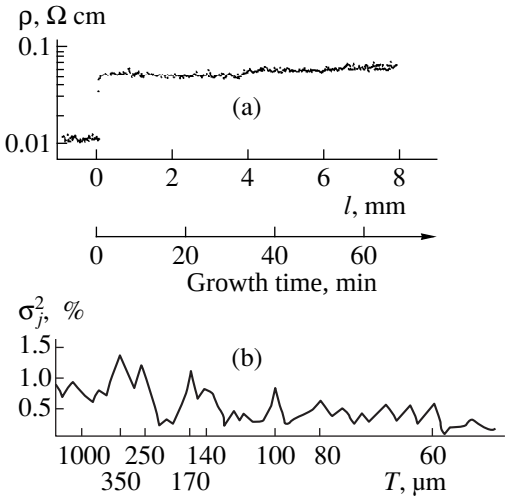

Fig. 2. (a) Axial resistivity distribution in the control Ge⟨Ga⟩ single crystals; $\bar{\rho}$ = 0.06 Ω cm, *StD* = 5.2%; in the seed, $\bar{\rho}$ = 0.012 Ω cm; and (b) spectral density of the function ρ(*l*).

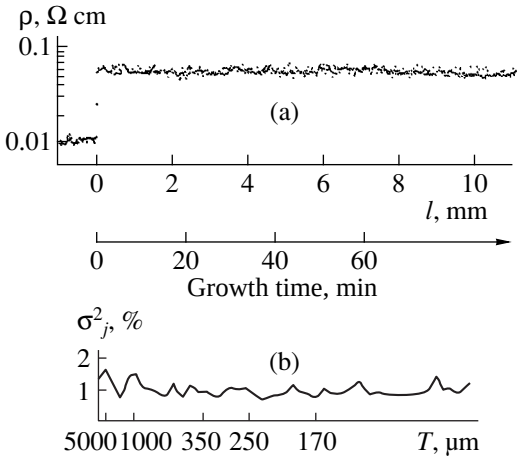

Fig. 3. (a) Axial resistivity distribution in a Ge⟨Ga⟩ single crystal grown from melt under the MHD effect; *B* = 0.2 mT, *H* = 160 A/m, $\bar{\rho}$ = 0.055 Ω cm, *StD* = 7.1%. In the seed, $\bar{\rho}$ = 0.012 Ω cm; and (b) spectral density of the function ρ(*l*).

reduced by a factor of 3 (from 6 to 2 mm) in comparison with the same part of R_s for the control specimen. Thus, the duration of the transient process of attaining the steady-state crystallization mode reduced from 50 to 17 min. In turn, this fact indicates a decrease of the δ_c-layer thickness in the melt.

It follows from Eqs. (2) and (1) that the MHD factor can change the *k* coefficients of the dopants and, thus, also can influence the resulting distribution of the electrophysical properties in the solid phase. The dopants most sensitive to such effects are those with $k \ll 1$. Intensification of stirring results in the approach of *k* to its equilibrium value ($k \longrightarrow k_0$), i.e., in a decrease of its absolute value. The interpretation of such effects is essentially more complicated for undoped semiconductors which contain residual impurities of a different nature in comparable concentrations. In this case, different sensitivities of coefficients *k* of different impurities to the MHD-effect can shift the donor–acceptor balance and considerably change the charge-carrier concentration.

The shift of the balance caused by the MHD effect uniquely indicates the existence of different types of conductivity in crystals grown. The thermoelectric-probe and Hall measurements show that, the control specimen has an *n*-type conductivity ($n \approx 10^{13}$ cm^{-3}), which indicates the prevalence of donor dopants ($N_d > N_a$). The specimen grown during MHD stirring preserves the hole-type conductivity and the charge-carrier concentration of the seed ($p \approx 10^{12}$ cm^{-3}). Therefore, in the specimen bulk, $N_a > N_d$. Comparing the properties of the seed and the grown crystals, one can qualitatively estimate the behavior of the distribution coefficients *k* of donors and acceptors making the major contributions to the compensation (k_d and k_a). Indeed, in the control specimen, $k_d > k_a$ in the process of zone melting, whereas in the specimen grown under the MHD-effect, $k_d \approx k_a$. This leads to the conclusion that residual donors in the melt are more sensitive to the field effect than acceptors (the absolute value of k_d considerably decreased).

The shift of the donor–acceptor ratio can be conveniently described by the change of the compensation coefficient *K*. The determination of the latter is a rather difficult problem; however, the estimations made for the simplest case of solving the neutrality equation can be very useful. These estimates are made on the following assumptions: (1) only one type of the "small" (completely ionized) residual donors of the impurity nature N_d and only one kind of analogous acceptors N_a can participate in the compensation; (2) no additional technological impurities can penetrate the melt during zone melting; (3) no thermal donors or thermal acceptors can be generated in the solid phase during postcrystallization cooling. Then, the following estimates are valid for the control crystal *1* (of the *n*-type): $N_d - N_a \approx 10^{13}$ at/cm^3 and $N_d N_a = n_i^2$ (where $n_i = 3 \times 10^{13}$ cm^{-3} is the concentration of intrinsic charge carriers in Ge at 300 K). Then $N_a \approx 1.7 \times 10^{13}$ at/cm^3, $N_d \approx 2.6 \times 10^{13}$ at/am^3, and $K = N_a/N_d \approx 0.6$. For crystal *2* (of the *p*-type) we have $N_a - N_d \approx 10^{12}$ at/cm^3 and $N_a N_d = n_i^2$. Then, $N_a \approx 2 \times 10^{13}$ at/cm^3, $N_d \approx 1.9 \times 10^{13}$ at/cm^3, and $K = N_d/N_a \approx 0.9$. Thus, in order to transform averaged curve *2* into curve *1* in Fig. 4a with the preservation of the approximately constant concentration of residual acceptors $N_a \approx (1.7–2) \times 10^{13}$ at/cm^3, it is sufficient to decrease the coefficient k_d of the residual donors by a factor as small as ~1.4. This crude estimate demon-

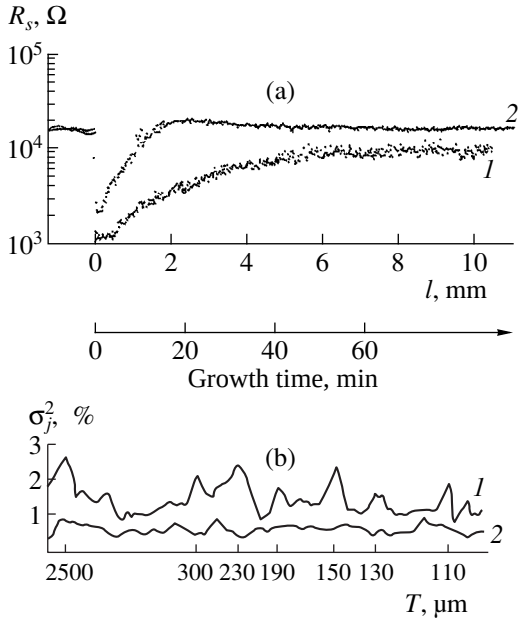

Fig. 4. (a) Spreading-resistance profiles along the axes of undoped Ge crystals, (*1*) control *n*-type crystal, *StD* = 8.8%; (*2*) *p*-type crystal grown from melt under the MHD effect; *B* = 0.15 mT, *H* = 120 A/m, *StD* = 2.9% and (b) Fourier spectra of the corresponding $R_s(l)$ functions.

strates the cause of the anomalous sensitivity of electrophysical properties of a compensated semiconductor to the MHD effect onto the melt.

The above estimates show that a crystal grown under the MHD effect is characterized by a higher compensation coefficient than the control specimen. At the same time, it is well known [15] that, at random (independent) distributions of the compensating donors and acceptors, the inhomogeneity in resistivity of the compensated material drastically increases with an increase of *K*. In our case, we observed the opposite effect (Fig. 4b): *StD* in the control crystal amounted to 8.8%, whereas in crystal *2*, its value was as low as 2.9%. This fact leads to an assumption on the correlated incorporation of donors and acceptors into a crystal during its growth in a magnetic field. Under the conditions of oscillating modes of melt stirring, this phenomenon is possible only if k_a and k_d have close values.

In order to make a reliable numerical evaluation and the detail characterization of the mechanisms of the MHD effect on the properties of grown crystals, one has to establish the atomic (chemical) nature and determine the concentration of the main centers participating in the compensation process and also the position of their energy levels in the forbidden gap of Ge. Only in this case, the determination of the reference values of the distribution coefficients, the exact solution of the neutrality equation, and the construction of the MHD-dependent compensation model become possible. Unfortunately, such studies are very labor-consuming and, therefore, another approach is more justified. Such an approach consists in the use of a model compensated Ge crystal doped simultaneously with the donor and acceptor impurities with the known physicochemical properties. The use of such materials as highly informative and sensitive objects in growth experiments would essentially facilitate the optimization of the MHD modes necessary for growing highly homogeneous single crystals in space.

CONCLUSIONS

It is shown experimentally that the application of weak (*B* = 0.15–0.20 mT) rotating (400 Hz) magnetic fields in crystallization of semiconductors by the floating-zone technique allows the control of the impurity and electrophysical-property distributions in a growing crystal. Even under the conditions of the terrestrial gravitational convection in the melted zone, we managed to decrease the coefficient *k* of the Ga dopant in Ge crystals by 10%. We believe that under the conditions of microgravitation, this effect would be more pronounced. On an example of undoped Ge single crystal, we managed to reveal for the first time the effect of the shift of the donor–acceptor balance of residual impurities in a compensated semiconductor grown under the conditions of the MHD-effect.

At the same time, we also observed a certain deterioration of the electrophysical homogeneity of doped crystal, which is caused, in our opinion, by high-frequency temperature oscillations at the crystallization front induced by the MHD-rotation of the melt. To perform successful space experiments, one has first to optimize the parameters of the MHD-factor and, first of all, the rotation-field frequency. The solution of this problem requires the invocation of methods of mathematical simulation and physical modeling.

ACKNOWLEDGMENTS

The study was supported by the NASA within the KHTC/STAC program, contract no. NAS15-10110, project no. TM-6.

REFERENCES

1. É. S. Kopeliovich, V. V. Rakov, and N. A. Verezub, Tsvetn. Met. (Moscow), No. 8, 52 (1991).
2. A. V. Kartavykh, É. S. Kopeliovich, M. G. Mil'vidskiĭ, and V. V. Rakov, Kristallografiya **43** (6), 1136 (1998) [Crystallogr. Rep. **43**, 1075 (1998)].
3. A. V. Kartavykh, E. S. Kopeliovich, M. G. Mil'vidskiĭ, and V. V. Rakov, J. Cryst. Growth **205** (4), 497 (1999).
4. M. G. Mil'vidskiĭ, A. V. Kartavykh, E. S. Kopeliovich, *et al.*, Journal of Journals (UNESCO) **2** (1), 6 (1998).
5. A. V. Kartavykh, Kristallografiya **45** (6), 2352 (2000) [Crystallogr. Rep. **45**, 1024 (2000)].

6. M. G. Mil'vidskiĭ, N. A. Verezub, A. V. Kartavykh, *et al.*, Kristallografiya **42** (5), 913 (1997) [Crystallogr. Rep. **42** (5), 843 (1997)].
7. M. T. Devdariani, O. V. Pelevin, A. I. Prostomolotov, *et al.*, Preprint No. 516, IPM RAN (Institute for Problems of Mechanics, Russian Academy of Sciences, Moscow, 1992), No. 516, p. 32.
8. A. B. Kapusta and A. F. Zibol'd, Magn. Gidrodin., No. 1, 77 (1983).
9. A. B. Kapusta, Magn. Gidrodin., No. 1, 63 (1984).
10. J. Burton, R. Prim, and W. Slichter, J. Chem. Phys. **21** (11), 1987 (1953).
11. W. C. Johnston and W. A. Tiller, Trans. AIME **221**, 331 (1961).
12. I. V. Barmin, A. V. Egorov, V. N. Kurokhtin, *et al.*, in *Proceedings of Joint X European and VI Russia Symposium on Physical Science in Microgravity, St. Petersburg, 1997*, Vol. II, p. 325.
13. I. V. Barmin and A. S. Senchenkov, Fluid Dyn. **29** (5), 620 (1994).
14. A. V. Kartavykh, É. S. Kopeliovich, M. G. Mil'vidskiĭ, *et al.*, Kristallografiya **42** (4), 755 (1997) [Crystallogr. Rep. **42**, 694 (1997)].
15. N. S. Rytova, E. S. Yurova, and V. V. Karataev, Fiz. Tekh. Poluprovodn. (Leningrad) **14** (10), 1979 (1980) [Sov. Phys. Semicond. **14**, 1176 (1980)].

Translated by L. Man

Crystallography Reports, Vol. 46, No. 1, 2001, pp. 154–156. Translated from Kristallografiya, Vol. 46, No. 1, 2001, pp. 165–167.

SOFTWARE

An Algorithm and Program of Exhaustive Search for Possible Tiling of a Plane with Polyominoes

A. V. Maleev

Vladimir State Pedagogical University, Vladimir, Russia

e-mail: laemail@mail.ru

Received on June 24, 1999

Abstract—Within the method of discrete modeling of packings in molecular crystals, an algorithm of the exhaustive search for all possible tiling variants of a plane with polyominoes with the given number of translationally independent cells has been developed on the basis of the packing code. The suggested algorithm was used to write the corresponding program for a personal computer. *© 2001 MAIK "Nauka/Interperiodica".*

The development of the theory of dividing a space into closed regions seems to be more important for geometric crystallography than for geometry. This problem of dividing a plane or tiling it with polygons, which are the fundamental domains of the planar Fedorov groups, was successfully solved by Delone (Delaunnay) [1]. Later, Delone and his students [2] extended this solution to arbitrary regular tiling of a plane with polygons or the so-called planigons. As far as we know, no analogous theory of dividing a plane into (or tiling it with) nonconvex or irregular polygons has been constructed as yet. In order to illustrate a new approach to the solution of this problem, we suggest here an algorithm for constructing translational (not necessarily regular) tiling of the plane with polyominoes (polygons), which, in the general case, are not convex. The algorithm is based on the method of discrete modeling of packings in molecular crystals [3, 4].

A polyomino [5] is an association of a finite number of unit squares (polyomino cells) with the vertices located at the points with the integral coordinates whose inner regions are connected figures. Tiling of a plane with polyominoes is a tiling where two cells do not have any common inner point. The translational tiling is a tiling of a plane which can be brought into coincidence with itself by two noncollinear parallel translations. The translational tiling of a plane with polyominoes can be characterized by the number of translationally independent polyomino cells (this number coincides with the ratio of the area of the primitive unit cell of the lattice of translations to the area of one polyomino cell). In the present communication, we suggest an algorithm of the exhaustive search for all the translational tilings of a plane with polyominoes at the given number of translationally independent cells.

In the translational tiling of a plane with polyominoes, the centers of the cells of all the polyominoes form an orthonormalized lattice, with respect to which the lattice of translations (is a sublattice of translations). The sublattice of translations sets a packing space (PS) on the lattice; i.e., for such a lattice, each point (the point of the packing space) is attributed a certain weight in such a way that any two points of the packing space having the same weights form a vector of the sublattice of translations, whereas any two points of the packing space with different weights form a vector which does not belong to this sublattice. The packing space is set by the packing-space matrix, which, in the two-dimensional case, has the form $\begin{pmatrix} l & n \\ 0 & m \end{pmatrix}$, where l and m are the natural numbers and n is an integer such that $0 \le n < l$. The matrix determinant of the packing space, $N = lm$, is called the order of the packing space; it coincides with the number of the translationally independent cells. For the sake of brevity, the planar packing spaces are denoted as Plm_n. The weight of the point (u, v) of the packing space is calculated by the formula $g(u, v) = \left\{ \frac{u - [v/m]n}{l} \right\} l$, where $[r]$ is the integral part of the number r, i.e., the integer closest to r such that $[r] \le r$ and $\{r\} = r - [r]$ is the fractional part of the number r.

The translational tiling of a plane with polyominoes can be set by the packing space and the tiling (packing) code [3]. In the two-dimensional case, the tiling code is an N-digit number $\overline{c(0)c(1)c(2)\ldots c(N-1)}$ in the quarternary number system, whose number $c(g)$ characterizes the boundedness (the presence or the absence of the boundaries) of the packing-space point with the weight g in the directions opposite to the directions of the basis vectors of the lattice used for constructing the packing space. Thus, if a point with the coordinates (u, v) has the weight g, then the number $c(g)$ in the tiling code is defined in such a way:

1063-7745/01/4601-0154$21.00

$c(g) = 3$ if the points $(u - 1, v)$ and $(u, v - 1)$ do not belong to the polyomino to which the point (u, v) belongs;

$c(g) = 2$ if the point $(u - 1, v)$ belongs and the point $(u, v - 1)$ does not belong to the polyomino to which the point (u, v) belongs;

$c(g) = 1$, if the point $(u, v - 1)$ belongs and the point $(u - 1, v)$ does not belong to the polyomino to which the point (u, v) belongs; and

$c(g) = 0$ if the points $(u - 1, v)$, $(u, v - 1)$, and (u, v) belong to the same polyomino.

Figure shows an example of the translational tiling of a plane with polyominoes in the packing space $P61_2$. The weight of the packing-space point in each cell is indicated. For packing-space points with the encircled weights, solid lines indicate the boundaries determining the corresponding number of the code; the code number is also indicated. Thus, the points with weights 0 and 3 located along the directions $-\mathbf{e}_1$ and $-\mathbf{e}_2$ have the boundaries and, therefore, $c(0) = c(3) = 3$. The point with weight 1 has no boundary in the direction $-\mathbf{e}_1$ but has the boundary in the direction $-\mathbf{e}_2$; therefore, this point has the code number $c(1) = 2$. The point with weight 2 has the boundary along the direction $-\mathbf{e}_1$ and has no boundary along the direction $-\mathbf{e}_2$. Therefore, it has the code number $c(2) = 1$. Finally, the points with weights 4 and 5 have no boundaries along the above directions; therefore, these points have the code number $c(4) = c(5) = 0$. Thus, such tiling is described by the packing code 321300 in the packing space $P61_2$.

For such a definition of the tiling code, the same planes (within the accuracy of the tiling translation) can correspond to different codes, because the code numbers and their sequence depend on the orientation of the basis and the position of the reference-system origin. Thus, using the shifts of the origin, one can obtain N different codes for tiling of the packing-space of the Nth order, N more variants of the code correspond to the opposite orientations of the basis vectors. For some packing spaces, other variants of the change of the signs or the orders of the basis vectors can not change the packing space itself. This property of the packing space is described by its point symmetry considered in detail elsewhere [6]. Such packing spaces have N more code variants for each variant of the basis. In order to solve the problem tiling-code uniqueness, one has to choose from the whole set of codes (determining the same tiling in the given packing space) the maximum code, which is hereafter called the reduced code.

The introduction of the tiling code allowed us to suggest the algorithm of the exhaustive search for all the variants of tiling a plane with polyominoes with the given number of translationally independent cells. This algorithm has four main steps, namely:

(1) Of all the packing spaces of the Nth order, one has to select only the independent packing spaces (the definition of the independent packing space is given elsewhere [6]);

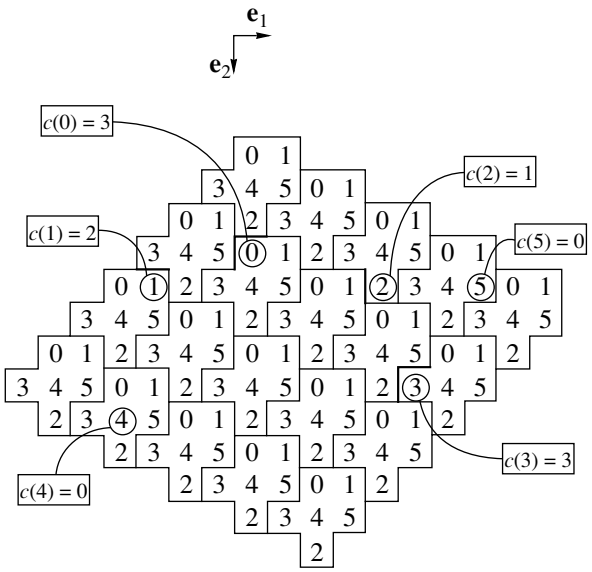

Tiling of a plane with polyominoes described by packing code 321300 in the packing space $P61_2$.

(2) One has to determine the point-symmetry groups [6] of the chosen packing spaces;

(3) For each of N-digit quaternary numbers in the range from 3333…3 to 3000…0 in the chosen packing space, one has to check whether this number is really a code of tiling a plane with polyominoes and, if so, also to determine whether this code is reduced or not;

(4) The researcher has to sort tilings either by the number of the translationally independent polyominoes or by the tiling symmetry (according to his option).

The theoretical justification and possible algorithms for implementation of steps (1) and (2) were considered earlier [4, 6]. Therefore, we have to consider here in more detail only steps (3) and (4).

Let us set a function

$$f(u, v) = \left[\frac{c(g(u, v))}{2}\right] + 2\left\{\frac{c(g(u, v))}{2}\right\} + \left[\frac{c(g(u-1, v))}{2}\right] + 2\left\{\frac{c(g(u, v-1))}{2}\right\} \quad (1)$$

on the set of points (u, v) of the packing space, where $g(u, v)$ is the weight of the point (u, v); $c(i)$ is the code under consideration; and $[r]$ and $\{r\}$ are the integral and fractional parts of the number r, respectively. If the N-digit quaternary number $\overline{c(0)c(1)c(2)\ldots c(N-1)}$ is to set the tiling of a plane with polyominoes in the given packing space, it is necessary that for any point (u, v) the following inequality would be satisfied: $f(u, v) \neq 1$.

Numbers of variants of tiling a plane with one translationally independent polyomino

Number of polyomino cells N	Number of tiling variants	Number of polyomino cells N	Number of tiling variants
4	10	9	253
5	12	10	632
6	43	11	815
7	48	12	3205
8	171		

In order to determine whether or not the tiling code is reduced, it is necessary to take into account the point symmetry of the packing space and to restore the set of all possible tiling codes of this packing space. The code under consideration is a reduced code then and only then if any code of the set does not exceed this code.

In order to determine the number Z of translationally independent polyominoes, we use the Eulerian characteristic of the fundamental domain of tiling with respect to the translation lattice of translations. Topologically, the fundamental domain of the translational tiling is isomorphous to the surface of a torus for which the Eulerian characteristic $\Gamma - P + B$ is zero. The number of vertices, B, is calculated, with due regard for Eq. (1), as the number of points (u, v) of the packing space such that $0 \le u < l$; $0 \le v < m$, and $f(u, v) \ge 3$. The number of edges, P, is calculated as $\frac{1}{2}\sum f(u, v)$, where summation is performed over all the points (u, v) of the fundamental domain of the packing space for which $f(u, v) \ge 3$. The number of faces, Γ, coincides with the number of translationally independent polyominoes, $Z = \Gamma = P - B$.

The tiling symmetry is determined in the following way. Taking into account the packing-space symmetry [6], one has to restore the complete set of codes of the given tiling, which correspond to all the "movements" in this packing space. Each code which coincides with the reduced code of this tiling determines one of the symmetry transformations possessed by this tiling.

The above algorithm was used to write the corresponding program for an IBM PC. The table lists the results of the exhaustive search for all possible translational tilings of a plane with polyominoes with different numbers of translationally independent cells ranging from four to twelve and one translationally independent polyomino.

REFERENCES

1. B. N. Delone, Izv. Akad. Nauk SSSR, Ser. Mat. **23**, 365 (1959).
2. B. N. Delone, N. P. Dolbilin, and M. I. Shtogrin, Tr. Mat. Inst. im. V. A. Steklova, Akad. Nauk SSSR **148**, 109 (1978).
3. A. V. Maleev, V. G. Rau, K. A. Potekhin, *et al.*, Dokl. Akad. Nauk SSSR **315** (6), 1382 (1990) [Sov. Phys. Dokl. **35**, 997 (1990)].
4. A. V. Maleev, Kristallografiya **40** (3), 394 (1995) [Crystallogr. Rep. **40**, 354 (1995)].
5. *The Mathematical Gardner*, Ed. by D. A. Klarner (Prindle, Weber and Schmidt, Boston, 1981; Mir, Moscow, 1983), p. 303.
6. A. V. Maleev, A. E. Lysov, and K. A. Potekhin, Kristallografiya **43** (5), 775 (1998) [Crystallogr. Rep. **43**, 721 (1998)].

Translated by L. Man

Crystallography Reports, Vol. 46, No. 1, 2001, pp. 157–160. Translated from Kristallografiya, Vol. 46, No. 1, 2001, pp. 168–172.

HISTORY OF CRYSTALLOGRAPHY

The Library as an Element of the Information Infrastructure of Crystallography (on the 75th Anniversary of the Library of the Institute of Crystallography of the Russian Academy of Sciences)

S. N. Smirnov

Shubnikov Institute of Crystallography, Russian Academy of Sciences, Leninskiĭ pr. 59, Moscow, 117333 Russia

e-mail: libr@ns.crys.ras.ru

Received June 6, 2000

Abstract—The role of a scientific library and, in particular, the library of the Institute of Crystallography of the Russian Academy of Sciences, in the development of crystallography has been considered as well as the place of the library of the Institute of Crystallography in the information flows based on the achievements in modern crystallographic research. *© 2001 MAIK "Nauka/Interperiodica".*

INTRODUCTION

The information infrastructure of crystallography is seen as a number of constituent disciplines that form this science.

Consider the major elements of the information infrastructure of crystallography by following the information flow from the moment of obtaining scientific results in the laboratories and interpreting them (preparation of scientific publications) back to the scientists in the form of published scientific articles—the "information rotation" [1]. Fundamental scientific data are displayed in special scientific and technological journals, e.g., journals of abstracts published in the Russian Institute of Scientific and Technological Information (VINITI), the bibliographic cards of the Russian Book Chamber, and electronic databases (the so-called secondary scientific information). By obtaining detailed information from various research fields, scientists can plan their further research. Recently, the ever-increasing importance in the system of information flow has been taken on by various foundations providing grants for numerous research projects and taking part in the publishing of information [2].

Below, we consider only the main elements of this infrastructure, i.e., journals of abstracts, scientific journals and books, and modern information technologies.

THE CONTRIBUTION OF MODERN INFORMATION TECHNOLOGIES TO THE DEVELOPMENT OF CRYSTALLOGRAPHY

In the last decade, the information infrastructure has been augmented by modern computer technologies, and has attained a qualitatively new level of information processing, which has considerably accelerated the information flows and, thus, increased the possibilities for scientists [3]. As is well known, computers were first applied to mathematical computations. In crystallography, computers were first used for processing experimental X-ray diffraction data in structure determinations. With the development of the methods for mathematical simulation, scientists started performing computer experiments providing a comparatively cheap and reliable prediction of the behavior of materials under various conditions. The creation of numerous databases accelerated the accumulation of all sorts of knowledge (including crystallographic). The advent of the Internet considerably facilitated access to information in all scientific fields. In particular, it became possible to find the necessary crystallographic information in a rather short time not only in the crystallographic databases but also in others. New electronic (virtual) libraries came into being. Some scientific information is available now only in the electronic form. Computers are widely used in scientific organizations, at conferences, in teaching and the exchange of scientific and business information, etc.

One of the most important elements of the information infrastructure is scientific libraries, which accumulate scientific information (journals, books, and modern informational technologies).

CRYSTALLOGRAPHY AND ITS INFORMATION INFRASTRUCTURE

Crystallography has some specific features reflecting its information infrastructure [4, 5]. As is well known, crystallography consists of three main parts—

1063-7745/01/4601-0157$21.00

crystal growth, crystal structure, and crystal properties. Historically, crystallography began in mineralogy and was developed in close relation with the information infrastructure of mineralogy; however, it became more closely related to chemistry and physics. In the beginning, crystallography was of a descriptive nature. The most powerful tool of obtaining new information then was an optical microscope.

The discovery of X-ray diffraction from crystals and its use for determining their structure marked a new stage of the development of crystallography (a science using precise X-ray data and their mathematical processing). The information flow associated with crystalline materials also qualitatively changed, being complemented with new structural data and physical characteristics of crystals under the effect of various factors under diverse conditions. The development of the science on crystal growth provided the industrial production of crystals with necessary properties. The corresponding information flow was also enriched with the data from neighboring fields of science.

After the second World war, the international character of crystallography was enhanced. The International Union of Crystallography was organized (www.iucr.org). Crystallography started studying biological objects; it was enriched with new mathematical, chemical, and biological knowledge.

The Institute of Crystallography of the Russian Academy of Sciences has an honorary place among numerous national and international crystallographic institutions. The Institute was founded by Shubnikov on the basis of the Laboratory of Crystallography of the USSR Academy of Sciences in 1943. Its library, which will celebrate its 75th anniversary in December, 2000 is an inseparable part of the institute.

SOME FACTS FROM THE HISTORY OF THE LIBRARY OF THE INSTITUTE OF CRYSTALLOGRAPHY

The library is somewhat older than the institute itself—its organization dates to December 1925, when Shubnikov organized the Quartz Laboratory within the Mineralogical Museum of the USSR Academy of Sciences (Leningrad).

Some remember [6, 7] that the library then consisted of various reference books, dictionaries, and articles cut from newspapers and journals and its volume did not exceed one book case. The books were registered in a conventional school notebook. Shubnikov insisted that a scientist should not only conduct experiments in the laboratory but should also work with the scientific literature. He used to say that all the laboratories should not only have scientific equipment but also a scientific library. E.V. Tsinzerling remembered that M.P. Shaskol'skaya was responsible for regular communications of the Laboratory with foreign scientists and registered the reprints of the publications. Each week, an exhibition of newly received books and articles was organized. The reprints received from abroad were reviewed by scientists and were discussed at Saturday seminars.

Shubnikov did not neglect the library even during hard years or the second World War. By his order on October 17, 1941, O.M. Shubnikova was appointed the head of the library. According to the order on March 17, 1942, the Laboratory of Crystallography, together with its library, was evacuated to the Urals.

Since the beginning of the 1950s, the library has been headed by K.V. Flint, N.V. Slesareva, N.I. Ryabova, and T.S. Tsvetkova. Since 1988, the library has been headed by M.V. Lavrent'eva. Since 1980, the library has been located in two buildings at the Institute of Crystallography. Today, the library widely uses modern information technologies and personal computers. The scientific activity of the library is controlled by the Library Council and is subjected to the Directory of the Institute. At various times, the Library Council has been headed by the leading scientists of the institute, such as G.G. Lemmlein and B.N. Grechushnikov. Many young scientists have also worked on the Library Council.

THE LIBRARY AS A COLLECTIVE INTERMEDIARY

The 1990s were marked by considerable changes in the life of our state, which greatly influenced the provision of information science. The situation was also aggravated because of serious economical problems. The information space has become more complicated. Access to scientific information (international in essence) has become more difficult and expensive. The volume of the world information flow has considerably increased and become much more diverse. Each year, a large number of new scientific journals come into being. Numerous publishing and printing houses constantly increase the volume of information. At the same time, the number of journals received by the libraries of the Russian Academy of Sciences has been dramatically reduced due to poor financing. New "market relations" have been formed. The information flow has been decentralized. The time necessary for the organizational activity (creation of new grants, solution of financial problems, various agreements, etc.) is constantly increasing. The search for information has become a new profession, because scientists have neither the possibilities nor time to follow an ever-increasing flow of in formation.

These new conditions require an intermediary between the scientist and the "sea of information." At the Institute of Crystallography, the role of such an intermediary is played by its library, which now has to perform some additional duties, making the library a certain information center.

According to [8], the task of a library as a collective intermediary is to help the readers to adapt themselves to modern informational technologies. The library of the Institute of Crystallography has an individual approach to each of its readers [9]. The specially developed information software saves both time and finances for the researchers.

INFORMATIONAL RESOURCES

The most valuable information is provided by the collections of the Library of the Institute of Crystallography, the Library of Natural Sciences (BEN), and various databases.

The library of the Institute of Crystallography possesses scientific literature on crystallography, physics, chemistry, mathematics, biology, mineralogy, informatics, etc., in Russian and English, French, and German. The library collection includes numerous works by A.V. Shubnikov, N.V. Belov, B.K. Vaĭnshteĭn, E.S. Fedorov, G.V. Wulff, etc., and the complete sets of *Kristallografiya* (published since 1956), *Acta Crystallographica* (published since 1948), and *Zeitschrift für Kristallographie* (published since 1877). The oldest book on crystallography in the collection was published in 1780. A part of the collection is comprised of books and journals presented by the authors and other scientists of the Institute of Crystallography.

In recent years, subscriptions to scientific journals and the purchase of scientific books have drastically reduced because of poor financing. The use of modern computer technologies can partly compensate this negative process [9]. The library has access to the Internet; it has access to numerous well-known world information sources across the world.

The efficiency of scientist's work depends on his (her) access to information and remote databases. Here, new computer technologies are of great help in the search for information even in our insufficiently computerized country. Yet, many scientists prefer classical printed editions. We also believe that one should not completely abandon the printed forms of the scientific literature and substitute books and journals with their electronic versions due to a number of objective and subjective reasons, including the problems of the incompatibility of software copyright laws, the low technical level of some libraries, and the insufficient quality of the communication channels. Another serious problem is financing, since access to most databases is charged.

In turn, the library itself made its contribution to the Internet with its own website (http://ns.crys.ras.ru/library/main.htm) within the site of the Institute of Crystallography (http://ns.crys.ras.ru), which has the windows *Library History*, *Library Structure*, *Exhibition of New Publications*, *Index of Periodic Editions*, and *Index of Internet Addresses*.

The library prepared a catalog of the works written by institute scientists over the last 50 years—altogether about 300 books (not taking into account the collections of articles and dissertations)—which can be used as a foundation of a computer database of the proceedings of the Institute of Crystallography within the framework of the project *Russian Science* (*ben.irex.ru*). One of the goals of the latter project is the creation of the Integrated System of the Informational Resources (ISIR RAS), which would facilitate access to the information files accumulated in various institutes of the Russian Academy of Sciences.

An honorary place in the information infrastructure is occupied by *Kristallografiya*, the journal created on the basis of the Proceedings of the Lomonosov Institute of Geochemistry, Crystallography, and Mineralogy (*Crystallographic Series*) and the journals *Proceedings of the Laboratory of Crystallography of the USSR* (in print since 1939) and *Proceedings of the Institute of Crystallography of the USSR Academy of Sciences* (in print since 1943).

To show the appropriate place of the library in the crystallography infrastructure, the library performs research work in the *Informational Provision of Research*. With the further development of the information space, the role of the library in accumulating knowledge and its role as an information intermediary is always increasing.

The information and library service is based on the inquiry of scientists. The method of subject information consists of two stages. At the first stage, the preliminary choice of the information materials, including those on the Internet, (i.e., the Internet addresses), is made. Then, the material is supplied to the researcher. At the second stage, the choice of the materials necessary is performed by a researcher himself. Alternatively, the second stage can also be performed by librarians. The search for information in various databases is made with the help of key words and the use of various search engines. During unstable information supply, the library should provide the necessary conditions for the creative work of scientists. The feedback between the reader and the librarian allows the librarian to refine the inquiry for information, i.e., to create flexible forms of the information service.

THE LIBRARY OF NATURAL SCIENCES (BEN)

The institute library is one of three hundred libraries of the academic institutes forming the net of the Library for Natural Sciences of the Russian Academy of Sciences (BEN RAS) [10]. The interlibrary loan allows a scientist of any of the institutes of the Academy of Sciences to order any book from any other library of the BEN net. The Library for Natural Sciences provides considerable support as well as methodical and information help to all its libraries; therefore, it is presently

one of the best scientific libraries of the Russian Federation.

The Library of the Institute of Crystallography enjoys numerous international contacts through the Library for Natural Sciences with numerous publishing houses abroad. Under the conditions of drastically reduced financing, the Library for Natural Sciences receives considerable support from the Russian Foundation for Basic Research and the government of Moscow. The Library for Natural Sciences is a member of the Consortium of Moscow Libraries, providing the libraries with electronic versions of various editions. Being, in fact, one of the departments of the Library for Natural Sciences, the library of the Institute of Crystallography has access to the complete electronic versions of numerous scientific journals published by Elsevier, Springer, Academic, Wiley, and other publishing houses; various editions of the European and American Institutes of Physics; and the American Physical Society. Among the most popular publications on compact disks is *Current Contents* (the operative representation of the tables of contents of various journals) and the *Science Citation Index* (with the lists of references to the corresponding articles).

CONCLUSION

The information infrastructure of crystallography is developed in close cooperation with the science of crystallography. The modern information technologies make the Library of the Institute of Crystallography an important intermediary between the science as a whole and individual scientists.

As is well known [8], the activity of the institution as an intermediary at various levels is an objective law of the development of the informational provision of new research. Unfortunately, considerable difficulties in financing the library hinder its transformation as an information intermediary into of an information coordinator, which would considerably increase its authority and render considerable help to scientists in their research work function of the information coordinator.

REFERENCES

1. S. N. Smirnov, *Library of Natural Sciences in Modern Information Space. Jubilee Collection of Articles (1973–1998)* (Biblioteka po Estestvennym Naukam RAS, Moscow, 1998), p. 20.
2. L. A. Kalinichenko, O. A. Plechova, and O. V. Syuntyurenko, Vest. Ross. Fond Fundam. Issled., No. 2 (16), 74 (1999).
3. E. P. Chelyshev and B. S. Elenov, Vest. Ross. Akad. Nauk **69**, 867 (1999).
4. M. V. Koval'chuk, Kristallografiya **44** (6), 967 (1999) [Crystallogr. Rep. **44**, 901 (1999)].
5. *Modern Crystallography*, Ed. by B. K. Vaĭnshteĭn, A. A. Chernov, and L. A. Shuvalov (Nauka, Moscow, 1979; Springer-Verlag, Berlin, 1981–1988), Vols. 1–4.
6. *Alekseĭ Vasil'evich Shubnikov (1887–1970)*, Ed. by N. V. Belov and I. I. Shafranovskiĭ (Nauka, Leningrad, 1984).
7. *Problems of Modern Crystallography: Collection of Articles in Memory of Academician A. V. Shubnikov* (Nauka, Moscow, 1975).
8. N. S. Soloshenko, Author's Abstract of Candidate's Dissertation in Pedagogics (Moscow State Univ., Moscow, 1999).
9. M. V. Lavrent'eva, S. N. Smirnov, and Yu. A. Sokolova, *Modern Technologies in the Information and Library Provision of Research* (Bioinformservis, Moscow, 1999), p. 54.
10. N. G. Alekseev, L. I. Gosina, A. G. Zakharov, and N. S. Soloshenko, *Information–Library Provision of Fundamental Research* (Pushchinskiĭ Nauchnyĭ Tsentr Ross. Akad. Nauk, Pushchino, 1996).

Translated by L. Man

Crystallography Reports, Vol. 46, No. 1, 2001, pp. 19–20. Translated from Kristallografiya, Vol. 46, No. 1, 2001, pp. 25–27.

THEORY OF CRYSTAL STRUCTURES

Formation of Planar and Space Lattices from Spherical Bodies with Mutually Penetrating Shells

D. B. Titorov

Physicotechnical Institute, Ural Division, Russian Academy of Sciences, ul. Kirova 132, Izhevsk, 426000 Russia

e-mail: uufti@fti.udmurtia.su

Received May 31, 1999; in final form, April 10, 2000

Inhomogeneous spherical bodies consisting of an internal sphere covered with a spherical shell are used to model atoms for simulating the crystal lattice formation (Fig. 1a). When approaching each other (Fig. 1b), the inhomogeneous spheres obey the following rule of pair interpenetration. (1) The shells cannot penetrate inner spheres (Fig. 1c). (2) The areas of mutual penetration cannot penetrate each other (Fig. 1d). According to the rule, the centers of inhomogeneous close-packed spheres occupy the positions at polygon vertices. The sides and the angles of such polygons can be determined from simple geometrical relationships, provided the sizes of the inhomogeneous spheres and their constituent parts are known (Fig. 1e); vice versa, if the polygon parameters are known, one can determine the radii of the inhomogeneous spheres.

Depending on relationship between the inner and the outer radii of the inhomogeneous spheres packed according to the above rule, their centers coincide with the sites of various Bravais lattices and other crystal lattices of simple compounds, e.g., diamond. The close-

[1] The full text of the paper is deposited at VINITI, 1996, no 2551.

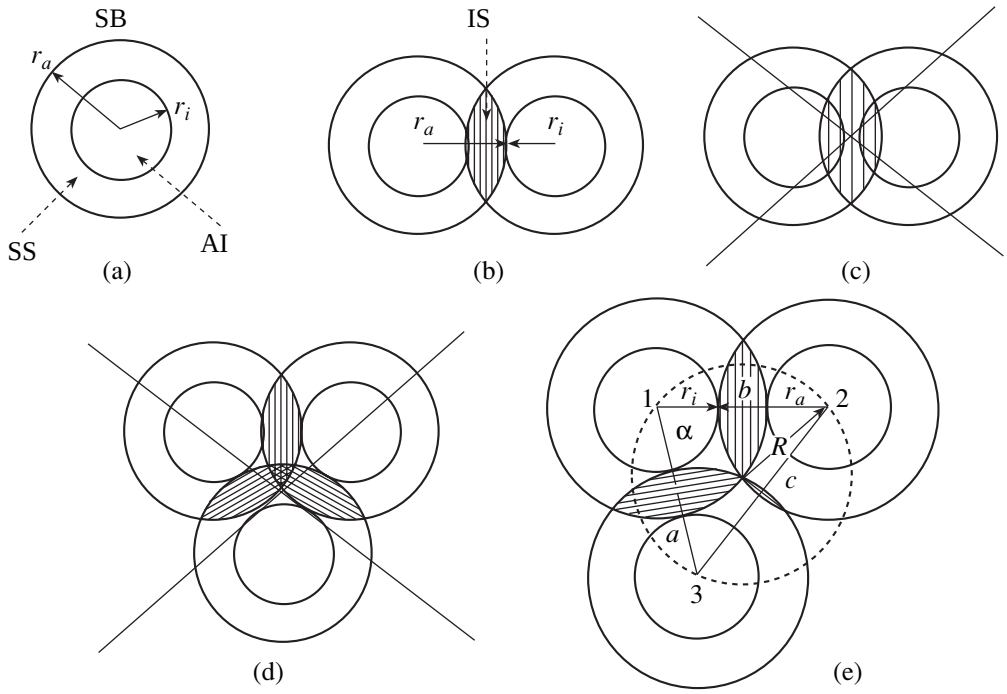

Fig. 1. Approaching inhomogeneous spherical bodies (SB) consisting of inner spheres (IS) and spherical shells (SS). The areas of interpenetration (AI) are hatched. For explanation see the text.

1063-7745/01/4601-0019$21.00 © 2001 MAIK "Nauka/Interperiodica"

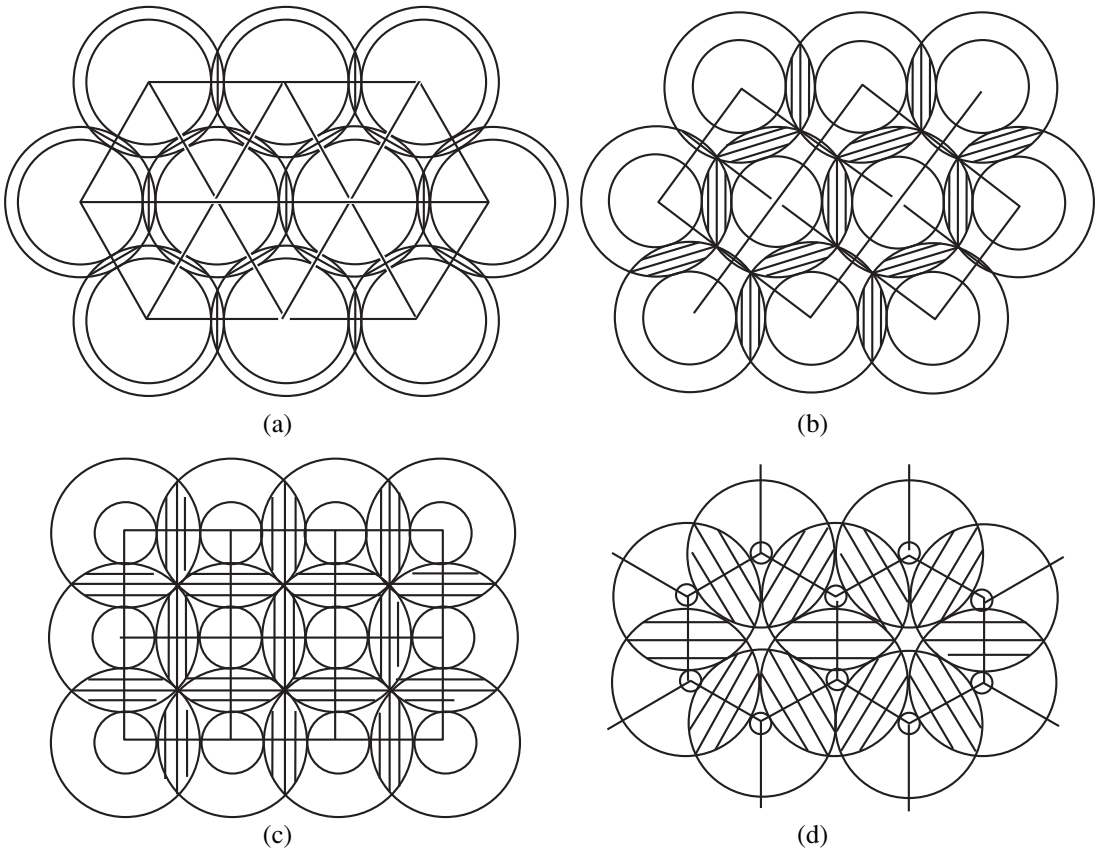

Fig. 2. Crystallographic planes formed by close-packed inhomogeneous spheres in accordance with the interpenetration rule. (a) $r_i/r_a = 0.732$, (111) plane, face-centered cubic lattice; (b) $r_i/r_a = 0.634$, (110) plane, body-centered cubic lattice; (c) $r_i/r_a = 0.414$, (100) plane, primitive cubic lattice; and (d) $r_i/r_a = 0.155$, basal plane, hexagonal lattice.

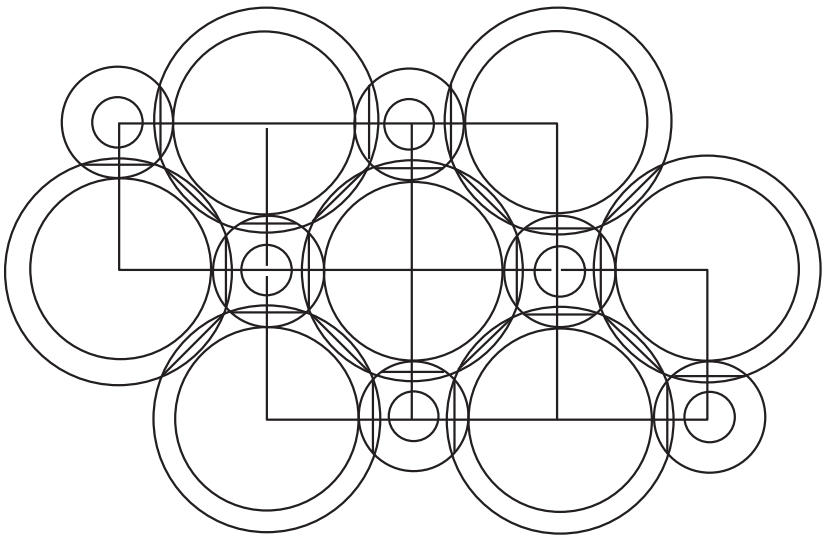

Fig. 3. Crystallographic (100) plane of NaCl-type lattice formed by close-packed inhomogeneous spheres according to the interpenetration rule.

packed crystallographic planes of some of such lattices are shown in Fig. 2. The low-symmetrical lattices are formed by inhomogeneous ellipsoids. Figure 3 illustrates a simulation of crystal lattices by nonequivalent inhomogeneous spheres.

Inhomogeneous mutually penetrating spheres and ellipsoids are more universal models of atoms than homogeneous solid spheres.

Translated by A. Zolot'ko

Crystallography Reports, Vol. 46, No. 1, 2001, pp. 21–25. Translated from Kristallografiya, Vol. 46, No. 1, 2001, pp. 28–32.

STRUCTURE OF INORGANIC COMPOUNDS

Neutron and X-ray Diffraction Study of Superstructure and Localized Magnetic Moments in $Cu_{0.5}Fe_{0.5}Cr_2S_4$ and $Cu_{0.5}In_{0.5}Cr_2S_4$ Compounds

R. A. Sadykov*, V. N. Zaritskiĭ*, J. Mesot, and F. Fauth*****

** Institute of High-Pressure Physics, Russian Academy of Sciences, Troitsk, Moscow oblast, 142092 Russia*

*** Institute Paul Scherrer, CH-5232 Villigen PSI, Switzerland*

**** Institut Laue–Langevin, 156X, Grenoble, 38042 France*

Received October 20, 1999

Abstract—The superstructure parameters for the $Cu_{0.5}Fe_{0.5}Cr_2S_4$ and $Cu_{0.5}In_{0.5}Cr_2S_4$ compounds have been determined by neutron and X-ray diffraction. The localized magnetic moments in different sublattices measured for $Cu_{0.5}Fe_{0.5}Cr_2S_4$ are equal to 3.06 ± 0.17 μB for Fe^{3+} ions in the *A*-site and 2.76 ± 0.22 μB for Cr^{3+} ions in the *B*-site (Cu^+ possess no magnetic moment), which are much less than the magnetic moments for the ions in the purely ionic state. *© 2001 MAIK "Nauka/Interperiodica".*

The $Cu_xFe_{1-x}Cr_2S_4$ system is characterized by the semiconductor–semimetal transition; at $x = 0.5$, the composition dependence of the Curie point and the maximum value of negative magnetic resistance suddenly change. However, the structural parameters and localized magnetic moments of ions in $Cu_{0.5}Fe_{0.5}Cr_2S_4$ have not been studied in detail as yet, despite the fact that their knowledge would allow one to estimate such an important parameter as the degree of 3*d*-electron localization in Fe and Cr, which specifies both the magnetic and the electric properties. The presence of Cu^+ and Fe^{3+} in the tetrahedral sublattice evidence their possible ordering [1]. Neutron diffraction study of $Cu_{0.5}Fe_{0.5}Cr_2S_4$ [2, 3] showed the formation of the 1:1-type superstructure in the *A*-sites of the spinel structure, with the simultaneous change of the sp. gr. $Fd3m$ to sp. gr. $F\bar{4}3m$. However, the insufficient measurement accuracy and the low level of data processing (especially, determination of magnetic moments) did not allow the establishment of all the structural parameters and localized magnetic moments in the *A*- and *B*-sites. The reliable establishment of the superstructure type seems to be important in the context of the discussion on the mechanism of superstructure formation in spinels [4, 5].

Below, we report our X-ray diffraction study of a specimen at the room temperature on a URD63A diffractometer (copper radiation, nickel filter). The study was performed in the angular range 6°–110° at a step of 0.02°. The diffraction pattern obtained (Fig. 1) shows only the reflections characteristic of the spinel structure: (111), (220), (311), etc. Short vertical lines in the pattern center indicate the positions of the possible Bragg reflections for the sp. gr. $F\bar{4}3m$. The superstructure (the (200), (420), etc., reflections corresponding to the extinction rule $h + k = 4n + 2(nk0)$) were not observed because of the small difference in the amplitudes of the X-ray scattering by copper and iron ions (which differs this compound from $Cu_{0.5}In_{0.5}Cr_2S_4$ where iron is substituted by indium). The powder neutron diffraction data from $Cu_{0.5}Fe_{0.5}Cr_2S_4$ specimens were obtained on a D1B diffractometer at $T = 300$–2 K on the high-flux reactor at the Laue–Langevin Institute (ILL, Grenoble, France). The neutron wavelength was 2.524 Å, and the measurements were performed in a standard ILL cryostat within the angular range 21°–100.80° at a step of 0.20°. The neutron diffraction pattern at $T = 2$ K is shown in Fig. 2. Short vertical lines indicate the positions of possible Bragg reflections for the sp. gr. $F\bar{4}3m$. Unlike the X-ray diffraction pattern, the neutron diffraction pattern has the (200) and (420) reflections. Although the difference in the scattering amplitudes from copper and iron nuclei (0.772×10^{-12} and 0.945×10^{-12} cm, respectively) is almost equal to that observed in X-ray diffraction, the contribution of this difference to the structure amplitude [3] in neutron diffraction is somewhat higher than X-ray diffraction (4.5 and 2.4%, respectively). Moreover, the neutron scattering at $T = 2$ K is superimposed with magnetic scattering ($Cu_{0.5}Fe_{0.5}Cr_2S_4$ is a ferrimagnetic with $T_c = 335$ K [3]) and, therefore, the magnetic contribution to these reflections is quite pronounced (Table 1). As a result, the superstructural reflections are seen both at $T = 2$ K and $T = 300$ K.

The X-ray and neutron diffraction data were subjected to the full-profile analysis by the Rietveld

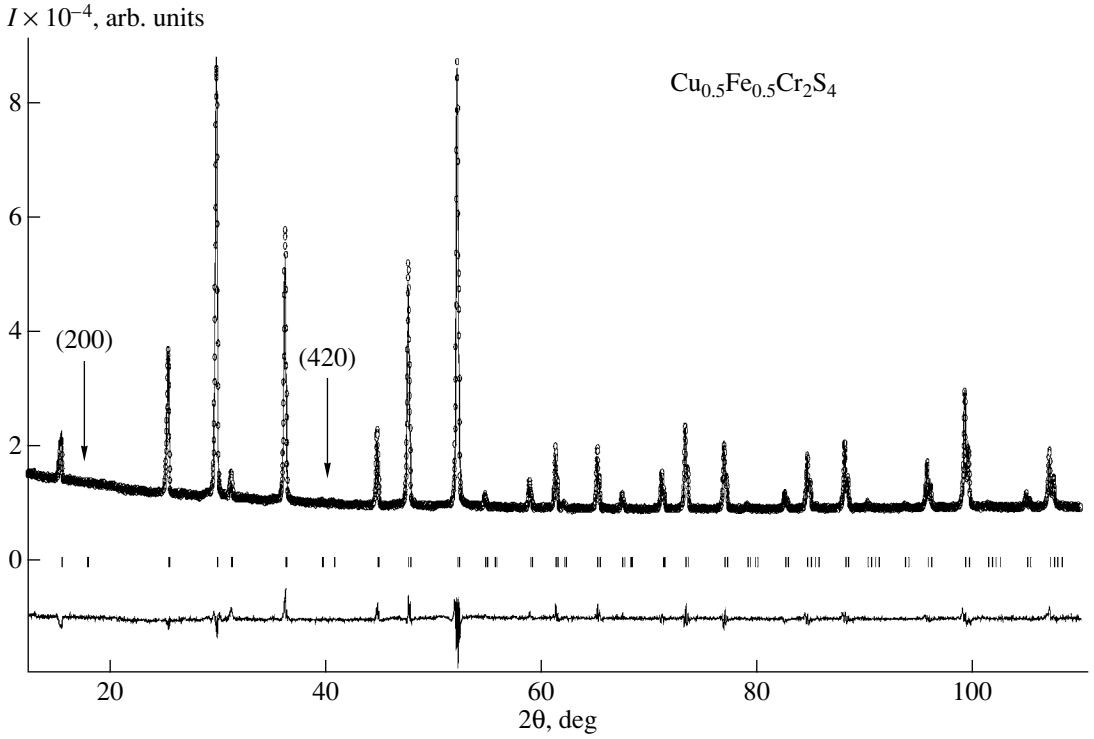

Fig. 1. X-ray diffraction spectrum of $Cu_{0.5}Fe_{0.5}Cr_2S_4$. Dots represent experimental data, solid line represents calculated data. The difference pattern is shown below. The calculations were made using the parameters given in Table 2.

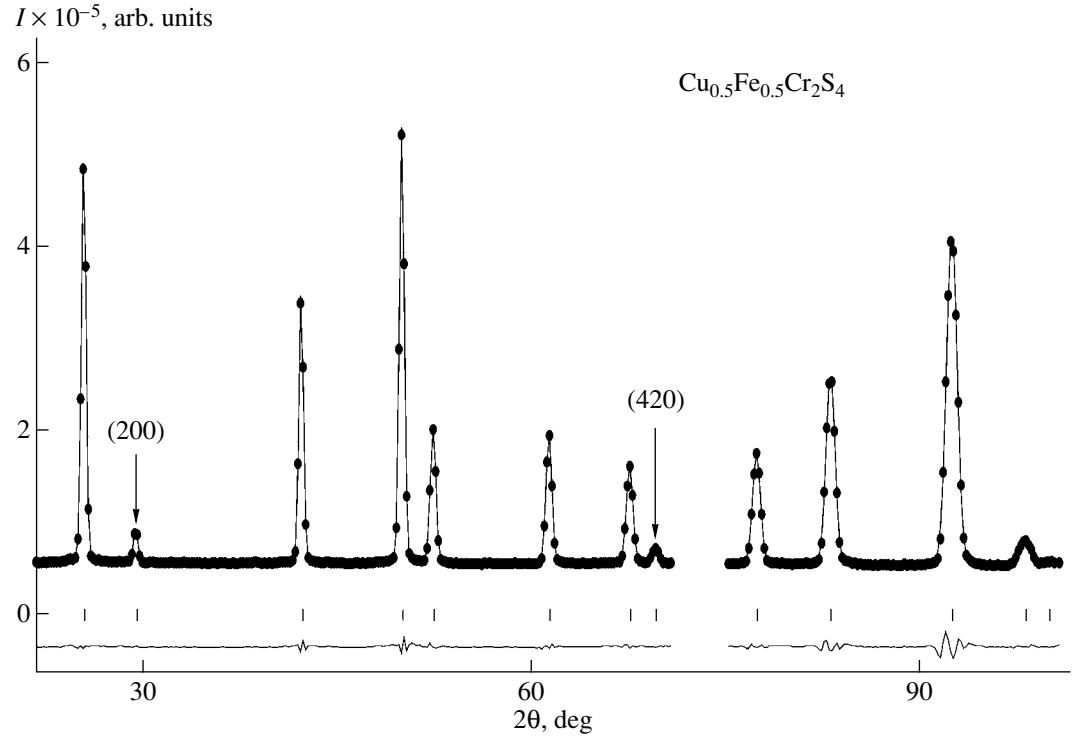

Fig. 2. Neutron diffraction pattern of $Cu_{0.5}Fe_{0.5}Cr_2S_4$ at $T = 2$ K. For notation see Fig. 1.

Table 1. Neutron powder diffraction data obtained for $Cu_{0.5}Fe_{0.5}Cr_2S_4$ at T = 2 K

hkl	*d*, Å	2θ, deg	Nuclear scattering		Magnetic scattering	
			I_{exp}	I_{calc}	I_{exp}	I_{calc}
111	5.7041	25.566	6527	6509	201704	200546
200	4.9399	29.605	2863	3032	11487	12921
220	3.4931	42.362	17024	16816	16353	16267
311	2.9789	50.135	206492	204213	27339	26584
222	2.8521	52.530	11994	12066	62168	62963
400	2.4700	61.458	40562	41350	39315	41196
331	2.2666	67.673	23242	23038	47655	46772
420	2.2092	69.681	47	48	11620	11558
422	2.0167	77.485	89285	88488	5954	5817
511	1.9014	83.178	158489	157145	3272	3199
333	1.9014	83.178	20857	20681	3087	3018
440	1.7465	92.545	377008	377433	7776	7799
531	1.6700	98.182	6111	6187	25797	26269
600	1.6466	100.076	305	274	1475	1350
442	1.6466	100.076	2228	2001	1796	1643

method within the sp. gr. $F\bar{4}3m$ (Fullprof program [6, 7]). Copper ions occupy the 4(*a*) (0, 0, 0) positions; iron ions are located in the 4(*c*) (1/4, 1/4, 1/4) positions; and chromium and sulphur ions occupy the 16(*e*) (*x*, *x*, *x*) positions with the positional parameters *x*(Cr), *x*[S(1)], and *x*[S(2)], respectively (Table 2). We also performed the calculations of the X-ray diffraction data for the spinel structure with the sp. gr. *Fd*3*m*. However, the

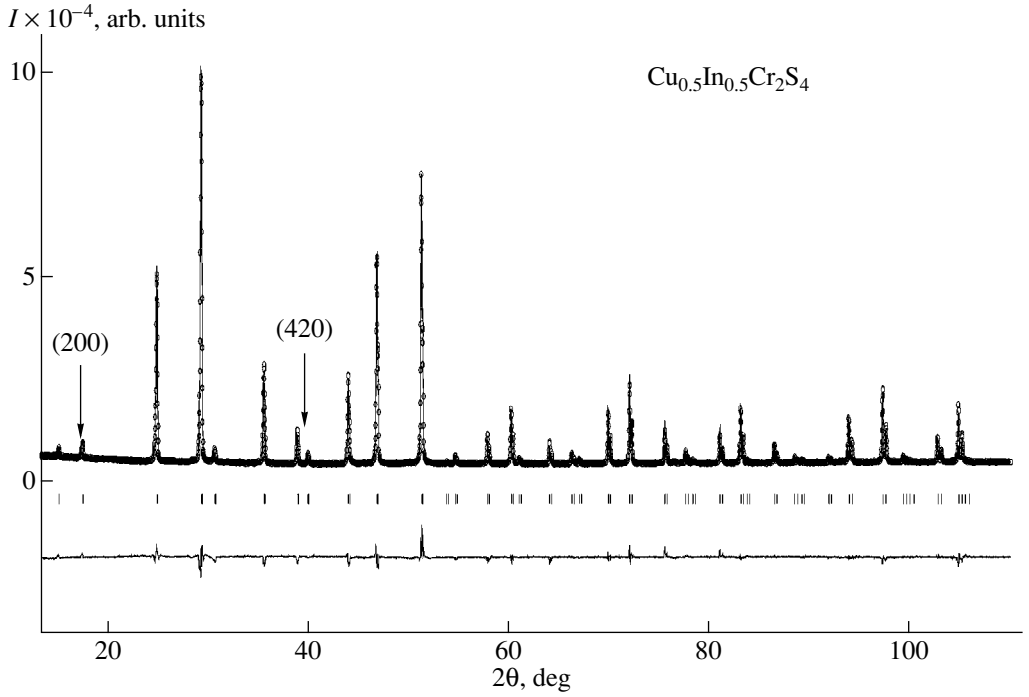

Fig. 3. X-ray diffraction spectrum of $Cu_{0.5}In_{0.5}Cr_2S_4$. For notation see Fig. 1. The calculations were made using the parameters given in Table 4.

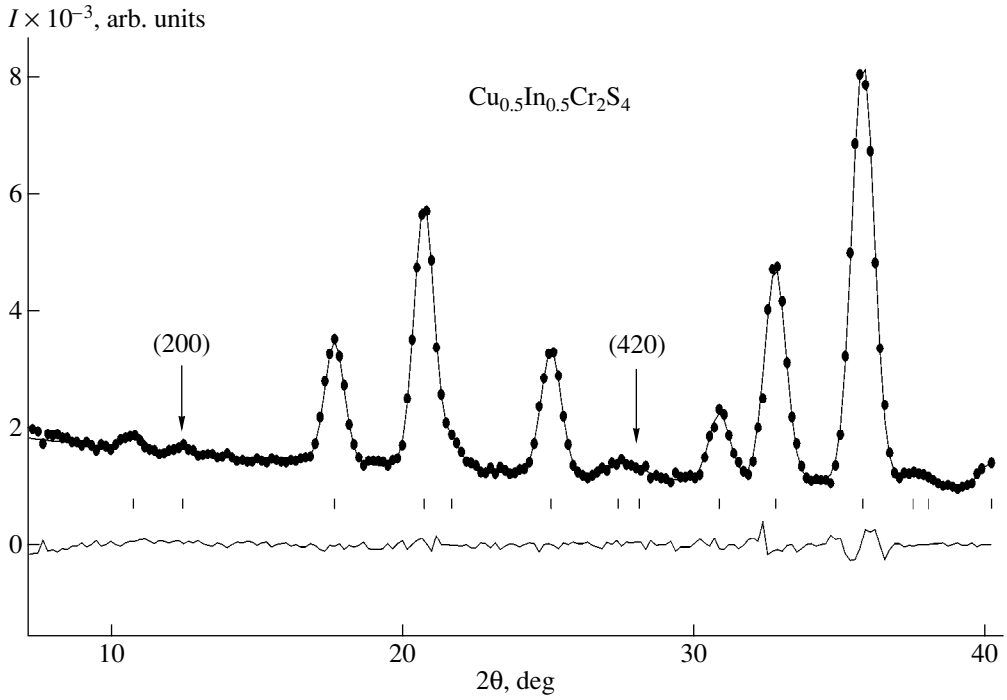

Fig. 4. Neutron diffraction pattern of $Cu_{0.5}In_{0.5}Cr_2S_4$ at T = 300 K. For notation see Fig. 1. The calculations were made using the parameters from Table 4.

lowest R-factor was obtained for the sp. gr. $F\bar{4}3m$. Neutron measurements at T = 2 K provided the determination of localized magnetic moments of Fe^{3+} ions in the A-sites (3.06 ± 0.17 μB) and Cr^{3+} ions in the B-sites (2.76 ± 0.22 μB); Cu^+ ions posses no magnetic moment at all. It is confirmed that $Cu_{0.5}Fe_{0.5}Cr_2S_4$ is a ferrimagnetic. The magnetic moments determined are less than those for the Fe^{3+} and Cr^{3+} in pure ionic states (5 and 3 μB, respectively), which, in our opinion, is explained by two reasons—covalent bonding and the partial escape of 3d-electrons to the valence band (because this compound is a magnetic semiconductor). Since the Cu^+ ions and Fe^{3+} ions are located at the same positions, their state should differ from being purely ionic.

Table 2. Characteristics of the $Cu_{0.5}Fe_{0.5}Cr_2S_4$ structure at T = 300 K (N and R indicate neutron and X-ray measurements, respectively)

Atom	Position	x	Parameter	Value
Cu	4(a)	0	B_{total}, Å^2	0.28(6) N
Fe	4(c)	1/4		0.37(4) R
Cr	16(e)	0.632(3) N	a, Å	9.896(2) N
		0.6282(4) R		9.8995(1) R
S(1)	16(e)	0.380(2) N	R_p, %	4.2 N
		0.3855(5) R		3.2 R
S(2)	16(e)	0.867(2) N	R_{wp}, %	5.7 N
		0.8688(4) R		4.7 R

The $Cu_{0.5}In_{0.5}Cr_2S_4$ compound has already been studied in [8], but most of its crystallographic parameters have not been determined. Therefore, we undertook new X-ray and the neutron diffraction studies at room temperature. Figure 3 shows the diffraction pattern obtained on an URD63A X-ray diffractometer (copper radiation, nickel filter). Unlike the X-ray diffraction pattern of $Cu_{0.5}Fe_{0.5}Cr_2S_4$, the diffraction pattern of $Cu_{0.5}In_{0.5}Cr_2S_4$ has (200) and (420) superstructural reflections. The results of the neutron diffraction study of the latter compound at room temperature at a neutron wavelength of 1.092 Å are presented in Fig. 4 (pure nuclear scattering) and listed in Table 3 (the first fifteen Bragg reflections). The structural parameters obtained in both neutron and X-ray studies are given in Table 4.

It is seen that the neutron and the X-ray data complement each other for $Cu_{0.5}Fe_{0.5}Cr_2S_4$, whereas for $Cu_{0.5}In_{0.5}Cr_2S_4$ they almost coincide with each other (although in the latter case, the statistics of measurements were much worse and the number of recorded reflections was much less on the neutron diffraction pattern). This is explained by the fact the effect of absorption for neutrons is much weaker than that for

Table 3. Neutron diffraction data for $Cu_{0.5}In_{0.5}Cr_2S_4$ obtained at T = 300 K (nuclear scattering, 15 reflections)

hkl	*d*, Å	2θ, deg	I_{exp}	I_{calc}
111	5.8067	10.791	273	266
200	5.0287	12.466	104	133
220	3.5559	17.665	1853	1830
311	3.0324	20.746	3978	3961
222	2.9033	21.679	389	372
400	2.5144	25.084	1926	1931
331	2.3073	27.376	244	247
420	2.2489	28.102	134	133
422	2.0530	30.847	1088	1074
511	1.9356	32.770	3272	3254
333	1.9356	32.770	237	236
440	1.7779	35.769	7000	6997
531	1.7000	37.468	193	187
600	1.6762	38.019	23	23
442	1.6762	38.019	44	44

Table 4. Characteristics of $Cu_{0.5}In_{0.5}Cr_2S_4$ structure at T = 300 K (*N* and *R* indicate neutron and X-ray measurements, respectively)

Atom	Position	*x*	Parameter	Value
Cu	4(a)	0	B_{total}, Å^2	1.12(9) *N*
In	4(c)	1/4		1.19(4) *R*
Cr	16(e)	0.629(1) *N*	*a*, Å	10.057(4) *N*
		0.6312(2) *R*		10.05610(9) *R*
S(1)	16(e)	0.3894(8) *N*	R_p, %	4.9 *N*
		0.3901(2) *R*		3.5 *R*
S(2)	16(e)	0.8658(9) *N*	R_{wp}, %	5.8 *N*
		0.8678(3) *R*		4.8 *R*

X-rays, which allows the more precise determination of structure factors from neutron-diffraction data.

Thus, the neutron and the X-ray diffraction data provided the determination of all the structural parameters for $Cu_{0.5}Fe_{0.5}Cr_2S_4$ and $Cu_{0.5}In_{0.5}Cr_2S_4$ crystals as well as the values of localized magnetic moments of iron and chromium ions in different sublattices of the $Cu_{0.5}Fe_{0.5}Cr_2S_4$ structure.

ACKNOWLEDGMENTS

The study was supported by the Russian Foundation for Basic Research, project no. 99-02-17884, and by the ICDD grant.

REFERENCES

1. F. K. Lotgering, R. P. Stapele, and G. H. van der Steen, J. Phys. Chem. Solids **30**, 799 (1969).
2. I. V. Gordeev, Ya. A. Kesler, V. V. Kelarev, and N. M. Chebotaev, Izv. Akad. Nauk SSSR, Neorg. Mater. **19**, 1587 (1983).
3. V. N. Zaritskiĭ, R. A. Sadykov, Ya. V. Kostyuk, *et al.*, Fiz. Tverd. Tela (Leningrad) **28**, 3292 (1986) [Sov. Phys. Solid State **28**, 1854 (1986)].
4. V. M. Talanov, Zh. Strukt. Khim. **27** (2), 172 (1986).
5. V. M. Talanov, Kristallografiya **41** (6), 979 (1996) [Crystallogr. Rep. **41**, 929 (1996)].
6. J. L. Rodríguez-Carvajal and M. A. Pannetier, Institut Laue Laungevin (ILL) Report 87TR014T, 1987.
7. J. L. Rodríguez-Carvajal, Physica B (Amsterdam) **192**, 55 (1993).
8. C. Wilkinson, B. M. Knapp, and J. B. Forsyth, J. Phys. C: Solid State Phys. **9**, 4021 (1976).

Translated by A. Zolot'ko

Crystallography Reports, Vol. 46, No. 1, 2001, pp. 26–29. Translated from Kristallografiya, Vol. 46, No. 1, 2001, pp. 33–36.

STRUCTURE OF INORGANIC COMPOUNDS

Structure and Phase Transitions in Trigonal $Cs_3Sb_2I_9$ Crystals

M. S. Novikova*, I. P. Makarova*, M. K. Blomberg, B. Sh. Bagautdinov***, and I. P. Aleksandrova******

** Shubnikov Institute of Crystallography, Russian Academy of Sciences, Leninskiĭ pr. 59, Moscow, 117333 Russia*

*** Department of Physics, University of Helsinki, Helsinki, Finland*

**** Institute of Solid-State Physics, Russian Academy of Sciences, Chernogolovka, Moscow oblast, 142432 Russia*

***** Institute of Physics, Siberian Division, Russian Academy of Sciences, Krasnoyarsk, Russia*

e-mail: irina@ns.crys.ras.ru

Received June 30, 1999

Abstract—The atomic structure of $Cs_3Sb_2I_9$ single crystals was refined using X-ray diffraction data (sp. gr. $P\bar{3}m1$; wR = 1.58% and R = 3.07%). The phase transitions revealed earlier were found to be accompanied by the appearance of superstructural reflections. At T_{c1} = 86 K, the reflections indicating doubling of the c parameter. At T_{c2} = 73 K, a first-order phase transition takes place accompanied by "freezing" of the satellites h, k + 1/2, l + 1/2 reflections. In the temperature range from 73 to 78 K, an incommensurate phase providing the satellites h, k + 1/2 + δ, l + 1/2 is formed. © *2001 MAIK "Nauka/Interperiodica".*

INTRODUCTION

The $Cs_3Sb_2I_9$ compound belongs to the $A_3B_2X_9$ family, where A is the alkali metal ion; B = Fe, As, Sb, Bi, Tl, or Mo; and X = Cl, Br, or I [1]. All the structures of this class are built by hexagonal layers of AX_3 and B ions occupying two-thirds of the octahedral cavities located between these layers. These structures are characterized by different packings of these layers. Earlier [1], the $Cs_3Sb_2I_9$ structure was refined in the sp. gr. $P6_3/mmc$ to the reliability factors wR = 4.8% and R = 6.2%. Later, the $Cs_3Sb_2I_9$ structure was refined within the sp. gr. $P\bar{3}m1$ to R = 14% using the X-ray powder diffraction data [2]. As a result, two polymorphous modifications of this compound were established. Below, we present the results of the study of the Bridgman-grown crystals of the trigonal modification. Their properties and phase transitions were reported earlier [3]. We refined the $Cs_3Sb_2I_9$ crystal structure by the methods of the X-ray diffraction analysis and analyzed the phase transitions revealed in [3].

REFINEMENT OF THE STRUCTURE MODEL

X-ray diffraction data were collected on an Enraf-Nonius CAD-4F diffractometer (MoK_α radiation) from two plateletlike crystals (Table 1). Since the crystals possessed the pronounced mosaicity, the reflections were measured using the ω scan technique within a hemisphere and the total sphere of the reciprocal space for crystals **I** and **II**, respectively. The absorption corrections were introduced by the method of numerical

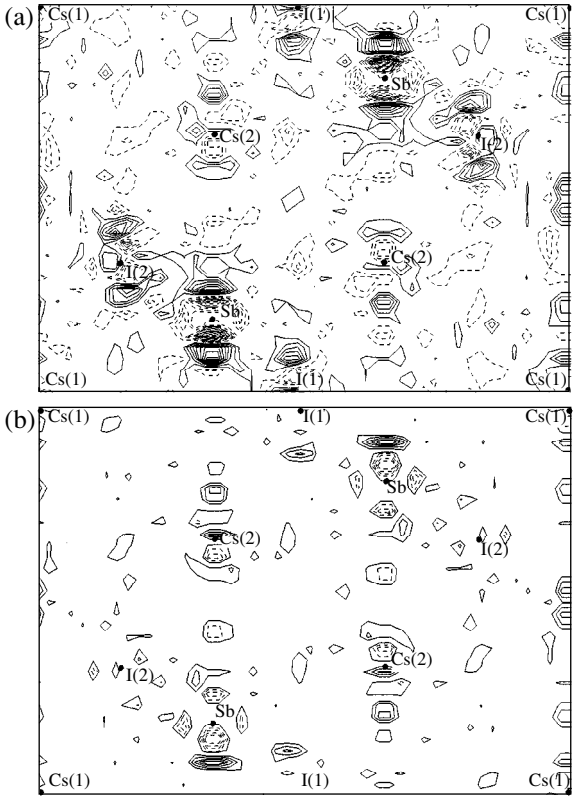

Fig. 1. Final (110) difference electron-density map for the $Cs_3Sb_2I_9$ crystals calculated after the refinement of the structural model (a) without and (b) with allowance for anharmonic parameters. The positive and negative values are indicated by solid and dashed isolines spaced by 0.2 e/Å^3, respectively.

1063-7745/01/4601-0026$21.00 © 2001 MAIK "Nauka/Interperiodica"

Main crystallographic data for $Cs_3Sb_2I_9$

Characteristic	Parameter	
	crystal **I**	crystal **II**
Diffractometer	Enraf-Nonius	Enraf-Nonius
λ, Å	0.71073	0.71073
Crystal dimensions, mm	$0.4 \times 0.35 \times 0.07$	$0.287(9) \times 0.256(9) \times 0.029(9)$
μ, cm^{-1}	173.2	172.9
Number of reflections used in the refinement of the unit cell	20	24
θ range, deg	14–18	12–18
Unit-cell parameters *a* and *c*, Å	8.440(3), 10.395(3)	8.408(5), 10.370(5)
h_{max}	10	12
k_{max}	10	12
l_{max}	14	15
$(\sin\theta/\lambda)_{max}$, $Å^{-1}$	1.0	0.75
Sp. gr.	$P\bar{3}m1$	$P\bar{3}m1$
Number of reflections	1715	10027
Number of reflections after averaging	513	876
Number of reflections in the refinement ($I > 3\sigma$)	442	742
R_{int} over equivalent reflections, %	10.8	5.6
Reliability factor, %	$R = 4.0$	$R = 3.1$
	$wR = 3.8$	$wR = 1.6$

integration with due regard for crystals habitus. With this procedure, we averaged the X-ray data.

The X-ray data for crystal **I** were processed and refined using the PROMETHEUS [4], JANA93 [5], and XABS2 [6] program packages. The computations for crystal **II** were made with the use of the PROMETHEUS program package. The atomic-scattering curves and the dispersion corrections $\Delta f'$ and $\Delta f''$ were taken from the International Tables for X-ray Crystallography [7]. The atomic coordinates determined in [2] were used as the starting model. For crystal **I**, the final reliability factors were $R = 4.0\%$ and $wR = 3.8\%$. For crystal **II**, the atomic thermal parameters were refined in the anharmonic approximation with the use of the formalism of Gram–Charlier series expansion of the probability-density function of atomic displacements from their equilibrium positions in terms of quasi-moments [8]. The parameter refinement in the anharmonic approximation yielded the following physically significant parameters: $C^{111} = 0.21(7) \times 10^{-6}$ and $D^{1111} = -0.20(4) \times 10^{-8}$ for Cs(2), $D^{3333} = 0.23(1) \times 10^{-8}$ for Sb, $D^{1111} = -0.29(7) \times 10^{-8}$, $D^{3333} = 0.33(2) \times 10^{-8}$, and $D^{1112} = -0.08(3) \times 10^{-8}$ for I(1), and $C^{111} = -0.20(4) \times 10^{-6}$, $D^{1111} = -0.18(4) \times 10^{-8}$, and $D^{3333} = 0.24(1) \times 10^{-8}$ for I(2). The final difference elec-

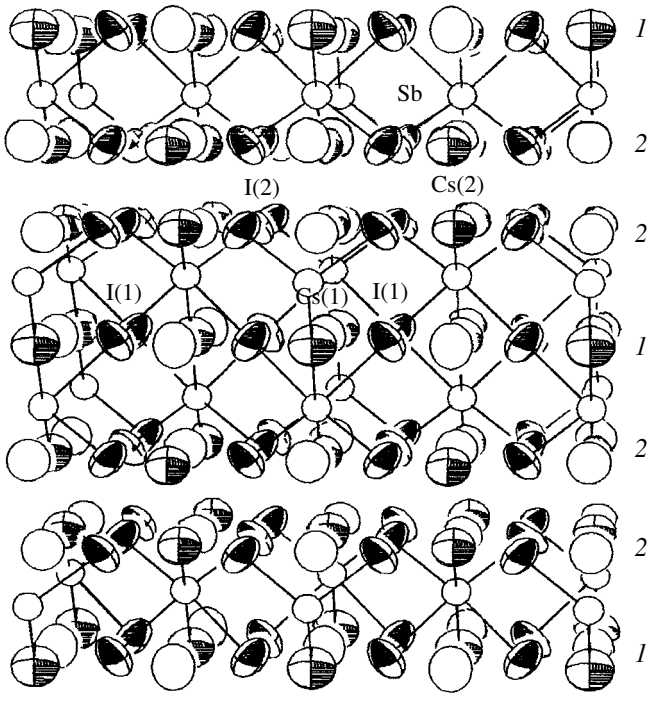

Fig. 2. $Cs_3Sb_2I_9$ structure projected normally to the [010] direction.

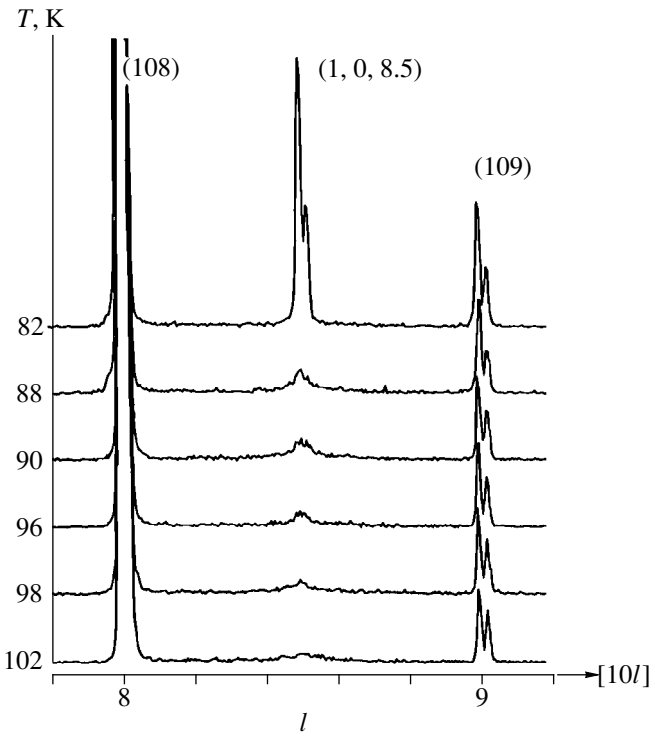

Fig. 3. Illustrating the appearance of the superstructural (1, 0, 8.5) reflection.

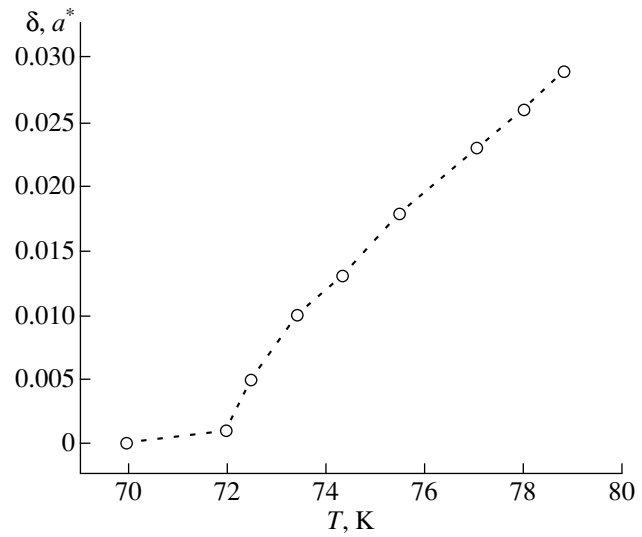

Fig. 4. Temperature dependence of the incommensurability parameter.

tron-density maps calculated after the refinement of all the atoms with the involvement of the anharmonic parameters became substantially "cleaner" (Fig. 1); the reliability factors decreased from $wR = 2.13\%$ and $R = 3.81\%$ to $wR = 1.58\%$ and $R = 3.07\%$, respectively, and provided the significance level, according to the Hamilton test [9], $\alpha < 0.005$.

The positional and thermal parameters of the corresponding basis atoms in the structures of both crystalline specimens were the same (within an accuracy of the calculations). The inconsistent data were obtained only for interatomic distances, which is explained by different unit-cell parameters of the crystals. The positional parameters for crystal **II** are given in table.

Simultaneously, $Cs_3Sb_2I_9$ crystals grown in the same experiment were also studied on a Syntex $P1$ diffractometer [10]. The structure was refined using the AREN program package [11] with due regard for absorption using the DIFABS program [12]. The final reliability factors were $R = 5.9\%$ in the sp. gr. $P\bar{3}m1$ and $R = 5.3\%$ in the acentric sp. gr. $P\bar{3}m1$ (the Cs atoms in the latter group are somewhat displaced). The close values of the R factors did not allow the authors to choose any of the two models. Finally, preference was given to the centrosymmetric sp. gr. $P\bar{3}m1$ because no generation of the second harmonic of laser radiation was revealed in the specimens [10].

We refined the structure up to the attainment of the wR factor as low as 1.58%. The corresponding final difference electron-density maps were clean, which indicated that Cs atoms were not displaced from their positions and, thus, confirmed the centrosymmetric model. This conclusion is consistent with the NQR spectral data according to which only the centrosymmetric sp. gr. $P\bar{3}m1$ corresponds to the number of I^{127} NQR lines observed for $Cs_3Sb_2I_9$ at room temperature [3].

The $Cs_3Sb_2I_9$ crystals are built by CsI_3 layers (Fig. 2) that form a cubic close packing with Sb ions occupying two-thirds of the iodine octahedra. The structure can arbitrarily be represented as the alternation of the layers of types 1 $(Cs(1)I(1)_3)$ and 2 $(Cs(2)I(2)_3)$ forming the sequence 212 212 212 212. The packing of the CsI_3 layers in the trigonal polytype differs from the packing in the hexagonal polytype [1], where SbI_6-octahedra share their edges and not the vertices.

X-RAY DIFFRACTION STUDY OF PHASE TRANSITIONS

We studied a number of physical properties of $Cs_3Sb_2I_9$ crystals as functions of temperature and established two phase transitions at $T_1 = 86$ and $T_2 = 73$ K [3]. The brief characterization of these phase transitions has already been reported [13]. Our aim was to study these phase transitions by the methods of X-ray diffraction analysis.

The study was performed on a four-circle Huber-5042 diffractometer (MoK_α radiation) equipped with a low-temperature helium Displex 202 attachment. The study of the reciprocal lattice in the temperature range of 273–50 K revealed reflections indicating doubling of the c period.

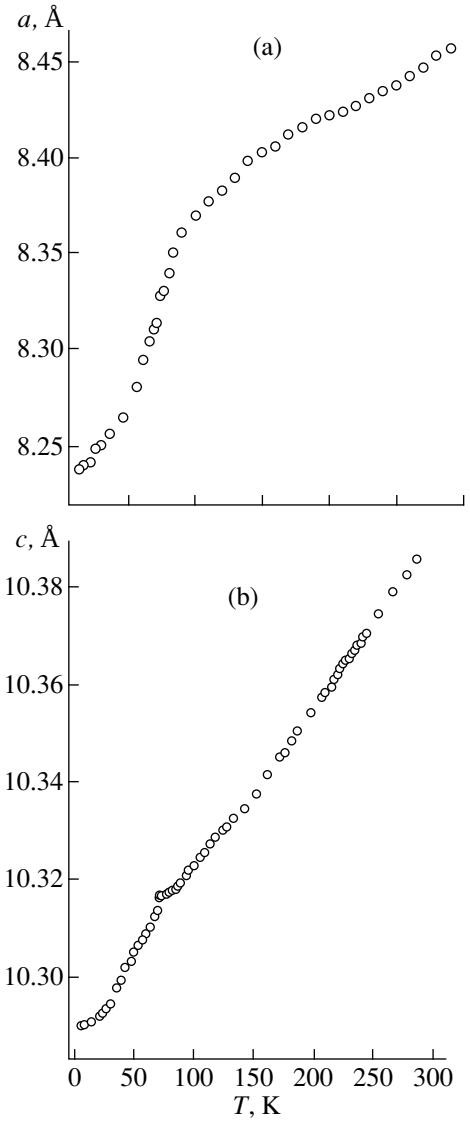

Fig. 5. Temperature dependences of the unit-cell parameters (a) *a* and (b) *c*.

Then the sample was studied on a two-circle Siemens *D*500 diffractometer (CuK_α radiation) adapted to the studies of individual planes in the reciprocal space. We examined (0*kl*) and (*h*0*l*) planes in the reciprocal space. The appearance of the superstructural (1, 0, 8.5) reflection is seen in Fig. 3. Thus, the phase transition at T_{c1} = 86 K observed earlier [3] is really associated with the doubling of the *c* parameter. In going through T_{c1}, neither doubling nor any changes in the reciprocal-lattice geometry were observed. According to the NQR data [3], one of the I^{127} lines is split into a triplet, whereas the second line showed no splitting in this phase transition. Comparing the X-ray diffraction and NQR data, one can assume that splitting of one iodine line is indicative to splitting of the iodine-atom position without the change of the trigonal symmetry.

Studies of the crystal on a two-circle diffractometer revealed a new system of superstructural reflections (h, k + 1/2, l + 1/2) below T = 78 K. The detailed examination of the (h, k + 1/2, l + 1/2) reflection showed that these satellite reflections should be attributed to the phase incommensurate in the temperature range from 78 to 73 K and that, in fact, their indices should be written as (h, k + 1/2 + δ, l + 1/2). The temperature dependence of the incommensurability parameter is shown in Fig. 4. At T = 73 K, we have δ = 0 and the satellite reflections indicate the formation of a commensurate phase. This phase transition is also seen on the curves of physical properties of these crystals [3]. We established that it is a first-order phase transition, which is also confirmed by the behavior of the structure parameters (Fig. 5).

ACKNOWLEDGMENTS

This study was supported by the Swiss National Science Foundation (grant no. 7SUPJ48718) and INTAS (grant no. 97-0177).

REFERENCES

1. B. Chabot and E. Parthe, Acta Crystallogr., Sect. B: Struct. Crystallogr. Cryst. Chem. **B34**, 645 (1978).
2. S. V. Kun, V. B. Lazarev, E. Yu. Peresh, *et al.*, Neorg. Mater. **29** (3), 410 (1993).
3. I. P. Aleksandrova, A. A. Sukhovskiĭ, J. J. Melero, *et al.*, Fiz. Tverd. Tela (St. Petersburg) **39** (5), 946 (1997) [Phys. Solid State **39**, 846 (1997)].
4. U. H. Zucker, E. Perenthaler, W. F. Kuhs, *et al.*, J. Appl. Crystallogr. **16** (3), 358 (1983).
5. V. Petricek, *Computing System JANA93*, Ed. by C. Novak (Institute of Physics, Academy of Sciences of the Czech Republic, Prague, 1993).
6. XABS2: An Empirical Absorption-Correction Program, S. Parkin, B. Moezzi, and H. Hope, J. Appl. Crystallogr. **28**, 53 (1995).
7. *International Tables for X-ray Crystallography* (Kynoch, Birmingham, 1974), Vol. 4.
8. L. A. Muradyan, M. I. Sirota, I. P. Makarova, and V. I. Simonov, Kristallografiya **30** (2), 258 (1985) [Sov. Phys. Crystallogr. **30**, 148 (1985)].
9. W. C. Hamilton, Acta Crystallogr. **18**, 502 (1965).
10. A. V. Arakcheeva, M. S. Novikova, A. I. Zaĭtsev, and G. U. Lubman, Zh. Strukt. Khim. **40** (4), 705 (1999).
11. V. I. Andrianov, Kristallografiya **34** (6), 592 (1989) [Sov. Phys. Crystallogr. **34**, 352 (1989)].
12. N. Walker and D. Stuart, Acta Crystallogr., Sect. A: Found. Cryslallogr. **A39**, 158 (1983).
13. B. Sh. Bagautdinov, M. S. Novikova, I. P. Aleksandrova, *et al.*, Solid State Commun. **111**, 361 (1999).

Translated by T. Safonova

Crystallography Reports, Vol. 46, No. 1, 2001, pp. 30–32. Translated from Kristallografiya, Vol. 46, No. 1, 2001, pp. 37–39.

STRUCTURE OF INORGANIC COMPOUNDS

Crystal Structure of High-Manganese Tinzenite from the Falotta Deposit in Switzerland

E. L. Belokoneva, A. N. Goryunova, P. A. Pletnev, and É. M. Spiridonov

Faculty of Geology, Moscow State University, Vorob'evy gory, Moscow, 119899 Russia

e-mail: elbel@geol.msu.ru

Received March 4, 1999

Abstract—The crystal structure of the natural high-manganese tinzenite of the axinite group has been refined. Using precision X-ray diffraction data, the fine details of the "isomorphous ratios" for atoms occupying the cationic positions were revealed. The final structural formula of the mineral is determined as $(Mn_{0.88}Mg_{0.03}Fe_{0.09})(Ca_{0.925}Mn_{0.075})$ $(Ca_{0.495}Mn_{0.505})(Al_{0.9}Fe_{0.1})(Al_{0.98}Fe_{0.02})[BSi_4O_{15}](OH)$. Examination of the isomorphous ratios provided the refinement of the classification of the axinite group. © *2001 MAIK "Nauka/Interperiodica".*

INTRODUCTION

The axinite group involves a series of isomorphous members—ferroaxinite $Ca_2Fe^{+2}Al_2BSi_4O_{15}(OH)$, magnesioaxinite $Ca_2MgAl_2BSi_4O_{15}(OH)$, manganaxinite $Ca_2MnAl_2BSi_4O_{15}(OH)$, and tinzenite $(Ca,Mn)_3Al_2BSi_4O_{15}(OH)$. The composition of axinite, after which the whole group is named, is intermediate between those of ferro- and manganaxinite and described by the formula $Ca_2(Fe_{0.5}Mn_{0.5})Al_2Si_4BO_{15}(OH)$. The diverse isomorphous inclusions of various elements result in the various colors of axinites—from deep brown, lilac, and red-violet to pale blue and almost colorless. The triclinic structure is characterized by five octahedral positions occupied by larger cations (Ca(1,2), Fe, and Al(1,2)) and five tetrahedral positions occupied smaller cations (Si(1–4) and B), which provides the complex character of isomorphous replacements and makes it necessary to perform the X-ray diffraction study of these minerals having different compositions in order to confirm the above-mentioned mineralogical classification. The crystal structure of axinite was established in [1]. The isomorphous ratios were investigated for axinite from Mexico [2], $Ca_2(Fe_{0.55}Mn_{0.13}Mg_{0.185})Al_2BSi_4O_{15}(OH)$. It was established that the Fe,Mn-position is occupied only partly and that Fe can enter the Al(1) position. Earlier, we studied low-manganese tinzenite (severgenite) with the molecular formula $Ca_{1.80}Mn^{2+}_{1.20}Mg_{0.10}Fe^{3+}_{0.20}Al_{1.80}Si_4BO_{15}(OH)$ [3]. In the latter mineral, Mn^{2+} ions together with a small amount of Mg atoms almost completely occupy the octahedral positions, and a small excess of Mn^{2+} ions is "isomorphically incorporated" into the Ca(1,2) positions. Both these positions have the same occupancy. It was also established that Fe^{3+} ions isomorphically replace Al in the octahedral positions.

Thus, we decided to examine the redistribution of Mn atoms over various positions in the structure with a higher Mn content, i.e., the structure of high-manganese tinzenite.

EXPERIMENTAL AND STRUCTURE REFINEMENT

High-manganese tinzenite occurs in metamorphogenetic quartz veins crosscutting metamorphosed manganese-bearing rocks (gondites) of prehnite–pumpellyite and greenschist facies in deposits of the southern Urals, Central Kazakhstan, Japan, and the western European Alps. Tinzenite with the highest manganese content was found in a number of deposits in the Graubünden canton (Switzerland), from which the tinzenite holotype derives. We studied a tinzenite specimen from the Falotta deposit from the Pekov collection.

High-manganese tinzenite from the Falotta deposit constitutes flattened brownish yellow and brownish orange crystals in quartz. Its optical characteristics are characteristic of the axinite group. The chemical composition of tinzenites varies from $Ca_{1.64}Mn^{2+}_{1.30}Fe_{0.10}$ to $Ca_{1.23}Mn^{2+}_{1.67}Fe_{0.10}$. We studied the structure of tinzenite, which is abundant in Falotta. This mineral has the following composition (wt %): SiO_2, 41.17; Al_2O_3, 16.51; Fe_2O_3, 1.93; FeO, 1.11; MnO, 17.75; MgO, 0.21; CaO, 13.65; Σ = 92.33 (a Camscan microprobe with a Link 1000 energy-dispersion attachment, the analysis was performed by E.V. Guseva). The Fe^{3+} and Fe^{2+} contents were calculated from the tinzenite stoichiometry. The molecular formula of the mineral is

Coordinates of the basis atoms and atomic thermal parameters in the structure of high-manganese tinzenite

Atom	*x/a*	*y/b*	*z/c*	B_{eq}, Å^2	Atom	*x/a*	*y/b*	*z/c*	B_{eq}, Å^2
Mn(1)*	0.76444(7)	0.59653(5)	0.10811(5)	0.761(9)	O(4)	0.1320(3)	0.3796(2)	0.3768(2)	0.89(4)
Ca(1)	0.74863(3)	0.34796(6)	0.39567(6)	0.79(1)	O(5)	0.0240(3)	0.2408(2)	0.5669(2)	0.66(4)
Ca(2)	0.18243(7)	0.09821(5)	0.08194(6)	0.765(9)	O(6)	0.3287(3)	0.3790(2)	0.6495(2)	0.58(4)
Al(1)	0.0505(1)	0.80208(9)	0.25116(9)	0.51(1)	O(7)	0.3815(3)	0.1279(2)	0.4968(2)	0.57(4)
Al(2)	0.3501(1)	0.93754(9)	0.41979(9)	0.50(2)	O(8)	0.5450(3)	0.3455(2)	0.8789(2)	0.60(4)
Si(1)	0.2106(1)	0.44713(9)	0.23749(8)	0.48(1)	O(9)	0.8845(3)	0.1498(2)	0.9394(2)	0.68(4)
Si(2)	0.2196(1)	0.27535(8)	0.52642(8)	0.42(1)	O(10)	0.7752(3)	0.3674(2)	0.1410(2)	0.84(4)
Si(3)	0.7066(1)	0.25565(9)	0.01412(8)	0.49(1)	O(11)	0.6038(3)	0.1382(2)	0.0877(2)	0.94(4)
Si(4)	0.6376(1)	0.02065(8)	0.22794(8)	0.46(1)	O(12)	0.4302(3)	0.9849(2)	0.2394(2)	0.73(4)
B(1)	0.4594(4)	0.6334(3)	0.2853(3)	0.46(5)	O(13)	0.7202(3)	0.0981(2)	0.3841(2)	0.59(4)
O(1)	0.0589(3)	0.6029(2)	0.1860(2)	0.63(4)	O(14)	0.7883(3)	0.8733(2)	0.1729(2)	0.71(4)
O(2)	0.2296(3)	0.3288(2)	0.1040(2)	0.94(4)	O(15)	0.3235(3)	0.7468(2)	0.3533(2)	0.55(4)
O(3)	0.4203(3)	0.4841(1)	0.3130(2)	0.67(4)	O(16)	0.0936(3)	0.9985(2)	0.3205(2)	0.63(4)

* Mn(1) = 0.88Mn + 0.03Mg + 0.09Fe; Ca(1) = 0.925Ca + 0.075Mn; Ca(2) = 0.495Ca + 0.505Mn; Al(1) = 0.90Al + 0.10Fe; Al(2) = 0.98Al + 0.02Fe.

$Ca_{1.42}Mn^{2+}_{1.46}Mg_{0.03}Fe^{2+}_{0.09}Al_{1.88}Fe^{3+}_{0.12}Si_{4.00}BO_{15}(OH)_{1.03}$.

The formula was calculated under the assumption of a constant boron content. The amount of water was calculated from the valence balance.

The X-ray from a $0.25 \times 0.25 \times 0.15$-mm-large isometric grain diffraction data for high-manganese tinzenite were collected on a Syntex $P\bar{1}$ diffractometer (λMoK_α radiation, graphite monochromator, $2\theta/\theta$ scanning technique; the scan rate ranged within 2–24 deg/min; $\sin\theta/\lambda \le 1.1$Å^{-1}, 4882 independent nonzero reflections). The parameters of the triclinic unit cell (a = 7.154(4) Å, b = 9.126(6) Å, c = 8.949(5) Å, α = 91.88(5)°, β = 98.80(4)°, γ = 77.05(5)°) satisfactorily agree with the data reported in [2, 3]. The coordinates of the basis atoms were taken from [3] and then were refined by the least squares method in the anisotropic approximation using the CSD program package; the weighting scheme was $1/w = \sigma^2(F) + 0.0002F^2$; $F > 5\sigma(F)$.

Similar to the structure of low-manganese tinzenite [3], the isomorphous ratios were analyzed with the use of mixed atomic scattering curves by setting various compositions in the cationic positions proceeding from the data on the chemical composition of the specimen of the new phase. Because of a high manganese content, it should necessarily enter all the three large-cationic positions. As earlier, it was assumed that Fe atoms replace Al atoms in the octahedral positions of smaller atoms. The tetrahedral positions of Si and B atoms are completely occupied both in low- and high-manganese tinzenites. When determining the isomorphous distribution of atoms over the positions in the crystal structure, we tried to achieve the best agreement between the structural formula and the data of the chemical analysis; the best agreement between the interatomic distances in polyhedra and the radii of the cations in these polyhedra; the reasonable values of the thermal parameters of the atoms in the corresponding positions, and the optimum refinement parameters (R, R_w, and S).

Not going into details of the computations, we indicate here only the final crystallochemical formula of the specimen under study, which can be written as $(Mn_{0.88}Mg_{0.03}Fe_{0.09})(Ca_{0.925}Mn_{0.075})(Ca_{0.495}Mn_{0.505}) \times (Al_{0.9}Fe_{0.1})(Al_{0.98}Fe_{0.02})[BSi_4O_{15}](OH)$. The refinement yielded R = 0.0417, R_w = 0.0417, S = 1.5. The coordinates of the basis atoms and their thermal parameters are given in the table.

RESULTS AND DISCUSSION

According to [1, 2], one can single out in the tenzenite structure an isolated borosilicate tetrahedral polyradical $[B_2Si_8O_{30}]$. This radical consists of four diortho groups $[Si_2O_7]$ linked via two B tetrahedra. In this radical, it is possible to separate a six-membered ring consisting of four Si tetrahedra and two B tetrahedra. As mentioned above, the structures of the minerals of the axinite group contain three positions of large cations. Two of these positions are occupied by Ca [1, 2] or (Ca,Mn) [3] atoms, whereas the third position is occupied by (Fe,Mn) [1] or (Fe,Mg,Mn) [2] atoms. In the low-manganese tinzenite [3], the (Fe,Mg,Mn) position, like that in the mineral described in [2], is occupied only partly by Mn and Mg atoms and has the composition $(Mn_{0.85}Mg_{0.1}\square_{0.05})$. In high-manganese tinzenite, this position (Mn(1)) differs from the corresponding position in low-manganese tinzenite—it is not fully occupied by a larger number of Mn atoms and a small amount of Fe atoms but has composition

$Mn_{0.88}Mg_{0.03}Fe_{0.09}$. In all the specimens, this position considerably differed from the other two Ca(1,2) positions—it had shorter interatomic distances correlating with the average ionic radii (the ionic radii of Mn, Mg, and Fe are smaller than the ionic radius of Ca). In the crystals under study, the Mn(1)–O distances range within 2.047–2.610(6), with the average distance being 2.237 Å. In [1], it was justly assumed that Mn atoms can isomorphically replace the atoms in the Ca(1,2) positions if the Mn content in the chemical formula exceeds unity, which is the case in tinzenites. However, these positions cannot be completely occupied by Mn atoms because of distortions occurring in the diortho group of a borosilicate radical, which shares the elongated edges with the trigonal-antiprismatic polyhedra of Ca(1,2). In the high-manganese tinzenite, Mn atoms isomorphically replace Ca atoms in two other positions of large cations. The compositions of these positions are Ca(1) = 0.925Ca + 0.075Mn and Ca(2) = 0.495Ca + 0.505Mn. Thus, the first position is occupied mainly by Ca atoms, and the second position is almost equally occupied by Ca and Mn atoms (in low-manganese tinzenite [3], both these positions are occupied in the same ratio by Mn and Ca atoms, 0.825Ca + 0.175Mn). The interatomic distances confirm that the distribution is isomorphic and that the Mn atoms prefer the Ca(2) position. The Ca(1)–O distances range within 2.331–2.853(5) Å; the average value is 2.476 Å. The Ca(2)–O distances range within 2.170–2.884(6) Å; the average value is 2.408 Å. Thus, the Mn content in high-manganese tinzenite seems to be the possible for the mineral type of tinzenite (which follows from the dimension factor necessary to preserve the structure). Similar to the structure described in [3], in the structure of high-manganese tinzenite there is only a small amount of Fe^{3+} ions, which isomorphically replace Al atoms in the octahedral Al(1,2) positions. The Al(1)–O and Al(2)–O distances range within 1.868–1.987(5) and 1.861–1.954(5) Å, and the average values are 1.915 and 1.900 Å, respectively.

Similar to the structure of low-manganese tinzenite (severgenite) and all the minerals of the axinite group, the structure of high-manganese tinzenite from the Falotta deposit has one hydrogen atom bound to the O(16) atom to form the hydroxyl group. The hydrogen bond is directed from the O(13) atom toward the O(16) atom, i.e., from the terminal atom of an isolated $[B_2Si_8O_{30}]$ polyradiron toward the oxygen atom of the Ca polyhedron. The length of this bond is 2.795 Å. The position of the H atom coincides with that reported in [2, 3].

ON CLASSIFICATION OF MINERALS OF THE AXINITE GROUP

X-ray diffraction analysis of axinites and the revision of the abundant chemical analysis data showed that the divalent Fe + Mn + Mg atoms occupy a special position, whereas Ca atoms occupy two other positions of large cations in the structures of the axinite-group minerals. In accordance with new approaches to the mineral classification, ferroaxinite, magnesioaxinite, and manganaxinite should be referred to as axinite-(Fe), axinite-(Mg), and axinite-(Mn), respectively.

The color of all the tinzenite varies from yellow to orange. The genetic conditions of occurrence of various tinzenites are also similar. According to the commonly used nomenclature, the tinzenite formula is written as $(Ca,Mn,Fe)_3[Al_2BSi_4O_{15}](OH)$. The boundary between axinite-(Mn) and tinzenite [4] is set by the formula coefficient of 1.5 for Mn atoms. In our opinion, this classification is erroneous because of the following reasons. The maximum number of Mn atoms in tinzenite corresponds to the formula coefficient ranging within 1.5–1.7, i.e., to the composition $Mn_{1.5–1.7}Ca_{1.5–1.3}$. This agrees with the stability factor of the structure, which "forbids" the composition Mn_2Ca_1. High- and low-manganese tinzenites are structurally similar: the Mn atoms are distributed over all three positions of large cations in distinction from axinite, where the Mn atoms are located only in one of the three positions. Therefore, the true tinzenite formula should be written as $Mn(Ca,Mn)_2Al_2[BSi_4O_{15}](OH)$. The boundary between axinite-(Mn) and tinzenite should be determined by the formula coefficient equal to 1 for Mn atoms.

ACKNOWLEDGMENTS

This study was supported by the Russian Foundation for Basic Research, project no. 98-05-64762.

REFERENCES

1. Y. Takeuchi, T. Ozawa, T. Ito, *et al.*, Z. Kristallogr. **140** (5/6), 289 (1974).
2. S. Swinnea, H. Steinfink, L. E. Rendon-Diaz Miron, and S. Enciso de le Vega, Am. Mineral. **66**, 428 (1981).
3. E. L. Belokoneva, P. A. Pletnev, and É. M. Spiridonov, Kristallografiya **42** (6), 1010 (1997) [Crystallogr. Rep. **42**, 934 (1997)].
4. M. Fleischer, *Glossary of Mineral Species* (Mineralogical Record, Tucson, 1987).

Translated by T. Safonova

Crystallography Reports, Vol. 46, No. 1, 2001, pp. 33–39. Translated from Kristallografiya, Vol. 46, No. 1, 2001, pp. 40–46.

STRUCTURE OF COORDINATION COMPOUNDS

Crystal Structure of [*N*-(2-Carbamoylethyl)iminodiacetato]-Aqua(1,10-phenanthroline)cobalt(III) Chloride 3.5 Hydrate

G. G. Sadikov*, A. L. Poznyak, A. S. Antsyshkina*, and V. S. Sergienko***

** Kurnakov Institute of General and Inorganic Chemistry, Russian Academy of Sciences, Leninskiĭ pr. 31, Moscow, 117907 Russia*

*** Institute of Molecular and Atomic Physics, Belarussian Academy of Sciences, pr. F. Skoriny 70, Minsk, 220072 Belarus*

e-mail: asants@ion.chran.rinet.ru

Received February 22, 1999

Abstract—The crystal structure of [*N*-(2-carbamoylethyl)iminodiacetato]-aqua(1,10-phenanthroline)cobalt(III) chloride 3.5 hydrate [Co(*Ceida*)(H_2O)(*Phen*)Cl · $3.5H_2O$ (**I**) has been determined by ^{1}H NMR technique and X-ray diffraction analysis. The crystals are triclinic, a = 10.352(2) Å, b = 12.534(3) Å, c = 20.665(4) Å, α = 107.02(3)°, β = 92.22(3)°, γ = 111.63(3)°, Z = 4, space group $P\bar{1}$, and R = 0.0438. The unit cell involves two crystallographically nonequivalent but virtually identical cationic complexes [Co(*Ceida*)(H_2O)(*Phen*)]$^+$. The tridentate chelate ligand *Ceida*$^{2-}$ (N + 2O) occupies the face in the coordination octahedron of the Co atom, and the propionamide group remains free. The mean bond lengths are as follows: Co–O_{Ceida}, 1.876 Å; Co–N_{Ceida}, 1.981 Å; Co–N_{Phen}, 1.945 Å; and Co–O_w, 1.915 Å. In the structure, the arrangement of cationic complexes and certain water molecules exhibits a pseudosymmetry (the 2_1 axis). The cations and water molecules are located in the layers, and the anions are arranged between the layers. The structural elements are linked by hydrogen bonds and van der Waals interactions. © *2001 MAIK "Nauka/Interperiodica".*

INTRODUCTION

The structure of the sole cobalt(III) complex with the *N*-(2-carbamoylethyl)iminodiacetate ion $NH_2C(O)CH_2CH_2N(CH_2CO_2^-)_2$ (*Ceida*), namely, *trans*-(*N*)-[Co(*Ceida*)$_2$]$^-$, has already been described [1]. In this complex, the propionamide groups of both ligands are not involved in the coordination, even though the *Ceida*$^{2-}$ ion can act as a tetradentate ligand at the expense of the oxygen or nitrogen atoms of the carbamoyl group (in the latter case, the ionization of the carbamoyl group should be expected). In the present work, the mixed-ligand Co(III) complex with the *Ceida*$^{2-}$ ion, additional H_2O ligands, and 1,10-phenanthroline, namely, [Co(*Ceida*)(H_2O)(*Phen*)]Cl · $3.5H_2O$ (**I**), was synthesized and then characterized by ^{1}H NMR technique, electronic spectroscopy, and X-ray diffraction.

EXPERIMENTAL

Synthesis. H_2*Ceida* acid was synthesized according to the procedure described in [2]. $NaHCO_3$ was added to a mixture of $Co(CH_3CO_2)_2 \cdot 4H_2O$ and H_2*Ceida* (at a ratio of 1 : 1) until a weakly alkaline solution (pH 7.5) was obtained. The mixture was oxidized by hydrogen peroxide, and an equivalent of 1,10-phenanthroline (*Phen*) and activated carbon were added. Then, the mixture was heated to 50°C with stirring until the solution color changed from violet to red. Carbon was filtered off, and a filtrate was passed through a column with Sephadex SP-25 in the H^+ form. Upon elution with a HCl solution (0.05 mol/l), a reddish violet band of singly charged cations began to move, followed by a rose band of doubly charged cations (most likely, Co^{2+}) and a yellow band of [Co*Phen*$_3$]$^{3+}$ ions remained in the initial part of the column. An eluate of the first band was taken, because the presence of mixed-ligand complexes could be expected only in this eluate. The eluate was concentrated on a vacuum evaporator (at temperatures below 50°C), and a reddish violet crystalline compound precipitated. According to the results of further investigations, the formula [Co(*Ceida*)(H_2O)(*Phen*)]Cl · $3.5H_2O$ (**I**) was assigned to this compound. Crystals for the X-ray structure analysis were obtained by low cooling of a warm saturated solution.

The ^{1}H NMR spectra were recorded on a Bruker WM 360 instrument (frequency, 360 MHz) in D_2O with *tert*-butanol as an internal standard (1.23 ppm).

X-ray structure analysis. Crystals **I** are triclinic, a = 10.352(2) Å, b = 12.534(3) Å, c = 20.665(4) Å, α = 107.02(3)°, β = 92.22(3)°, γ = 111.63(3)°, V = 2350.7(9) Å^3, M = 2231.3, F(000) = 1156, ρ_{calcd} = 1.576 g/cm^3, μ_{Mo} = 0.9 mm^{-1}, Z = 4, and space group $P\bar{1}$.

The experimental data (4312 reflections) were collected on a Syntex $P2_1$ diffractometer (λMoK_α, graphite monochromator, $\theta/2\theta$ scan mode, $2\theta_{max}$ = 54°).

Table 1. Atomic coordinates and thermal parameters U_{eq}

Atom	*x*	*y*	*z*	U_{eq}, Å^2
Co(1)	0.08940(8)	0.34878(7)	0.14380(4)	0.0254(2)
Co(2)	0.73769(8)	0.64690(8)	0.34972(4)	0.0294(2)
C1(1)	−0.0521(2)	0.1114(2)	0.2621(1)	0.0578(5)
C1(2)	−0.4447(2)	0.1285(2)	−0.1825(1)	0.0664(6)
N(1*A*)	0.2556(5)	0.4888(4)	0.1405(2)	0.023(1)
N(2*A*)	0.7426(6)	0.6182(6)	0.1029(3)	0.051(2)
N(3*A*)	0.0753(5)	0.2487(4)	0.0496(2)	0.029(1)
N(4*A*)	0.2010(5)	0.2644(5)	0.1656(3)	0.030(1)
O(1*A*)	0.0986(4)	0.4372(4)	0.2358(2)	0.035(1)
O(2*A*)	0.2122(5)	0.6186(4)	0.3151(2)	0.044(1)
O(3*A*)	−0.0214(4)	0.4242(4)	0.1187(2)	0.037(1)
O(4*A*)	−0.0077(5)	0.5830(5)	0.0879(3)	0.054(1)
O(5*A*)	0.5851(5)	0.4362(4)	0.0364(2)	0.045(1)
C(1*A*)	0.2008(6)	0.5435(6)	0.2588(3)	0.036(2)
C(2*A*)	0.3116(6)	0.5673(5)	0.2138(3)	0.031(1)
C(3*A*)	0.0463(7)	0.5200(6)	0.1041(3)	0.037(2)
C(4*A*)	0.2006(6)	0.5504(6)	0.1021(3)	0.032(1)
C(5*A*)	0.3707(5)	0.4601(5)	0.1074(3)	0.028(1)
C(6*A*)	0.5002(6)	0.5709(6)	0.1122(3)	0.031(1)
C(7*A*)	0.6124(6)	0.5341(6)	0.0801(3)	0.031(1)
C(8*A*)	0.0004(7)	0.2388(6)	−0.0067(4)	0.042(2)
C(9*A*)	0.0004(9)	0.1588(7)	−0.0710(4)	0.055(2)
C(10*A*)	0.0822(9)	0.0957(7)	−0.0762(4)	0.061(2)
C(11*A*)	0.1628(7)	0.1035(6)	−0.0174(4)	0.051(2)
C(12*A*)	0.2500(9)	0.0393(7)	−0.0136(5)	0.067(3)
C(13*A*)	0.3138(8)	0.0470(7)	0.0452(5)	0.062(2)
C(14*A*)	0.2965(7)	0.1184(6)	0.1096(4)	0.046(2)
C(15*A*)	0.3539(7)	0.1279(7)	0.1740(5)	0.059(2)
C(16*A*)	0.3326(8)	0.2036(7)	0.2316(4)	0.056(2)
C(17*A*)	0.2572(6)	0.2723(6)	0.2257(4)	0.041(2)
C(18*A*)	0.2183(6)	0.1876(5)	0.1078(4)	0.034(1)
C(19*A*)	0.1517(6)	0.1791(5)	0.0454(3)	0.033(1)
N(1*B*)	0.7780(5)	0.5044(4)	0.3514(3)	0.028(1)
N(2*B*)	1.1620(5)	0.3921(5)	0.3857(3)	0.047(2)
N(3*B*)	0.8281(6)	0.7443(5)	0.4433(3)	0.036(1)
N(4*B*)	0.9189(5)	0.7309(5)	0.3254(3)	0.032(1)
O(1*B*)	0.6523(4)	0.5586(4)	0.2585(2)	0.037(1)
O(2*B*)	0.5998(5)	0.3818(4)	0.1772(2)	0.045(1)
O(3*B*)	0.5640(4)	0.5736(4)	0.3766(3)	0.045(1)
O(4*B*)	0.4357(5)	0.4097(5)	0.4019(3)	0.063(2)
O(5*B*)	1.1595(5)	0.5564(5)	0.4654(2)	0.050(1)

Table 1. (Contd.)

Atom	*x*	*y*	*z*	U_{eq}, Å^2
C(1*B*)	0.6608(6)	0.4550(6)	0.2334(3)	0.031(1)
C(2*B*)	0.7584(6)	0.4301(5)	0.2772(3)	0.033(1)
C(3*B*)	0.5444(6)	0.4742(7)	0.3880(3)	0.040(2)
C(4*B*)	0.6683(6)	0.4384(6)	0.3867(4)	0.036(2)
C(5*B*)	0.9219(6)	0.5332(6)	0.3866(3)	0.029(1)
C(6*B*)	0.9491(7)	0.4221(6)	0.3858(3)	0.034(1)
C(7*B*)	1.1006(6)	0.4633(6)	0.4160(3)	0.034(1)
C(8*B*)	0.7745(8)	0.7509(7)	0.5013(4)	0.048(2)
C(9*B*)	0.859(1)	0.8247(8)	0.5647(4)	0.064(2)
C(10*B*)	0.998(1)	0.8930(8)	0.5680(4)	0.069(3)
C(11*B*)	1.0548(9)	0.8917(7)	0.5085(4)	0.053(2)
C(12*B*)	1.196(1)	0.9621(8)	0.5044(5)	0.066(2)
C(13*B*)	1.2409(8)	0.9582(7)	0.4457(6)	0.068(3)
C(14*B*)	1.1529(7)	0.8812(6)	0.3796(4)	0.047(2)
C(15*B*)	1.1911(8)	0.8742(7)	0.3148(5)	0.058(2)
C(16*B*)	1.0927(8)	0.7946(7)	0.2580(4)	0.053(2)
C(17*B*)	0.9576(7)	0.7243(6)	0.2652(3)	0.039(2)
C(18*B*)	1.0136(6)	0.8098(5)	0.3829(3)	0.032(1)
C(19*B*)	0.9652(7)	0.8158(6)	0.4456(3)	0.038(2)
O(*w*1)	−0.0765(4)	0.2202(4)	0.1495(2)	0.037(1)
O(*w*2)	0.6896(4)	0.7782(4)	0.3440(2)	0.039(1)
O(*w*3)	0.7235(5)	0.8422(4)	0.2291(3)	0.059(1)
O(*w*4)	0.4247(7)	0.7581(6)	0.5041(3)	0.087(2)
O(*w*5)	0.4655(5)	0.8076(5)	0.3826(3)	0.061(1)
O(*w*6)	0.4426(8)	0.9484(6)	0.6160(4)	0.103(2)
O(*w*7)	0.3444(7)	0.8655(5)	0.7249(3)	0.080(2)
O(*w*8)	−0.3354(7)	0.2395(6)	−0.0184(3)	0.079(2)
O(*w*9)	−0.3241(5)	0.1970(4)	0.1048(2)	0.044(1)

The structure was solved by the heavy-atom method using 4180 reflections with $I \geq 2\sigma(I)$. All the hydrogen atoms (except for one H atom of the *w*4 molecule, which is possibly disordered over two positions toward the *w*5 and *w*6 molecules) were located from the difference Fourier syntheses. The refinement (838 parameters) was performed by the full-matrix least-squares procedure in the anisotropic (isotropic for the H atoms) approximation according to the SHELXL93 software package [3]. The final values of R_1 were equal to 0.0438 (for the observed reflections) and 0.0449 (for all the reflections); wR_2 = 0.0848 and 0.0853, respectively; *GOOF* = 0.9; $\Delta\rho_{max}$ = 0.32 e Å^{-3}, and $\Delta\rho_{min}$ = –0.27 e Å^{-3}.

Table 1 lists the atomic coordinates and thermal parameters U_{eq}/U_{iso}. The coordinates of the hydrogen atoms are available from the authors.

RESULTS AND DISCUSSION

The preliminary data on the structure of compound **I** were obtained in the study of a solution of this compound by the ^{1}H NMR technique. The ^{1}H NMR spectrum contains the *AB*-type quartet (δ_A = 3.57 ppm, δ_B = 4.03 ppm, and J_{AB} = 16.4 Hz), which is typical of the $CH_2CO_2^-$ group. Moreover, the spectrum involves the A_2X_2-type doublet of triplets (1 : 2 : 1) at 1.76 and 2.34 ppm with J_{AX} = 7.3 Hz, which corresponds to the methylene protons of the propionamide group. Signals of both types have the same integrated intensity. Such a spectrum indicates that two acetate groups are equivalent, and the propionamide group is free (noncoordinated).

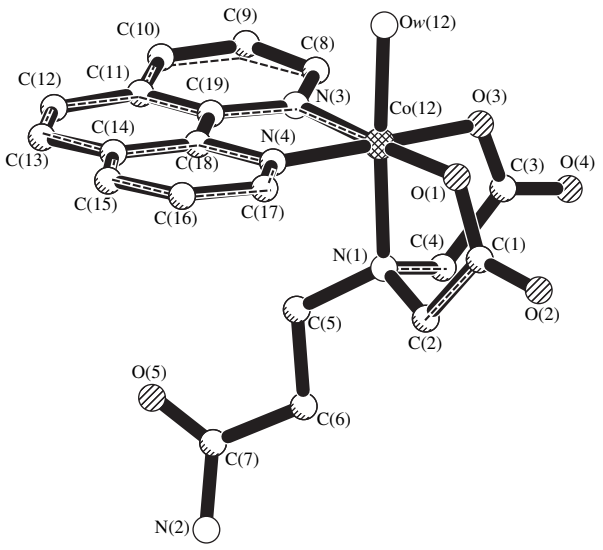

Fig. 1. Structures of the Co(1) (solid line) and Co(2) (dashed line) complexes.

The ^{1}H NMR spectrum of compound **I** also demonstrates that protons in halves of the *Phen* ligand are magnetically equivalent. Actually, the protons in the 2,2' and 4,4' positions exhibit partly overlapping doublets at 9.1 ppm; protons in the 3,3' positions are characterized by a quadruplet at 8.34 ppm; and protons in the 5,5' positions show a singlet at 8.41 ppm. In the case when halves of the ligand are nonequivalent, the singlet of protons in the 5,5' positions should transform into the *AB* quartet and the lines of the other protons should be doubled.

In complex **I**, the described properties of protons in the $Ceida^{2-}$ ion and the *Phen* molecule can be observed only in one variation of their arrangement around the Co(III) ion, namely, in the case when the oxygen atoms of the carboxyl groups and the nitrogen atom of the $Ceida^{2-}$ ligand occupy the octahedron face and the nitrogen atoms of the *Phen* ligand are located in the *trans* position with respect to the oxygen atoms. This isomer can be referred to as the symmetric face isomer.

The electronic absorption spectrum of the solution of compound **I** is consistent with the above conclusions and suggests that the sixth coordination site is occupied by the oxygen atom of a water molecule. This spectrum involves the 532-nm unsplit band associated with the $^1A_{1g} \longrightarrow {}^1T_{1g}$ transition, which corresponds to a cubic symmetry of the crystal field at the same set of the donor atoms (N and O) along three mutually perpendicular axes C_4 of the octahedron. If the sixth coordination site was occupied by the Cl^- ions rather than by H_2O molecules, the band of the $^1A_{1g} \longrightarrow {}^1T_{1g}$ transition would be observed at longer wavelengths and would gradually shift toward the short-wavelength range due to the aquation of the Cl^- ions.

The results of the spectroscopic investigation are in agreement with the X-ray diffraction data.

According to the X-ray structure analysis, the unit cell of compound **I** contains the Cl^- anions; crystallization water molecules; and two crystallographically nonequivalent cationic complexes $[Co(Ceida)(H_2O)(Phen)]^+$, whose parameters, however, are almost identical (Fig. 1).

The $Ceida^{2-}$ ligand in both complexes fulfills the tridentate chelate function, occupies the octahedron face, and coordinates the Co atom by the central nitrogen atom [Co–N(1), 1.975(5) and 1.988(5) Å] and two oxygen atoms of two acetate groups [Co–O(1), 1.879(4) and 1.868(4) Å and Co–O(3), 1.876(5) and 1.883(5) Å]. Similar distances are typical of iminodiacetate and other monoamine compounds of Co(III) (see [1, 4] and references therein).

In both complexes, the phenanthroline ligands [Co–N(3), 1.948(5) and 1.935(5) Å and Co–N(4), 1.948(6) and 1.951(6) Å] each involve three planar (within 0.01–0.02 Å) six-membered rings. However, the *Phen* molecule as a whole is not quite planar. Two peripheral rings and the central cycle form dihedral angles of 4.5° and 2.9° in the *A* complex and 1.6° and 2.3° in the *B* complex. In both cases, these rings deviate in the same direction [toward the vertex occupied by the N(1) atom]. A similar tendency for a change in the conformation of the *Phen* molecules toward a boat conformation was observed earlier, for example, in structures of the $[Ce(Phen)_4(CH_3CN)_2](ClO_4)_3 \cdot 3CH_3CN$ (two independent phenanthroline molecules) [5] and $[Eu\{CH_3(CH_2)_4COO\}_3(Phen)]$ [6] complexes and a free phenanthroline molecule [7].

The plane that coincides with the phenanthroline plane and passes through the O(1) and O(3) atoms can be considered an equatorial plane of the Co coordination octahedron in structure **I**. The water molecule [Co–O(*w*), 1.910(5) and 1.919(5) Å] and the N(1) nitrogen atom occupy the axial positions. The noncoordinated propionamide group of the *Ceida* ligand lies in the diagonal plane, which is perpendicular to the equatorial plane and virtually coincides with the plane of Fig. 1. The diagonal plane serves only as the internal symmetry plane of the complexes. The terminal carbamoyl groups deviate from the symmetry plane (by 28° and 38.5°).

The crystallographically nonequivalent cationic complexes in the crystal are related by the 2_1 pseudoaxis aligned along the *x*-axis of the crystal (Fig. 2). As can be seen from Fig. 2, the cationic complexes are grouped to form the layers parallel to the (012) plane, and the Cl^- anions are arranged in chains extended along the *x*-axis between the layers. The water molecules are predominantly located inside the layers and are omitted in Fig. 2, because they are virtually eclipsed by other atoms. It is evident that the crystal is formed by single layers separated by single interlayers.

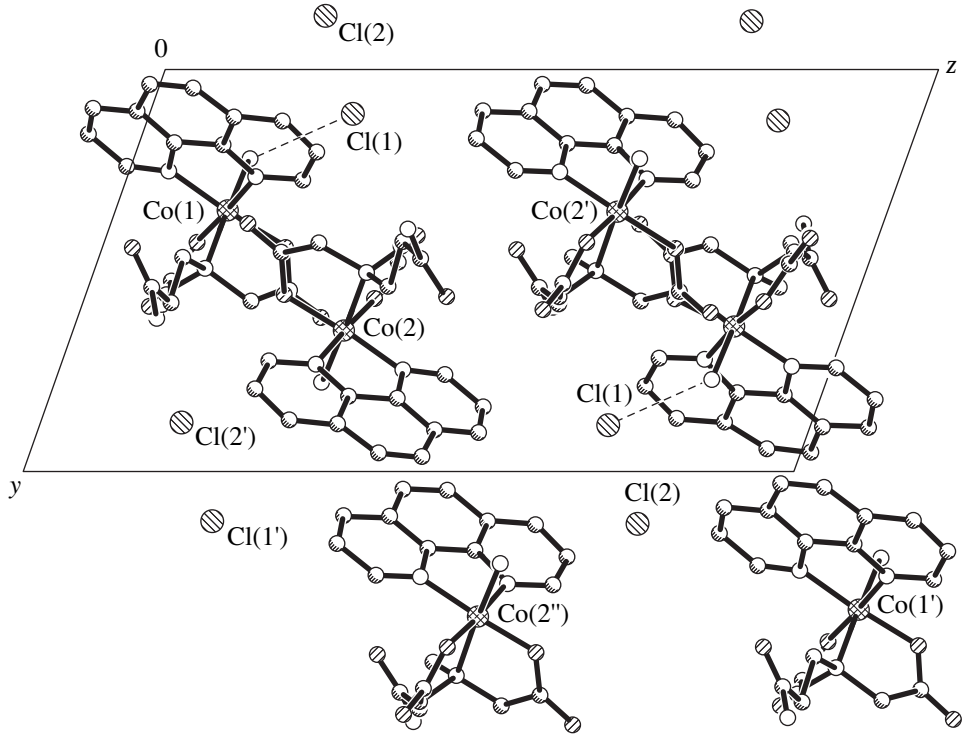

Fig. 2. Projection of the structure along the triclinic *x*-axis. Coordinates of the 2_1 unique pseudoaxis are (∞, 1/2, 1/4).

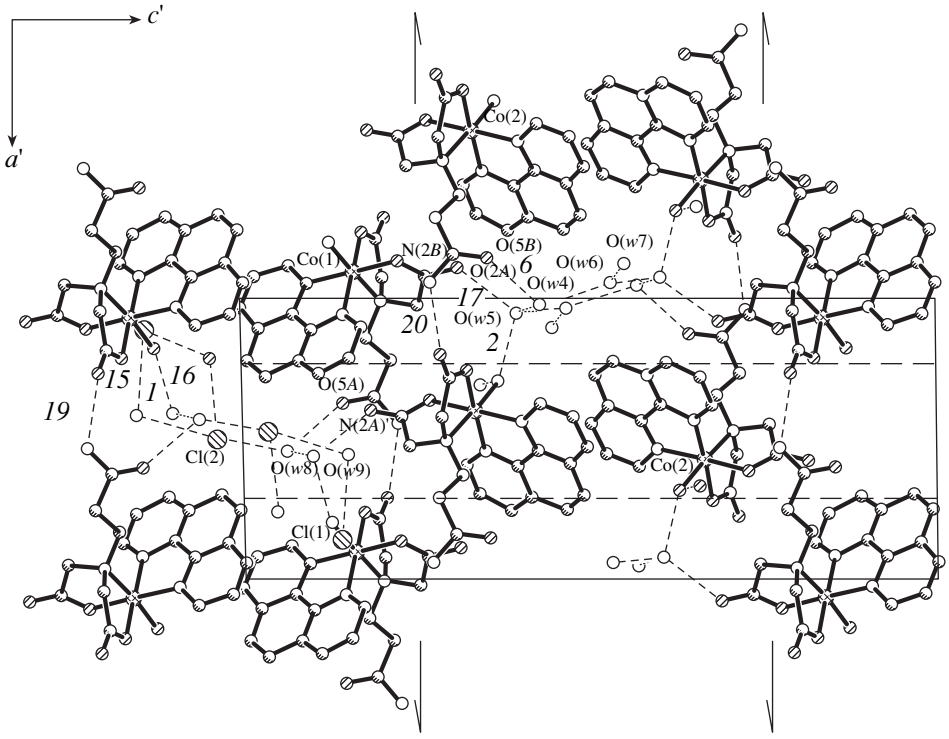

Fig. 3. Projection of the layer formed by the cationic complexes onto the (010) plane of the reference coordinate system. Numbering of hydrogen bonds matches that in Table 2.

Table 2. Geometric parameters of the hydrogen bonds and the shortest intermolecular contacts in structure **I**

No.	*A*–H ···*X** bond	Distance, Å			*AHX* angle, deg	Cell
		A ···*X*	*A*–H	H ···*X*		
1	O(*w*1)–H···O(*w*9)	2.57(2)	0.83(2)	1.75(2)	171(10)	*A***
2	O(*w*2)–H···O(*w*5)	2.60(2)	0.83(2)	1.77(1)	173(10)	*B*
3	O(*w*8)–H···O(*w*9)	2.76(2)	1.06(2)	1.73(2)	159(10)	*A*
4	O(*w*5)–H···O(*w*4)	2.75(1)	1.18(9)	1.60(9)	163(9)	*B*
5	O(*w*8)–H···O(5*a*)	2.83(1)	0.75	2.11	161(9)	*A*
6	O(*w*4)–H···O(5*b*)	2.86(1)	1.08(1)	1.85(1)	167(10)	*B*
7	O(*w*2)–H···O(*w*3)	2.72(1)	0.88(2)	1.84(2)	175(12)	*B*
8	O(*w*6)–H···O(*w*4)	2.75(2)	1.14(2)	1.64(2)	164(10)	*B*
9	O(*w*6)–H···O(*w*5)[1]	2.84(2)	0.97(2)	2.01(2)	140(10)	*B*
10	O(*w*7)–H···O(*w*6)	2.82(2)	1.15(2)	1.75(2)	150(10)	*B*
11	O(*w*1)–H···Cl(1)	3.06(1)	0.86(2)	2.21(2)	175(12)	*A*
12	O(*w*8)···Cl(2)	3.24(1)				*A*
13	O(*w*3)–H···Cl(1)	3.16(1)	0.86(2)	2.34(2)	159(12)	
14	O(*w*7)–H···Cl(2)	3.16(1)	0.94(2)	2.26(2)	160(12)	
15	O(*w*7)···Cl(1)	3.16(1)				
16	O(*w*3)–H···Cl(2)	3.19(1)	0.81(2)	2.41(2)	163(12)	
17	O(*w*5)–H···O(2*a*)	2.76(2)	0.58(2)	2.23(1)	154(10)	
18	O(*w*9)–H···O(2*b*)	2.77(1)	0.58(9)	2.20(9)	173(9)	
19	N(2*a*)–H···O(4*a*)	2.79(1)	0.64(2)	2.32(2)	132(12)	
20	N(2*b*)–H···O(4*b*)	2.76(1)	0.76(2)	2.06(2)	153(12)	
21	C(9*a*)···C(13*a*)[2]	3.50(1)				*A*
22	C(9*a*)···C(14*a*)[2]	3.53(1)				*A*
23	C(9*b*)···C(13*b*)[3]	3.30(1)				*B*
24	C(11*b*)···C(11*b*)[3]	3.40(1)				*B*
25	C(12*b*)···C(8*b*)[3]	3.54(1)				*B*

* Symmetry codes for the *X* atom: [1](1 – *x*, 2 – *y*, 1 – *z*), [2](–*x*, –*y*, –*z*), and [3](2 – *x*, 2 – *y*, 1 – *z*).
** The *A* cell consists of the Co(1) complexes, and the *B* cell is composed of the Co(2) complexes.

The translational periodicity of the Co(1) and Co(2) atoms along the *x*-axis to within 3σ corresponds to the presence of the 2_1 axis with a ratio of 0.49984(8) : 0.50026(8). For the N(2) atoms, which most strongly violate the internal symmetry of the complex, this ratio is 0.468 : 0.532.

The Cl(1) and Cl(2) atoms exhibit a stronger deviation from the symmetric arrangement: the ratio between the shifts along the 2_1 pseudoaxis is equal to 0.401 : 0.599. A further, very considerable violation of the symmetry is the absence of "vis-á-vis" for the *w*(6) molecule.

The crystal structure can be better understood with another unit cell defined using the matrix |1 0 0, 0 0 –1, 1 2 1| (|1 –0.5 0, 0 0.5 –1, 0 0.5 0| for the transformation of the atomic coordinates). In this case, the parameters of the unit cell (whose volume is doubled) are as follows: $a' = 10.352$ Å, $b' = 20.665$ Å, $c' = 25.524$ Å, $\alpha' = 120.43°$, $\beta' = 89.30°$, $\gamma' = 87.78°$, and space group $I\bar{1}$ (for a pseudomonoclinic analogue, *C*2/*c* in the *I*2/*c* setting). The 2_1 pseudoaxis is parallel to the *x*-axis and almost perpendicular to the (100) coordinate plane. In this setting, the layer of complexes lies in the (010) coordinate plane. This layer exhibits a cellular structure with cells in the form of tetragons built up of complexes of the same type [the *A* cell for Co(1) and the *B* cell for Co(2)]. A front projection of the layer is shown in Fig. 3. The complexes are related in pairs by the inversion centers and the *a*' translation. The bonds between the neighboring complexes in the cell are different in character: in one case, the short van der Waals contact occurs via strongly (by 2/3) overlapping phenanthroline molecules, and in the other case, the N(2) atoms and the terminal O(4) atoms of the carboxylate groups are linked by the hydrogen bonds (Table 2, hydrogen bonds 19, 20). The centrosymmetrically arranged water molecules are located in the central part of the cells.

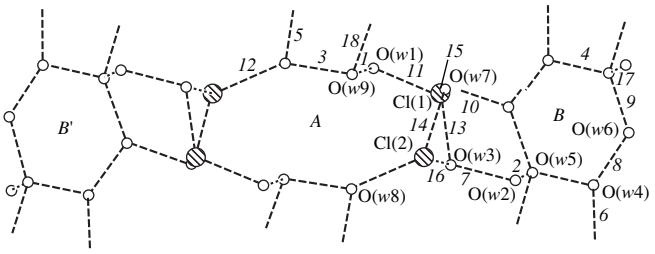

Fig. 4. A system of hydrogen bonds in aquachloro anion chains.

The 2_1 pseudoaxis and the inversion center in the structure give rise to one more pseudosymmetry element—the glide-reflection plane *c*. Thus, in the newly defined unit cell, the space group $P2_1/c$ with the special direction *a*' is realized within a particular layer. In this layer, the aforementioned cells *A* and *B* are equivalent, because they are related by the *c* plane.

The presence of the Cl^- ions, even if it slightly violates the crystal symmetry, does not affect the structure of a particular layer: only an insignificant redistribution of water molecules is observed and the adjacent layers are displaced relative to each other, thus lowering the crystal symmetry as a whole. Nonetheless, this does not affect the coordinated water molecules *w*1 and *w*2 (Table 2, hydrogen bonds 1, 2) and four molecules *w*4, *w*5, *w*8, and *w*9 (out of six water molecules), whose positions are determined by strong hydrogen bonds within the layer in the cells *A* (hydrogen bonds 3, 5) and *B* (hydrogen bonds 4, 6). In the *A* cell, in which no molecule equivalent to the *w*6 molecule occurs, one of the Cl^- anions forms the hydrogen bond with the coordinated water molecule *w*1 (hydrogen bond 11), and the other Cl^- anion forms the hydrogen bond with one of the water molecules (*w*8) contained in the *B* cell (hydrogen bond 12). Consequently, four Cl^- ions linked by the hydrogen bonds are located in the *A* cell. At the same time, the crystallization water molecules are concentrated in the *B* cell. Actually, apart from the *w*4 and *w*5 molecules equivalent to the *w*8 and *w*9 molecules of the *A* cell, the *B* cell contains the *w*6, *w*7, and *w*3 water molecules (hydrogen bonds 7–10), which form a hydroshell over the *B* cell.

The *w*6 molecule, which completely resides within the *B* cell, together with the *w*4 and *w*5 molecules, forms the characteristic six-membered rings (Fig. 3). In the crystal, the anionic moieties of the *A* cells [i.e., the Cl(1) and Cl(2) atoms] of one layer interact with hydroshells of the *B* cells of the adjacent layers to form hydrogen bonds 13–16. This results in the formation of aquachloro anion "rods," which penetrate the layers along the direction *y*' with a spacing of 20.66 Å at an angle of ~60° and pass alternately through the *A* and *B* cells (Fig. 4).

The mutual penetration of the lattices built up of the layer of cationic complexes and aqua anion rods is responsible for the strength of the crystal. The strength of the layers themselves, in which the van der Waals interactions are rather strong, is enhanced by hydrogen bonds (17 and 18) acting between the *A* and *B* cells.

ACKNOWLEDGMENTS

This work was supported in part by the Belarussian Foundation for Basic Research, project no. F98-243.

REFERENCES

1. F. Pavelchic, P. Novomesky, J. Soldanova, and T. N. Polinova, Collect. Czech. Chem. Commun. **53** (8), 1725 (1988).
2. A. S. Antsyshkina, G. G. Sadikov, V. S. Sergienko, and A. L. Poznyak, Zh. Neorg. Khim. **43** (2), 241 (1998).
3. G. M. Sheldrick, *SHELXL93: Program for the Refinement of Crystal Structures* (Univ. of Göttingen, Göttingen, 1993).
4. A. S. Antsyshkina, G. G. Sadikov, V. S. Sergienko, and A. L. Poznyak, Zh. Neorg. Khim. **42** (7), 1137 (1997).
5. L. Kh. Minacheva, L. S. Skogareva, G. A. Razgonyaeva, *et al.*, Zh. Neorg. Khim. **42** (12), 1990 (1997).
6. M. A. Poraĭ-Koshits, A. S. Antsyshkina, G. G. Sadikov, *et al.*, Zh. Neorg. Khim. **40** (5), 748 (1995).
7. S. Nishigani, H. Yoshika, and K. Nakatsu, Acta Crystallogr., Sect. B: Struct. Crystallogr. Cryst. Chem. **B34**, 875 (1978).

Translated by O. Borovik-Romanova

Crystallography Reports, Vol. 46, No. 1, 2001, pp. 4–12. Translated from Kristallografiya, Vol. 46, No. 1, 2001, pp. 10–18.

THEORY OF CRYSTAL STRUCTURES

In Memory of Linus Pauling

Parsimony

N. L. Smirnova

Moscow State University, Vorob'evy gory, Moscow, 119899 Russia

Received October 10, 1996

Abstract—Ordered isomorphism and parsimony are universal laws of nature. Consideration has been given to the ordered isomorphs in systems composed of crystal structures, cation charges in minerals, indices for dimensions of physical quantities, compositions of homomolecular structures, etc. It is shown that parsimony is a general law and nature is an "architect of sustained styles." *© 2001 MAIK "Nauka/Interperiodica".*

The present paper reports the results of system crystallogy research on the realization of the parsimony principle and ordered isomorphism.[1] The problems of parsimony and ordered isomorphism primarily concern the problem of choosing constituents into which a particular object can be decomposed or which can form an object.

In a broad sense, ordered isomorphism can be considered to mean an ordered differentiation–integration of compositions (qualitative and quantitative), spatial structures, and other systems at which heterotype compositions, structures, and other systems (consisting of two and more constituents) appear instead of single-type compositions, structures, etc. In this case, an ordering of constituents suggests ordered isomorphism, a statistical disordering of constituents implies disordered isomorphism, and a partial ordering–disordering of constituents is an indication of microscopic and macroscopic imperfection.

As early as the 5th century BC, Empedocles (484–424 BC) chose earth, water, air, and fire as constituents. More recently, Dalton (1766–1844) noted that ratios between constituents in chemical compounds are equal to small integers and the highest stability of compounds is achieved when the ratio of constituents is 1 : 1. Haüy (1743–1822) established that indices in symbols designating crystal faces are small integers. Bogdanov (1873–1928) [1] asserted that any object can be hierarchically separated into constituents, and the constituents of a certain next level (the number of levels is small) can qualitatively differ from the constituents of the higher levels. For example, a considerable number of electrons can be removed from an atom, but it remains the atom. Upon splitting a nucleus into elementary particles, the atom ceases to exist as a unit. In 1929, Pauling [2] published his five well-known rules which define the structural features of inorganic crystalline substances. The fifth rule—"the number of essentially different kinds of constituents in a crystal tends to be small"—was referred to by Pauling as parsimony.

In my earlier works [3, 4], this rule was modified and formulated as the system law: among numerous different attributes characterizing an object, it is always possible to find at least one attribute according to which the number of chosen constituents tends to be small: from one to four (larger numbers are not ruled out, but their occurrence is extremely small). For example, it is known that there are four types of chemical elements (*s*, *f*, *d*, and *p* elements), four different quarks, four dimensionalities (zero-, one-, two-, and three-dimensional spaces and the corresponding symmetries), four types of polyhedron connection (isolated and vertex-, edge-, and face-shared polyhedra), four planetary constituents (core, mantle, crust, and planetary atmosphere), four DNA bases (adenine, guanine, thymine, and cytosine), and four types of protein structures (primary, secondary, ternary, and quaternary); intermetallic compounds containing more than four elements are virtually absent; etc. The parsimony phenomenon was also revealed in a system of mineral species [5–7], specifically for their crystal structures [3, 4] in which even one chemical element can be located in no more than four different Wyckoff positions (four regular systems of points with different multiplicities).

Although the objects of a system are characterized by four constituents, each individual object can have a different number *j* of these constituents. At the number

[1] This article involves the materials of the author's papers presented at the conferences "Informational Products, Processes, and Technologies," Moscow, Russia, October 19–20, 1995; "Structure and Properties of Crystalline and Amorphous Materials," Nizhni Novgorod, Russia, March 12–14, 1996; XVII International Congress of Crystallographers, Seattle, USA, August 8–17, 1996; "Regularities of the Earth Crust Evolution," St. Petersburg, Russia, October 15–18, 1996; and "Mineralogy on the Threshold of XXI Century," St. Petersburg, Russia, December 17–19, 1996.

1063-7745/01/4601-0004$21.00

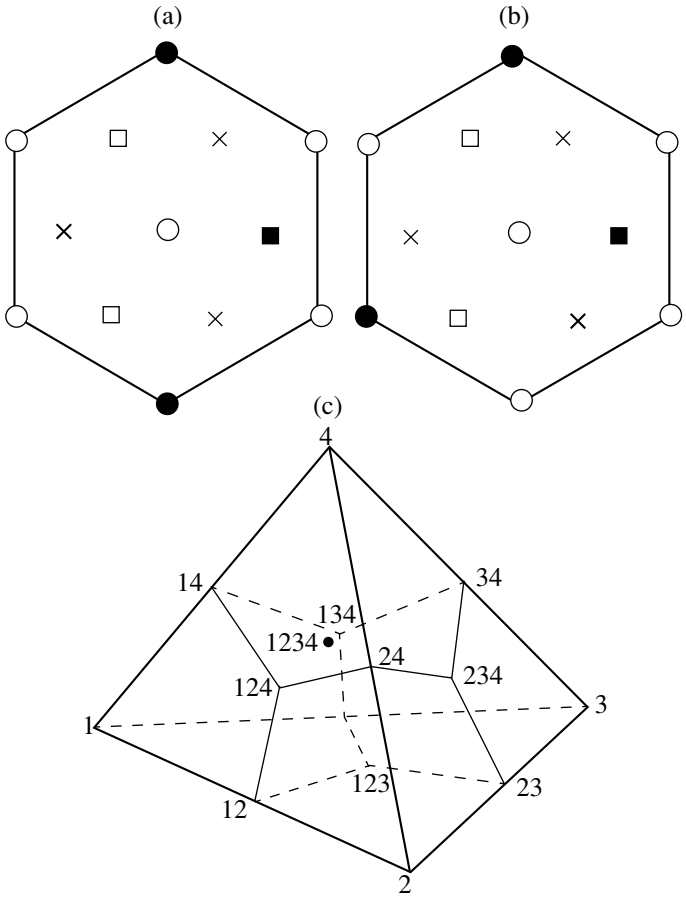

Fig. 1. (a) Square and (b) tetrahedral coordination of a white atom by four black atoms in a cubic cubooctahedron. Atoms denoted by crosses and squares lie, respectively, above and below a hexagon consisting of atoms designated by circles. (c) A schematic representation of the 1234 tetrahedron. Vertices, edges, faces, and a center (a total of 15 elements) of the tetrahedron are indicated by one, two, three, and four, respectively.

of constituents $j = 1, 2, 3$, and 4, the objects are considered to be single-, double-, triple-, and quadruple-arity systems, respectively [8]. Single-type constituents form a single-arity object, and different-type constituents make up double-, triple-, and quadruple-arity objects. If all the objects contain only one constituent, it is the strict parsimony, whereas the differentiation (an object is composed of constituents of two or more types) implies a nonstrict parsimony.

In the modeling of ordered isomorphs (superstructures) [9–12], it was shown that strict parsimony, according to which all atoms of a system and their local coordination should be of a single type (for example, a regular cubic cubooctahedron with equal interatomic distances), leads to a change-over from the zero-dimensional to three-dimensional periodicity with the structural type Cu ($Fm3m$). However, strict parsimony can also take place in binary compounds. For a single-type arrangement of atoms *A* in the centers of cubooctahedra and atoms *B* in their vertices, strict parsimony requires an identical coordination of the *B* atoms by the *A* atoms. It was theoretically proven that, among 12 atoms in its nearest environment, the *B* atom can have from one to four *A* atoms (the rest are the *B* atoms) [10]. For each coordination number (two, three, and four) with respect to the *A* atoms, there are several variants of the arrangement of the *A* atoms relative to the *B* atoms. In particular, when the coordination number is four, the *A* atoms can occupy vertices of a square or a distorted tetrahedron (Figs. 1a, 1b). In the case of the strict parsimony, i.e., when the coordination number is four and the nearest environment (coordination) is a square, the short-range order unambiguously ensures the realization of a long-range order, specifically the structural type $Cu_3^{[4]}Au^{[12]}$. Nonstrict parsimony (the coordination number is four, and the coordination is a square and a tetrahedron) leads to the polytype series $Cu_3^{[4]}Au^{[12]}$–$Al_3^{[4]}Ti^{[12]}$.

For the initial four coordination numbers (constituents), there are fifteen variants of combinations of different constituents: 1, 2, 3, 4, 12, 13, 14, 23, 24, 34, 123, 124, 134, 234, and 1234. These fifteen combinations correspond to four vertices, six edges, four faces, and one center of a tetrahedron (Fig. 1c).

Table 1. A system of fundamental formulas and their occurrence

j	FF (occurrence of types, cations, and dimension indices)					
1	**1**(40, 16, 4)	**2**(6, 68, 1)	**3**(60, 25, 0)	**4**(26, 6, 0)		
2	**11**(18, 1, 1)	**12**(8, 20, 2)	**22**(0, 33, 1)	**13**(37, 12, 2)	**23**(4, 43, 0)	**33**(17, 2, –)
	14(19, 4, –)	**24**(5, 8, 0)	**34**(28, 2, –)	**44**(8, 0, –)		
3	**111**(2, –, 1)	**112**(1, 1, 2)	**122**(0, 3, 2)	**222**(–, 2, –)	**113**(7, 1, 0)	**123**(1, 11, 1)
	223(–, 8, –)	**133**(5, 0, –)	**233**(0, 1, –)	**333**(1, –, –)	**114**(7, 0, 0)	**124**(0, 3, 0)
	224(0, 1, –)	**134**(5, 1, –)	**234**(0, 1, –)	**334**(4, 0, –)	**144**(0, 0, –)	**244**(0, 0, –)
	344(6, –, –)	**444**(0, –, –)				
4	**1111**(0, –, –)	**1112**(–, 0, 0)	**1122**(–, –, 1)	**1222**(–, 0, 0)	**2222**(–, –, –)	**1113**(1, –, 0)
	1123(0, 0, 1)	**1223**(–, 2, 1)	**2223**(–, 1, –)	**1133**(1, –, –)	**1233**(–, 0, 0)	**2233**(–, 0, –)
	1333(0, –, –)	**2333**(–, –, –)	**3333**(–, –, –)	**1114**(1, –, –)	**1124**(0, 0, 0)	**1224**(–, 1, 0)
	2224(–, 0, –)	**1134**(2, –, –)	**1234**(–, 0, 0)	**2234**(–, 0, –)	**1334**(0, –, –)	**2334**(–, 0, –)
	3334(–, –, –)	**1144**(–, –, –)	**1244**(–, –, –)	**2244**(–, –, –)	**1344**(0, –, –)	**2344**(–, –, –)
	3344(0, –, –)	**1444**(–, –, –)	**2444**(–, –, –)	**3444**(0, –, –)	**4444**(–, –, –)	
5, 6	**11122**(–, –, 0)	**11223**(–, 0, –)	**12223**(0, –, –)	**11133**(0, –, –)	**11233**(0, –, –)	**11333**(0, –, –)
	12333(0, –, –)	**11124**(–, 0, –)	**12224**(–, 0, –)	**11134**(0, –, –)	**12234**(–, 0, –)	**22234**(–, 0, –)
	22244(–, 0, –)	**11344**(0, –, –)	**112223**(0, –, –)	**111334**(0, –, –)	**122334**(–, 0, –)	
1–5	**5**(–, 0, –)	**15**(–, 2, –)	**25**(–, 6, –)	**35**(–, 4, –)	**45**(–, 0, –)	**125**(–, 1, –)
	225(–, 2, –)	**135**(–, 1, –)	**235**(–, 1, –)	**145**(–, 0, –)	**245**(–, 0, –)	**345**(–, 0, –)
	1235(–, 0, –)	**2235**(–, 0, –)	**1245**(–, 0, –)	**2345**(–, 0, –)	**12235**(–, 0, –)	**22335**(–, 0, –)
	13345(–, 0, –)	**6**(–, 1, –)	**16**(–, 0, –)	**26**(–, 3, –)	**36**(–, 1, –)	**46**(–, 0, –)
	126(–, 0, –)	**226**(–, 0, –)	**236**(–, 0, –)	**146**(–, 0, –)	**1126**(–, 0, –)	**1236**(–, 0, –)
	66(–, 0, –)	**266**(–, 0, –)	**56**(–, 0, –)	**256**(–, 0, –)	**2256**(–, 0, –)	

Note: The FFs are marked with the bold type, and the occurrence is given in parentheses.

Four constituents also allow one to compose 69 combinations, which are termed the fundamental formulas (FFs) [4]. Each FF can contain only identical (12 FFIs), identical and different (42 FFIDs), and only different (15 FFDs) constituents. In Table 1, all the FFs are marked with the bold type. A set of 69 FFs is separated into four blocks according to the arity (*j*) of combinations: 4 FFs in a single-component system ($j = 1$), 10 FFs in a binary system ($j = 2$), 20 FFs in a ternary system ($j = 3$), and 35 FFs in a quaternary system ($j = 4$).

By assigning each of the constituents (symbols **1**, **2**, **3**, and **4**) in the FF to a particular type of the *s*, *f*, *d*, and *p* chemical elements (cations) and calculating the occurrence of FFs in the system containing more than 3300 mineral species [5–7], we can see that the occurrence decreases with an increase in *j*. The occurrence of the FFs (in tens) is the first number in the parentheses (see Table 1). Note that zero corresponds to an occurrence of 1–4, and the dash indicates the complete absence of the occurrence of FFs.

If each of the constituents is assigned to a particular positive cation charge (+1, +2, +3, or +4), the 69 FFs represent the possible combinations of cations with different charges. The occurrences of these combinations (the second number in the parentheses) for ~3065 mineral species [5–7] confirm the aforementioned tendency for a decrease in the occurrence of minerals with an increase in the arity of the cationic part.

As is known, the qualitative and quantitative relationships revealed by the science between physical phenomena different in their nature made it possible to develop the Self-Consistent International System of Units (SI) [13], which is used in all natural sciences. The International System is based on the seven fundamental units of physical quantities, which are denoted by the following symbols (constituents): *M* (mass), *L* (length), *T* (time), θ (temperature), *I* (current strength), *J* (luminous flux), and *N* (amount of substance). The dimensions of derived units can be represented as monomials in the form of products of the symbols of the fundamental units to different powers. These powers are referred to as the dimension indices *k*. For example, the dimension of volume is L^3 (m^3), where $k = 3$, and the dimension of velocity (linear) is $L^{+1}T^{-1}$ (m/s), where $k = +1$ and –1. Analysis of all combinations of the absolute values $|k|$ (in the above examples, these are 3 and 11) demonstrates that they correspond to 69 FFs in Table 1. The occurrence of the combinations of the absolute values $|k|$ among 235 physical quantities [13]

is given by the third number in the parentheses and shows the same tendency—a decrease in the occurrence with an increase in the number of constituents.

It can be seen from Table 1 that 40 tens of mineral species with one cation of the *s* type, 16 tens of mineral species with singly charged cation, and four tens of physical quantities with $|k| = 1$ correspond to the arity $j = 1$ and constituent **1**. As follows from Table 1, the objects with the FFs at $j = 1$ and 2 are widespread in nature. The maximum frequency of occurrence is equal to 68 tens for the mineral species with one bivalent cation (Table 1, symbol **2**), 60 tens for the mineral species with *d* cations (Table 1, symbol **3**), and four tens for the physical quantities with $|k| = 1$ (Table 1, symbol **1**). The maximum frequencies of occurrence of the above mineral species and physical quantities at $j = 3$ and 4 are equal to 8, 7, and 2 and 2, 2, and 1, respectively.

The FFs with constituents **1**, **2**, **3**, and **4** at $j = 5$ and 6 can be found in all three systems considered in this work (the *s*, *f*, *d*, and *p* cations; charges; and dimension indices $|k|$). Among the 140 theoretically possible FFs at $j = 5$ and 6 [4], only a few specific realized FFs are listed in Table 1 (the fifth block). Note that the occurrence frequency of these FFs does not exceeds 4.

The FFs in the first five blocks of Table 1 involve only constituents **1**, **2**, **3**, and **4**. However, in addition to these constituents, there exist constituents **5** and **6.** For example, the cation charge can be equal to +5 and +6. The realized FFs with constituents **5** and **6** and also with additional constituents **1**–**4** at $j = 1$–5 are presented in the sixth block of Table 1. It can be seen that the FFs with constituents **5** and **6** can be realized only in a system of charges. In this case, the total number of cations (*j*) is no more than 5. For constituents **5** and **6** at $j = 1$ and 2, the maximum frequencies of occurrence are equal to six and three tens, respectively. For constituents **5** and **6** at $j = 4$ and 5, the maximum frequency of occurrence does not exceed 4.

Many interesting details are contained in Table 1. Specifically, at $j = 1$, the occurrence frequencies of the *s*, *f*, *d*, and *p* cations are equal to 40, 6, 60, and 26 tens, respectively. This distribution indicates that minerals with the main rare-earth cations are rare in occurrence.

Seven constituents (*M*, *L*, *T*, θ, *I*, *J*, and *N*), which represent seven fundamental units of physical quantities, theoretically can form 127 combinations rather than 15 (dimensions of derived units without regard for *k*, i.e., FFDs). However, only 32 combinations appear to be realized (Table 2). Analysis of the products of the symbols of the fundamental units shows that three symbols, namely, θ, *I*, and *J*, never occur together, and the symbol *N* is combined with θ and *I* only two times. As a result, only 39 theoretically possible products of the symbols can be obtained. Moreover, 24 combinations with [θ*N*], [*IN*], and [*JN*] turn out to be theoretically possible. Out of the 39 and 24 combinations, only 30 and 2 combinations are realized, respectively (i.e., 32 out of 63 combinations). The dimensionless physical quantities (such as the efficiency, relative elongation, relative density, mole fraction, etc.) are designated by symbol □ (Table 2).

It should be noted that all 235 known (and possible) dimensions of physical quantities [13] are included in Table 2. Except for *MLT*[θ*N*] with $j = 5$, the total number of symbols in the dimensions (their arity) does not exceed 4. However, if the combination [θ*N*] is treated as a unit, the arity of this FF is also equal to 4, which determines the possible combinations of the fundamental units.

The relations between the *M*, *L*, and *T* symbols can be represented by placing them in vertices of the 123 triangle (Fig. 1c). Then, the *ML*, *MT*, and *LT* combinations are the edges of this triangle, and the *MLT* combination is the triangle itself (its center). Addition of the fourth symbol to the above three symbols (*M*, *L*, and *T*) transforms the triangle into the 1234 tetrahedron (Fig. 1c). Note that the fourth vertex can be occupied by any one of the θ, *I*, *J*, and *N* symbols and also by the [θ*N*], [*IN*], and [*JN*] combinations with the formation of three additional edges, three faces, and one center. In this case, the combinations of the *M*, *L*, and *T* symbols with the fourth symbol are the tetrahedron edges, and the combinations of the triangle edge symbols with the symbol of the fourth vertex are the tetrahedron faces. A combination of *MLT* (triangle center) with the symbol of the fourth vertex (*MLT*□, *MLT*θ, *MLTI*, etc.) is the tetrahedron center. This results in the formation of eight tetrahedra with the same base rather than one tetrahedron composed of 15 FFs. It should be mentioned that certain vertices, edges, and faces of tetrahedra that symbolize the combinations of the fundamental physical quantities are nonexistent in reality. Indeed, many elements (edges, face, and centers) are absent in three tetrahedra in which the fourth vertex is occupied by the [θ*N*], [*IN*], and [*JN*] combinations. Therefore, we obtain 32 realized FFDs, of which two FFDs contain [θ*N*] or [*IN*]. Within the framework of the model under consideration (Table 2), the [θ*N*], [*JN*], and [*IN*] combinations should be treated as a unit. Otherwise, the tetrahedron transforms into a more complex figure—a five-vertex polyhedron. Since only two formulas, namely, *MLT*[θ*N*] and *MT*[*IN*], are obtained in practice, there are no grounds for deeper analysis.

All the formulas in Table 2 are termed full (*f*). However, many of them enter into the composition of other formulas as the partial (*p*) formulas. For example, the full formula *ML* is involved as the partial formula in the *MLT*, *ML*θ, and other formulas. Hence, each of the 39 squares in Table 2 is divided into two rows: *f* and *p*. Four numerals in each square correspond to the occurrence of the formulas among the 39 theoretical FFDs (*t*), 30 realized FFDs (*r*1), 89 formulas for dimensions with due regard for *k* (FFM, where M is the modulus, i.e., the symbol with *k*) (*r*2), and 231 physical quantities (*r*3). The occurrence of all the realized FFDs (*r*1) is nine less than that of the theoretical FFDs (*t*). Among

Table 2. Occurrence of dimension formulas: theoretical (*t*), realized (*r*), full (*f*), partial (*p*), without indices *k* (*r*1), with indices *k* (*r*2), and in physical quantities (*r*3)

Dimension		□				*M*				*L*				*T*				*ML*				*MT*				*LT*				*MLT*				Σ			
	fp	*t*	*r1*	*r2*	*r3*	*t*	*r1*	*r2*	*r3*	*t*	*r1*	*r2*	*r3*	*t*	*r1*	*r2*	*r3*	*t*	*r1*	*r2*	*r3*	*t*	*r1*	*r2*	*r3*	*t*	*r1*	*r2*	*r3*	*t*	*r1*	*r2*	*r3*	*t*	*r1*	*r2*	*r3*
□	*f*	□				1	1	1	2	1	1	7	31	1	1	3	15	1	1	5	9	1	1	5	16	1	1	9	23	1	1	10	43	7	7	40	139
	p	□				20	13	48	125	20	16	64	174	20	17	60	163	10	6	33	93	10	8	38	108	10	9	43	118	5	4	27	83	95	73	313	864
θ	*f*	1	1	2	2	1	0	0	0	1	1	1	1	1	0	0	0	1	0	0	0	1	1	1	2	1	1	1	3	1	1	2	3	8	5	7	11
	p	8	5	7	11	4	2	3	5	4	3	4	7	4	3	4	8	2	1	2	3	2	2	3	5	2	2	3	6	1	1	2	3	27	19	28	48
I	*f*	1	1	1	2	1	1	1	1	1	1	3	7	1	1	1	3	1	1	1	1	1	1	4	6	1	1	3	6	1	1	14	31	8	8	28	57
	p	8	8	28	57	4	4	20	39	4	4	21	45	4	4	22	46	2	2	15	32	2	2	18	37	2	2	17	37	1	1	14	31	27	27	155	324
J	*f*	1	1	1	1	1	0	0	0	1	1	1	3	1	1	1	1	1	0	0	0	1	0	0	0	1	1	1	1	1	0	0	0	8	4	4	6
	p	8	4	4	6	4	0	0	0	4	2	2	4	4	2	2	2	2	0	0	0	2	0	0	0	2	1	1	1	1	0	0	0	27	9	9	13
N	*f*	1	0	0	0	1	1	2	4	1	1	3	4	1	1	1	1	1	0	0	0	1	1	1	1	1	1	2	2	1	1	1	6	8	6	10	18
	p	8	6	10	18	4	3	4	11	4	3	6	12	4	4	5	10	2	1	1	6	2	2	2	7	2	2	3	8	1	1	1	6	27	22	32	78
Σ	*f*	4	3	4	5	5	4	4	7	5	5	15	46	5	4	6	20	5	2	6	10	5	4	11	25	5	5	16	35	5	4	27	83	39	30	89	231
Σ	*p*	32	23	49	92	36	22	75	180	36	28	97	242	36	34	93	229	18	10	51	134	18	14	61	157	18	16	67	170	9	7	44	123	203	150	537	1237
[θ*N*]	*f*																													1	1	1	2	1	1	1	2
[*IN*]	*f*																					1	1	2	2									1	1	2	2
[*JN*]	*f*																																				

Note: The FFDs are formed by combining the formulas in the upper row and the left column. Seven full theoretical formulas in the upper row and eight full theoretical formulas in each next row constitute fifteen fundamental formulas.

Table 3. Thesaurus of physical quantities

FFD without regard for k	Dimension indices of physical quantities $\langle k \rangle$	FFD without regard for k	Dimension indices of physical quantities $\langle k \rangle$
M	⟨1⟩ 10.1.1*, 10.1.2	θ	⟨1⟩ 4.1, ⟨**1**⟩ 4.2
L	⟨1⟩ 7.4, 10.29, 10.32.1–2, 10.42, 10.44.1–3, ⟨**1**⟩ 2.4, 2.6.1–3, 8.16, 10.26, 10.31, 10.41, ⟨**2**⟩ 1.1, 7.15, 10.6, 10.22, 10.23, 10.27, 10.43, ⟨**2**⟩ 10.9, ⟨3⟩ 1.2, 3.11, ⟨**3**⟩ 8.6, 10.39, ⟨4⟩ 3.10.1–3	*M*θ	⟨**1**1⟩ 4.3
		*L*θ	
		*T*θ	
T	⟨1⟩ 2.1, 7.1, 7.16, 10.18.1–2, ⟨**1**⟩ 1.5, 2.2, 2.3, 2.5, 7.2, 9.7, 10.13, 10.19, 10.38, ⟨**2**⟩ 1.6	*ML*θ	
		*MT*θ	⟨13**1**⟩ 4.8.1–2
ML	⟨1**2**⟩** 10.30, ⟨12⟩ 3.5, ⟨**12**⟩ 8.17, 10.28.1–3, ⟨1**3**⟩ 3.1, 8.7, ⟨**1**3⟩ 3.2	*LT*θ	⟨2**21**⟩ 4.11.1–2, 4.13
MT	⟨1**1**⟩ 7.14, ⟨**11**⟩ 10.14, ⟨1**2**⟩ 6.2, 3.14, 10.7, 10.11, ⟨**1**2⟩ 10.24, 10.25, ⟨1**3**⟩ 6.4.1–3, 6.6, 4.6, 7.11, 9.6, 10.12	*MLT*θ	⟨12**21**⟩ 4.10, 4.12, ⟨11**31**⟩ 4.7
		J	⟨1⟩ 6.7
LT	⟨1**1**⟩ 1.3, 7.5, 7.7, ⟨2**2**⟩ 4.15.1–4, 9.2.1–2, ⟨1**2**⟩ 1.4, ⟨2**1**⟩ 3.13, 4.9, 8.11, ⟨**21**⟩ 10.10, –9.8, 10.17, ⟨3**1**⟩ 7.6, ⟨**31**⟩ 10.16, 10.40.1–2, ⟨2**3**⟩ 9.3.1–2, ⟨4**2**⟩ 10.36	*MJ*	
		LJ	⟨**2**1⟩ 6.9, 6.10, 6.11
		TJ	⟨1**1**⟩ 6.8
MLT	⟨11**1**⟩ 3.3, 3.8, ⟨1**11**⟩ 3.12, ⟨11**2**⟩ 3.6.1–2, 10.33.1–2, ⟨1**12**⟩ 3.9.1–6, 7.3, 7.9, 8.10.1–2, ⟨1**21**⟩ 7.13, ⟨12**1**⟩ 3.4, ⟨12**2**⟩ 3.7, 3.15.1–2, 4.4, 4.14.1–3, 5.28, 6.1, 7.8, 8.3, 9.1, 10.8.1–2, 10.34, ⟨12**3**⟩ 3.16, 4.5, 5.27, 6.3, 6.5, 7.10.1–2, ⟨1**41**⟩ 7.12, ⟨14**2**⟩ 10.35	*MLJ*	
		MTJ	
		LTJ	⟨**2**11⟩ 6.12
		MLTJ	
I	⟨1⟩ 5.14.1–2	*N*	
MI	⟨**1**1⟩ 9.5	*MN*	⟨1**1**⟩ 8.1, ⟨**1**1⟩ 8.9.1–2, 8.22
LI	⟨**1**1⟩ 5.12, 5.13, 5.20, ⟨21⟩ 5.19.1, 10.3, 10.4, ⟨**2**1⟩ 5.11	*LN*	⟨**2**1⟩ 8.18, ⟨**3**1⟩ 8.8, 8.26, ⟨3**1**⟩ 8.2
TI	⟨11⟩ 5.1, 5.6, 10.2	*TN*	⟨**11**⟩ 10.15
MLI	⟨**1**21⟩ 10.21	*MLN*	
MTI	⟨**1**11⟩ 9.4, 10.5, ⟨1**21**⟩ 5.15, ⟨**1**21⟩ 8.27, 10.37, ⟨**1**42⟩ 8.20	*MTN*	⟨**11**1⟩ 8.13
LTI	⟨**2**11⟩ 5.3.1–2, 5.7, ⟨**3**11⟩ 5.2, ⟨111⟩ 5.10, 8.19	*LTN*	⟨**21**1⟩ 8.14, ⟨**31**1⟩ 8.12
MLTI	⟨**1**211⟩ 10.20, ⟨11**2**2⟩ 5.18.1–2, ⟨12**21**⟩ 5.16, ⟨12**22**⟩ 5.17.1–2, 5.26, ⟨**12**22⟩ 5.25, ⟨1**131**⟩ 5.4, ⟨12**31**⟩ 5.5.1–4, 8.25.1–3, ⟨13**21**⟩ 5.19.2, ⟨1**232**⟩ 5.21.1–4, ⟨**12**32⟩ 5.22.1–4, ⟨13**32**⟩ 5.23, ⟨**13**32⟩ 5.24, 8.23, ⟨**12**42⟩ 5.8, ⟨**13**42⟩ 5.9.1–2	*MLTN*	⟨12**21**⟩ 8.4.1–5, 8.15
		MT[*IN*]	⟨**1**42**1**⟩ 8.21, ⟨**1**32**1**⟩ 8.24
		MLT[θ*N*]	⟨12**211**⟩ 8.5.1–2

* The ordinal number of the physical quantity in [13].

** Dimension indices are given in angle brackets. Indices 1 and **2** refer to symbols *M* and *L*, respectively. Negative indices are marked with the bold type.

these nine FFDs, five partial formulas are realized and four formulas containing symbols *M* and *J* occur neither among the full formulas nor among the partial formulas; i.e., their occurrence is equal to zero (apparently, this can be explained by the fact that the light has no mass). The occurrence frequency of the formulas in Table 2 varies from 0 to 174 (the frequency of occurrence of *L* among the 231 physical quantities with the nonzero occurrence is maximum). As the number of constituents *j* increases from 1 to 4, the maximum frequency of occurrence changes as follows: 174 (*L*), 118 (*LT*), 83 (*MLT*), and 31 (*MLTI*).

Addition of the dimension indices *k* (from 1 to 4) to each of the 63 theoretical and 32 realized formulas results in 279 theoretical formulas (even without permutations and without regard for the sign of *k*) but only in 92 realized formulas even with due regard for the sign of *k* (FFM). A decrease in the number of the realized formulas (89) even in comparison with 174 theoretical formulas, which are obtained only from the 39 initial formulas (instead of 63 formulas), can be explained by the fact that the indices of *M*, θ, *J*, and *N* are universally equal to unity; the indices of *I* are equal to 1 and 2; and, although the magnitudes of *k* for *L* and *T* are equal to 1–4, the values of $k = 3$ and, especially, $k = 4$ are few and far between (Table 3, Fig. 2a).

Each FFM represents the dimension of one out of 235 physical quantities. Note that the same FFM can

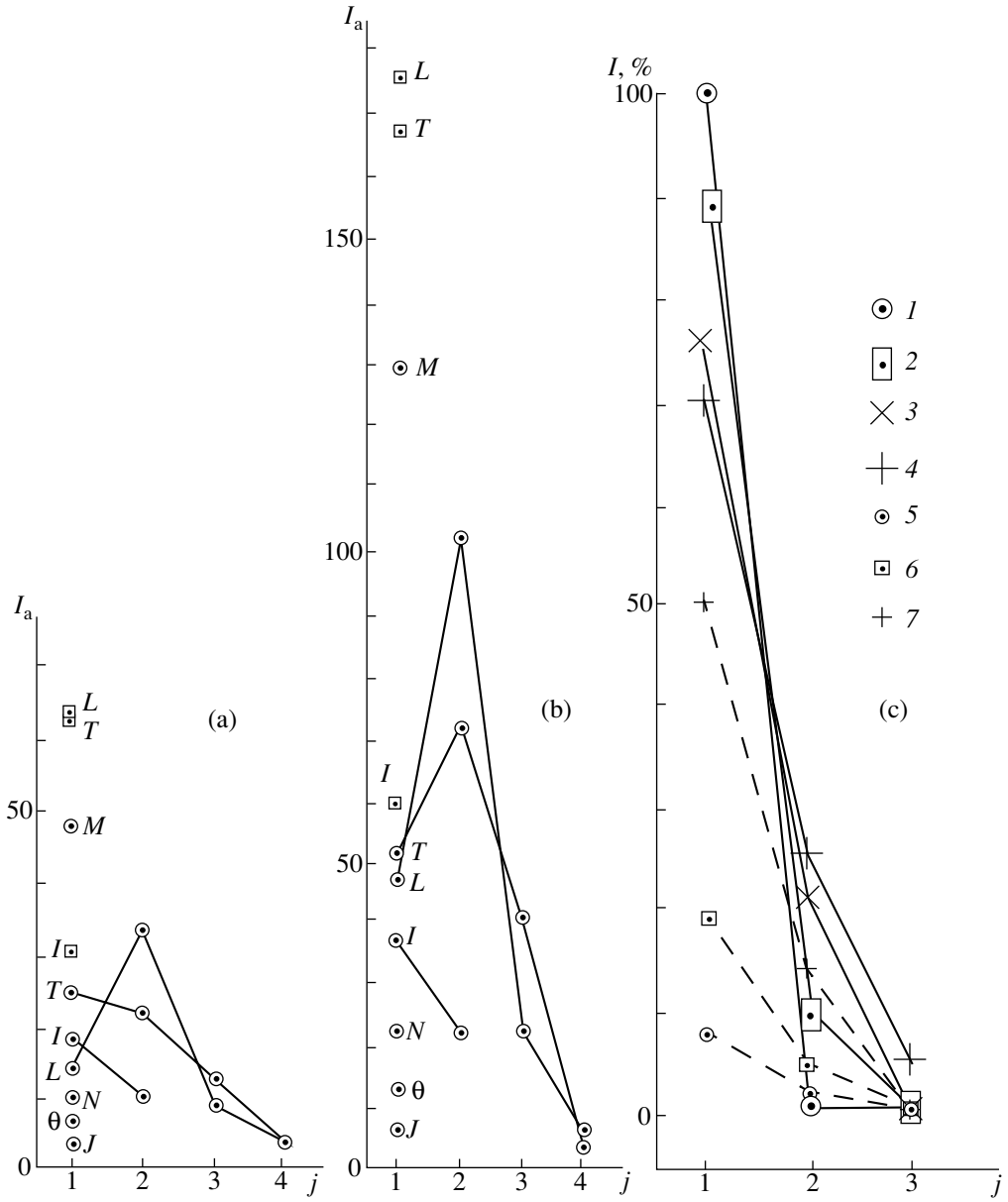

Fig. 2. Absolute frequencies of occurrence I_a of the seven fundamental units of physical quantities among (a) 92 different formulas and (b) 235 physical quantities with due regard for k at $j = 1, 2, 3$, and 4. The occurrence frequencies of the fundamental units with dimension indices k are designated by open circles, and the total occurrence frequencies of L, T, and I at any k are denoted by open squares. (c) Relative frequencies of occurrence I (%) of 36 formulas at $j = 1, 2$, and 3 among (*1*) homomolecular crystal structures, (*2*) their structural classes, (*3*) 60 formulas with the stabilizers, and (*4*) 36 formulas with the stabilizers and relative frequencies of occurrence of crystal structures, structural classes, and formulas with the invariant stabilizer among (*5*) the total number of crystal structures, (*6*) the total number of structural classes, and (*7*) 36 formulas.

represent the dimension of several physical quantities (for example, the mass of a particle at rest, atomic and nuclear masses, and the mass defect have the dimension M). The distribution of k for 235 physical quantities is displayed in Fig. 2b. The occurrences of the L, M, and T quantities are maximum, and the dimensions of I, N, θ, and J are encountered considerably more rarely.

In this work, a thesaurus of the physical quantities (Table 3) is proposed for the first time. The thesaurus includes the designations of physical quantities by symbols, their dimension indices k with specifying the sign ("+" or "–"), and their ordinal numbers taken from [13]. In the thesaurus, all 235 physical quantities are represented by the 92 FFMs, which are divided into 32 FFDs. In turn, these FFDs can be subdivided into eight families. Each of eight families contains only of the sets M, L, T, and □; M, L, T, and I; M, L, T, and θ; M, L, T, and J; and M, L, T, and N; three families contain

M, *L*, *T*, and [*IN*]; *M*, *L*, *T*, and [θ*N*]; and *M*, *L*, *T*, and [*JN*] (vertices of eight tetrahedra in Fig. 1c).

The above approach can be applied to analysis of a system involving ~20000 homomolecular crystal structures (CS), which were divided into 306 structural classes (SC) by Belsky *et al.* [14]. This subdivision was performed taking into account the space group, the number of formula units (molecules) *Z*, and the number of different regular systems of points occupied by molecules with specifying the stabilizers—the point symmetry groups of the positions occupied by molecules. Reasoning from the statistical analysis of the structural classes, Belsky *et al.* [14] separated the entire set of structural classes and the corresponding structures into six families (supergiant, giant, large, small, rare, and anomalous structural classes). However, the principle of separating a particular family was not described. The absolute occurrences of homomolecular crystal structures for different numbers *k* of the positions occupied by molecules was also reported in [14]. The number *k* is the stabilizer index and can be equal to 1, 2, 3, 4, 5, 6, 8, 9, and 16.

Each crystal structure can be represented as a combination of stabilizers with index *k*, which indicates the number of identical stabilizers. As a result, we obtain 60 variants of FFMs with specifying *k* and 36 FFDs (i.e., the formulas without specifying *k*). Out of these 60 and 36 formulas, there are 45 and 25 formulas with one stabilizer, 13 and 9 formulas with two different stabilizers, and 2 and 2 formulas with three different stabilizers; i.e., the arities *j* of these formulas are equal to 1, 2, and 3. The stabilizers 4*mm*, 432, 6, 622, 6*mm*, 6/*m*, and 6/*mmm*, i.e., only seven among the 32 theoretically possible stabilizers, were not realized.

Thirty-six formulas in curly brackets, *k* for 60 formulas in angle brackets, and the occurrence frequencies of 36 formulas in parentheses (the first and second parenthetic numbers are the frequencies of occurrence among the crystal structures and the structural classes, respectively) are given below. These data at $j = 1$ are as follows: {1} ⟨*k* = 1; 2; 3; 4; 5; 6; 8; 9; 16⟩ (16654, 118); {$\bar{1}$} ⟨1; 2; 3; 4⟩ (1425, 16); {2} ⟨1; 2; 3⟩ (725, 46); {*m*} ⟨1; 2; 3; 4⟩ (474, 30); {2/*m*} ⟨1; 2⟩ (53, 7); {*mm*} ⟨1; 2⟩ (26, 5); {222} ⟨1⟩ (12, 5); {*mmm*} ⟨1⟩ (7, 2); {$\bar{4}$} ⟨1; 2⟩ (42, 8); {4} ⟨1⟩ (11, 8); {$\bar{4}$2*m*} ⟨1⟩ (7, 3); {4/*m*} ⟨1⟩ (1, 1); {422} ⟨1⟩ (1, 1); {4/*mmm*} ⟨1⟩ (1, 1); {3} ⟨1; 3⟩ (63, 8); {3*m*} ⟨1⟩ (16, 5); {$\bar{3}$} ⟨1⟩ (16, 4); {$\bar{6}$} ⟨1⟩ (12, 1); {32}⟨1⟩ (5, 1); {$\bar{3}$*m*} ⟨1⟩ (2, 1); {$\bar{6}$*m*2} ⟨1⟩ (1, 1); {*m*$\bar{3}$*m*} ⟨1⟩ (11, 2); {$\bar{4}$3*m*} ⟨1⟩ (4, 1); {*m*$\bar{3}$} ⟨1⟩ (2, 1); {23} ⟨1⟩ (1, 1). The number of binary and ternary mixed formulas is equal to 11. In these formulas, the numbers of positions, for example, ⟨1, 1⟩, corresponds to the stabilizers {1, $\bar{1}$}. The data at $j = 2$ and 3 are as follows: {1, $\bar{1}$} ⟨1, 1; 1, 2⟩ (29, 6); {1, 2} ⟨1, 1; 1, 2⟩ (24, 11); {1, *m*} ⟨1, 1; 1, 2; 4, 1⟩ (5, 5); {$\bar{1}$, 2} ⟨1, 1⟩ (2, 2); {2/*m*, *m*} ⟨1, 1⟩ (2, 2); {2, *m*} ⟨1, 1⟩ (2, 1); {3, $\bar{3}$} ⟨1, 2⟩ (1, 1); {1, $\bar{4}$} ⟨1, 1⟩ (1, 1); {23, $\bar{4}$} ⟨1, 1⟩ (1, 1); {1, $\bar{1}$, 2} ⟨1, 1, 1⟩ (1, 1); {1, *m*, *mm*} ⟨1, 4, 4⟩ (1, 1). Only for two FFMs {1, *m*, *mm*} and {3, $\bar{3}$} are all the values of *k* not equal to 1 but ⟨1, 4, 4⟩ and ⟨1, 2⟩; i.e., the first terms of these series are absent.

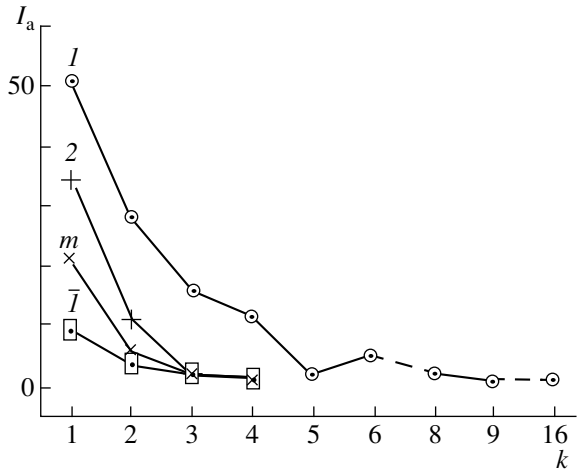

Fig. 3. Dependences of the absolute frequency of occurrence I_a on *k* for structural classes at different stabilizers: (○) 1_k, (+) 2_k, (×) m_k, and (□) $\bar{1}_k$.

The occurrence frequency of crystal structures is maximum (thousands of crystal structures) for the FFD 1; large (hundreds of crystal structures) for the FFDs $\bar{1}$, 2, and *m*; and small (tens of crystal structures) for the FFDs 2/*m*, *mm*, $\bar{4}$, 3, 3*m*, $\bar{3}$, {1, $\bar{1}$}, and {1, 2}. The occurrence of structures with the other FFDs is no more than 10. All the mixed formulas ($j = 2$ and 3) contain all if not one stabilizer from the first three groups. Figure 2c demonstrates the dependences of the occurrence on the arity ($j = 1$, 2, and 3) for ~20000 homomolecular crystal structures, 306 structural classes, and 60 and 36 formulas. As can be seen, the occurrence drastically decreases with an increase in *j*. It is worth noting that all four sets under consideration are uniquely divided only into three groups, each with a specific value of *j*; i.e., it is not an arbitrary division into 6 and 16 sets.

The dependences of the absolute frequency of occurrence I_a on *k* for the structural classes at the most commonly encountered stabilizers (1, 2, *m*, and $\bar{1}$) are depicted in Fig. 3. It is seen that stabilizer 1 has the longest sequence of *k*. The other stabilizers (2, *m*, and $\bar{1}$) are characterized by $k \le 4$.

Let us choose the formulas containing an invariant stabilizer (without degrees of freedom) in each set and determine the fraction of their occurrence with respect to all the formulas of the given set. The data obtained (see Fig. 2c) demonstrate that the occurrence of formulas with invariant stabilizers is substantially less than

the occurrence of the total number of these formulas. It should be noted that the formulas with two invariant stabilizers {23, $\bar{4}$ } are found for only one crystal structure.

Thus, the parsimony law is valid ($j \leq 3$) only in the case when different stabilizers without regard for k serve as constituents. When different and identical stabilizers are treated as constituents, the arity j can be as large as 16. However, if all identical stabilizers with different k are combined into one constituent with $j = 1$, the parsimony law is fulfilled much more strictly. This indicates that the proper choice of the attribute is extremely important for the rigorous manifestation of the parsimony law.

The fulfillment of the parsimony law can also be illustrated by analyzing the number of medalists at the Olympic Games in 1996 in Atlanta (i.e., in the field of manifestation of physical human abilities). A comparison between the number of medalists awarded 1, 2, 3, 4, and 6 medals and the data on the occurrence of structural classes with $j = 1$, 2, and 3 shows their virtually strict analogy. The number of medalists awarded one medal amounts to 87% of their total number (the number of structural classes with $j = 1$ is equal to 89% of their total number). Ten percent of medalists were awarded two medals (10% of structural classes with $j = 2$), 2% of medalists were awarded three medals (1% of structural classes with $j = 3$), ~1% of medalists were awarded four medals (0% of structural classes with $j = 4$), and one sportsman (~0% of medalists) was awarded six medals (0% of structural classes with $j = 6$).

The results of the investigation performed confirm the universality of the parsimony law and the ordered isomorphism, which manifest themselves in systems of superstructures, physical quantities, their dimensions, dimension indices, cation charges of mineral species, qualitative cation formulas, and stabilizers of the space groups of homomolecular structures. The selection of the most stable objects is obeyed by the parsimony law.

ACKNOWLEDGMENTS

I am grateful to L.A. Shuvalov and Yu.K. Egorov-Tismenko for careful reading of the manuscript and helpful remarks.

REFERENCES

1. A. A. Bogdanov, *Essays in Tectology* (Seaside, Calif., Intersystem, 1984; Ékonomika, Moscow, 1989), Vols. 1, 2.
2. L. Pauling, J. Am. Chem. Soc. **51**, 1010 (1929).
3. N. L. Smirnova, Kristallografiya **38** (5), 117 (1993) [Crystallogr. Rep. **38**, 646 (1993)].
4. N. L. Smirnova, Kristallografiya **39** (3), 1032 (1994) [Crystallogr. Rep. **39**, 946 (1994)].
5. M. Fleischner, *Glossary of Mineral Species* (Mineralogical Record, Tucson, 1987; Mir, Moscow, 1990).
6. *Mineralogical Tables* (Nedra, Moscow, 1981).
7. *Thesaurus of Minerals* (VINITI, Moscow, 1976–1981), Vols. 1–4.
8. A. M. Mishin and V. B. Orlov, *Explanatory Mathematical Dictionary: Basic Terms* (Russkiĭ Yazyk, Moscow, 1989).
9. N. L. Smirnova, Vestn. Mosk. Univ., Ser. Geol., No. 8, 181 (1952).
10. N. L. Smirnova, Kristallografiya **1** (2), 165 (1956) [Sov. Phys. Crystallogr. **1**, 128 (1956)].
11. N. L. Smirnova, Kristallografiya **4** (1), 13 (1959) [Sov. Phys. Crystallogr. **4**, 10 (1960)]; Kristallografiya **4**, 20 (1959) [Sov. Phys. Crystallogr. **4**, 17 (1960)].
12. N. L. Smirnova, Kristallografiya **9** (2), 265 (1964) [Sov. Phys. Crystallogr. **9**, 206 (1964)].
13. *Methodical Instructions: Introduction and Application of the Standards of the Council for Mutual Economic Aid 1052-78 "Metrology: Units of Physical Quantities" RD 50-160-179* (Izd. Standartov, Moscow, 1979).
14. V. K. Belsky, O. N. Zorkaya, and P. M. Zorky, Acta Crystallogr., Sect. A: Fundam. Crystallogr. **A51**, 473 (1995).

Translated by O. Borovik-Romanova

Crystallography Reports, Vol. 46, No. 1, 2001, pp. 40–45. Translated from Kristallografiya, Vol. 46, No. 1, 2001, pp. 47–52.

STRUCTURE OF COORDINATION COMPOUNDS

Crystal Structures of Acid Ethylenediaminetetraacetates $[Cd(H_2Edta)(H_2O)] \cdot 2H_2O$ and $[Mn(H_2O)_4][Mn(HEdta)(H_2O)]_2 \cdot 4H_2O$

I. N. Polyakova*, A. L. Poznyak, V. S. Sergienko*, and L. V. Stopolyanskaya****

** Kurnakov Institute of General and Inorganic Chemistry, Russian Academy of Sciences, Leninskiĭ pr. 31, Moscow, 117907 Russia*

*** Institute of Molecular and Atomic Physics, Belarussian Academy of Sciences, pr. F. Skoriny 70, Minsk, 220072 Belarus*

e-mail: sokol@ionchran.rinet.ru

Received December 27, 1999

Abstract—The crystal structures of $[Cd(H_2Edta)(H_2O)] \cdot 2H_2O$ (**I**) and $[Mn(H_2O)_4][Mn(HEdta)(H_2O)]_2 \cdot 4H_2O$ (**II**) are studied by X-ray diffraction [$R_1 = 0.0209$ (0.0272), $wR_2 = 0.0571$ (0.0730) for 2551 (4025) reflections with $I > 2\sigma(I)$ in **I** (**II**), respectively]. Structure **I** contains mononuclear $[Cd(H_2Edta)(H_2O)]$ complexes with the C_2 symmetry, and structure **II** contains centrosymmetric trinuclear $[Mn(H_2O)_4][Mn(HEdta)(H_2O)]_2$ complexes. In **I** and **II**, the protonated ligands are hexadentate (2N + 4O), and the water molecule increases the coordination number of the metal atom to seven. The acid protons participate in short intermolecular hydrogen bonds, which are symmetric in **II** and asymmetric in **I**. © *2001 MAIK "Nauka/Interperiodica".*

INTRODUCTION

The polybasic ethylenediaminetetraacetic acid H_4Edta forms acid complexes in which it exhibits different protonation degrees. In [1], the structures of the Fe^{2+} complexes, namely, $[Fe(H_2O)_4][Fe(HEdta)(H_2O)]_2 \cdot 4H_2O$ and $[Fe(H_2Edta)(H_2O)] \cdot 2H_2O$, with mono- and diprotonated anions were determined. The former compound is isostructural to the Mn^{2+} [2] and Cd^{2+} [3] compounds of similar composition. We made an attempt to obtain the complexes of Mn^{2+} and Cd^{2+} with the H_2Edta^{2-} anion. However, we only achieved half of this goal: compound $[Cd(H_2Edta)(H_2O)]_2H_2O$ (**I**) was synthesized. For Mn^{2+}, we obtained the $[Mn(H_2O)_4][Mn(HEdta)(H_2O)]_2 \cdot 4H_2O$ (**II**) complex with the monoprotonated ligand, which had already been characterized. Both substances were isolated in the form of high-quality single crystals and studied by X-ray diffraction. The structure of **II** was redetermined, because the determination performed earlier in [2] was based on the photographic data.

EXPERIMENTAL

Synthesis of I. Equimolar amounts of $CdSO_4 \cdot 8/3H_2O$ and $Na_2H_2Edta \cdot 2H_2O$ were dissolved in the minimum amount of water on heating to 85°C. Colorless transparent crystals **I** were obtained by slow cooling of this solution in a Dewar flask.

X-ray diffraction study of I and II. Sets of intensities were collected on a CAD4 automated diffractometer (λMoK_α, graphite monochromator). The data for **I** were corrected for absorption by the azimuthal-scan method. The structures were solved by the direct method (SHELXS86 [4]). The H atoms were located from difference Fourier syntheses. The non-hydrogen atoms were refined by the least-squares procedure in the anisotropic approximation, and the hydrogen atoms were refined isotropically with the SHELXL93 program package [5]. In **I**, the secondary extinction was taken into account [$g = 0.0134(5)$]. In **II**, the four most disagreeable reflections were excluded from the refinement.

Main crystal data and parameters of data collection and refinement for structures **I** and **II** are summarized in Table 1. The coordinates and parameters of thermal vibrations of atoms are listed in Table 2.

RESULTS AND DISCUSSION

Crystal structure I. Structure **I** is built of the discrete $[Cd(H_2Edta)(H_2O)]$ complexes and crystallization water molecules (Fig. 1). The crystallographic symmetry of the complex is C_2. The twofold rotation axis passes through the Cd(1) and O(1*w*) atoms and the midpoint of the C(5)–C(5)' bond. The coordination number of the Cd atom is seven. The environment of the Cd atom is formed by pairs of the centrosymmetrically related atoms O(1), O(1)', O(3), O(3)', N(1), and

1063-7745/01/4601-0040$21.00 © 2001 MAIK "Nauka/Interperiodica"

Table 1. Main crystal data and parameters of data collection and refinement for structures **I** and **II**

Parameter	**I**	**II**
Formula	$C_{10}H_{20}CdN_2O_{11}$	$C_{20}H_{46}Mn_3N_4O_{26}$
Molecular weight	456.68	923.42
Space group	*C*2/*c*	$P2_1/n$
a, Å	11.912(2)	9.200(2)
b, Å	9.900(2)	16.129(3)
c, Å	14.363(3)	11.876(2)
β, deg	110.81(3)	90.59(3)
V, Å^3	1583.3(5)	1762.1(6)
Z	4	2
$\rho_{calcd.}$, g/cm^3	1.916	1.740
μ_{Mo}, mm^{-1}	1.441	1.162
θ_{max}, deg	32	30
No. of reflections collected	2793	4986
No. of unique reflections (R_{int})	2704 (0.0303)	4786 (0.0455)
No. of reflections with $I > 2\sigma(I)$	2551	4025
R factors for reflections with	$R_1 = 0.0209$,	$R_1 = 0.0272$,
$I > 2\sigma(I)$	$wR_2 = 0.0571$	$wR_2 = 0.0730$
R factors for the complete data set	$R_1 = 0.0228$, $wR_2 = 0.0582$	$R_1 = 0.0390$, $wR_2 = 0.0870$
GOOF	1.056	1.014
$\Delta\rho_{min}/\Delta\rho_{max}$, e/Å^3	−0.577/0.664	−0.480/0.447

N(1)' of the H_2Edta^{2-} hexadentate ligand and the O(1*w*) atom of the water molecule. The same coordination of the Cd atoms is observed in the compounds with the completely deprotonated and monoprotonated anions $[Mg(H_2O)_6][Cd(Edta)(H_2O)] \cdot 3H_2O$ (**III**) [6] and $[Cd(H_2O)_4][Cd(HEdta)(H_2O)]_2 \cdot 4H_2O$ (**IV**) [3]. The Cd complex in $[Mn(H_2O)_4][Cd(Edta)] \cdot 2H_2O$ [7] has a similar structure, but the seventh coordination site in the metal polyhedron is occupied by the oxygen atom of the bridging carboxyl group of the neighboring ligand instead of the water molecule. The polyhedron of the Cd(1) atom in **I** is a distorted monocapped trigonal prism in which the O(1), O(3), N(1) and O(1)', O(3)', N(1)' atoms form the bases and the O(1*w*) atom centers the O(1)O(1)'O(3)O(3)' face. The triangular bases of the prism are almost parallel (the dihedral angle is 2.3°) but are twisted by an angle of ~20°.

Complex **I** belongs to the *ER*/*G* conformational class [8]. The protonated and deprotonated acetate arms close the *G* and *R* rings, respectively. The Cd–O(3) bond with the protonated carboxyl group is substantially weaker than the Cd–O(1) bond with the deprotonated group [2.508(1) and 2.303(1) Å, respectively]. A similar ratio between the bond lengths could be expected for the acid complex **IV**. However, in this compound, the spread in length of the Cd–O bonds formed by the carboxyl groups is only 0.05 Å and the longest bond [2.387(2) Å] is formed by the deprotonated group, which is also involved in the coordination of the hydrated $[Cd(H_2O)_4]^{2+}$ cation. In cadmium aqua complexes **I**, **III**, and **IV**, the Cd–O(*w*) bond [2.210(2), 2.246(9), and 2.252(3) Å, respectively] is the strongest in the metal environment. The Cd(1)–N(1) bond length in **I** [2.395(2) Å] is intermediate between the lengths of two symmetrically independent and unequivalent bonds in **III** and **IV** [2.282(9) and 2.414(7) Å in **III** and 2.381(3) and 2.421(3) Å in **IV**.

Intermolecular interactions in the crystal are achieved through the hydrogen bonds (Table 3). The strong O(4)–H(4O)···O(1)' hydrogen bonds link the complexes into chains running along the *x*-axis. The hydrogen bonds involving water molecules crosslink the chains into a three-dimensional framework.

Crystal structure of **I** resembles the $[Fe(H_2Edta)(H_2O)] \cdot 2H_2O$ (**V**) [1] structure. Both compounds crystallize in space group *C*2/*c*. The unit cells

Table 2. Coordinates and parameters of thermal vibrations U_{eq} (for H atoms, U_{iso}) of atoms in structures **I** and **II**

Atom	*x*	*y*	*z*	U_{eq}/U_{iso}, Å^2
		I		
Cd(1)	0.5	0.04557(1)	0.75	0.0235(1)
O(1)	0.3474(1)	0.0661(2)	0.5978(1)	0.0404(3)
O(2)	0.1522(1)	0.1063(2)	0.5296(1)	0.0499(4)
O(3)	0.3942(1)	0.0079(1)	0.8708(1)	0.0344(2)
O(4)	0.3282(2)	0.1229(2)	0.9750(1)	0.0427(3)
N(1)	0.3780(1)	0.2350(1)	0.7566(1)	0.0228(2)
C(1)	0.2557(1)	0.2089(2)	0.6855(1)	0.0278(3)
C(2)	0.2506(1)	0.1216(2)	0.5968(1)	0.0300(3)
C(3)	0.3762(2)	0.2494(2)	0.8574(1)	0.0283(3)
C(4)	0.3668(1)	0.1130(2)	0.9016(1)	0.0267(3)
C(5)	0.4318(1)	0.3543(1)	0.7264(1)	0.0263(2)
O(1*w*)	0.5	−0.1777(2)	0.75	0.077(1)
O(2*w*)	0.5298(2)	0.3716(2)	0.3905(1)	0.0517(4)
H(4O)	0.341(3)	0.055(3)	1.004(3)	0.06(1)
H(1*A*)	0.212(2)	0.284(3)	0.666(2)	0.036(6)
H(1*B*)	0.210(2)	0.164(2)	0.718(2)	0.034(5)
H(3*A*)	0.446(2)	0.289(3)	0.898(2)	0.041(6)
H(3*B*)	0.322(2)	0.306(3)	0.861(2)	0.038(6)
H(5*A*)	0.401(2)	0.352(2)	0.652(2)	0.033(5)
H(5*B*)	0.401(2)	0.438(2)	0.747(2)	0.030(6)
H(1*w*1)	0.488(3)	−0.213(4)	0.702(2)	0.07(1)
H(1*w*2)	0.483(4)	0.373(5)	0.421(3)	0.09(1)
H(2*w*2)	0.582(4)	0.374(5)	0.424(3)	0.08(1)
		II		
Mn(1)	0.15979(2)	0.77670(1)	0.22079(1)	0.0191(1)
Mn(2)	0	0.5	0.5	0.0246(1)
O(1)	0.1400(1)	0.8770(1)	0.0937(1)	0.0298(3)
O(2)	0.1036(2)	0.9033(1)	−0.0882(1)	0.0478(4)
O(3)	0.2102(1)	0.6660(1)	0.1165(1)	0.0284(3)
O(4)	0.1187(1)	0.5426(1)	0.0752(1)	0.0329(3)
O(5)	0.2119(1)	0.8805(1)	0.3431(1)	0.0285(2)
O(6)	0.1250(1)	1.0034(1)	0.3929(1)	0.0338(3)
O(7)	0.1246(1)	0.6747(1)	0.3489(1)	0.0306(3)
O(8)	0.0022(2)	0.6364(1)	0.5021(1)	0.0319(3)
N(1)	−0.0400(1)	0.7459(1)	0.0958(1)	0.0214(2)
N(2)	−0.0484(1)	0.8111(1)	0.3229(1)	0.0197(2)
C(1)	−0.1728(2)	0.7852(1)	0.1395(2)	0.0254(3)
C(2)	−0.1803(2)	0.7782(1)	0.2665(1)	0.0251(3)
C(3)	−0.0020(2)	0.7816(1)	−0.0141(1)	0.0271(3)
C(4)	0.0868(2)	0.8608(1)	−0.0018(1)	0.0281(3)
C(5)	−0.0472(2)	0.6553(1)	0.0906(2)	0.0249(3)
C(6)	0.1059(2)	0.6202(1)	0.0944(1)	0.0225(3)
C(7)	−0.0447(2)	0.9019(1)	0.3326(1)	0.0243(3)
C(8)	0.1100(2)	0.9291(1)	0.3575(1)	0.0232(3)
C(9)	−0.0332(2)	0.7728(1)	0.4346(1)	0.0243(3)
C(10)	0.0364(2)	0.6877(1)	0.4269(1)	0.0224(3)

Table 2. (Contd.)

Atom	*x*	*y*	*z*	U_{eq}/U_{iso}, Å^2
		II		
O(1*w*)	0.3999(1)	0.7903(1)	0.2018(1)	0.0275(2)
O(2*w*)	0.1654(2)	0.4999(1)	0.3723(1)	0.0387(3)
O(3*w*)	0.1608(2)	0.4968(2)	0.6325(2)	0.0691(7)
O(4*w*)	0.5433(2)	0.6429(1)	0.1950(1)	0.0428(3)
O(5*w*)	0.0669(2)	0.5779(1)	0.8215(1)	0.0409(3)
H(1*A*)	−0.257(3)	0.763(1)	0.102(2)	0.034(6)
H(1*B*)	−0.173(2)	0.841(1)	0.118(2)	0.032(5)
H(2*A*)	−0.188(2)	0.720(1)	0.289(2)	0.023(5)
H(2*B*)	−0.267(2)	0.806(1)	0.293(2)	0.030(5)
H(3*A*)	−0.090(2)	0.793(1)	−0.060(2)	0.025(5)
H(3*B*)	0.056(3)	0.740(2)	−0.055(2)	0.042(6)
H(5*A*)	−0.092(2)	0.635(1)	0.027(2)	0.030(5)
H(5*B*)	−0.099(2)	0.633(1)	0.156(2)	0.036(6)
H(7*A*)	−0.077(2)	0.925(1)	0.261(2)	0.029(5)
H(7*B*)	−0.104(2)	0.926(1)	0.393(2)	0.029(5)
H(9*A*)	0.032(2)	0.803(1)	0.480(2)	0.026(5)
H(9*B*)	−0.125(2)	0.768(1)	0.471(2)	0.028(5)
H(4)	0.251(4)	0.523(2)	0.094(3)	0.09(1)
H(1*w*1)	0.440(3)	0.742(2)	0.202(2)	0.051(7)
H(2*w*1)	0.423(4)	0.815(2)	0.137(3)	0.08(1)
H(1*w*2)	0.252(3)	0.472(2)	0.384(2)	0.062(8)
H(2*w*2)	0.197(4)	0.546(2)	0.361(3)	0.07(1)
H(1*w*3)	0.224(3)	0.479(2)	0.624(2)	0.050(9)
H(2*w*3)	0.147(3)	0.512(2)	0.692(3)	0.056(8)
H(1*w*4)	0.555(3)	0.630(2)	0.266(2)	0.054(8)
H(2*w*4)	0.481(3)	0.604(2)	0.166(3)	0.066(9)
H(1*w*5)	0.034(3)	0.543(2)	0.859(3)	0.07(1)
H(2*w*5)	0.004(5)	0.604(3)	0.796(4)	0.12(2)

Table 3. Characteristics of hydrogen bonds (Å) in structures **I** and **II**

D–H···A	Symmetry operation for *A*	*D*···*A*	*D*–H	H···A	*DHA*, deg
		I			
O(4)–H(4O)···O(1)	*x*, –*y*, 0.5 + *z*	2.525(2)	0.78(3)	1.78(3)	159(4)
O(1*w*)–H(1*w*1)···O(2*w*)	1 – *x*, –*y*, 1 – *z*	2.716(3)	0.74(3)	2.02(3)	157(4)
O(2*w*)–H(1*w*2)···O(2)	0.5 – *x*, 0.5 – *y*, 1 – *z*	2.797(3)	0.82(5)	1.98(5)	169(5)
		II			
O(4)···H(4)···O(6)	0.5 – *x*, –0.5 + *y*, 0.5 – *z*	2.468(2)	1.27(4)	1.20(4)	178(3)
O(1*w*)–H(1*w*1)···O(4*w*)	*x*, *y*, *z*	2.720(2)	0.86(3)	1.87(3)	174(3)
O(1*w*)–H(2*w*1)···O(8)	0.5 + *x*, 1.5 – *y*, –0.5 + *z*	2.821(2)	0.90(4)	1.93(4)	172(3)
O(2*w*)–H(1*w*2)···O(1)	0.5 – *x*, –0.5 + *y*, 0.5 – *z*	2.698(2)	0.92(3)	1.85(3)	152(3)
O(2*w*)–H(2*w*2)···O(7)	*x*, *y*, *z*	2.857(2)	0.81(4)	2.18(4)	141(3)
O(3*w*)–H(1*w*3)···O(2)	0.5 – *x*, –0.5 + *y*, 0.5 – *z*	2.697(3)	0.66(3)	2.05(3)	168(4)
O(3*w*)–H(2*w*3)···O(5*w*)	*x*, *y*, *z*	2.745(3)	0.76(3)	2.01(3)	162(3)
O(4*w*)–H(1*w*4)···O(2)	0.5 + *x*, 1.5 – *y*, 0.5 + *z*	2.731(2)	0.87(3)	1.86(3)	173(3)
O(4*w*)–H(2*w*4)···O(6)	0.5 – *x*, –0.5 + *y*, 0.5 – *z*	2.919(2)	0.91(3)	2.02(3)	169(3)
O(5*w*)–H(1*w*5)···O(4)	–*x*, 1 – *y*, 1 – *z*	2.870(2)	0.77(3)	2.13(3)	160(3)
O(5*w*)–H(2*w*5)···O(1*w*)	–0.5 + *x*, 1.5 – *y*, 0.5 + *z*	2.976(2)	0.78(5)	2.25(5)	157(5)

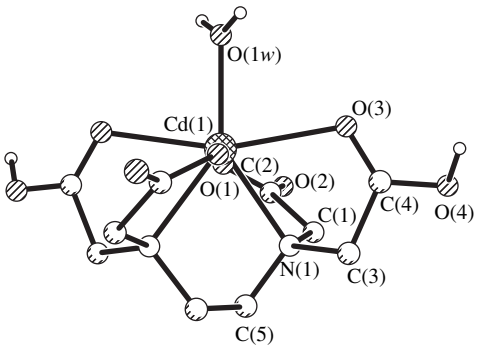

Fig. 1. Structure of the $[Cd(H_2Edta)(H_2O)]$ complex in **I**. The H(C) atoms are omitted.

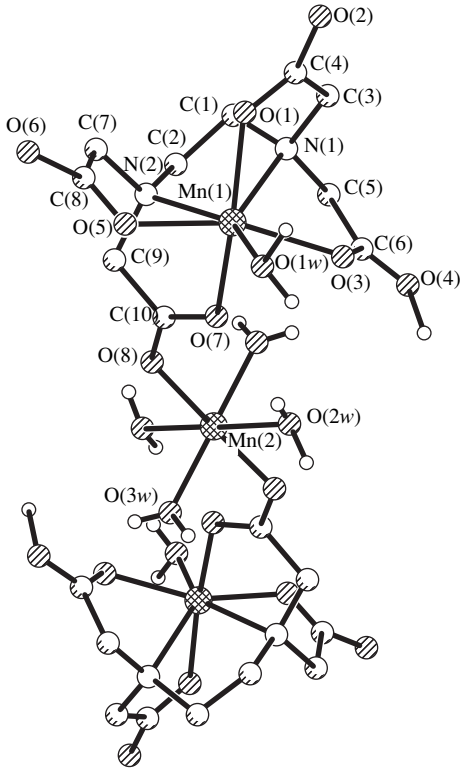

Fig. 2. Structure of the $[Mn(H_2O)_4][Mn(HEdta)(H_2O)]_2$ trimer in **II**. The H(C) atoms are omitted. The coordination bond lengths have the following values (Å): Mn(1)–O(1), 2.219(1); Mn(1)–O(3), 2.225(1); Mn(1)–O(5), 2.264(1); Mn(1)–O(7), 2.266(1); Mn(1)–O(1*w*), 2.234(1); Mn(1)–N(1), 2.402(2); Mn(1)–N(2), 2.344(1); Mn(2)–O(8), 2.200(1); Mn(2)–O(2*w*), 2.160(2); and Mn(2)–O(3*w*), 2.150(2).

have close linear parameters, but the unique angles differ by ~15° (for **V**, a = 11.074(2) Å, b = 9.856(2) Å, c = 14.399(2) Å, and β = 95.86(1)°]. The Cd and Fe complexes are characterized by identical site symmetry and a close ratio between the coordination bond lengths. Moreover, the metal atoms in **I** and **V** are situated at approximately equal distances from the glide reflection planes: the Fe atom (0, 0.1906, 0.25) from the *n* plane and the Cd atom (0.5, 0.0456, 0.75) from the *c* plane. In an alternative unit cell of **I**, which is related to the standard cell by the [–1 0 0, 0 –1 0, 1 0 1] transformation matrix, the *c* and *n* glide planes change places and the coordinates of the Cd atom are brought to the coordinates of the Fe atom. In the transformed unit cell, the unique angle is even larger than that in the standard cell (β = 116.89°) and the positions of the ligand atoms and water molecules differ from the corresponding atomic positions in **V**. As a consequence, crystals **I** and **V** have different hydrogen-bond systems. Thus, compounds **I** and **V** are not isostructural.

Crystal structure II. Crystals **II** are built of centrosymmetric trinuclear $[Mn(1)(HEdta)(H_2O)]_2[Mn(2)(H_2O)_4]$ complexes (Fig. 2) and crystallization water molecules. The environment of the Mn(1) atom is formed by the N(1), N(2), O(1), O(3), O(5), and O(7) atoms of the $HEdta^{3-}$ hexadentate ligand and the O(1*w*) atom of a water molecule. The environment of the Mn(2) atom includes the O(8) atom of the bridging carboxyl group, the O(2*w*) and O(3*w*) atoms of water molecules, and the atoms related to the three above atoms by the center of symmetry. Specific structural features of **II** were discussed in [2] and review [9]. We dwell on only some aspects.

Due to the unambiguous location of the hydrogen atoms in structure **II**, we can state that the H(4) atom forms the symmetric O(4)···H(4)···O(6)' hydrogen bond (Table 3). Therefore, the C(6)O(3)O(4) and C(8)O(5)O(6) carboxyl groups, which are linked through the acid proton, are half-protonated. In accord with the identical structural functions, these groups have almost equal C–O bond lengths [C(6)–O(3), 1.237(2) Å; C(6)–O(4), 1.277(2) Å; C(8)–O(5), 1.235(2) Å; and C(8)–O(6), 1.276(2) Å]. However, contrary to the expectations, the Mn(1)–O(3) and Mn(1)–O(5) bond lengths differ significantly [2.225(1) and 2.264(1) Å, respectively]. In the isostructural Fe^{2+} compound [1], the difference between the corresponding bond lengths is not so large [the Fe–O distances are 2.215(2) and 2.200(2) Å], and in the Cd^{2+} compound [3], this difference is absent [the Cd–O distances are 2.345(2) and 2.349(2) Å]. Another unexpected feature of compound **II**—the inequality of the Mn(1)–N bond lengths [2.344(1) and 2.402(1) Å]—is also characteristic of its isostructural analogues: the difference in the *M*–N bond lengths is 0.069 Å for *M* = Fe and 0.040 Å for *M* = Cd.

The H(4) atoms link the $[Mn(1)(HEdta)(H_2O)]^-$ complexes into chains running along the screw axes and the trimers into layers. All H atoms of water molecules are involved in hydrogen bonding (Table 3). The *w*2 molecule links the complexes within the layer, and the remaining water molecules link the layers into a three-dimensional framework.

REFERENCES

1. T. Mizuta, J. Wang, and K. Miyoshi, Inorg. Chim. Acta **230** (1–2), 119 (1995).
2. S. Richards, B. Pedersen, J. V. Silverton, and J. L. Hoard, Inorg. Chem. **3** (1), 27 (1964).
3. X. Solans, M. Font-Bardia, M. Aguilo, *et al.*, Acta Crystallogr., Sect. C: Cryst. Struct. Commun. **43** (4), 648 (1987).
4. G. M. Sheldrick, Acta Crystallogr., Sect. A: Found. Crystallogr. **46** (6), 467 (1990).
5. G. M. Sheldrick, *SHELXL93: Program for the Refinement of Crystal Structures* (Univ. of Göttingen, Göttingen, 1993).
6. X. Solans, S. Gali, M. Font-Altaba, *et al.*, Acta Crystallogr., Sect. C: Cryst. Struct. Commun. **39** (4), 438 (1983).
7. X. Solans, M. Font-Altaba, J. Oliva, and J. Herrera, Acta Crystallogr., Sect. C: Cryst. Struct. Commun. **41** (7), 1020 (1985).
8. M. A. Poraĭ-Koshits, A. I. Pozhidaev, and T. N. Polynova, Zh. Strukt. Khim. **15** (4), 1118 (1974).
9. T. N. Polynova and M. A. Poraĭ-Koshits, Itogi Nauki Tekh., Ser. Kristallokhim. **18**, 64 (1984).

Translated by I. Polyakova

Crystallography Reports, Vol. 46, No. 1, 2001, pp. 46–50. Translated from Kristallografiya, Vol. 46, No. 1, 2001, pp. 53–57.

STRUCTURE OF COORDINATION COMPOUNDS

Crystal Structure of Disordered Diethylammonium Oxo(1-hydroxyethane-1,1-diphosphonato)vanadate(IV) Hydrate

G. G. Aleksandrov*, V. S. Sergienko*, and E. G. Afonin**

** Kurnakov Institute of General and Inorganic Chemistry, Russian Academy of Sciences, Leninskiĭ pr. 31, Moscow, 117907 Russia*

*** State Enterprise "Chemical Engineering Laboratory," Kaluga, Russia*

Received March 24, 1999

Abstract—Crystals of diethylammonium oxo(1-hydroxyethane-1,1-diphosphonato)vanadate(IV) hydrate have been synthesized, and their structure has been determined by X-ray diffraction analysis. In the crystal, three metal atoms of the disordered anionic complex in two orientations (the occupancies are 0.67 and 0.33) are linked in pairs by the tetradentate bis(chelate)-μ_2-bridging ligands H_nL^{4-n} with the formation of the $[V_3O_4(H_nL)_3]$ cyclic trimers. As a first approximation, the coordination polyhedron of the V(1) and V(2) atoms in both orientations can be considered a tetragonal pyramid completed to a strongly distorted octahedron by the O atom of the terminal hydroxo ligand in the case of the V(2) atom or by the μ_3-bridging oxo O atom for the V(1) atom. The diethylammonium cations and crystallization water molecules are disordered. The structural formula of the complex can be most correctly represented as $[(C_2H_5)_2NH_2]_2[\{V^{4+}O(\mu_2\text{-}H_2L)\}_3(\mu_3\text{-}O)]_{0.67}[\{V^{4+}(OH)(\mu_2\text{-}HL)\}_3(\mu_3\text{-}O)]_{0.33} \cdot 2H_2O$. © *2001 MAIK "Nauka/Interperiodica".*

INTRODUCTION

Bivalent metals and 1-hydroxyethane-1,1-diphosphonic acid $CH_3C(OH)(PO_3H_2)_2$ (*Hedp*, H_4L) can form a large number of complexes with different stoichiometric compositions and various degrees of H_4L deprotonation. A wide variety of compounds is observed in the series $M_2^{1+}M^{2+}(H_2L)_2 \cdot nH_2O$, where M^{1+} are the K^+, Cs^+, $[NH_4]^+$, and $[(C_2H_5)_2NH_2]^+$ cations [1–5]. The oxovanadium(IV) cation also forms the $K_2VO(H_2L)_2 \cdot 5H_2O$ complex [6], which belongs to this series. However, another complex can be isolated from an aqueous solution of diethylammonium oxo(1-hydroxyethane-1,1-diphosphonato)vanadate(IV) $[(C_2H_5)_2NH_2]_2VO(H_2L)_2$. In the present work, the composition and crystal structure of this complex were determined by X-ray diffraction.

EXPERIMENTAL

Synthesis. A solution of $(C_2H_5)_2NH_2(H_3L)$ (5.58 g, 2×10^{-2} mol) in water (20 ml) was added to a suspension of $VO(OH)_2 \cdot nH_2O$ (10^{-2} mol) in water (30 ml) and then was heated with water bath to the complete dissolution of the precipitate. The solution was allowed to evaporate slowly until an ample precipitate was obtained. The precipitate was filtered off and dissolved in water upon heating. The solution was left to evaporate slowly at room temperature. Then, the solution was poured out and the precipitate was quickly washed with water, wrung out using a paper filter, and dried in air at room temperature to a constant weight. Single crystals suitable for X-ray structure analysis were chosen from the obtained crystal samples of complex **I**.

X-ray diffraction analysis. Crystals **I** ($C_{4.67}H_{15.33}N_{0.67}O_9P_2V$) are hexagonal, $a = 13.509(5)$ Å, $c = 14.607(4)$ Å, $V = 2309(1)$ Å^3, $\rho_{calcd} = 1.460$ g/cm^3, $\mu_{Mo} = 8.81$ cm^{-1}, $M = 337.8$ amu, $F(000) = 1042$, $Z = 6$, and space group $P6_3/m$.

The experimental data were collected at room temperature on an Enraf–Nonius CAD4 automated four-circle diffractometer (λMo, graphite monochromator, ω scan mode, $2\theta_{max} = 60°$). A total of 2759 reflections were measured, of which 1160 unique reflections with $I > 2\sigma(I)$ were used in the structure determination ($R(int) = 0.0344$; $-11 < h < 0$, $-5 < k < 17$, and $-20 < l < 0$).

The structure was solved by the direct method and refined by the least squares procedure (on F^2) in the full-matrix anisotropic approximation for the V, P, O, and C(*L*) atoms and in the full-matrix isotropic approximation for the N and C atoms of the diethylammonium cation (SHELXL93 [7]). In the course of the structure determination, it was revealed that the majority of atoms in the anionic complex and, especially, in the $(C_2H_5)_2NH_2^+$ cation are substantially disordered, which predetermined a low accuracy of the structure solution: a high value of *R*, large errors in determination of the

atomic coordinates, and a considerable scatter in the geometric parameters (for more detail, see below).

The final structure refinement parameters for the nonstoichiometric composition $[(C_2H_5)_2NH_2]_{0.67}[VO(OH)_{0.33}(H_2L)_{0.67}(HL)_{0.33}] \cdot 0.67H_2O$ were as follows: $R_1 = 0.071$, $wR_2 = 0.185$, and $GOOF = 1.144$ for 1160 nonzero reflections (139 refined parameters); $R_1 = 0.087$ and $wR_2 = 0.199$ for all the reflections; the extinction coefficient was 0.005(2); and $\Delta\rho_{max} = 0.544$ e/Å^3 and $\Delta\rho_{min} = -0.430$ e/Å^3.

An attempt was made to refine the structure in a rigidly fixed model using the stoichiometric formula $[(C_2H_5)_2NH_2][VO(HL)]$ under the constraints that the site occupancies of atoms in the anionic complex in two different orientations tend to 0.67 and 0.33 and that the N–C and C–C bond lengths and the CNC and NCC angles in the diethylammonium cation approach the normal values. However, this attempt led to a substantial deterioration of the refinement parameters and decreased the accuracy of structure determination ($R_1 = 0.094$, $wR_2 = 0.271$, and $GOOF = 1.622$ for 1160 reflections).

The atomic coordinates and thermal parameters U_{eq}/U_{iso} of structure **I** are listed in the table.

Atomic coordinates and thermal parameters U_{eq}/U_{iso}

Atom	*x*	*y*	*z*	U_{eq}/U_{iso}, Å^2
V(1)	0.7439(2)	0.1828(2)	0.25	0.0601(7)
V(2)	0.7145(3)	0.2302(4)	0.25	0.0457(9)
P(1)	0.4914(1)	0.0705(1)	0.3507(1)	0.0601(6)
O(11)	0.616(2)	0.117(3)	0.3391(9)	0.064(4)
O(21)	0.446(2)	0.152(1)	0.348(2)	0.056(4)
O(31)	0.447(2)	–0.010(2)	0.437(1)	0.076(8)
O(12)	0.624(3)	0.124(4)	0.360(2)	0.053(6)
O(22)	0.476(3)	0.178(3)	0.343(4)	0.060(8)
O(32)	0.432(4)	0.005(3)	0.435(2)	0.046(5)
O(4)	0.3078(9)	–0.072(1)	0.25	0.165(5)
O(51)	0.7847(8)	0.0976(7)	0.25	0.107(2)
O(52)	0.6667(2)	0.3333	0.25	0.071(3)
C(1)	0.4311(8)	–0.0206(7)	0.25	0.072(2)
C(2)	0.466(1)	–0.1097(8)	0.25	0.098(4)
N, O(1)	0.375(2)	0.204(2)	0.511(2)	0.136(9)
N, O(2)	0.6667(2)	0.3333	0.521(2)	0.245(9)
C(3)	0.472(1)	0.256(1)	0.532(1)	0.062(4)
C(4)	0.578(2)	0.267(2)	0.567(2)	0.094(6)
C(5)	0.263(3)	0.138(3)	0.542(3)	0.16(1)
C(6)	0.233(6)	0.061(6)	0.612(5)	0.28(3)
C(7)	0.358(2)	0.142(2)	0.577(2)	0.100(7)
C(8)	0.315(3)	0.190(3)	0.494(3)	0.122(9)
C(9)	0.251(5)	0.230(5)	0.445(4)	0.22(2)

RESULTS AND DISCUSSION

Complex **I** is the green crystalline compound, which is soluble in water with the formation of the bright blue solution. The compound is readily soluble in aqueous solutions of strong mineral acids, ammonia water, and alkalis and poorly soluble in dimethyl sulfoxide, dimethylformamide, acetic acid, ethanol, glycerol, ethyl acetate, carbon tetrachloride, and benzene.

The structural units of crystal **I** are the anionic complexes, diethylammonium cations, and crystallization water molecules. In the anionic complex (figure), four out of nine atoms are disordered over two positions, each with an occupancy ratio of 2 : 1. Actually, the site occupancy is equal to 0.67 for the V(1), O(11), O(21), and O(31) atoms and 0.33 for the V(2), O(12), O(22), and O(32) atoms. Six atoms—P(1), O(4), C(1), C(2), O(51), and O(52)—are completely ordered. The O(51) and O(52) atoms occupy the special positions 6*h* (symmetry *m*) and 2*d* (symmetry $\bar{6}$), respectively. As a result, the occupancies of the O(51) and O(52) atoms (for the composition $[VO(H_nL)]$) are equal to 1.0 and 0.33, respectively; the stoichiometric ratio $V : O_{oxo} = 1 : 1$ breaks down; and the actual ratio $V : O_{oxo}$ is 1 : 1.33. As noted above, our attempt to refine the structure with a constant occupancy of 0.67 for the V(1) and O(51) atoms led to an increase in the *R* value.

In the two main variants of bonding the V(1) and V(2) atoms with the O(1*n*), O(2*n*), and O(5*n*) atoms (where *n* = 1 and 2, respectively), the corresponding atoms [except for the O(51) and O(52) atoms] are drawn closer together in pairs.[1] This results in two additional variants of the orientational disordering of the anionic complex: V(1), O(12), O(22), O(51) and V(2), O(11), O(21), O(52).

The coordination polyhedron of the vanadium atoms lying in the *m* plane, to a first approximation, can be described as a tetragonal pyramid with two pairs of oxygen atoms O(1*n*) and O(2*n*) (O_{equat}) of four phosphonate groups belonging to two H_nL^{4-n} ligands in the equatorial plane [V–O, 1.86(2)–2.11(4) Å] and the doubly bonded oxo O(5*n*) atom (O_{oxo}) in the axial position. For each orientation of the anionic complex, three vanadium atoms are linked together in pairs through the μ_2-bridging *Hedp* ligands around the sixfold axis of inversion with the formation of a cyclic trimer. However, the trinuclear complexes containing the V(1) and V(2) atoms differ considerably. In the case of the anionic complex with the V(1) atom, the vanadyl O(51) atom (in the *m* plane) is terminal [V(1)–O(51),

[1] The distances are as follows: V(1)–V(2), 0.908(6) Å; O(11)–O(12), 0.32(3) Å; O(21)–O(22), 0.39(5) Å; and O(31)–O(32), 0.35(6) Å.

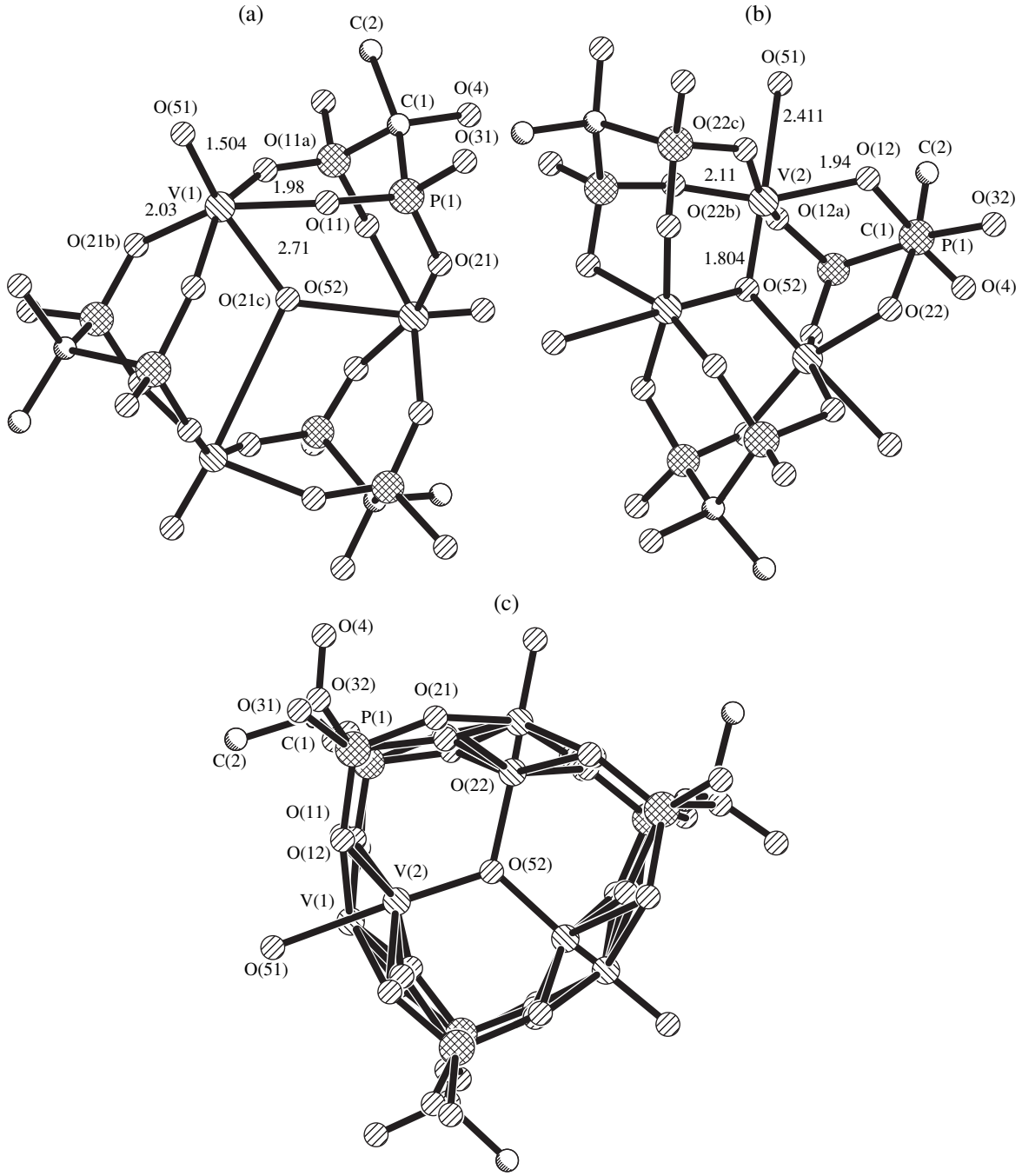

Fig. 1. Structures of cyclic trinuclear complexes (a) $[\{V(1)O_{oxo}(\mu_2\text{-}H_2L)\}_3(\mu_3\text{-}O)]_{0.67}$ and (b) $[\{V(2)(OH)(\mu_2\text{-}HL)\}_3(\mu_3\text{-}O)_{oxo}]_{0.33}$ and (c) the overall pattern of superposing two orientations of the cyclic trimer in the anionic complex of structure **I**.

1.504(7) Å]. At the same time, in the anionic complex with the V(2) atom, the oxo O(52) atom occupies the special position in the $\bar{6}$ axis and fulfills the function of μ_3-bridging ligand [V(2)–O(52), 1.804(5) Å]. The tetragonal–pyramidal environment of the vanadium atoms is completed to a strongly distorted octahedron by the weak V–O_{trans} contact [2.411(9) Å] with the O(51) atom of the terminal hydroxy group in the case of the V(2) atom (for more detail, see below) and by the considerably weaker V–O_{trans} contact with the μ_3-bridging O(52) atom [2.71(3) Å] for the V(1) atom. It is believed that a site occupancy equal to unity for the O(51) atom in fact results from the overlapping of the positions of two atoms, namely, the terminal O_{oxo} atom (occupancy is 0.67) in the V(1) polyhedron and the $O(OH)_{trans}$ atom (occupancy is 0.33) in the V(2) polyhedron. By analogy, a site occupancy equal to 0.33 for the O(52) atom

is contributed by the O_{oxo} and O_{trans} μ_3-bridging atoms in the V(2) and V(1) polyhedra in the ratio 1 : 2 (0.11 : 0.22).

The structural manifestation of the *trans* effect of the doubly bonded oxo ligand (elongation of the metal–ligand bond in the *trans* position to the $M{=}O_{oxo}$ bond) is typical of the d^0 and d^1 metal complexes, specifically the d^1 vanadium(IV) complexes [8]. In the structure under consideration, the V(1)–O(52) bond [*trans* to the strong terminal bond $V(1)–O(51)_{oxo}$] is substantially more weakened (lengthened) than the V(2)–O(51) bond [*trans* to the weaker bridging bond $V(2)–O(52)_{oxo}$]. As a consequence, the vanadium atoms are appreciably shifted from the equatorial plane of the coplanar atoms O(*L*) toward the oxo O(5*n*) atoms by 0.41 and 0.57 Å for two orientations of the V(1) polyhedron and by 0.34 and 0.49 Å for two orientations of the V(2) polyhedron. The bond angles in the coordination polyhedra of the vanadium atoms lie in the following ranges: $O_{oxo}VO_{equat}$, 97(1)°–103(1)°; $O_{oxo}VO_{trans}$, 178.1(3)° and 179.0(3)°; $O_{equat}VO_{equat}$, 80(1)°–100(2)° and 156(1)°–160(1)°; and $O_{equat}VO_{trans}$, 76(1)°–82(1)°.

The H_nL^{4-n} ligand acts as a tetradentate bis(chelate)-μ_2-bridging ligand and closes two pairs of the six-membered metallocycles

$$\overbrace{V(n)–O(1n)–P(1)–C(1)–P(1)^a–O(1n)^a}$$
(A and B)

and $$\overbrace{V(n)–O(2n)^b–P(1)^b–C(1)^b–P(1)^c–O(2n)^c}$$
(C and D)

for every of two orientations: n = 1 (A and C) and 2 (B and D).[2] All four rings have a chair conformation in which the V(*n*) and C(1) atoms deviate from the planes of the remaining four atoms by 0.239 and –0.92 Å for the A ring, 0.437 and –0.95 Å for the C ring, 0.948 and –0.90 Å for the B ring, and 0.601 and –0.80 Å for the D ring. The dihedral angles between the planar tetraatomic fragments of metallocycles are equal to 59.0° for A and C and 43.3° for B and D.

As follows from the X-ray structure analysis, the structural elements are disordered, the stoichiometric ratio V : O_{oxo} is violated, and the atomic positions of the $(C_2H_5)_2NH_2^+$ cation are only partly occupied (see below). All these factors make the determination of the charge and the degree of protonation of the *Hedp* anion more difficult. Usually, this problem is solved either by the direct location of hydrogen atoms or from analysis of the P–O bond lengths: the P–O bonds with both the terminal oxygen atoms and the oxygen atoms coordinated by metal atoms are considerably shorter than the P–O(H) bonds.[3] However, in our case, because of the disordering and low accuracy in the location of atoms, the range of the P(1)–O(1*n*)[O(2*n*)] distances to the oxygen atoms bonded to metal atoms overlaps with the range of the P(1)–O(3*n*) distances to the terminal oxygen atoms: 1.48(2)–1.57(4) and 1.50(3)–1.57(2) Å, respectively [the mean values are 1.53 and 1.53(5) Å].[4]

All three oxygen atoms of the phosphonate group in one orientation (n = 2) and two O(*L*) atoms in the other orientation (n = 1) are involved in the short intermolecular contacts with the diethylammonium cations and (or) water molecules in the N,O(1) position: N,O(1)···O(21), 2.79(4) Å; N,O(1)···O(31), 3.00(4) Å; N,O(1)···O(12), 3.03(4) Å; N,O(1)···O(22), 2.91(6) Å; and N,O(1)···O(32), 2.90(5) Å.

It is believed that either of the two positions of light atoms N,O(1) and N,O(2) is statistically occupied by nitrogen atoms of the diethylammonium cation and by oxygen atoms of the crystallization water molecules. The N,O(1) position is only partly filled (occupancy is equal to 0.67). A number of orientations of ethyl groups containing seven carbon atoms—C(3), C(4), C(5), C(6), C(7), C(8), and C(9)—correspond to the N,O(1) position [on the average: N–C, 1.20(4) Å; C–C, 1.45(4) Å; and NCC, 133(4)°]. The disordering has a very complex character: it is possible to distinguish four overlapping orientations of the N–C(*m*)–C(*p*) fragments (m = 3, 5, 7, and 8; p = 4, 6, 6, and 9). Similar to the C(4), C(6), and C(9) atoms, the C(3), C(5), C(7), and C(8) atoms were refined under the constraint that the total occupancy for either of the two groups of atoms tends to 0.67. The N,O(2) atom is located in the special position at axis 3. Three orientations of the $(C_2H_5)_2$ groups, which are rotated through 120° [N,O(2)–C(4), 1.27(4) Å; C(4)–C(3), 1.45(3) Å; and angle N,O(2)C(4)C(3), 115.(2)°], correspond to the N,O(2) atom. It can be supposed that the symmetric orientational disordering about the threefold axis "blocks" the possible short interionic contacts N–H···O(*L*), (*L*)O–H···O(H_2O), and (H_2O)O···O(*L*). Moreover, we can assume that the contribution from the oxygen atom of the water molecule to the N,O(1) position is greater than that to the N,O(2) position.

As regards the structure of the trinuclear anionic complex $[\{V(2)O(\mu_2\text{-}H_nL)\}_3(\mu_3\text{-}O)_{oxo}]_{0.33}$ in one of its orientations, we note that the terminal O(51) atom separated from the metal atom by a large distance of 2.41 Å cannot be the oxo atom. It is reasonable to assume that the doubly bonded oxo ligand [at the V(1) atom] and the OH hydroxo ligand [at the V(2) atom] are "mixed" in this position with an occupancy ratio of

[2] Symmetry operations: (a) *x*, *y*, 0.5 – *z*; (b) 1 – *y*, *x* – *y*, *z*; and (c) 1 – *y*, *x* – *y*, 0.5 – *z*.

[3] For *Hedp* compounds with alkali metals and cations of organic bases, the mean P–O(H) and P=O bond lengths are equal to 1.575 and 1.490 Å, respectively [9].

[4] The other geometric parameters of the H_nL^{4-n} ligands are as follows: P(1)–C(1), 1.828(5) Å; C(1)–O(4), 1.45(1) Å; C(1)–C(2), 1.49(1) Å; angles OP(1)O, 104(1)°–119(2)°; OP(1)C(1), 103(1)°–113(2)°; VOP(1), 113(1)°–135(2)°; O(4)P(1)C(1), 110.0(5)°; O(4)C(1)C(2), 112.2(9)°; P(1)C(1)C(2), 109.2(5)°; and $P(1)C(1)P(1)^a$, 107.2(4)°.

2 : 1.[5] In this case, the doubly charged H_2L^{2-} ligand for V(1) and the triply charged ligand HL^{3-} for V(2) are most consistent with the balance of positive and negative charges of structural elements. Therefore, the structural formula of the studied compound can be represented as $[(C_2H_5)_2NH_2]_2[\{V^{4+}O(\mu_2\text{-}H_2L)\}_3(\mu_3\text{-}O)]_{0.67}[\{V^{4+}(OH)(\mu_2\text{-}HL)\}_3(\mu_3\text{-}O)]_{0.33} \cdot 2H_2O$.

Sanna *et al.* [10] studied the complex formation between VO^{2+} and H_4L in an aqueous solution and found the $VO(HL)^-$ and $(VO)_3L_3^{6-}$ complexes. The results of our work demonstrate that the trinuclear vanadium(IV) complexes with *Hedp* are formed not only in a solution but also in the solid phase, even though their compositions are not completely identical.

[5] In principle, this position can be occupied by the oxygen atom of the water molecule. However, in this case, reasoning from the charge balance condition, the Hedp ligand should be completely deprotonated (L^{4-}), which is highly improbable.

REFERENCES

1. V. S. Sergienko, G. G. Aleksandrov, and E. G. Afonin, Zh. Neorg. Khim. **42** (8), 1291 (1997).
2. V. S. Sergienko, E. G. Afonin, and G. G. Aleksandrov, Koord. Khim. **24** (4), 293 (1998).
3. V. S. Sergienko, G. G. Aleksandrov, and E. G. Afonin, Koord. Khim. **24** (6), 455 (1998).
4. V. S. Sergienko, E. G. Afonin, and G. G. Aleksandrov, Zh. Neorg. Khim. **43** (6), 1002 (1998).
5. V. S. Sergienko, G. G. Aleksandrov, and E. G. Afonin, Koord. Khim. **25** (6), 451 (1999).
6. E. G. Afonin, Zh. Obshch. Khim. **69** (3), 368 (1999).
7. G. M. Sheldrick, *SHELXL93: Program for the Refinement of Crystal Structures* (Univ. of Göttingen, Göttingen, 1993).
8. M. A. Poraĭ-Koshits and V. S. Sergienko, Usp. Khim. **59** (1), 86 (1990).
9. V. S. Sergienko, Kristallografiya **45** (1), 69 (2000) [Crystallogr. Rep. **45**, 64 (2000)].
10. D. Sanna, G. Micera, P. Buglyo, and T. Kiss, J. Chem. Soc., Dalton Trans., No. 1, 87 (1996).

Translated by O. Borovik-Romanova

Crystallography Reports, Vol. 46, No. 1, 2001, pp. 51–55. Translated from Kristallografiya, Vol. 46, No. 1, 2001, pp. 58–62.

STRUCTURE OF COORDINATION COMPOUNDS

Crystal Structure of Zinc Iodide Complex with Carbamide, $ZnI_2 \cdot 2CO(NH_2)_2$

N. G. Furmanova*, V. F. Resnyanskiĭ, K. S. Sulaĭmankulov**, Sh. Zh. Zhorobekova**, and D. K. Sulaĭmankulova****

** Shubnikov Institute of Crystallography, Russian Academy of Sciences, Leninskiĭ pr. 59, Moscow, 117333 Russia*

*** Institute of Chemistry and Chemical Technology, National Academy of Sciences of Kyrgyzstan, Bishkek, 720071 Kyrgyzstan*

e-mail: furm@rsa.crystal.msk.su

Received July 8, 1999

Abstract—The structure of $ZnI_2 \cdot 2CO(NH_2)_2$ is determined by single-crystal X-ray diffraction. The crystals are monoclinic, a = 12.694(3) Å, b = 6.886(2) Å, c = 13.161(3) Å, β = 110.58(2)°, Z = 4, space group $P2_1/a$, and R = 0.0337 for 2481 reflections. Similar to the chloride analogue, the structure consists of discrete molecules with tetrahedrally coordinated Zn atoms. The bond lengths and angles are as follows: Zn–I, 2.5749(8) and 2.5473(8) Å; Zn–O, 1.954(3) and 1.985(4) Å; IZnI, 113.74(3)°; OZnO, 100.5(2)°; and IZnO, 108.5°–113.1(1)°. The crystal structure agrees with the IR and electronic absorption spectra of the crystals. © *2001 MAIK "Nauka/Interperiodica".*

INTRODUCTION

In the course of systematic X-ray diffraction studies of the carbamide complexes of zinc and cadmium, we have found that crystals of $MX_2 \cdot 2CO(NH_2)_2$ (M = Zn or Cd, and X = Cl or I) have different structures. Crystals of $ZnCl_2 \cdot 2CO(NH_2)_2$ have a molecular structure [1], and the Zn atom is tetrahedrally coordinated by two Cl atoms and two O atoms of the urea molecules. At the same time, crystals of $CdCl_2 \cdot 2CO(NH_2)_2$ have a chain-like structure [2] with bridging Cl atoms and the octahedrally coordinated Cd atom (a similar structure, but with double chains, is observed in crystals of the $CdCl_2 \cdot CO(NH_2)_2$ monocarbamide complex [3]). The crystal structure of $CdI_2 \cdot 2CO(NH_2)_2$ appeared to be unusual [4]. It contains two types of Cd atoms. One of them is tetrahedrally coordinated by the I atoms. This Cd atom occupies a general position and enters into the composition of the anionic chain $[CdI_3]^-_\infty$. The other Cd atom is situated on the twofold axis and has an octahedral coordination formed by the carbamide molecules.

In this respect, the crystal structure of the last representative of the series considered, namely, $ZnI_2 \cdot 2CO(NH_2)_2$ (**I**), was of special interest, and its determination was the goal of this work.

EXPERIMENTAL

Large-sized (up to 1 cm) colorless crystals **I** are slightly turbid and poorly faceted. The crystals were grown by slow cooling [5]. A crystal fragment ~0.12 × 0.35 × 0.50 mm in size was chosen for our X-ray diffraction study. The data were collected on an Enraf–Nonius automated X-ray diffractometer (MoK_α radiation, graphite monochromator) at room temperature. The unit cell parameters were determined from 24 reflections with the ϑ angles ranging from 15.0° to 16.6°. The crystals are monoclinic, a = 12.694(3) Å, b = 6.886(2) Å, c = 13.161(3) Å, β = 110.58(2)°, d_{calcd} = 2.709 g/cm^3, μ(MoK_α) = 79.82 cm^{-1}, Z = 4, and space group $P2_1/a$. The intensities of 6650 reflections were measured in the range ϑ ≤ 30° by the ω scan technique; 4803 of them had $I > 0$. After averaging the intensities of symmetrically equivalent reflections, the data set contained 2601 reflections (R_{av} = 0.122).

All the non-hydrogen atoms were revealed by the direct method in the automatic mode with the AREN program package [6] and the following phase correction of the structure amplitudes [7]. This model was refined by the least-squares method in the isotropic approximation to R = 0.122. The data were then corrected for absorption with the DIFABS program [8]. This reduced the R factor to 0.085, and the R factor for averaging of equivalent reflections decreased to 0.024.

Further refinement was performed with the SHELXL93 program package [9]. The hydrogen atoms were located from the difference Fourier synthesis, their isotropic thermal parameters were fixed, and their positions were refined with restrained N–H bond lengths and the CNH and HNH angles. The final discrepancy factors are R_1 = 0.0365, wR_2 = 0.0809, and $GOOF$ = 1.266 for all 2601 reflections and R_1 = 0.0337 and wR_2 = 0.0797 for 2481 reflections with $I \geq 2\sigma(I)$. The final atomic coordinates and thermal parameters are listed in Table 1.

Table 1. Atomic coordinates ($\times 10^4$ for non-hydrogen atoms and $\times 10^3$ for H atoms) and equivalent (isotropic for H atoms) thermal parameters ($\times 10^3$ Å^2)

Atom	*x*	*y*	*z*	U_{eq}/U_{iso}	Atom	*x*	*y*	*z*	U_{eq}/U_{iso}
Zn	7474(1)	5287(1)	766(1)	40(1)	N(3)	5304(6)	787(10)	6332(9)	124(4)
I(1)	7759(1)	7140(1)	6113(1)	49(1)	N(4)	4962(6)	3942(12)	6157(8)	123(4)
I(2)	6471(1)	7259(1)	8721(1)	52(1)	H(1)	820(3)	123(7)	780(4)	80
O(1)	8877(3)	4282(5)	8741(3)	44(1)	H(2)	926(4)	−0(4)	841(5)	80
O(2)	6669(3)	2821(5)	7136(3)	52(1)	H(3)	1088(3)	154(6)	942(5)	70
C(1)	9401(4)	2709(7)	8806(4)	40(1)	H(4)	1079(3)	360(6)	984(4)	70
C(2)	5668(5)	2541(8)	6557(5)	47(1)	H(5)	456(2)	57(7)	606(8)	140
N(1)	8907(5)	1150(8)	8249(6)	73(2)	H(6)	578(4)	–17(5)	628(9)	140
N(2)	10455(4)	2583(7)	9452(5)	55(1)	H(7)	424(3)	366(8)	574(7)	130
					H(8)	524(4)	508(6)	598(8)	130

The electronic absorption spectrum of crystal **I** was recorded on a PVE UNICAM spectrophotometer (England). The IR spectrum was taken from a KBr pellet on a UP-20 instrument.

RESULTS AND DISCUSSION

Similar to $ZnCl_2 \cdot 2CO(NH_2)_2$ (**II**) [1], compound **I** has a molecular structure with tetrahedrally coordinated Zn atom (Fig. 1). Hence, the structural behavior of the zinc carbamide complexes differs essentially from the behavior of similar cadmium complexes. At the same time, in combination with pyridine N oxide, ZnI_2 forms both molecular crystals $ZnI_2 \cdot 2C_5H_5NO$ [10] similar to **I** and ionic crystals of the composition $3ZnI_2 \cdot 8C_5H_5NO$ with different functions of Zn atoms, namely, $[Zn(C_5H_5NO)_6]^{2+}[Zn(C_5H_5NO)I_3]_2^-$ (a search for crystal structures containing the Zn–I bonds was performed using the Cambridge Structural Database [12]). It is known (see [11] and references therein) that the behavior of polar covalent halides of bivalent metals with respect to a monodentate oxo ligand is primarily determined by the competition between this ligand and the halide. The formation of the $[Zn(C_5H_5NO)I_3]^-$ anionic complex gives evidence for the competition between pyridine N oxide and iodide. We found a similar zinc carbamide complex in the $[Cr(OCN_2H_4)_6]^{3+}[ZnCl_4]^{2-}\{Zn(OCN_2H_4)Cl_3\}^-$ structure [13]. Therefore, it is quite possible that with urea in sufficient excess, ionic complexes of zinc halides, similar to $CdI_2 \cdot 2CO(NH_2)_2$ (**III**) [4], can be obtained in addition to molecular complexes.

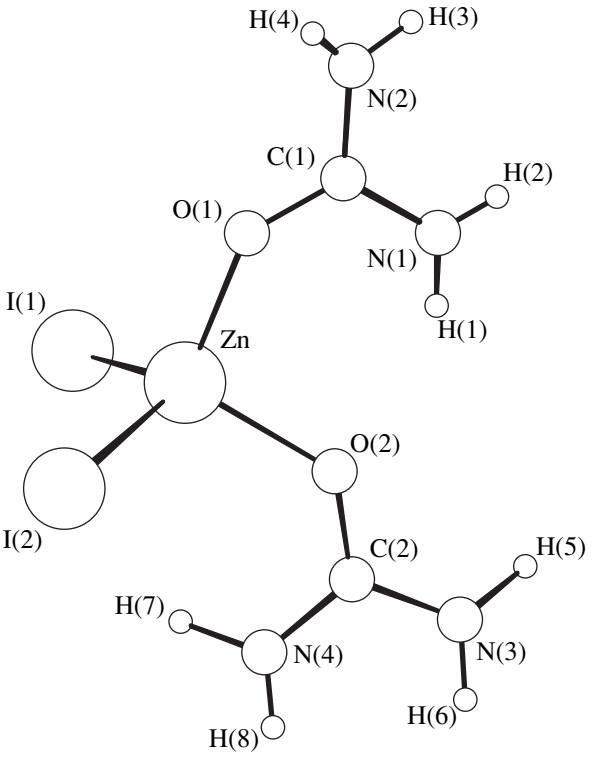

Fig. 1. Molecular structure of $ZnI_2(OCN_2H_4)_2$ and the atomic numbering.

The examination of the electronic absorption spectrum of **I** (Fig. 2) showed that the crystal is transparent in the visible region and the absorption edge lies in the range 260–265 nm. The band with a minimum energy can be interpreted in terms of the Frenkel model as a transfer of an *np* electron of the halide ion to the broadened excited orbital bounded by surrounding cations [14]. The absorption region for crystal **I** differs noticeably from that for crystal **III** (the absorption edge lies at 340–342 nm) in which the iodide ions are included in the $[CdI_3^-]_\infty$ anionic chains [4].

The IR spectrum of **I** (Fig. 3) is similar to that of **II**, as would be expected from the similarity of their structures.

The Zn–I bond lengths in **I** are slightly different [2.5749(8) and 2.5473(8) Å], possibly, because of the

different parts played by the I atoms in the hydrogen bonding (see below). These bond lengths are close to those observed in the L_2ZnI_2 complexes with pyridine N oxide [2.56(5) and 2.58(5) Å] [10] and also with the neutral nitrogen-containing pyrroline [15] and pyridine [16] ligands [2.557(1) Å in the former compound and 2.553(2) and 2.551(2) Å in the latter compound]. At the same time, these bonds are noticeably shorter than the bonds in the $[ZnI_4]^{2-}$ anion in the Cs_3ZnI_5 structure (2.594–2.620 Å) [17].

The Zn–O bond lengths in **I** and **II** agree very closely: their mean values are 1.970(3) and 1.966(2) Å, respectively. The ZnOC angles in **I** [av. 131.4(3)°] are slightly larger than those in **II** [av. 128.2(1)°]. This difference can be explained by a more covalent character of the Zn–O bond in **II** as compared to that in **I** due to the higher electronegativity of the Cl atoms. The difference in intensity of the bands at 1155, 1040, 780, 620, and 535 cm^{-1} in the IR spectra of **I** and **II** indicates the same feature: the higher intensity of absorption in crystal **II** suggests that the Zn–O bond in this complex is stronger than that in **I**. The difference in electronegativity of the Cl and I atoms also manifests itself in the degree of distortion of tetrahedral coordination of the Zn atoms: although the OZnO angles in **I** and **II** are close [100.5(2)° and 99.24(8)°, respectively], the *X*Zn*X* angles differ significantly [IZnI, 113.74(3)° and ClZnCl, 118.56(2)°]. Undoubtedly, this difference is determined by the electronic structure of the complexes, because the steric factor should, on the contrary, increase the IZnI angle with respect to the ClZnCl angle. In the pyridine complexes, the tetrahedral coordination is even more distorted, but the *X*Zn*X* angle also decreases in going from chloride [18] to iodide [16] [121.8(1)° and 120.3(1)°, respectively]. In the complexes with the zwitterionic nicotinamide N^1 acetate ligand, the Zn atom has a slightly different coordination geometry: the *X*Zn*X* and OZnO angles are smaller than the ideal tetrahedral angle. Nonetheless, these angles follow the same pattern; i.e., with an increase in the size of the *X* atom, the *X*Zn*X* angle decreases (107.52(3)° for *X* = Cl [19], 105.9(1)° for *X* = Br [20], and 104.29(2)° for *X* = I [21]) and the OZnO angle increases [in the same series, 106.44(8)°, 107.8(1)°, and 109.24(9)°, respectively].

In crystal **I**, the molecules are linked by an extensive network of hydrogen bonds. These bonds affect the vibrational frequencies of the amino groups in the range 3200–3600 cm^{-1}: in the IR spectrum of **I**, the bands at 3220 and 3270 cm^{-1} appear as shoulders and the band at 3350 cm^{-1} is shifted by 10 cm^{-1} compared to the IR spectrum of free carbamide. Our X-ray diffraction study showed that the N(3)–H(5)···I(1)^3 and N(4)–H(7)···I(1)^5 bonds (for symmetry codes, see Table 2) form helical chains running along the twofold screw axes at the level $z = 1/2$ (Fig. 4), whereas the N(2)–H(3)···I(2)^1 and N(2)–H(4)···O(1)^2 hydrogen bonds form helical chains at the level $z = 1$. In the direction of the *a*-axis, the helices of the first type are linked through the centrosymmetric rings involving the additional N(3)–H(6)···I(1)^4 hydrogen bonds between the molecules related by the *b* translation, and the helices

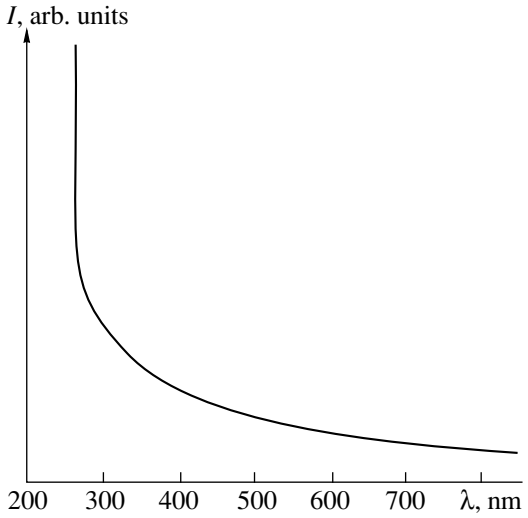

Fig. 2. Electronic absorption spectrum of crystal **I**.

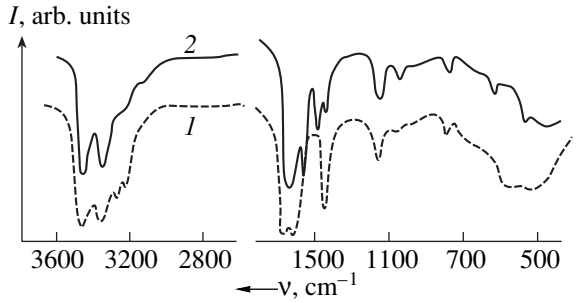

Fig. 3. IR absorption spectra of (*1*) carbamide and (*2*) crystal **I**.

Table 2. Hydrogen bonds in structure **I**

No.	Bond	*D*···*A*, Å	H···*A*, Å	*D*–H···*A*, deg
1	N(1)–H(1)···O(2)	2.935(6)	2.13(3)	150(2)
2	N(1)–H(2)···I(2)^1	3.882(6)	3.11(4)	145(3)
3	N(2)–H(3)···I(2)^1	3.819(5)	2.96(4)	159(4)
4	N(2)–H(4)···O(1)^2	3.101(6)	2.29(5)	153(5)
5	N(3)–H(5)···I(1)^3	3.734(7)	2.98(4)	143(3)
6	N(3)–H(6)···I(1)^4	4.088(8)	3.22(5)	162(4)
7	N(4)–H(7)···I(1)^5	3.762(7)	2.89(5)	162(5)
8	N(4)–H(8)···I(1)	4.196(8)	3.44(5)	140(5)

Note: Symmetry codes: ^{1} $x + 0.5, 0.5 - y, z$; ^{2} $2 - x, 1 - y, 2 - z$; ^{3} $x - 0.5, 0.5 - y, z$; ^{4} $x, y - 1, z$; ^{5} $1 - x, 1 - y, 1 - z$.

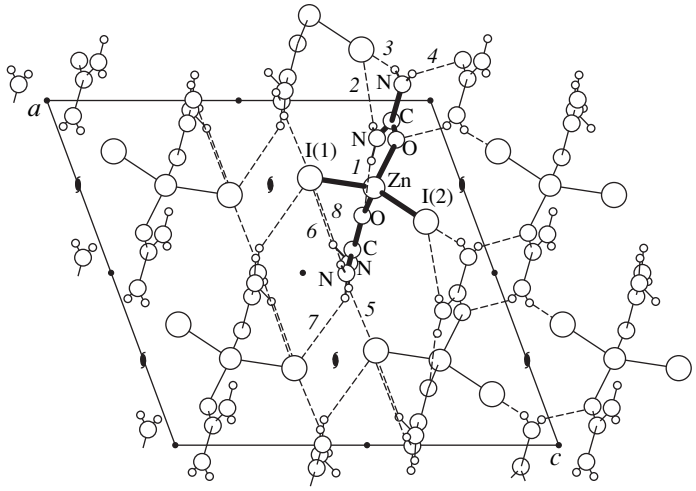

Fig. 4. Molecular packing in crystal **I**. The molecule whose coordinates are given in Table 1 is shown by heavy lines. Hydrogen bonds are shown by dashed lines; their numbering matches that in Table 2.

of the second type are linked through the centrosymmetric H rings formed by the urea molecules of the neighboring complexes. Thus, two slightly different layered systems of hydrogen bonds are formed in the structure in the planes parallel to (001). The layer of the second type is additionally strengthened by the N(1)–H(2)···I(2)[1] hydrogen bonds. The intramolecular N(1)–H(1)···O(2) hydrogen bond and, possibly, the N(4)–H(8)···I(1) bond are also formed in the structure. However, the latter bond, if it even exists, is very weak (Table 2).

As expected, the hydrogen-bond system in crystal **I** differs from that in crystal **II**, which is characterized by space group $P\bar{1}$. However, a common fragment is distinguished in these systems: one of the H atoms of both NH_2 groups of the urea molecule is bound with the halide ion, and the remaining H atoms form the N–H···O hydrogen bonds

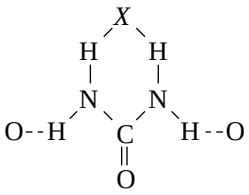

This fragment is also characteristic of other carbamide complexes.

ACKNOWLEDGMENTS

We acknowledge the support of the Russian Foundation for Basic Research in the payment of the license for using the Cambridge Structural Database, project no. 99-07-90133.

REFERENCES

1. N. G. Furmanova, V. F. Resnyanskiĭ, K. S. Sulaĭmankulov, *et al.*, Kristallografiya **43** (2), 269 (1998) [Crystallogr. Rep. **43**, 234 (1998)].
2. M. Nardelli, L. Cavalca, and G. Fava, Gazz. Chim. Ital. **87**, 1232 (1957).
3. N. G. Furmanova, D. K. Sulaĭmankulova, V. F. Resnyanskiĭ, and K. S. Sulaĭmankulov, Kristallografiya **41** (4), 669 (1996) [Crystallogr. Rep. **41**, 632 (1996)].
4. N. G. Furmanova, V. F. Resnyanskiĭ, D. K. Sulaĭmankulova, *et al.*, Kristallografiya **42** (3), 467 (1997) [Crystallogr. Rep. **42**, 421 (1997)].
5. V. F. Resnyanskiĭ, D. K. Sulaĭmankulova, V. A. Kuznetsov, *et al.*, Kristallografiya **38** (5), 212 (1993) [Crystallogr. Rep. **38**, 696 (1993)].
6. V. I. Andrianov, Kristallografiya **32** (1), 228 (1987) [Sov. Phys. Crystallogr. **32**, 130 (1987)].
7. V. I. Andrianov, T. A. Shibanova, and V. I. Simonov, Kristallografiya **32** (1), 41 (1987) [Sov. Phys. Crystallogr. **32**, 20 (1987)].
8. N. Walker and D. Stuart, Acta Crystallogr., Sect. A: Found. Crystallogr. **39**, 158 (1983).
9. G. M. Sheldrick, *SHELXL93: Program for the Refinement of Crystal Structures* (Univ. of Göttingen, Göttingen, 1993).
10. G. Sawitzki and H.-G. von Schnering, Chem. Ber. **107**, 3266 (1974).
11. S. Jin, M. Nieuwenhuysen, and G. J. Wilkins, J. Chem. Soc., Dalton Trans., 2071 (1992).
12. F. H. Allen and O. Kennard, Chem. Design Automat. News **8**, 31 (1993).
13. N. G. Furmanova, V. B. Bergo, V. F. Resnyanskiĭ, *et al.*, Kristallografiya **43** (4), 646 (1998) [Crystallogr. Rep. **43**, 598 (1998)].
14. S. V. Volkov and K. B. Yatsimirskiĭ, *Spectroscopy of Molten Salts* (Naukova Dumka, Kiev, 1977), p. 33.

15. A. A. Freer, G. McDermott, J. C. Melville, and D. J. Robins, Acta Crystallogr., Sect. C: Cryst. Struct. Commun. **C49**, 2115 (1993).
16. J. F. Le Querler, M. M. Borel, and A. Leclaire, Acta Crystallogr., Sect. B: Struct. Crystallogr. Cryst. Chem. **B33**, 2299 (1977).
17. K. Friese, G. Madariaga, and T. Breczewski, Acta Crystallogr., Sect. C: Cryst. Struct. Commun. **C54**, 1737 (1998).
18. W. L. Steffen and G. L. Palenik, Acta Crystallogr., Sect. B: Struct. Crystallogr. Cryst. Chem. **B32**, 298 (1976).
19. V. Zelenak, K. Gyoryova, I. Cisarova, and J. Loub, Acta Crystallogr., Sect. C: Cryst. Struct. Commun. **C52**, 808 (1996).
20. V. Zelenak, K. Gyoryova, and I. Cisarova, Main Group Met. Chem. **18**, 211 (1995).
21. V. Zelenak, K. Gyoryova, I. Cisarova, and J. Loub, Acta Crystallogr., Sect. C: Cryst. Struct. Commun. **C52**, 1917 (1996).

Translated by I. Polyakova

Crystallography Reports, Vol. 46, No. 1, 2001, pp. 56–59. Translated from Kristallografiya, Vol. 46, No. 1, 2001, pp. 63–66.

STRUCTURE OF ORGANIC COMPOUNDS

Structure of a New Crystalline Modification of 4-Amino-5-Ethoxymethyl-1,2-Dimethylpyrimidinium Iodide

N. E. Zhukhlistova and G. N. Tishchenko†

Shubnikov Institute of Crystallography, Russian Academy of Sciences, Leninskiĭ pr. 59, Moscow, 117333 Russia

Received April 21, 1999

Abstract—The structure of a new crystalline modification (**II**) of 4-amino-5-ethoxymethyl-1,2-dimethylpyrimidinium iodide, $C_9H_{16}IN_3O$, the major product of methylation of 4-amino-5-ethoxymethyl-2-methylpyrimidine has been determined. The lattice parameters are a = 6.528(4) Å, b = 15.325(7) Å, c = 12.653(6) Å, γ = 97.57(50)°, sp. gr. $P2_1/b$, Z = 4, R = 0.0348 (over 1480 independent reflections). The molecule is planar. Its pyrimidine ring has the 2,5-diene structure and shows a weak tendency to adopt the C(2)-sofa conformation. Molecules in the crystal structure are linked into centrosymmetric dimers by N(8)–H···N(3) hydrogen bonds. These dimers, in turn, are linked into a three-dimensional framework by I^--ions. The structure of modification **II** is compared with the structures of other 4-aminopyrimidines. © *2001 MAIK "Nauka/Interperiodica".*

INTRODUCTION

Heteroaromatic nitrogen-containing compounds are widely used in the chemistry of dyes and polymers and in manufacturing of drugs. In particular, 4-amino-5-ethoxymethyl-2-methylpyrimidine is used to synthesize vitamin B_1. Methylation of this compound yielded a mixture of two isomers of 4-amino-5-ethoxymethyl-1,2-dimethylpyrimidine, in which the nitrogen atoms of the pyrimidine ring are quaternized. The structure of the crystalline modification (**I**) of the major isomer was established in [1]; it belongs to the monoclinic system and is described by the sp. gr. *B*2/*b*. In this study, the structure of another crystalline modification (**II**) of this isomer was established.

STRUCTURE DETERMINATION

Crystals of a new modification of 4-amino-5-ethoxymethyl-1,2-dimethylpyrimidinium iodide were grown by slow evaporation of the solvent from DMSO in air at room temperature. The parameters of the monoclinic unit cell were determined on a Syntex-$P2_1$ diffractometer; a = 6.528(4) Å, b = 15.325(7) Å, c = 12.653(6) Å, γ = 97.57(50)°, sp. gr. $P2_1/b$, M = 309.151, V = 1254(11) Å^3, Z = 4, ρ_{calcd} = 1.562 g/cm^3.

A total of 1626 reflections were collected on a Syntex $P2_1$ diffractometer using the θ/2θ scanning technique, the CuK_α radiation, and a graphite monochromator. The absorption correction was introduced by the semiempirical method using a transmission curve.

The structure was solved by the direct method with the use of the SHELXS86 program package [2] and refined with the use of the SHELXL93 program package [3]. The coordinates of 11 hydrogen atoms were determined from difference electron-density maps. The coordinates of the remaining seven hydrogen atoms were geometrically calculated. The values of the thermal parameters of hydrogen atoms were assumed to be 1.2 times higher than B_{eq} of those non-hydrogen atoms to which these hydrogen atoms were attached. The coordinates of the geometrically calculated hydrogen atoms were refined using the riding model. The final R factor calculated over 1480 reflections with $I \geq 2\sigma(I)$ was equal to 0.0348 and that calculated over all the 1626 reflections, 0.0383. The atomic coordinates and thermal parameters obtained are given in table. The C(12) atom is statistically disordered over two positions.

DESCRIPTION OF THE STRUCTURE AND DISCUSSION

The molecular structure is shown in Fig. 1. The molecule is almost planar, and its conformation is similar to that in the iodide form of modification **I** [1] and the conformations of 4-amino-5-ethoxymethyl-2-methylpyrimidine hydrobromide in two crystal modifications [4, 5]. The most pronounced difference between iodides and bromohydrates reduces to C(5)–C(9)–O(10)–C(11) torsion angles (up to 14.5°), which seems to be caused by specific hydrophobic interactions in these structures. In the crystal structure of iodide modification **II**, the pyrimidine ring is planar. The average deviation of atoms from the mean plane does not exceed 0.003 Å (cf. with 0.012 Å in modification **I**). The character of atomic displacements in modification **I** indicates that the molecule adopts the feebly marked C(2),C(5)-boat conformation, whereas the molecule in modification **II** shows a weak tendency to the forma-

† Deceased.

Atomic coordinates and thermal parameters

Atom	*x/a*	*y/b*	*z/c*	U_{eq}/U_{iso}, Å^2
I	0.31399(6)	0.19847(2)	0.18119(3)	0.0525(2)
N(1)	−0.0366(6)	0.3129(3)	0.0224(3)	0.0386(10)
C(2)	0.1412(8)	0.3418(3)	−0.0278(4)	0.0376(12)
N(3)	0.2589(7)	0.4136(3)	0.0014(3)	0.0392(10)
C(4)	0.2036(8)	0.4595(3)	0.0856(4)	0.0396(12)
C(5)	0.0179(9)	0.4308(4)	0.1417(5)	0.0425(13)
C(6)	−0.0958(9)	0.3580(4)	0.1074(4)	0.0417(13)
C(7)	0.2089(11)	0.2897(5)	−0.1174(6)	0.055(2)
N(8)	0.3277(9)	0.5323(3)	0.1116(4)	0.0515(13)
C(9)	−0.0419(11)	0.4813(4)	0.2355(6)	0.061(2)
O(10)	−0.2192(9)	0.4351(4)	0.2809(5)	0.095(2)
C(11)	−0.3213(14)	0.4836(7)	0.3512(8)	0.094(3)
C(12)**	−0.5188(16)	0.4346(7)	0.3777(8)	0.072(3)
C(12')**	−0.1968(68)	0.4937(28)	0.4455(34)	0.145(23)
C(13)	−0.1670(11)	0.2309(5)	−0.0098(6)	0.059(2)
H(6)	−0.227(10)	0.336(4)	0.138(5)	0.050
H(71)	0.145(13)	0.295(5)	−0.170(6)	0.066
H(72)	0.364(12)	0.316(5)	−0.145(6)	0.066
H(73)	0.228(10)	0.225(5)	−0.098(5)	0.066
H(81)	0.447(11)	0.544(4)	0.081(5)	0.062
H(82)	0.300(11)	0.566(5)	0.156(6)	0.062
H(91)	0.064(11)	0.493(5)	0.280(6)	0.074
H(92)	−0.087(11)	0.550(5)	0.198(5)	0.074
H(111)*	−0.3388(14)	0.5411(7)	0.3212(8)	0.112
H(121)*	−0.5768(48)	0.4040(35)	0.3162(15)	0.087
H(122)*	−0.6105(35)	0.4744(8)	0.4023(48)	0.087
H(123)*	−0.5005(21)	0.3928(29)	0.4323(36)	0.087
H(12*A*)*	−0.1098(363)	0.5492(96)	0.4436(125)	0.173
H(12*B*)*	−0.1126(372)	0.4469(122)	0.4494(133)	0.173
H(12*C*)*	−0.2851(68)	0.4915(216)	0.5064(36)	0.173
H(131)	−0.300(12)	0.220(4)	0.034(6)	0.071
H(132)	−0.085(12)	0.187(5)	−0.011(6)	0.071
H(133)	−0.219(12)	0.239(5)	−0.063(6)	0.071

* The atomic coordinates were calculated.

** The occupancies of the positions of the C(12) and C(12') atoms and the H atoms bound to the C atoms are equal to 0.73(2) and 0.27(2), respectively.

tion of the C(2)-sofa conformation. In the two crystal modifications of 4-amino-5-ethoxymethyl-2-methylpyrimidine hydrobromide mentioned above, the pyrimidine rings tend to adopt the C(2),C(5)-boat conformation in the trigonal modification and the N(3),C(6)-boat and C(2),N(3)-half-chair conformations in two independent molecules in the monoclinic modification [5]. These results are indicative of the flexibility of the pyrimidine ring, whose conformation is affected by the participation of the constituent atoms in hydrogen bonding or in interactions with I^- ions.

In the crystal structure of modification **II**, the I^- ion is linked to the amino group of the neighboring molecule (x, $-0.5 + y$, $0.5 - z$) via the $I^-\cdots H(82)–N(8)$ hydrogen bond ($I^-\cdots N(8)$ equals 3.663(5) Å, $I^-\cdots H(82)$ equals 2.89(8) Å, and the $I^-\cdots H(82)–N(8)$ bond angle equals 166(7)°) and through the ionic bond with the N(1) atom of the basis molecule ($I^-\cdots N(1)$ equals 3.662(10) Å)

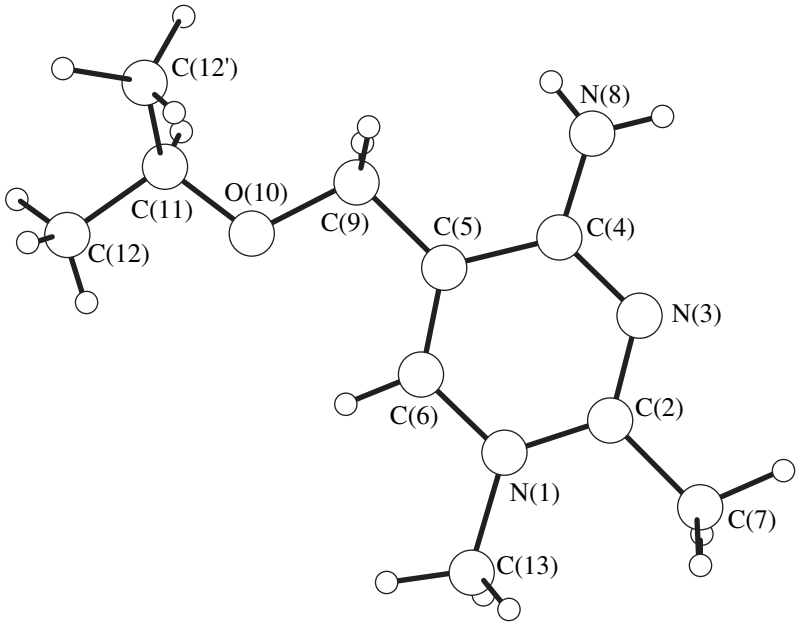

Fig. 1. Molecular structure of 4-amino-5-ethoxymethyl-1,2-dimethylpyrimidine in the crystals of modification **II**.

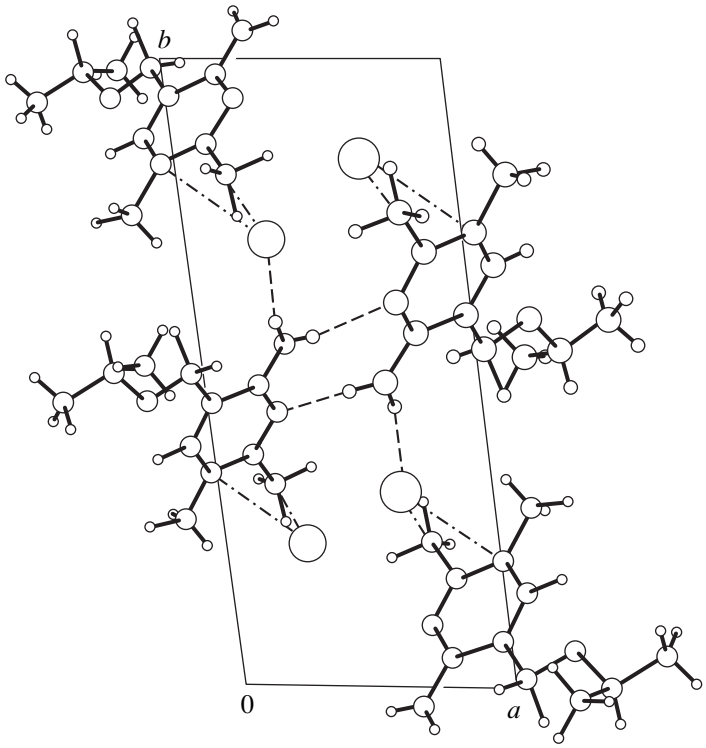

Fig. 2. Crystal packing of 4-amino-5-ethoxymethyl-1,2-dimethylpyrimidine molecules and I^--ions in modification **II** projected onto the *xy* plane.

(Fig. 2). In other words, a positive charge should be localized at the N(1) atom, and the bonds should acquire a pyramidal configuration. In fact, the bonds at the N(1) atom are approximately coplanar and the deviation of this atom from the C(2)C(6)C(13) plane almost equals 0.017(6) Å (i.e., is within the 3σ), the vertex of the pyramid "looks at" the I^--ion rather than away from it. This may be indicative of the delocalization of the positive charge of the molecule. It should be emphasized that the $I^-\cdots N(1)$ and $I^-\cdots N(8)$ contacts are of a

different nature but have equal lengths. There is also a contact between the I^- ion and the C(2) atom (3.707(8) Å; the sum of the corresponding van der Walls radii equals 3.66 Å; the sum of the van der Waals radius of the C atom and the ionic radius of the I^- ion equals 3.76 Å [6]). One should not forget that the $I^-(1)\cdots N(1)$ contact and, particularly, the $I^-(1)\cdots C(2)$ contact in modification **I** [1] are much shorter (3.598 and 3.573 Å, respectively), whereas the bonds at the N(1) atom also have an almost planar trigonal configuration.

The molecules in both iodide modifications form centrosymmetric pairs via N(8)–H···N(3) hydrogen bonds (3.070(9) Å). These dimers are similar to those observed in hydrobromides [4, 5]. Apparently, the formation of dimers is typical of 4-aminopyrimidines. Dimers in the crystal structure of modification **II** are linked via the I^- ions to form the above-mentioned hydrogen and ionic bonds. The crystal structure of iodide modification **I** [1] contains the I^- ions of two types. The ions of the first type are involved in hydrogen bonds linking two dimers. The ions of the second type link the dimers via the C(2) and N(1) atoms. In the structure of modification **II**, the bonds between the I^- ion and the C(2) and N(1) atoms and, particularly, between the I^- ion and the C(2) atom are much weaker.

The projection of the crystal structure of iodide modification **II** of the iodide is shown in Fig. 3. It is seen that the molecular dimers are oriented in such a way that the packing resembles a herring-bone motif, which can be loosely called the "pseudo-herring-bone" packing.

The bond lengths and bond angles in the molecule of modification **II** are close to those in modification **I** [1], with one exception—the C(9)–O(10) and C(11)–C(12) bonds are slightly shortened (by 0.0323 and 0.049 Å, respectively), which is accompanied by an increase in the C(9)–O(10)–C(11) angle (by 2.7°). The distribution of the bond lengths in the ring indicates that the molecule structure is very similar to that of 2,5-diene, whereas the double and single bonds show no expected alternation. Thus, the C(5) and C(6), N(3) and C(2) atoms form almost double bonds (1.328(10) and 1.309(9) Å, respectively), whereas all the remaining bonds are only partly double (C(4)–C(5) is 1.424(8) Å and N–C range within 1.346(7)–1.362(7) Å). The exocyclic C(2)–C(7) and C(4)–N(8) bonds (1.488(9) and 1.331(9) Å, respectively) are also shorter than the single bonds, which is typical, e.g., of the analogous bonds in the aromatic ring [7]. The N(1) and C(13) atoms form a single bond (1.480(10) Å). The bond angles for all the atoms in the ring, except for C(2) and C(5), are close to 120°. The endocyclic angle at the C(2) atom increases to 122.0°, and the angle at the C(5) atom decreases to 117.1°.

Thus, unlike the crystals of the same compound grown from acetone (modification **I**) [1], the pyrimidine ring in the crystals of 4-amino-5-ethoxymethyl-1,2-dimethylpyrimidinium iodide grown from DMSO (modification **II**) has the 2,5-diene structure and shows a weak tendency to acquiring a C(2)-sofa conformation. In modification **II**, the centrosymmetric molecular dimers are also connected by hydrogen bonds, but the packing of such dimers and I^- ions in modification **II** considerably differs from that of modification **I**. Although the $I^-\cdots N(1)$ and $I^-\cdots N(8)$ contacts are of different nature, their lengths are equal.

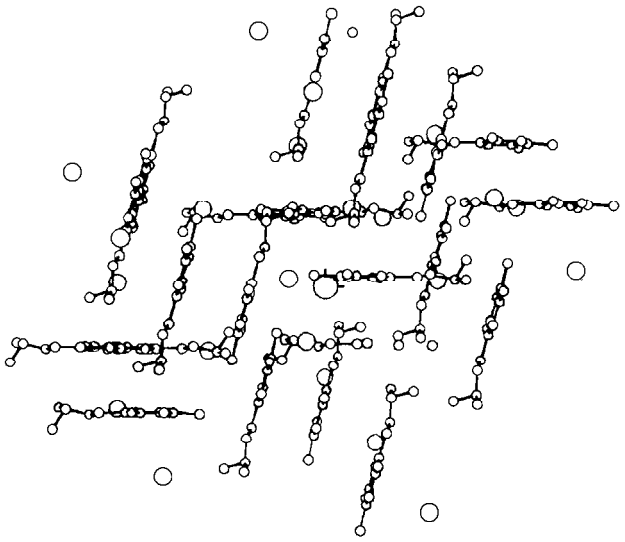

Fig. 3. Fragment of the crystal structure projected along the direction lying in the glide symmetry plane *b* and forming an angle of 46° with the *y*-axis.

ACKNOWLEDGMENTS

We thank V.I. Popovich for supplying us with the crystals and Yu.V. Nekrasov for collecting the X-ray data.

REFERENCES

1. N. E. Zhukhlistova, V. I. Smirnova, G. N. Tishchenko, *et al.*, Kristallografiya **35** (3), 668 (1990) [Sov. Phys. Crystallogr. **35**, 388 (1990)].
2. G. M. Sheldrick, *SHELXS86: Program for the Solution of Crystal Structures* (Univ. of Göttingen, Germany, 1986).
3. G. M. Sheldrick, *SHELXL93: Program for the Refinement of Crystal Structures* (Univ. of Göttingen, Germany, 1993).
4. N. E. Zhukhlistova, V. I. Smirnova, G. N. Tishchenko, *et al.*, Kristallografiya **33** (2), 400 (1988) [Sov. Phys. Crystallogr. **33**, 236 (1988)].
5. V. I. Smirnova, N. E. Zhukhlistova, G. N. Tishchenko, *et al.*, Kristallografiya **33** (4), 869 (1988) [Sov. Phys. Crystallogr. **33**, 513 (1988)].
6. B. K. Vainshtein, V. M. Fridkin, and V. L. Indenbom, in *Modern Crystallography*, Vol. 2: *Structure of Crystals*, Ed. by B. K. Vainshtein, A. A. Chernov, and L. A. Shuvalov (Nauka, Moscow, 1979; Springer-Verlag, Berlin, 1995, 2nd ed.).
7. I. Kraut and H. I. Reed, Acta Crystallogr. **15**, 747 (1962).

Translated by T. Safonova

Crystallography Reports, Vol. 46, No. 1, 2001, pp. 60–64. Translated from Kristallografiya, Vol. 46, No. 1, 2001, pp. 67–71.

STRUCTURE OF ORGANIC COMPOUNDS

Crystal Structure and IR and Electronic Spectra of 3-*o*-Tolyl-5,5-Dimethyl-5,6-Dihydro-1,2,4-Triazolo[3,4-*a*]isoquinoline Hemihydrate

V. I. Sokol*, V. V. Davydov, M. A. Ryabov**, N. Yu. Merkur'eva**, Yu. V. Shklyaev***, V. A. Glushkov***, and V. S. Sergienko***

** Kurnakov Institute of General and Inorganic Chemistry, Russian Academy of Sciences, Leninskiĭ pr. 31, Moscow, 117907 Russia*

*** Russian University of People's Friendship, ul. Miklukho-Maklaya 6, Moscow, 117198 Russia*

**** Institute of Technical Chemistry, Ural Division, Russian Academy of Sciences, ul. Lenina 13, Perm, 614600 Russia*

Received February 25, 1999

Abstract—The crystal and molecular structures of 3-*o*-tolyl-5,5-dimethyl-5,6-dihydro-1,2,4-triazolo[3,4-*a*]isoquinoline hemihydrate $L \cdot 0.5H_2O$ are determined. The crystal is built of the $2L \cdot H_2O$ dimers, which are formed by the O–H···N hydrogen bonds between the water molecule and the nitrogen atoms in the 1-position of the *L* molecules. IR and electronic spectra of the compound are studied. Model quantum-chemical calculations are performed. © *2001 MAIK "Nauka/Interperiodica".*

Derivatives of hydrated isoquinolines and 1,2,4-triazoles exhibit a wide spectrum of pharmacological and pesticide properties [1, 2]. In this respect, 3,4-dihydroisoquinolines containing annelated heterocycles in the 1,2-position are of interest as promising pharmacological substances. The synthesis of 3-*o*-tolyl-5,5-dimethyl-5,6-dihydro-1,2,4-triazolo[3,4-*a*]isoquinoline (*L*) was reported earlier [3]. The present paper is concerned with the detailed structural characterization of *L* by X-ray diffraction, IR and electronic spectroscopy, and quantum-chemical calculations.

EXPERIMENTAL

X-ray structure analysis. Light yellow prismatic crystals of $C_{19}H_{19}N_3 \cdot 0.5H_2O$ (**I**) were obtained by crystallization of *L* from isopropanol. The crystals are monoclinic, a = 23.785(5) Å, b = 8.191(2) Å, c = 17.944(4) Å, β = 112.00(3)°, V = 3241.3(1) Å^3, ρ_{calcd} = 1.260 g/cm^3, μ_{Mo} = 8.6 cm^{-1}, $F(000)$ = 1392, Z = 8, and space group $C2/c$.

A set of intensities was collected on an Enraf–Nonius CAD4 automated four-circle diffractometer (MoK_α radiation, graphite monochromator, ω scan mode, $2\theta_{max}$ = 58°). A total of 2263 reflections were measured, of which 2181 reflections with $I \geq 2\sigma(I)$ were used in the calculations.

The structure was solved by the direct method (SHELXS86 [4]) and refined by the least squares procedure in the full-matrix anisotropic approximation with the SHELXL93 program [5]. The H(1) hydrogen atom of the water molecule was located from the difference Fourier synthesis and refined isotropically. The remaining hydrogen atoms were included in the refinement in the calculated positions (C–H 0.96 Å) with fixed isotropic thermal parameters (U_j = 0.08 Å^2). The final parameters of the refinement are R_1 = 0.0405, wR_2 = 0.0921, and $GOOF$ = 0.877 for 2181 reflections with $I \geq 2\sigma(I)$; R_1 = 0.0687 and wR_2 = 0.1660 for all 2263 reflections. The extinction coefficient is 0.0027(3). The maximum and minimum values of the residual electron density are 0.207 and –0.220 e Å^{-3}, respectively.

The atomic coordinates and thermal parameters are listed in Table 1.

IR spectra of polycrystalline samples (prepared as KBr pellets and nujol mulls) were recorded on a Specord 75IR spectrophotometer.

Electronic absorption spectra of the solutions at a concentration of 5×10^{-5} mol/l solutions were taken on a Specord UV VIS spectrophotometer.

Quantum-chemical calculations were performed within the Pariser–Parr–Pople (PPP) approach. The optimization of the interatomic distances was achieved by minimizing the heats of atomization [6].

RESULTS AND DISCUSSION

Compound *L* is a 1,2,4-triazole derivative containing substituents that show the capacity for π-conjuga-

Table 1. Atomic coordinates ($\times 10^4$; for the H(1) atom, $\times 10^3$) and thermal parameters U_{eq} (for the H(1) atom, U_{iso}; $\times 10^3$) in structure **I**

Atom	*x*	*y*	*z*	U_{eq}/U_{iso}, Å^2	Atom	*x*	*y*	*z*	U_{eq}/U_{iso}, Å^2
O(1)	0	5208(4)	7500	118(1)	C(9)	1455(1)	−1203(3)	8948(1)	48(1)
N(1)	1431(1)	529(2)	8664(1)	42(1)	C(10)	1868(1)	−2234(3)	8668(2)	66(1)
N(2)	1044(1)	2994(2)	8366(1)	54(1)	C(11)	1664(1)	−1158(3)	9860(2)	66(1)
N(3)	1635(1)	3021(2)	8389(1)	54(1)	C(12)	1860(1)	1546(3)	8580(1)	45(1)
C(1)	934(1)	1492(3)	8537(1)	46(1)	C(13)	2499(1)	1120(3)	8701(1)	47(1)
C(2)	396(1)	882(3)	8641(1)	46(1)	C(14)	2659(1)	687(3)	8061(1)	50(1)
C(3)	−43(1)	1898(3)	8732(2)	61(1)	C(15)	3266(1)	325(3)	8212(2)	59(1)
C(4)	−531(1)	1240(4)	8861(2)	72(1)	C(16)	3696(1)	403(3)	8981(2)	64(1)
C(5)	−588(1)	−429(4)	8904(2)	74(1)	C(17)	3536(1)	840(3)	9613(2)	65(1)
C(6)	−156(1)	−1445(4)	8814(2)	66(1)	C(18)	2937(1)	1189(3)	9477(2)	57(1)
C(7)	337(1)	−814(3)	8681(1)	52(1)	C(19)	2197(1)	589(3)	7218(2)	69(1)
C(8)	810(1)	−1872(3)	8555(2)	57(1)	H(1)*	33(14)	449(45)	780(24)	165(17)

* The calculated coordinates of the remaining H atoms are omitted.

Table 2. IR spectra of **I** and related compounds in the range 1700–1400 cm^{-1}

Compound	Medium	ν, cm^{-1}
I	KBr nujol	1655, 1604, 1586, 1539, 1521, 1473, 1461, 1663, 1606, 1590, 1540, 1523
1,2,4-Triazole [8]	KBr	1486, 1479, 1385, 1368
1,3,3-Trimethyl-3,4-dihydroisoquinoline [9]	KBr	1629, 1602, 1575, 1555
3,3-Dimethyl-3,4-dihydroisocarbostyryl azine [10]	KBr	1608, 1600, 1562

Table 3. Electronic absorption spectra of **I** and related compounds

Compound	Medium	$\lambda_{max}(\log\varepsilon)$, nm
I	Ethanol	214 (4.4), 260 (4.3), 267(sh), 283 (sh), 291 (sh)
	Acetonitrile	216 (4.3), 262 (4.2), 269 (sh), 283 (sh), 291 (sh)
	Nujol*	260
1,2,4-Triazole	Water [15]	186.2
	Tetrahydrofuran [16]	205
3,3-Dimethyl-3,4-dihydroisocarbostyryl azine [10]	Ethanol	218 (4.3), 249(4.4), 352 (sh), 369 (4.4), 383 (sh)
3,3-Dimethyl-1-N-(1-phenyl-2,3-dimethyl-5-oxo-3-pyrazolin-4-yl)imino-1,2,3,4-tetrahydroisoquinoline [19]		208 (4.33), 247 (4.28), 326 (3.92)

* In the crystalline state, prepared as a nujol mull.

Table 4. Calculated π-charges at the nitrogen atoms (*q*, e), wavelengths (λ, nm), and oscillator strengths (*f*) for model compounds *A*–*E*

Parameter	*A*	*B*	*C*	*D*	*E*
*q*N(1)	+0.562	+0.562	+0.549	+0.542	+0.544
*q*N(2)	−0.218	−0.214	−0.222	−0.221	−0.220
*q*N(3)	−0.217	−0.214	−0.214	−0.215	−0.233
λ, nm, *f*	184 (0.22)	277 (0.01)	289 (0.16)	302 (0.46)	311 (0.62)
		252 (0.73)	250 (0.47)	287 (0.02)	295 (0.02)
		202 (0.31)	210 (0.69)	276 (0.62)	269 (0.42)
		201 (0.45)	202 (0.30)	242 (0.13)	244 (0.02)
				220 (0.26)	225 (0.06)
				217 (0.22)	220 (0.74)
				214 (0.42)	210 (0.59)

tion with the π-system of the five-membered heterocycle in the 3- and 5-positions

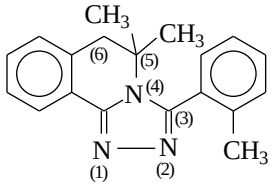

L

According to the data for 1,2,4-triazole derivatives [7], the spectrum of a polycrystalline sample *L* recrystallized from isopropanol is characterized by intense bands at 1473 and 1461 cm^{-1} (Table 2). The substituents in the 3- and 5-positions of the triazole ring (the phenyl and tolyl radicals) are responsible for the low-intensity bands in the range 1700–1500 cm^{-1} (1604, 1586, 1539, and 1521 cm^{-1}), in which unsubstituted triazole exhibits no absorption [7, 8, 11–13]. The spectrum of the polycrystalline sample *L* also contains the bands attributed to the stretching and bending vibrations of the OH groups of a water molecule involved in hydrogen bonding [14]: the broad ν(O–H) band with a maximum at about 3410 cm^{-1} and the δ(O–H) band at 1655 cm^{-1} were retained upon weak heating of the sample. These bands indicate that water molecules are incorporated into the structure of sample *L*.

It is known that the electronic absorption spectrum of unsubstituted 1,2,4-triazole is characterized by a single band (at 186.2 nm in water [15] and at 205 nm in tetrahydrofuran [16]). No absorption bands are observed in the long-wavelength range. Introduction of the substituents that are capable of conjugating with the triazole ring results in a bathochromic shift of the above band and in an increase in its intensity; moreover, new long-wavelength bands can appear [16–19]. The band maxima of the electronic absorption spectrum of an ethanol solution of *L* are presented in Table 3.

In order to characterize the electron density distribution in molecule *L* and to interpret its electronic absorption spectra, we performed quantum-chemical calculations within the π-electron PPP approach for a series of model compounds *A*–*E*

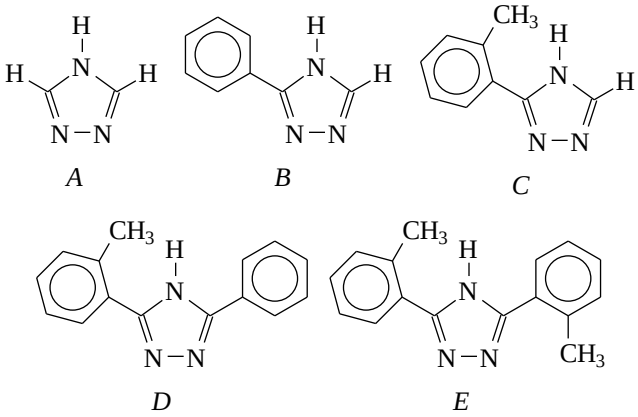

A *B* *C*

D *E*

Here, atoms free of π electrons are omitted.

The calculated electronic absorption spectra of planar molecules *A*–*E* (Table 4) adequately reflect the changes observed in the spectrum of 1,2,4-triazole upon introduction of substituents into the triazole ring. The calculated spectrum of compound *C* most closely agrees with the experimental spectrum of the *L* molecule.

As follows from Table 4, introduction of the phenyl and tolyl radicals into the triazole molecule changes the electron density at the nitrogen atoms. In compound *C*, the calculated charge at the N(2) atom is slightly greater than that at the N(3) atom. This suggests that in molecule *L*, the basicity of the N(2) atom is slightly higher than that of the N(3) atom. (This conclusion is confirmed by the fact that two *L* molecules in structure **I**

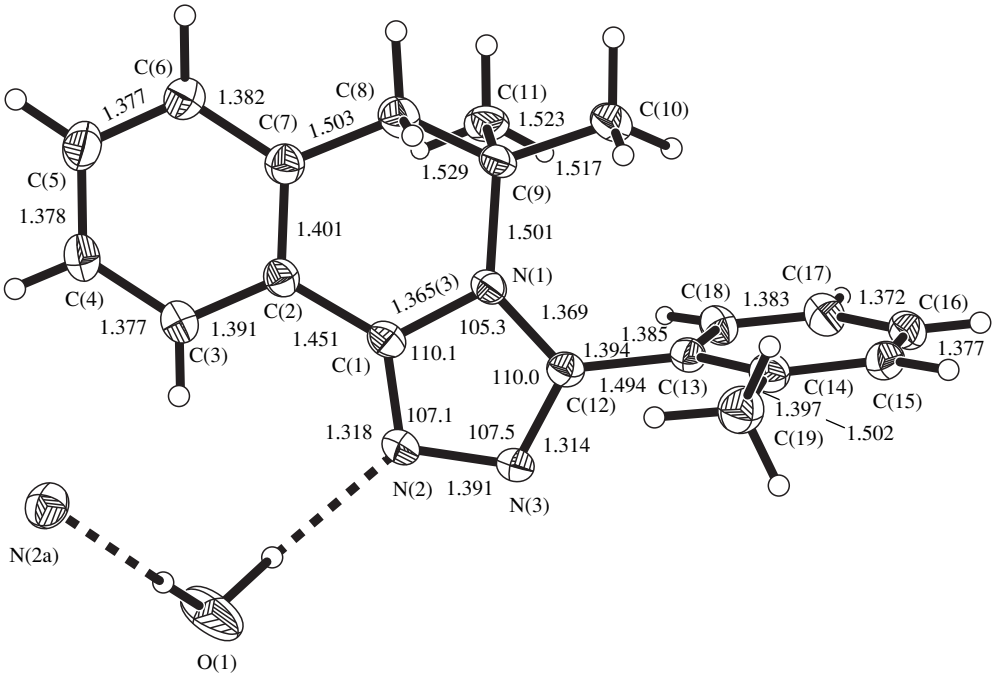

Molecular structure of **I** (an independent half of the $2L \cdot H_2O$ dimer is shown). The main bond lengths and angles are given [σ(N–N) = 0.002 Å, σ(N–C) = 0.003 Å, σ(C–C) = 0.003–0.004 Å, and σ(NCN, CNC, CNN) = 0.2°].

are linked by hydrogen bonds with the water molecule through the N(2) atom: see below.) In this connection, we expect that the *L* molecule is coordinated to the metal ions primarily through the N(2) atom. At the same time, the difference in charges is small, so that the possibility of coordinating the *L* ligand to the metal by the N(3) atom cannot be ruled out.

The results of the spectral and quantum-chemical studies agree with the data of our X-ray diffraction analysis of compound **I**.

The structural units of crystal **I** are molecules of *L* and crystallization water (figure). The O(1) atom of the H_2O molecule occupies a special position at the two-fold axis and links the *L* molecules into pairs by the two O(1)–H(1)···N(2) hydrogen bonds. The dihydroisoquinoline fragment of molecule *L* in **I** adopts its typical conformation: the neighboring C(9) and N(1) atoms deviate from the plane of the remaining eight atoms C(1)–C(8), which are coplanar within ±0.01 Å, in the same direction by 0.822 and 0.398 Å, respectively. The N(2), N(3), and C(12) atoms of the planar (within ±0.006 Å) triazole ring conjugated with the dihydroisoquinoline fragment deviate from the plane of the C(1)–C(8) atoms in the same direction. The triazole ring is folded to the C(1)C(2)C(3)C(4)C(5)C(6)C(7)C(8) plane by 16°. The folding angle between the C(1)C(2)N(1)C(9) and C(1)N(1)N(2)N(3)C(12) planes is 6°. Note that, in the conjugated tricyclic system of the *L* molecule, the exocyclic angles at the N(1) and C(1) atoms increase up to 133° and 128°, respectively.

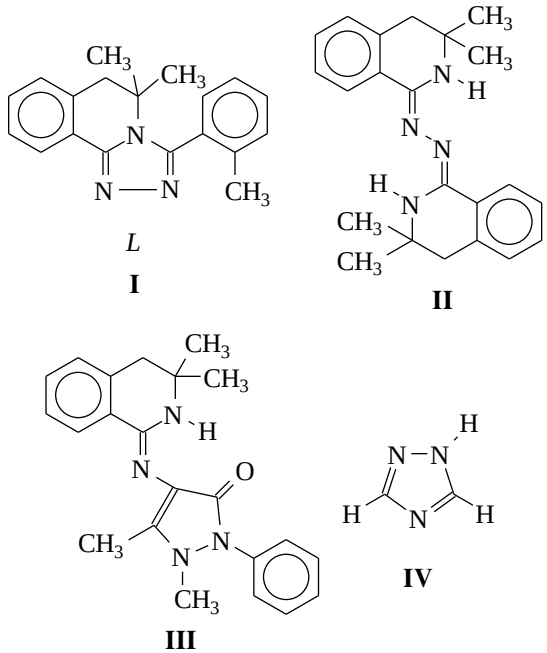

Similar to all 3,4-dihydroisoquinoline derivatives, whose structures were studied earlier, the N–C bond lengths in the dihydroisoquinoline fragment of structure **I** are substantially different: N(1)–C(1), 1.365(3) Å and N(1)–C(9), 1.501(3) Å. In **I**, owing to the annelation of the triazole ring, both bonds are slightly longer than those in other 3,4-dihydroisoquinoline derivatives, for example, 3,3-dimethyl-3,4-dihydroisocarbostyryl

azine (**II**) [10] (N–C, 1.349 and 1.462 Å) and 3,3-dimethyl-1-*N*-(1-phenyl-2,3-dimethyl-5-oxo-3-pyrazolin-4-yl)imino-1,2,3,4-tetrahydroisoquinoline (**III**) [19] (N–C, 1.349 and 1.470 Å). Unlike free 1,2,4-triazole (**IV**) [20], in which the π-electron density is almost uniformly delocalized over all bonds of the five-membered ring, in the triazole fragment of compound **I** it is predominantly localized at the N(2)–C(1) [1.318(3) Å] and N(3)–C(12) [1.314(3) Å] bonds. Two other bonds are significantly longer: N(1)–C(1), 1.365(3) Å and N(1)–C(12), 1.369(3) Å. The difference between the average lengths of the two pairs of bonds (Δ) in **I** is 0.029 Å larger than that in **IV** (Δ = 0.051 and 0.022 Å, respectively). The N(2)–N(3) bond in **I** [1.391(3) Å] is also longer than that in the free triazole molecule (1.359 Å). The bonds at the N(1), C(1), and C(12) atoms form planar sp^2 configurations (the sums of angles about all these atoms are 360°).

The intermolecular hydrogen bond between the N(2) atom and the molecule of crystallization water has no effect on the electron density distribution in the triazole ring. This bond is characterized by the following parameters: O(1)–H(1), 0.97(5) Å; O(1)···N(2), 2.996(3) Å; and H(1)···N(2), 2.02(5) Å; and the O(1)H(1)N(2) angle is 177(4)°.

The C(12)–C(13) distance between the triazole ring and the phenyl ring of the toluene fragment [1.494(3) Å] is close to the lengths of the C_{aryl}–C_{aryl} bonds in biphenyl compounds (1.437–1.493 Å [21]). There is no conjugation between these rings.

The C(12) atom lies in the plane of the phenyl ring. The phenyl and triazole rings are almost perpendicular to each other; the angle between their planes is 85°. The phenyl ring is rotated relative to the mean plane of dihydroisoquinoline by 95°. The methyl substituents of the dihydroisoquinoline and phenyl rings are oppositely directed.

In crystal **I**, the dimeric $2L \cdot H_2O$ fragments are stretched along the *x*-axis and packed according to a centered motif. Columns of molecules running along the *z*-axis are distinguished in the structure. They are formed by stacking of the benzene rings, which are approximately perpendicular to the *z*-axis. The interplanar distance between the benzene rings in the column is 4.5 Å.

ACKNOWLEDGMENTS

This work was supported by the Federal Program "Integration" (project no. K0512) and the Russian Foundation for Basic Research (project no. 98-03-32689a).

REFERENCES

1. M. D. Mashkovskiĭ, *Medicinals* (Novaya Volna, Moscow, 1996), Part 1.
2. G. I. Kaplan and S. S. Kukolenko, *Triazoles and Their Pesticide Activity* (NIITÉKhIM, Moscow, 1983), Vol. 2 (140).
3. B. B. Aleksandrov, V. A. Glushkov, E. N. Glushkova, *et al.*, Khim. Geterotsikl. Soedin., No. 4, 511 (1994).
4. G. M. Sheldrick, Acta Crystallogr., Sect. A: Found. Crystallogr. **46**, 467 (1990).
5. G. M. Sheldrick, *SHELXL93: Program for the Refinement of Crystal Structures* (Univ. of Göttingen, Göttingen, Germany, 1993).
6. M. Dewar, *The Molecular Orbital Theory of Organic Chemistry* (McGraw-Hill, New York, 1969; Mir, Moscow, 1972), p. 464.
7. V. Ya. Grinshteĭn, A. A. Strazdin', and A. K. Grinvalde, Khim. Geterotsikl. Soedin., No. 2, 248 (1970).
8. V. V. Mel'nikov, V. V. Stolpakova, and B. V. Gidaspov, Khim. Geterotsikl. Soedin., No. 11, 1567 (1972).
9. V. V. Davydov, E. V. Balebanova, I. V. Kartashova, *et al.*, Koord. Khim. **21** (6), 489 (1995).
10. V. I. Sokol, M. A. Ryabov, N. Yu. Merkur'eva, *et al.*, Izv. Akad. Nauk, Ser. Khim., No. 12, 2468 (1995).
11. D. Bougeard, N. le Calve, B. Saint Roch, and A. Novak, J. Chem. Phys. **64** (12), 5152 (1976).
12. V. A. Lopyrev, N. K. Beresneva, and B. Kh. Strelets, Khim. Geterotsikl. Soedin., No. 4, 732 (1969).
13. W. Otting, Chem. Ber. **89** (12), 2887 (1956).
14. K. Nakamoto, *Infrared and Raman Spectra of Inorganic and Coordination Compounds* (Wiley, New York, 1986; Mir, Moscow, 1991), p. 223.
15. E. G. Kovalev, Candidate's Dissertation in Chemistry (Sverdlovsk, 1970), p. 10.
16. H. A. Staab, Chem. Ber. **89** (8), 1927 (1956).
17. G. I. Chipen and V. Ya. Grinshteĭn, Izv. Akad. Nauk Latv. SSR, Ser. Khim., No. 3, 411 (1962).
18. L. I. Bagal and M. S. Pevzner, Khim. Geterotsikl. Soedin., No. 2, 272 (1971).
19. V. I. Sokol, M. A. Ryabov, N. Yu. Merkur'eva, *et al.*, Kristallografiya **41** (3), 483 (1996) [Crystallogr. Rep. **41**, 457 (1996)].
20. P. Goldstein, J. Ladell, and G. Abowitz, Acta Crystallogr., Sect. B: Struct. Crystallogr. Cryst. Chem. **B25**, 135 (1969).
21. F. H. Allen, O. Kennard, D. G. Watson, *et al.*, J. Chem. Soc., Perkin Trans. **11**, 51 (1987).

Translated by I. Polyakova

Crystallography Reports, Vol. 46, No. 1, 2001, pp. 65–68. Translated from Kristallografiya, Vol. 46, No. 1, 2001, pp. 72–75.

STRUCTURE OF ORGANIC COMPOUNDS

Molecular Structures of Some 8-Isoanalogues of Steroid Estrogens

G. L. Starova, I. I. Eliseev, Sh. N. Abusalimov, S. B. Tsogoeva, and A. G. Shavva

St. Petersburg State University (Petrodvorets Branch), Universitetskiĭ pr. 2, Petrodvorets, 198904 Russia

Received March 23, 1999

Abstract—The molecular structures of three steroids, namely, 17β-acetoxy-3-methoxy-8-isoestra-1,3,5(10)-triene (**I**), 17β-acetoxy-3-methoxy-7α-methyl-8-isoestra-1,3,5(10)-triene (**II**), and 17β-acetoxy-3-methoxy-1-methyl-8-isoestra-1,3,5(10)-triene (**III**), are determined by X-ray diffraction analysis. It is shown that the substituents in the *A* and *B* rings of the compounds of the 8-iso series have a slight effect on the conformation of the steroid skeleton as a whole, which manifests itself only in insignificant distortions of the *B* and *D* rings. The methyl group in the 1-position (compound **III**) affects the geometric parameters of the steroid nucleus less than the same substituent in the 7-position (compound **II**). A sharp decrease in the uterotropic activity of compounds **II** and **III** (compared to compound **I**) revealed in biological studies can be attributed to unfavorable steric interactions of the substituents in the *A* and *B* rings with the estradiol receptor. © *2001 MAIK "Nauka/Interperiodica".*

Steroid estrogens are widely used in medicine at substitution therapy [1]. However, their side effects stimulate the search for new substances with improved properties. We agree with the opinion expressed in [2] that the "ideal" estrogen should exhibit the cardioprotector activity, block the development of osteoporosis and the Alzheimer's disease, give no rise to proliferation processes in endometrium, and serve as a prophylactic of some hormone-dependent diseases. Designing the compounds exhibiting these properties is a complex problem. It involves the development of the model of binding of estrogens and their analogues to the receptors of estradiol.

One of the stages in solving this problem is the study of the structures of modified estrogens whose hormone effect is well understood and whose three-dimensional structures differ considerably from the structures of the corresponding natural hormones. Estrogens of the 8-iso series [3] fit this criterion; therefore, at the first stage, we studied the molecular structures of racemic steroids, namely, 17β-acetoxy-3-methoxy-8-isoestra-1,3,5(10)-triene (**I**), 17β-acetoxy-3-methoxy-7α-methyl-8-isoestra-1,3,5(10)-triene (**II**), and 17β-acetoxy-3-methoxy-1-methyl-8-isoestra-1,3,5(10)-triene (**III**) (Fig. 1). These compounds were synthesized according to the Torgov–Ananchenko procedure [4], and their structures were confirmed by means of ^{1}H and ^{13}C NMR spectroscopy.

Crystals of all the compounds were grown from hexane solutions as colorless transparent plates. The three-dimensional sets of unique nonzero reflections were obtained from single crystals on a Syntex $P2_1$ automated diffractometer (graphite monochromator, MoK_α radiation) at room temperature. The main crystal data and selected data-collection parameters are summarized in Table 1. All the structures were solved by the direct method and refined on F^2 with due regard for the anisotropy of thermal vibrations of the non-hydrogen atoms. The positions of the hydrogen atoms were calculated. No correction for absorption was introduced. The CSD [5] and SHELXL93 [6] program pack-

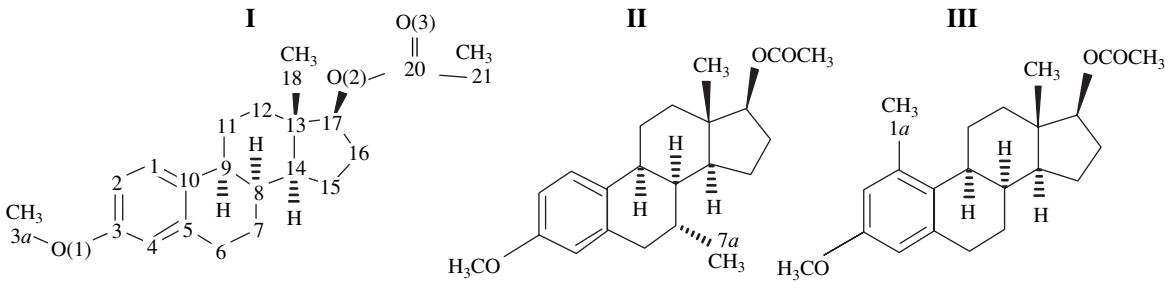

Fig. 1. Structural formulas of the compounds studied.

1063-7745/01/4601-0065$21.00 © 2001 MAIK "Nauka/Interperiodica"

Table 1. Crystal data

Parameter	**I**	**II**	**III**
Formula	$C_{21}H_{28}O_3$	$C_{22}H_{30}O_3$	$C_{22}H_{30}O_3$
Molecular weight	328.43	342.46	342.46
Space group	$P\,2_1/c$	$P\,2_1/c$	$P\,2_1/b$
a, Å	14.871(3)	16.686(3)	16.888(5)
b, Å	7.671(2)	15.672(3)	17.899(5)
c, Å	17.557(4)	7.229(3)	8.302(5)
α, deg	90	90.50(5)	90
β, deg	115.57(2)	90	90
γ, deg	90	90	130.58(5)
V, Å^3	1806.7(7)	1890.3(9)	1906.0(14)
Z	4	4	4
d_{calcd}, g/cm^3	1.207	1.203	1.193
μ, cm^{-1}	0.79	0.78	0.77
F(000)	712	744	744
Crystal size, mm	$0.3 \times 0.2 \times 0.3$	$0.15 \times 0.2 \times 0.3$	$0.2 \times 0.25 \times 0.3$
θ range, deg	1.52–27.89	1.78–29.56	1.59–29.95
No. of reflections with $I > 4\sigma(I)$	928	1093	1209
$R(F)$	0.0517	0.0399	0.0451
$wR(F^2)$	0.1185	0.0849	0.1030

Table 2. Atomic coordinates ($\times 10^4$) and thermal parameters (Å$^2 \times 10^3$) in structure **I** (U_{eq} is equal to 1/3 of the sum of the projections of the U_{ij} tensor onto the orthogonal axes)

Atom	x	y	z	U_{eq}	Atom	x	y	z	U_{eq}
O(1)	2094(3)	5009(7)	−843(3)	66(2)	C(9)	5376(4)	1448(8)	1705(4)	42(2)
O(2)	8962(3)	−1525(6)	3443(3)	54(1)	C(10)	4516(5)	2406(10)	1027(4)	41(2)
O(3)	9122(3)	−3054(7)	4578(3)	81(2)	C(11)	5896(4)	226(9)	1331(4)	48(2)
C(1)	3633(5)	1508(9)	533(4)	53(2)	C(12)	6743(4)	−806(8)	2023(4)	48(2)
C(2)	2808(5)	2284(11)	−86(4)	57(2)	C(13)	7509(4)	398(9)	2660(4)	38(2)
C(3)	2858(5)	4037(12)	−244(4)	53(2)	C(14)	6969(4)	1644(8)	3019(4)	38(2)
C(3A)	1219(5)	4086(11)	−1369(5)	84(3)	C(15)	7805(5)	2483(9)	3786(4)	59(2)
C(4)	3721(6)	4986(9)	243(5)	53(2)	C(16)	8578(5)	1012(9)	4140(4)	59(2)
C(5)	4538(5)	4182(10)	874(4)	41(2)	C(17)	8180(4)	−477(9)	3506(4)	46(2)
C(6)	5436(4)	5282(8)	1397(4)	41(2)	C(18)	8156(4)	1271(8)	2298(4)	56(2)
C(7)	6362(4)	4215(8)	1922(4)	45(2)	C(20)	9364(5)	−2786(10)	4021(5)	51(2)
C(8)	6112(4)	2708(8)	2361(4)	39(2)	C(21)	10154(5)	−3778(9)	3886(4)	69(2)

ages were used in the calculations. The atomic coordinates are listed in Tables 2–4 (the coordinates of the hydrogen atoms and the anisotropic thermal parameters of the non-hydrogen atoms are available from the authors or in the Editorial Office).

Conformations of steroids depend, to a large extent, on the type and position of the substituents [7–9] and the mode of ring junction [10]. The structures studied here (Fig. 2), as well as the structures of estrogen 8-isoanalogues reported in the literature [10, 11], are characterized by a twist of the steroid nucleus in the region of the *B*/*C* ring junction.

A comparison of the conformational parameters allows the conclusion that the substituents in the *A* and *B* rings of the compounds of the 8-iso series produce only a slight effect on the conformation of the steroid skeleton as a whole: only slight distortions in the *B* and *D* rings are observed (Fig. 2).

Table 3. Atomic coordinates ($\times 10^4$) and thermal parameters ($Å^2 \times 10^3$) in structure **II**

Atom	*x*	*y*	*z*	U_{eq}	Atom	*x*	*y*	*z*	U_{eq}
O(1)	−6546(2)	2099(2)	−2899(5)	59(1)	C(8)	−6127(3)	−1969(2)	−3475(6)	40(1)
O(2)	−6096(2)	−4528(2)	−7614(5)	54(1)	C(9)	−6580(3)	−1401(3)	−4907(6)	39(1)
O(3)	−7026(3)	−5524(2)	−7086(6)	92(1)	C(10)	−6539(3)	−464(3)	−4438(7)	40(1)
C(1)	−7081(3)	103(3)	−5232(7)	51(1)	C(11)	−6325(3)	−1595(3)	−6884(6)	46(1)
C(2)	−7100(3)	965(3)	−4794(7)	53(1)	C(12)	−6466(3)	−2532(3)	−7390(7)	50(1)
C(3)	−6564(3)	1269(3)	−3525(7)	45(1)	C(13)	−6049(3)	−3142(3)	−6058(6)	39(1)
C(3A)	−7036(3)	2708(3)	−3839(8)	76(2)	C(14)	−6264(3)	−2898(3)	−4063(7)	44(1)
C(4)	−6009(3)	719(3)	−2736(7)	47(1)	C(15)	−6002(3)	−3671(3)	−2891(7)	60(1)
C(5)	−5984(3)	−144(3)	−3182(6)	41(1)	C(16)	−6159(3)	−4440(3)	−4187(7)	60(1)
C(6)	−5375(3)	−724(3)	−2276(8)	51(1)	C(17)	−6388(3)	−4049(3)	−6040(7)	50(1)
C(7)	−5285(3)	−1596(3)	−3186(7)	44(1)	C(18)	−5144(3)	−3159(3)	−6437(7)	55(1)
C(7A)	−4704(3)	−2134(3)	−2022(7)	63(2)	C(20)	−6476(3)	−5252(3)	−7979(8)	57(2)
					C(21)	−6159(3)	−5675(3)	−9675(7)	68(2)

Table 4. Atomic coordinates ($\times 10^4$) and thermal parameters ($Å^2 \times 10^3$) in structure **III**

Atom	*x*	*y*	*z*	U_{eq}	Atom	*x*	*y*	*z*	U_{eq}
O(1)	7784(3)	1936(2)	−575(5)	59(1)	C(8)	3840(3)	1249(3)	2462(5)	37(1)
O(2)	1090(2)	−480(2)	6768(4)	53(1)	C(9)	4668(3)	1330(3)	3444(5)	35(1)
O(3)	919(4)	472(3)	8164(6)	102(2)	C(10)	5508(3)	1503(3)	2388(6)	35(1)
C(1)	6483(3)	1906(3)	3040(6)	42(1)	C(11)	4159(4)	429(4)	4560(6)	46(1)
C(1A)	6776(4)	2254(4)	4773(6)	56(2)	C(12)	3359(4)	298(4)	5705(6)	46(1)
C(2)	7253(4)	2059(3)	2077(7)	45(1)	C(13)	2502(3)	175(3)	4787(6)	39(1)
C(3)	7064(4)	1810(3)	464(7)	44(1)	C(14)	3029(3)	1066(3)	3621(6)	36(1)
C(3A)	8701(4)	2199(5)	117(7)	75(2)	C(15)	2126(4)	999(4)	3025(6)	51(1)
C(4)	6116(4)	1422(3)	−196(6)	42(1)	C(16)	1376(4)	569(4)	4473(7)	55(2)
C(5)	5347(3)	1274(3)	738(6)	38(1)	C(17)	1866(3)	363(3)	5745(6)	44(1)
C(6)	4344(4)	906(4)	−86(6)	43(1)	C(18)	1756(3)	−850(3)	3996(6)	51(1)
C(7)	3456(4)	526(3)	1069(6)	44(1)	C(20)	683(4)	−319(4)	7948(7)	59(2)
					C(21)	−146(4)	−1231(4)	8861(8)	75(2)

In molecules **I** and **III**, the conformations of the *B* and *C* rings are 7β,8α-half-chair and chair, respectively; the conformation of the five-membered *D* ring is a 13β-envelope. The methyl group in the 1-position (compound **III**) affects the geometric parameters of the steroid nucleus weaker than the same substituent in the 7-position (compound **II**). In molecule **III**, only one torsion angle changes considerably [the C(5)–C(10)–C(9)–C(11) angle decreases by $\Delta\varphi = 3.8°$], whereas in molecule **II**, the C(5)–C(6)–C(7)–C(8), C(5)–C(10)–C(9)–C(11), and C(6)–C(7)–C(8)–C(9) torsion angles considerably increase ($\Delta\varphi$ = 4.3°, 2.9°, and 3.6°, respectively) and the C(11)–C(12)–C(13)–C(14), C(9)–C(8)–C(14)–C(15), C(10)–C(9)–C(8)–C(14), C(15)–C(16)–C(17)–O(2), and C(14)–C(13)–C(17)–O(2) angles decrease ($\Delta\varphi$ = 4.2°, 4.3°, 2.9°, 3.4°, and 2.7°, respectively). The shape of the *D* ring becomes intermediate between 13β-envelope and 13β,14α-half-chair, and the conformation of the *B* ring is a distorted 7β,8α-half-chair. In the molecular structures of all the compounds studied, the C(3a) carbon atom of the methoxy group has a *cis* orientation relative to the C(2)–C(3) bond. The distances between the O(1) and O(2) atoms in the 8-iso analogues studied are equal to 10.942(8) (**I**), 10.926(7) (**II**), and 10.892(7) Å (**III**). These values are comparable to the distance of 10.93 Å in the estradiol molecule [12] but contradict the assumption [13] that the O(1)–O(2) bond in the compounds of the 8-iso series shorten to ~10.3 Å.

It was shown earlier [10, 14] that, in the derivatives of estra-1,3,5(10)-triene steroids, the C(7)–C(8), C(8)–C(14), and C(6)–C(7) bonds shorten relative to the length of the usual C(sp^3)–C(sp^3) bond (1.531 Å). In

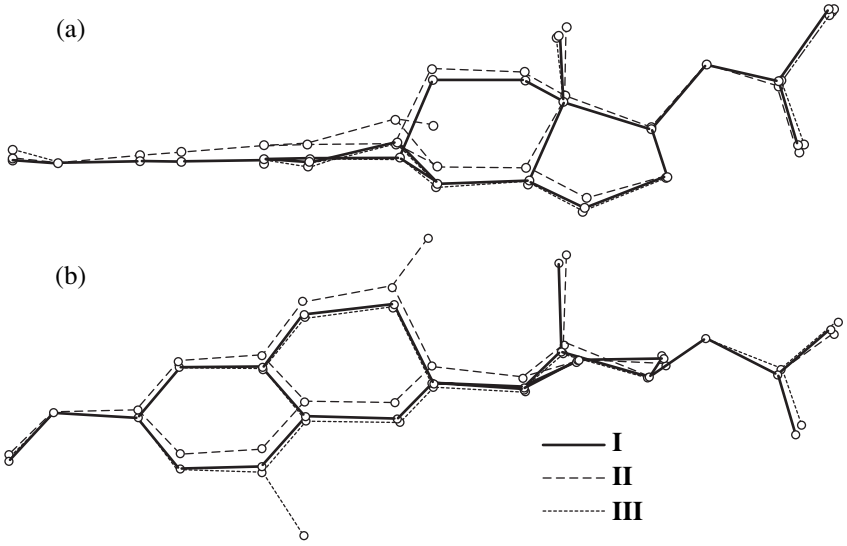

Fig. 2. Comparison of the molecular conformations. The molecules are projected onto the planes perpendicular to the planes of the (a) *A* and (b) *C* rings at superposition of the sites of binding to the receptor [atoms O(1) and O(2)].

the compounds studied, these bonds either shorten insignificantly (within 2 esd's) or do not shorten at all.

The results of biological studies indicate that the uterotropic activity of compounds **II** and **III** is considerably weaker than that of compound **I**. Since the conformations of molecules **II** and **III** differ insignificantly from the conformation of steroid **I**, we can assume that the hormone activity of the modified molecules decreases as a result of unfavorable steric interactions of the substituents in the *A* and *B* rings with the receptor of estradiol.

REFERENCES

1. E. von Angerer, *The Estrogen Receptor as a Target for Rational Drug Design* (Springer-Verlag, New York, 1996).
2. J. E. Compston, Clin. Endocrinol. (Oxf) **48**, 389 (1998).
3. F. B. González, G. Neef, U. Eder, *et al.*, Steroids **40** (2), 171 (1982).
4. I. V. Torgov, Bioorgan. Khim. **10** (8), 1059 (1984).
5. L. G. Acselrud, Yu. N. Griun, P. Yu. Zavalii, *et al.*, in *Collected Abstracts of XII European Crystallography Meeting, Moscow, 1989* (Nauka, Moscow, 1989), Vol. 3, p. 155.
6. G. M. Sheldrick, Acta Crystallogr., Sect. A: Found. Crystallogr. **49**, S53 (1993).
7. I. L. Shamovskiĭ, G. M. Barenboĭm, and A. A. Ovchinnikov, Bioorgan. Khim. **9** (8), 1113 (1983).
8. E. Palomino, M. J. Heeg, J. P. Horwitz, *et al.*, J. Steroid Biochem. **35** (2), 219 (1990).
9. F. Kayser, D. Maes, L. Wyns, *et al.*, Steroids **60**, 713 (1995).
10. M. Kh. Dzhafarov, M. V. Dodonov, S. N. Ananchenko, *et al.*, Bioorgan. Khim. **12** (7), 970 (1986).
11. H. P. Weber and E. Galantay, Helv. Chim. Acta **55** (57), Fasc. 2, 544 (1972).
12. B. Busetta and M. Hospital, Acta Crystallogr., Sect. C: Cryst. Struct. Commun. **43**, 1206 (1972).
13. G. M. Anstead, K. E. Carlson, and J. A. Katzenellenbogen, Steroids **62** (3), 268 (1997).
14. M. A. Dzhafarov, M. V. Dodonov, S. N. Ananchenko, *et al.*, Bioorgan. Khim. **12** (7), 981 (1986).

Translated by I. Polyakova

Crystallography Reports, Vol. 46, No. 1, 2001, pp. 69–74. Translated from Kristallografiya, Vol. 46, No. 1, 2001, pp. 76–81.

Architecture of Phosphates with $\{[L_2(PO_4)_3]^{p-}\}_{3\infty}$ Frameworks

V. I. Pet'kov*, G. I. Dorokhova, and A. I. Orlova***

** Nizhni Novgorod State University, pr. Gagarina 23, Nizhni Novgorod, 603600 Russia*
e-mail: petkov@uic.nnov.ru
*** Moscow State University, Vorob'evy gory, Moscow, 119899 Russia*

Received March 26, 1999

Abstract—The general principles of the structural organization for the existing types of orthophosphates with the $\{[L_2(PO_4)_3]^{p-}\}_{3\infty}$ frameworks, where L is an octahedrally coordinated ion, are discussed. Representing these frameworks by double LP_6-octahedra, it is possible to find out the related structures and analyze their symmetry relation. © *2001 MAIK "Nauka/Interperiodica".*

INTRODUCTION

The structures with a mixed $\{[L_2(TO_4)_3]^{p-}\}_{3\infty}$ frameworks sharing the vertices of LO_6-octahedra and TO_4-tetrahedra and containing different number of cations to compensate the framework charge are characteristic of different classes of compounds including phosphates [1]. The nature of the constituent atoms, their ratios, and the growth conditions (temperature, pressure, etc.) play the determining role in their formation of these structures and their characteristics.

Several review papers are devoted to the synthesis and properties of phosphates with such frameworks [2–4]. Nevertheless, the general mechanisms responsible for their architecture have not been adequately described. Therefore, it is important to find a unified approach for the analysis of their architecture to be able to understand the relation between the chemical composition, structure, and properties of these compounds important for fundamental research and to perform the purposeful "design" and synthesis of novel materials with special and important functions for various practical applications.

The present study was undertaken to establish the principles underlying the structural organization of phosphates with $\{[L_2(PO_4)_3]^{p-}\}_{3\infty}$ frameworks and to analyze the symmetric relation between these structures on the bases of numerous experimental data.

MAIN STRUCTURE TYPES OF PHOSPHATES WITH $\{[L_2(PO_4)_3]^{p-}\}_{3\infty}$ FRAMEWORKS

Depending on the choice of main building units, the structures of orthophosphates with the $\{[L_2(PO_4)_3]^{p-}\}_{3\infty}$ frameworks can be described by a number of ways and be compared with other close structure types.

The analysis of our results and the data reported in other publications on phosphates with mixed $\{[L_2(PO_4)_3]^{p-}\}_{3\infty}$ frameworks formed by LO_6-octahedra and PO_4-tetrahedra sharing vertices showed that these phosphates have nine main structural varieties (see table). These are the structures of the rhombohedral $NaZr_2(PO_4)_3$, $NaGe_2(PO_4)_3$, $Na_4[NaZr](PO_4)_3$, orthorhombic ($Li_2TiIn(PO_4)_3$, $Li_{2.72}Ti_2(PO_4)_3$), monoclinic ($Na_4Sc_2(PO_4)_3$, $Li_3In_2(PO_4)_3$, α-$Na_3Sc_2(PO_4)_3$, and cubic ($NH_4Zr_2(PO_4)_3$) symmetries.

Some phosphates, e.g., $A_3L_2(PO_4)_3$ (A = Li, Na, L = Sc, Cr, Fe, In), can exist in several polymorphic modifications reversibly transforming into one another [14–17], which shows their close relations and the common structural motif. As a rule, the symmetry of these structures becomes lower with the decrease in temperature. This lowering of the symmetry is accompanied by the redistribution of ions occupying the framework voids, whereas the ions framework-forming atoms are only slightly displaced from their sites. As a result, several crystallographic positions in the structure have different occupancies [e.g., in $LiL_2(PO_4)_3$ (L = Zr, Hf)] [18, 19].

CORRELATION BETWEEN DIFFERENT PHOSPHATE STRUCTURES

The relation between different structural modifications of phosphates can be most clearly demonstrated by representing their mixed $\{[L_2(PO_4)_3]^{p-}\}_{3\infty}$ frameworks by LP_6-octahedra. The transformation from the conventional representation of the building units of such frameworks by the fragments of (two LO_6-octahedra connected a PO_4-tetrahedron) to the fragments of two octahedra with L atoms in their centers and phosphorus atoms at the vertices is illustrated in Fig. 1. Such a description allows one to reveal the relation between the structures with mixed frameworks and the corundum (Al_2O_3) structure, sp. gr. $R\bar{3}c$ (Fig. 2a).

Figure 2b demonstrates that the structures described by sp. gr. $R\bar{3}$, $R32$, Bb (three possible transition matri-

Crystallographic characteristics of phosphates. Main structure types

Phosphate	Sp. gr.	*a*, Å	*b*, Å	*c*, Å	β, γ, deg	*Z*	References
$NaZr_2(PO_4)_3$	$R\bar{3}c$	8.815	–	22.746	–	6	[5]
$NaGe_2(PO_4)_3$	$R\bar{3}$	8.112	–	21.531	–	6	[6]
$Na_4[NaZr](PO_4)_3$	*R*32	9.217	–	22.39	–	6	[7]
$Li_2TiIn(PO_4)_3$	*Pbca*	8.647	8.807	24.328	–	4	[8]
$Li_{2.72}Ti_2(PO_4)_3$*	*Pbcn*	12.064	8.663	8.711	–	4	[9]
$Na_4Sc_2(PO_4)_3$	*C*2/*c*	15.464	8.936	9.024	124.7 (β)	4	[10]
$Li_3In_2(PO_4)_3$	$P2_1/n$	8.592	8.908	12.390	90.0 (β)	4	[11]
α-$Na_3Sc_2(PO_4)_3$	*Bb*	16.10	9.109	8.928	127.15 (γ)	4	[12]
$NH_4Zr_2(PO_4)_3$**	$P2_1/3$	10.186	–	–	–	4	[13]

* $Sc_2(MoO_4)_3$ structure type.
** Langbeinite structure type.

ces, of which one is (1/3 –1/3 2/3, –1/3 1/3 1/3, 1 1 0)), and *C*2/*c* (the transition matrix is 1 –1 0, 1 1 0, –1/3 1/3 1/3) are the subgroups of the $R\bar{3}c$ group. The symmetry changes in these structures are associated with insignificant distortions of the frameworks caused by incorporation of atoms of different types (Fig. 2b, panel *3*) and various occupancies of the framework voids (Fig. 2b, panels *1*, *2*, *3*, *4*, and *5*).

The next group of compounds (Fig. 2c) is characterized by the somewhat different frameworks also related to the initial corundum-like motif. In the initial corundum-like motif, one can single out blocks (volume layers, Fig. 2a) retaining two translations of initial *R* lattice.

The $Li_2TiIn(PO_4)_3$ structure (sp. gr. *Pbca*) "inherits" from the symmetry elements of the sp. gr. $R\bar{3}c$ only clino-planes *n* alternating with the planes *c* of the gliding reflection, which is transformed in this group into gliding-reflection plane b_x (see Fig. 2c, panel *1*).

For the $Sc_2(MoO_4)_3$ (*2* in Fig. 2) structure, one can use two different approaches—either to single out a thin layer with the above orientation inheriting the clinoplane *n* of the initial corundum motif into c_y or to "cut" from the structure a thick layer formed in the pre-

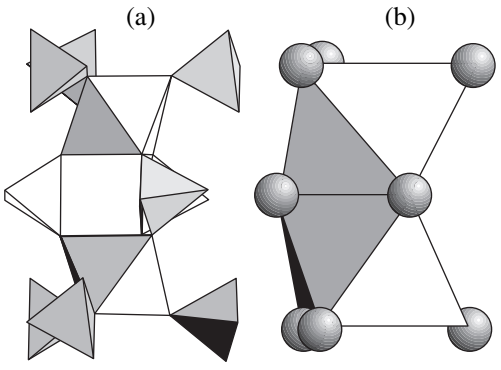

Fig. 1. Schematic representation of the main building unit of the mixed frameworks in the form of: (a) conventional LO_6 octahedra and PO_4-tetrahedra; (b) LP_6-octahedra (the spheres denote phosphorous atoms).

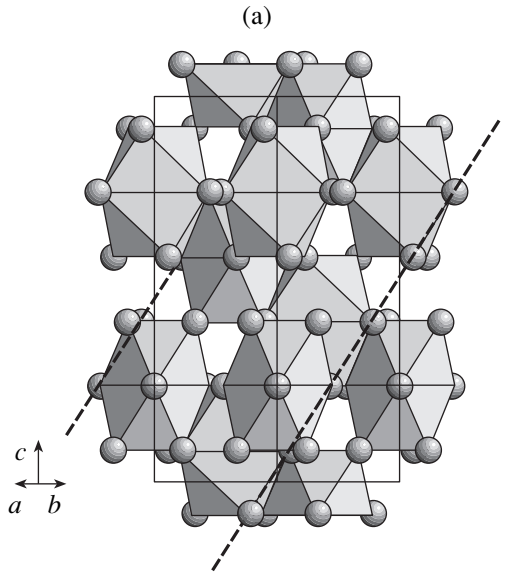

Fig. 2. Projections of the structures with corundum-like mixed frameworks: (a) Al_2O_3 framework. Dashed lines show thick layers cut off in such a way that two translations of the initial *R* lattice are retained; (b) frameworks with slight distortions of the corundum motif (*1*) $NaZr_2(PO_4)_3$; (*2*) $NaGe_2(PO_4)_3$; (*3*) $Na_4[NaZr](PO_4)_3$; (*4*) α-$Na_3Sc_2(PO_4)_3$; and (*5*) $Na_4Sc_2(PO_4)_3$; (c) the frameworks based on the fragments of the corundum motif (*1*) $Li_2TiIn(PO_4)_3$; (*2*) $Sc_2(MoO_4)_3$; and (*3*) $Li_3Ti_2(PO_4)_3$; and (d) langbeinite framework.

(b)

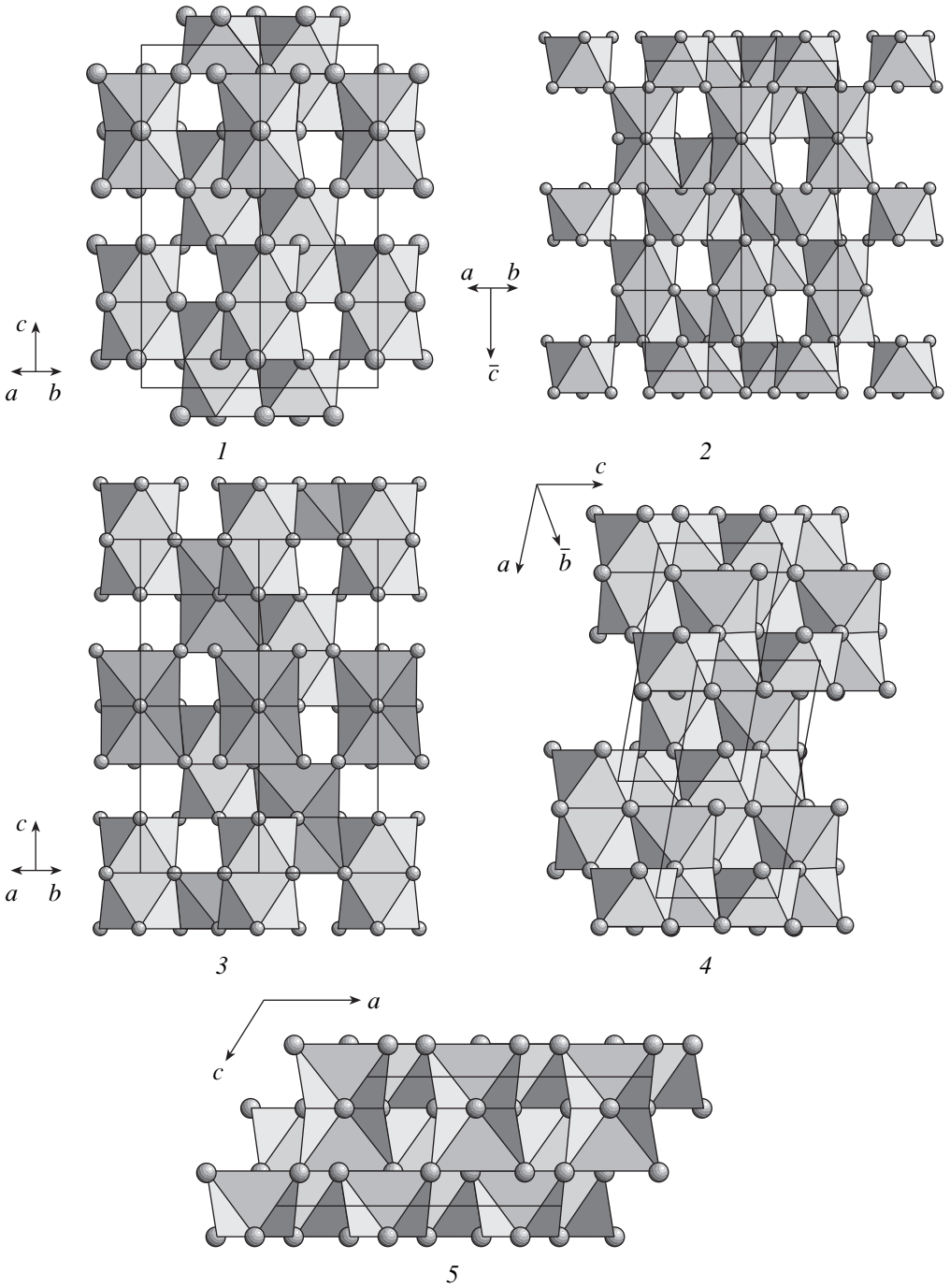

Fig. 2. (Contd.)

vious structure at the junction of two fragments cut out from the corundum-like framework.

The framework of the $Li_3In_2(PO_4)_3$ structure (Fig. 2c, panel *3*) is similar to the previous one, but owing to a slight violation of the $P2_1/n$ symmetry, only the symmetry elements of the sp. gr. *Pbcn* are inherited, not those of the sp. gr. $R\bar{3}c$.

The frameworks of langbeinite and, especially, garnet are built quite differently. In the garnet structure, the mixed framework obeys the different principle: individual (and not double) LO_6-octahedra are combined. Using the data of the analysis and taking into account that the size of PO_4-tetrahedra prevents the orthophosphates from stabilizing the cubic garnet-type structure, this structure is not considered here. Such a structure

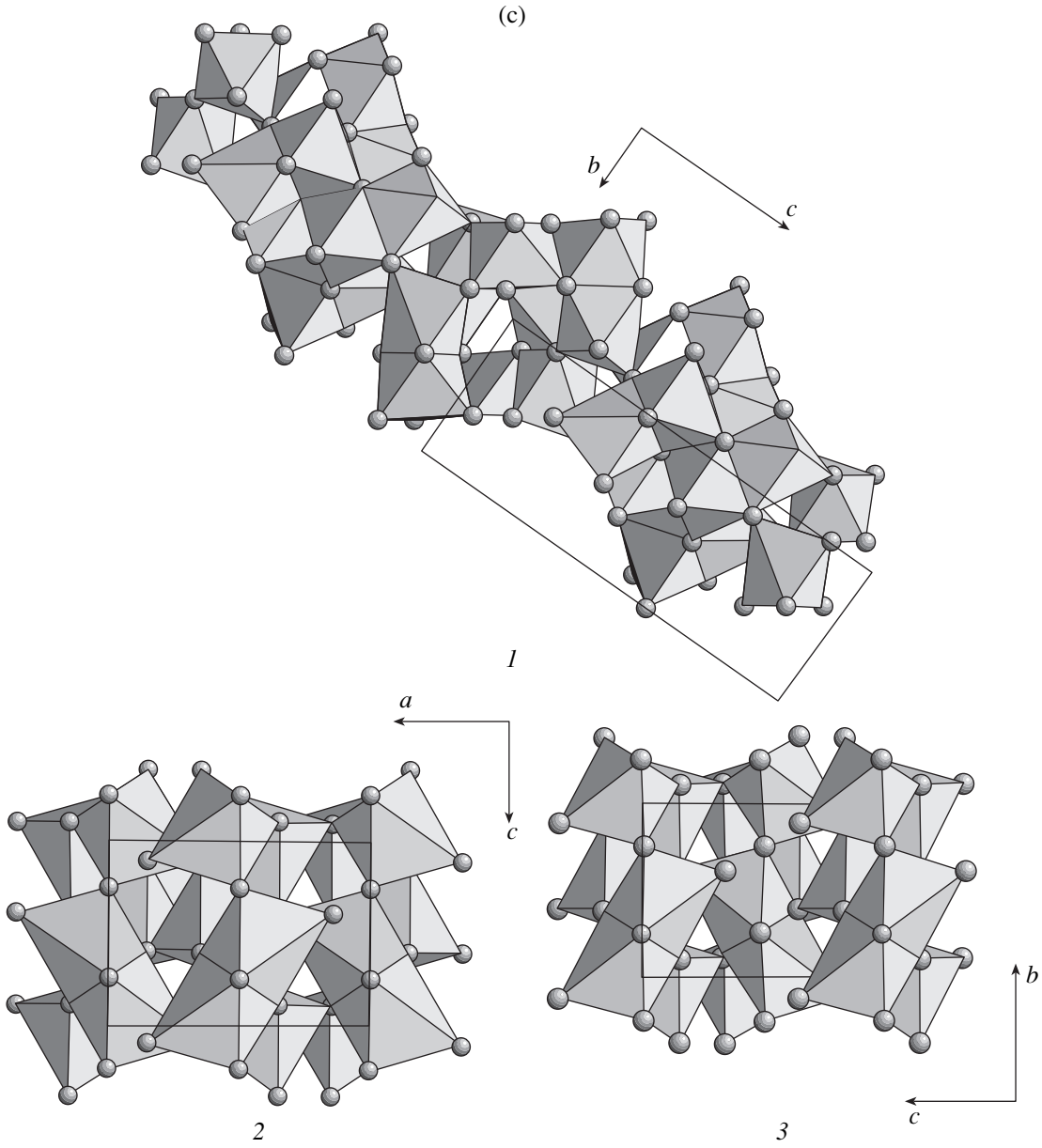

Fig. 2. (Contd.)

can exist in the compounds with larger tetrahedrally coordinated anions. In the langbeinite structure (Fig. 2d), the framework is formed by the double LP_6-octahedra, but the type of their connection differs from that in the aforementioned frameworks. The langbeinite and rhombohedral varieties of $\{[L_2(PO_4)_3]^{p-}\}_{3\infty}$ frameworks are topologically different, although their structures are close to each other. This fact is confirmed by the reconstructional phase transition $P2_13 \longrightarrow R\bar{3}c$, observed, e.g., in $NH_4Zr_2(PO_4)_3$ crystals [13]. This phosphate has a langbeinite structure under high pressures, whereas under the normal conditions the structure is rhombohedral.

Figure 3 shows a diagram illustrating the symmetric relation between the phosphates structures discussed above. The space group of corundum, $R\bar{3}c$, is placed in the center. Above it, those space groups of phosphates which completely or with slight distortions inherit the corundum framework are located. These groups are the subgroups of the initial group. Below the center, the space groups of phosphates with the frameworks consisting of the fragments of the original corundum framework are located. Langbeinite and garnet are not included into the diagram, since there is no direct transition between their symmetries and the structural characteristic of the phosphates under study.

The orthophosphate structures related by symmetry have much in common, since they are characterized by the structural invariant consisting of two P-tetrahedra forming a ring with two *L*-octahedra and also by a large secondary circular structural unit formed by two octahedra and three tetrahedra. In these structure types, stable individual groups form columns parallel to the threefold (or quasi-threefold) axes. This explains the widespread occurrence of hexagonal (trigonal) and pseudohexagonal (pseudoorthorhombic) structures with the $[L_2(PO_4)_3]$ frameworks. The most important consequence from the different spatial arrangements of the *L*- and P-based polyhedra observed in different variants of the mixed framework is the different numbers and shapes of the voids arising in this framework.

$NaZr_2(PO_4)_3$ STRUCTURE TYPE

The structure of $NaZr_2(PO_4)_3$-type with the symmetry highest of all the compounds under study provides good possibilities for incorporation of metal cations [3, 20–24]. The enhanced stability of the rhombohedral network with the maximum number of the cationic positions is a result of optimum filling of the crystal space with octahedra and tetrahedra and also small uniformly distributed framework voids. The analysis of the number of polyhedra and their environment demonstrates that the crystallochemical formula of the $NaZr_2(PO_4)_3$ structure type should be written as $(M1)(M2)_3[L_2(PO_4)]_3$. The *L* position can be populated with the same cations having the oxidation degree +4 or +3. The number of individual phases considerably increases because of the ability of different cations to occupy simultaneously the *L* positions. The oxidation degrees of cations can be the same (+3 or +4) or different (for example, +1 and +4, +2 and +3, +3 and +4, +4 and +5). The substitution of atoms in the centers of LO_6-octahedra causes the change in the negative charge of the framework, which is compensated by occupancy of the positions *M*1 and *M*2. These positions can be filled with cations with an oxidation degree ranging from +1 to +4. The occupancy of these positions varies from zero to unity. The structure type discussed illustrates an important property of the mixed-type frameworks, namely, their plasticity combined with a high strength, which favors the existence of a large variety of possible ions that can substitute the ions occupying the cationic positions without destroying or drastically rearranging the original motif.

Depending on the set of cations and their distribution over the framework positions, the ideal trigonal unit cell can be distorted into the orthorhombic or monoclinic cells. The high-symmetry cell is characteristic of the compounds with the filled *M*1 position. This group of structures includes, for example, orthophosphates $A\square_3Zr_2(PO_4)_3$, where *A* are alkali metals, H^+, Cu^+, Ag^+, Hg^+, and Tl^+. Phosphates with the general formula $B_{0.5}\square_3Zr_2(PO_4)_3$, where *B* = Ca, Sr, and Ba, are

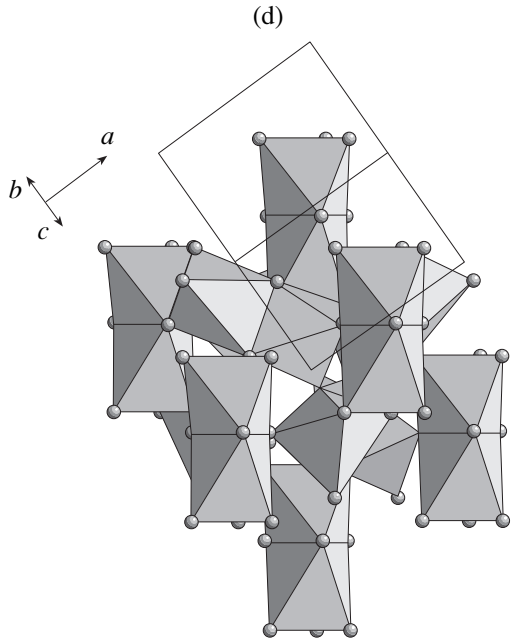

Fig. 2. (Contd.).

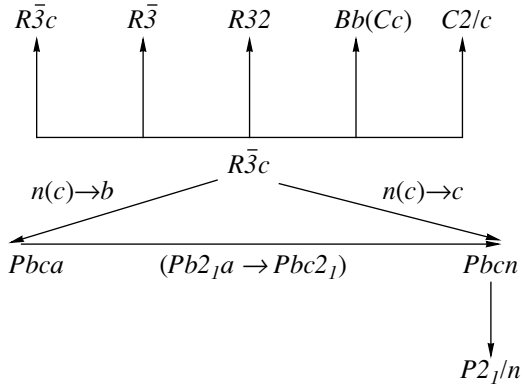

Fig. 3. Symmetry relation between the phosphate structures with mixed frameworks.

characterized by statistically half-filled *M*1 positions and their structures remain rhombohedral [24]. The substitution of large alkali-earth cations (Ca^{2+}, Sr^{2+}, and Ba^{2+}) by small 3*d* transition-element cations (Mn^{2+}, Co^{2+}, Ni^{2+}, Cu^{2+}, Zn^{2+}) or by Mg^{2+} promotes the transition to more symmetrical structures retaining the general architecture of the initial structure [25, 26]. In our opinion, the lower number of domains in the rhombohedral framework at passing from alkali-earth to 3*d* transition elements, is explained by pronounced deformability of the oxygen cationic environment with the oxidation degree +2, a sufficient flexibility of the configurations of the Zr and P coordination polyhedra sharing only the vertices, and the varying coordination number of cations with the oxidation degree +2.

In conclusion, we should like to emphasize that the general architecture of the framework is stable irrespectively of complete or partial occupancy or even empty positions outside the structure-forming framework. This stability provides the opportunity of modeling and synthesizing novel compounds by forming and occupying vacancies and by substituting central atoms of the octahedra and tetrahedra. The relation between the structure types of the framework-based orthophosphates gives a clear indication to possible formation of large series of substitutional solid solutions. This opens new vistas for modifying one-phase phosphate materials with the aim to change their useful parameters.

ACKNOWLEDGMENTS

This study was supported by the Russian Foundation for Basic Research, project no. 98-03-32571a.

REFERENCES

1. P. A. Sandomirskiĭ and N. V. Belov, *Crystal Chemistry of Mixed Anionic Radicals* (Nauka, Moscow, 1984).
2. S. E. Sigarev, Kristallografiya **37** (4), 1055 (1992) [Sov. Phys. Crystallogr. **37**, 563 (1992)].
3. S. E. Sigarev, Kristallografiya **38** (3), 203 (1993) [Crystallogr. Rep. **38**, 399 (1993)].
4. J. Alamo, Solid State Ionics **63–65** (5), 547 (1993).
5. H. Y.-P. Hong, Mater. Res. Bull. **11**, 173 (1976).
6. M. P. Carrasco, M. C. Guillem, and J. Alamo, Mater. Res. Bull. **28**, 793 (1993).
7. J. P. Boilot, G. Collin, and R. Comes, J. Solid State Chem. **50**, 91 (1983).
8. D. Tran Qui and S. Hamdoune, Acta Crystallogr., Sect. C: Cryst. Struct. Commun. **44**, 1360 (1988).
9. S. Wang and S.-J. Hwu, J. Solid State Chem. **90**, 377 (1991).
10. I. Sotofte and D. C. Fu, Solid State Ionics **26**, 307 (1988).
11. D. Tran Qui and S. Hamdoune, Acta Crystallogr., Sect. C: Cryst. Struct. Commun. **43**, 397 (1987).
12. V. A. Efremov and V. B. Kalinin, Kristallografiya **23** (4), 703 (1978) [Sov. Phys. Crystallogr. **23**, 393 (1978)].
13. A. Ono, J. Mater. Sci. Lett. **4**, 936 (1985).
14. I. P. Kondratyuk, M. I. Sirota, B. A. Maksimov, *et al.*, Kristallografiya **31** (3), 488 (1986) [Sov. Phys. Crystallogr. **31**, 287 (1986)].
15. F. D'Yvoire, M. Pintard-Screpel, E. Bretey, and M. de la Rochere, Solid State Ionics **9** (10), 851 (1983).
16. V. V. Tkachev, V. I. Ponomarev, and L. O. Atovmyan, Zh. Strukt. Khim. **25**, 128 (1984).
17. M. Pintard-Screpel, F. d'Yvoire, and F. Remy, C. R. Seances Acad. Sci., Ser. C **286**, 381 (1978).
18. F. Sudreau, D. Petit, and J. P. Boilot, J. Solid State Chem. **83**, 78 (1989).
19. E. R. Losilla, M. A. Arand, M. Martínez-Lara, and S. Bruque, Chem. Mater. **9** (7), 1678 (1997).
20. Yu. F. Volkov and A. I. Orlova, Radiokhimiya **38**, 3 (1996).
21. V. I. Pet'kov, A. I. Orlova, and O. V. Egor'kova, Zh. Strukt. Khim. **37**, 1104 (1996).
22. O. V. Egor'kova, A. I. Orlova, V. I. Pet'kov, *et al.*, Radiokhimiya **39**, 491 (1997).
23. O. V. Egor'kova, A. I. Orlova, and V. I. Pet'kov, Neorg. Mater. **34**, 373 (1998).
24. V. I. Pet'kov, A. I. Orlova, and D. A. Kapranov, Zh. Neorg. Khim. **43**, 1540 (1998).
25. V. I. Pet'kov, A. I. Orlova, G. I. Dorokhova, and Ya. V. Fedotova, Kristallografiya **45** (1), 36 (2000) [Crystallogr. Rep. **45**, 30 (2000)].
26. A. Jouanneaux, A. Verbaere, Y. Piffard, *et al.*, Eur. J. Solid State Inorg. Chem. **28**, 683 (1991).

Translated by K. Kugel

Crystallography Reports, Vol. 46, No. 1, 2001, pp. 75–80. Translated from Kristallografiya, Vol. 46, No. 1, 2001, pp. 82–87.

CRYSTAL CHEMISTRY

Simulation of a Defect Region in KDP Crystals Doped with Divalent Iron Ions. Comparison of Defects Induced by Di- and Trivalent Metals

T. A. Eremina*, N. N. Eremin, N. G. Furmanova*, V. A. Kuznetsov*, T. M. Okhrimenko*, and V. S. Urusov****

** Shubnikov Institute of Crystallography, Russian Academy of Sciences, Leninskiĭ pr. 59, Moscow, 117333 Russia*

*** Faculty of Geology, Moscow State University, Vorob'evy gory, Moscow, 119899 Russia*

e-mail: furm@rsa.crystal.msk.su

Received September 29, 1999

Abstract—The crystal structure of Fe^{II}-doped KDP crystals was simulated with the use of specially developed partly covalent potentials. Different variants of introduction of impurity into the structure were analyzed. The *M*1 position was found to be more favorable for both isolated divalent and trivalent metal ions. Upon optimization, the coordinates of the Fe^{II} ion are (0.25, 0.44, 0.125). The Fe^{II} ions can aggregate to form "clusters" energetically more favorable than isolated defects. It seems that Fe^{III} ions cannot form aggregates. © *2001 MAIK "Nauka/Interperiodica".*

INTRODUCTION

Impurities of di- and trivalent metals, in particular, of di- and trivalent iron ions, considerably influence physical properties of technically important potassium dihydrophosphate (KDP) crystals. Crystallochemical analysis [1] and computer simulation [2] confirmed the assumption [3, 4] that Fe^{III} dopants can occupy the *M*1 (0.25 0.35 0.125) and *M*2 (0.75 0.22 0.125) cavities, with the former ones being preferable. It was also shown that the impurity ion is displaced from the center of the *M*1 cavity to the position with the coordinates (0.25 0.39 0.125). The structure is distored mainly by the rotation of the PO_4-tetrahedra directly adjacent to the interstitial cation. The orientational changes of more remote tetrahedra are insignificant. Below, we consider the mechanism of incorporation of divalent impurity ions on an example of Fe^{II}. The results obtained are compared with the known data on trivalent iron ions.

SIMULATION

The problem was solved by simulation of crystal structures by minimizing the energy of atiomic interactions in the partly covalent approximation as is described elsewhere [2]. All the computations were performed by the GULP program package [5] adapted to a personal computer with a Pentium II processor (Red Hat Linux 5.2 operation system). We refined the parameters of the pair potentials of atomic interactions determined earlier [2] by fitting the model to the experimentally determined crystal structure and physical properties of KDP crystals. The refinement provided a better agreement between the observed and the calculated unit-cell parameters and atomic coordinates (Table 1). The effective charges of the H, K, P, and O atoms determined in [2] within the framework of the partly covalent model of pair potentials are +0.89, +0.98, +1.8, and –1.14 *e*, respectively. The potential of the Fe^{II}–O interaction was taken from [6], where, this potential was determined by fitting the data obtained to the FeO structure. With due regard for the valence bal-

Table 1. Observed and calculated unit-cell parameters and the fractional atomic coordinates in the KDP structure

Characteristic		Experiment [11]	Calculation
a, Å		7.434	7.571
c, Å		6.945	6.841
V, Å^3		383.91	392.12
K	*x*	0.0	0.0
	y	0.0	0.0
	z	0.5	0.5
P	*x*	0.0	0.0
	y	0.0	0.0
	z	0.0	0.0
O	*x*	0.0805	0.0822
	y	0.144	0.150
	z	0.1274	0.126
H	*x*	0.25	0.25
	y	0.144	0.161
	z	0.125	0.125

1063-7745/01/4601-0075$21.00 © 2001 MAIK "Nauka/Interperiodica"

Table 2. Parameters of the pair potentials V_{ij}^{*} used in the simulation of defect regions in KDP crystals

Potential	λ, eV	ρ, Å	*c*, eV/Å^6	*D*, eV	σ, Å^{-1}	R_0, Å	Cut-off radius, Å
K–O	5414.95	0.2734	1.20	0.3545	1.8788	2.81	11
P–O	533.96	0.223	1.90	1.4350	2.2422	1.56	11
O–H	8565.1	0.138	1.34	0.1135	3.62	1.24	11
O–O	15327.6	0.245	27.54	–	–		11
Fe^{II}–O	1207.40	0.3084	–	–	–	–	13

* $V_{ij}(R_{ij}, f) = f^2[Z_iZ_j/R_{ij}] + \lambda_{ij}\exp(-R_{ij}/\rho_{ij}) - (1 - f^2)D_{ij}\{\exp[2\sigma_{ij}(R_{ij}^0 - R_{ij}) - 2\exp[\sigma_{ij}(R_{ij}^0 - R_{ij})]\} - c_{ij}/R_{ij}^6$.

ance, the charge of a divalent iron was varied from 1.76 to 1.96 *e* depending on the incorporation mode (see below). In all the computations of local defect regions, the Fe^{II} charge was taken to be +1.90 *e*. Thus, in all the other cases, only a very low local charge concentration is observed. However, the computations showed that the contribution of the charge component to the total energy of the defect is insignificant and produces practically no effect on the final results. The parameters of the pair potentials used in this study are given in Table 2.

In our computations, we used the maximum defect regions I and II (6.5 and 16.5 Å, respectively) admissible by the PC version of the GULP program package.

RESULTS

Similar to trivalent impurity ions, ions of divalent metals can be incorporated into the KDP structure in different ways. They can occupy the position of potassium ions (K), the *M*1 position, or the *M*2 position and thus form different types of vacancies. Divalent impurity ions provide the formation of various types of vacancies, which are somewhat larger than those formed due to trivalent cations. We examined all the possible types of ion incorporation. The results are presented in Table 3. Since we used the set of the refined pair potentials (in comparison with those used earlier [2]) the energies of Fe^{III} defects also slightly changed (the refined data are given in Table 4). As is seen from Table 3, the mode of defect formation upon the removal of two protons is less favorable for both Fe^{II} and Fe^{III} ions. Thus, the energy of formation of a Fe^{II} defect in the *M*2 position decreases from +4.57 eV (two protons are removed) to +2.33 eV (one proton and one K ion are removed). The removal of two K atoms (1.45 eV) was not considered, because the optimization led to the displacement of the impurity ion to the position located in the *M*1 cavity. Therefore, in fact, such a situation is a particular case of the filling of a much more favorable *M*1 position (+1.44 eV) (see Table 4). Other modes of defect formation in this position make the structure unstable. The location of iron ion in the position of K ion upon the removal of one proton (in order to preserve electroneutrality) is also less favorable (+2.16 eV). Therefore, similar to the case of a trivalent impurity, the *M*1 position proved to be the most favorable for the formation of an isolated defect center in the KDP structure.

The incorporation of Fe^{III} into the structure requires the removal of two K atoms and one proton, which is dictated by both geometric requirements and the valence balance, which results in break of the hydrogen bond. At the same time, the incorporation of Fe^{II} does not require the removal of the H atom and in order to satisfy the condition of the electroneutrality, this atom is only displaced along the *y*-axis (from the position (0.25 0.161 0.125) to the position (0.25 0.099 0.125)). This results in a certain structure distortion but without the break of the hydrogen bond (the O–H distance increases from 1.27 to 1.29 Å, whereas the corresponding angle decreases to 149°). This difference between the Fe^{III} and Fe^{II} ions results in the fact that the incorporation of a divalent ion does not change the structure rigidity, whereas the incorporation of a trivalent ion provide the reduction of the stresses caused by the rotation of phosphorus tetrahedra. Therefore, the coordination of a Fe^{III} ion can be considered as a tetrahedronal with rather close Fe–O distances (according to the refined data, they are 2.09 and 2.22 Å). In this case, remote oxygen atoms can be ignored, whereas the difference between the Fe–O distances in the case of Fe^{II} impurity is quite pronounced (2.17 and 2.52 Å, Table 5). Correspondingly, the total energy of formation of a Fe^{II} point defect (+1.44 eV) is substantially higher than that of a Fe^{III} point defect (–2.86 eV).

Up to now, we considered impurity atoms that form isolated defects. The geometric analysis of the defect region formed demonstrated possible formation of groups of impurity atoms (clusters) in the structure. The simultaneous break (in the case of a trivalent impurity) or distortion (in the case of a divalent impurity) of the hydrogen bond and the formation of two vacancies in the potassium positions lead not only to considerable changes in the chemical composition and substantial deformations of the nearest environment of the impu-

Table 3. Characteristics of different modes of incorporation of Fe^{II} impurity

Region	*M*2	*M*2	*M*2	*M*2	Position K	*M*1	3Fe (*ABD*)	3Fe (*ABC*)	3Fe (*ABG*)
Center of the defect	0.75 0.22 0.125	0.75 0.22 0.125	0.75 0.22 0.125	0.75 0.22 0.125	0.5 0.5 0.0	0.25 0.35 0.125	0.25 0.75 0.4	0.20 0.60 0.25	0.05 0.50 0.375
Position of a Fe cation	0.75 0.22 0.125	0.75 0.22 0.125	0.75 0.22 0.125	0.75 0.22 0.125	0.5 0.5 0.0	0.25 0.35 0.125	0.25 0.35 0.125 0.15 0.75 0.375 0.25 1.15 0.625	0.25 0.35 0.125 0.15 0.75 0.375 0.35 0.75 0.125	0.25 0.35 0.125 0.15 0.75 0.375 –0.25 0.85 0.625
K-vacancy		0.5 0.5 0.0	0.5 0.5 0.0	0.5 0.5 0.0 1.0 0.5 0.25	0.5 0.5 0.0	0.5 0.5 0.0 0.0 0.5 0.25	0.0 0.5 0.25 0.5 0.5 0.0 0.0 1.0 0.5 0.5 1.0 0.75	0.5 0.5 0.0 0.0 0.5 0.25 0.0 1.0 0.5 0.5 1.0 –0.25	0.0 0.5 0.25 0.5 0.5 0.0 0.0 1.0 0.5 –0.5 1.0 – 0.25
H-vacancy	0.856 0.25 –0.125 0.644 0.25 0.375	0.644 0.25 0.375	0.856 0.25 –0.125		0.25 0.144 0.125		0.356 0.75 0.375 0.25 1.356 0.625	0.356 0.75 0.375 0.144 0.75 0.875	0.356 0.75 0.375 –0.25 0.644 0.625
Radius of region I, Å (number of atoms in the region)	6.5 (97)	6.5 (97)	6.5 (97)	6.5 (97)	6.5 (98)	6.5 (93)	6.5 (96)	6.5 (94)	6.5 (97)
Radius of region II, Å (number of atoms in the region)	16.5 (~1500)	16.5 (~1500)	16.5 (~1500)	16.5 (~1500)	16.5 (~1500)	16.5 (~1500)	16.5 (~1500)	16.5 (~1500)	16.5 (~1500)
Fe impurity upon optimization	0.75 0.25 0.125	0.52 0.46 0.02	0.75 0.49 0.125	0.75 0.56 0.125	0.42 0.43 0.02	0.25 0.44 0.125	0.49 0.52 0.03 0.03 0.56 0.32 0.43 0.97 0.73	0.49 0.05 –0.24 0.03 0.40 0.27 0.31 0.71 0.08	0.49 0.35 –0.14 0.03 0.48 0.02 –0.20 0.76 0.55
Maximum displacements in region II, Å	0.01	0.02	0.02	0.03	0.02	0.02	0.07	0.07	0.07
Total defect energy, eV	4.57	2.33	2.84	1.45	2.61	1.44	4.22 (1.41)	4.43 (1.48)	4.34 (1.45)

Table 4. Characteristics of different modes of incorporation of Fe^{III} impurity

Region	*M*1	*M*1	*M*2	Position K	*M*2
Center of the defect	0.25 0.22 0.125	0.25 0.35 0.125	0.75 0.22 0.125	0.5 0.5 0.0	0.75 0.22 0.125
Position of a Fe cation	0.25 0.22 0.125	0.25 0.35 0.125	0.75 0.22 0.125	0.5 0.5 0.0	0.75 0.22 0.125
K-vacancy	0.5 0.5 0.0 0.0 0.5 0.25	0.5 0.5 0.0 0.0 0.5 0.25	0.5 0.5 0.0 1.0 0.5 0.25	0.5 0.5 0.0	0.5 0.5 0.0
H-vacancy	0.25 0.144 0.125	0.25 0.144 0.125	0.856 0.25 –0.125	0.25 0.144 0.125 0.75 0.856 0.125	0.856 0.25 –0.125 0.644 0.25 0.375
Radius of region I, Å (number of atoms in the region)	6.5 (97)	6.5 (98)	6.5 (95)	6.5 (97)	6.5 (96)
Radius of region II, Å (number of atoms in the region)	16.5 (~1500)	16.5 (~1500)	16.5 (~1500)	16.5 (~1500)	16.5 (~1500)
Fe impurity after optimization	⇒ ⇐ 0.25 0.39 0.125		0.7 0.34 0.04	0.5 0.5 0.03	0.66 0.31 0.06
Maximum displacements in region II, Å	0.02		0.04	0.03	0.01
Total defect energy, eV	–4.79		–3.35	–1.24	–2.86

Table 5. Distances between the Fe^{II} ion and the nearest neighbors (Å) in the ideal structure and the structure with one defect upon optimization

Atom	Ideal structure	Upon optimization
H(1)	1.93	2.55
O(1)	1.98	2.52
O(2)	1.98	2.52
O(3)	2.57	2.17
O(4)	2.57	2.17
O(5)	3.51	3.58
O(6)	3.51	3.58

rity ion (*A*) but also to distortions (sometimes significant) of similar adjacent pseudocavities. Thus, the configuration of one of the adjacent *B* or *C* cavities (Fig. 1) (equivalent with respect to the initial cavity) can change its configuration in such a way that it becomes more "suitable" for the incorporation of one more impurity ion. Thus, one of the two shortest Fe–O distances increases from 1.98 (Table 5) to 2.05 Å.[1] If the cavity *B* (or *C*), in turn, is occupied by an iron ion, the geometrically favorable conditions for the incorporation of the next impurity ion are created either in the *G*- (one of the shortened distances increases from 1.98 to 2.01 Å) or in the *D*-cavity (the elongated distances chortens; one of the distances decreases only slightly, whereas the second one decreases from 2.57 to 2.39 Å). Therefore, the chain of interstitial positions may arise along the direction close either to the *y*- or to the *x*-axis (at a small angle to the *xy* plane). The subsequent energy computations for triatomic *ABC*, *ABG*, and *ABD* "clusters" for Fe^{II} (Table 3) demonstrated that the *ABD* "cluster" characterized by the least bent chain is most favorable. Since the incorporation of the impurity atom into the *D* position should change the geometry of its environment in a way similar to changes around the primary defect, the second short iron–oxygen distance in the *B* and *C* cavities should increase to ~2.05 Å, and one of two shortened distances in the *E* cavity should increase up to ~2.02 Å.

It should be emphasized that the adjacent pseudoplanes change in such a way that the cavity configurations are changed only in one direction—approximately along the *x*- or *y*-axis—so that these cavities become more appropriate to incorporate impurity ions. The changes along all the other directions only hinder the incorporation of impurity ions. Therefore, a chain of cavities can be found in a plane parallel to (100) so that the incorporation of an impurity ion into one of the voids facilitates the incorporation of the equivalent ion into the next void of this chain.

The processes with the participation of Fe^{III} and Fe^{II} ions proceed differently because the condition of the electroneutrality should necessarily be satisfied. Thus, the geometric conditions for the incorporation of M^{II} and M^{III} impurity ions are equivalent, whereas the conditions for formation vacancies to compensate the impurity charge are different.

In the incorporation of Fe^{III} into the *A* position (primary defect), the principle of electroneutrality is ful-

[1] All the values in Table 5 are given for the Fe^{II}–O distances; the character of distortions in the case of Fe^{III} incorporation is similar.

filled. Indeed, the charge of a trivalent cation incorporated into the cavity is compensated by the removal of two K^+ cations and one proton. The incorporation of the trivalent impurity cation into the next cavity of the chain (for example, into the *B* position) leads to an excessive positive charge caused by the removal of only one K^+ cation and one proton necessary for the formation of the cavity (the second "excessive" potassium atom had already been removed to form a defect cavity). The same situation is also observed if a Fe^{III}-impurity ion is incorporated into the next cavity of the chain, namely, into the *D* position. If the impurity continues "propagating" along the chain, the next cavity is the *E* (or *F*) position, crystallographically equivalent to the center of the *B* (or *C*) cavity. If an Fe^{III} ion occupies this void, the defect region still remains electrically neutral. If the next two links of the chain incorporate trivalent impurity ions, the chain again acquires an excessive positive charges. Thus, the "clusters" formation is advantageous for Fe^{III} impurities for geometric reasons, whereas the accumulation of excessive positive charges in some chain links hinders this process and "dictates" the formation of new vacancies, which is energetically disadvantageous.

The situation becomes quite different if an impurity is a divalent Fe^{II} cation. Its incorporation into the position of a primary defect (*A*) leaves the defect region electrically neutral. The subsequent incorporation of a Fe^{II} cation into the *B* (or *C*) position and then into the *D* position does not lead to accumulation of an excessive charge. In other words, the favorable geometric conditions for a divalent impurity are combined with the conditions of electrical neutrality. Therefore, the formation of clusters of divalent impurity ions can be assumed, whereas trivalent impurities are apparently incorporated into the structure only as isolated ions.

Our computations showed that the simultaneous incorporation of three Fe^{II} ions is energetically more advantageous than the incorporation of an isolated defect (Table 3). The formation of a cluster is accompanied by migration of Fe^{II} ions from the *M*1 position to the cavities of removed potassium ions (Table 3). The Fe^{II} ions in this defect center stick to one of the walls of too large potassium cavities (Fig. 2). The Fe–O distances in this cluster are indicated in Table 6. It should be emphasized that the potassium position becomes favorable only if an impurity is incorporated in the form of a "cluster." The incorporation of isolated cations makes the situation is the least favorable. The instances of such displacements of cations from the centers of cavities are substantially larger than the cation dimensions are well known, e.g., for zeolites [7, 8].

Table 6. Distances between a Fe^{II} impurity and the nearest neighbors (Å) in a three-particle cluster

Fe(*A*)		Fe(*B*)		Fe(*D*)	
P	3.07	P	2.97	P	3.41
		P	3.79	P	3.75
O(1)	2.42	O(9)	2.26	O(13)	2.13
O(2)	2.38	O(2)	2.34	O(14)	2.33
O(3)	2.53	O(10)	2.51	O(15)	2.88
O(4)	2.69	O(11)	2.53	O(16)	2.91
O(5)	2.89	O(4)	3.13	O(17)	2.98
O(6)	2.96	O(12)	3.25	O(18)	3.37
O(7)	3.97				
O(8)	3.08				

Nevertheless, it should be emphasized that the Fe^{II}–O potential should be considered as a purely ionic potential within our model and is quite satisfactory to describe a Fe^{II} ion in its conventional coordination with the characteristic Fe–O distances. However, for the adequate description of the behavior of Fe^{II} cations in

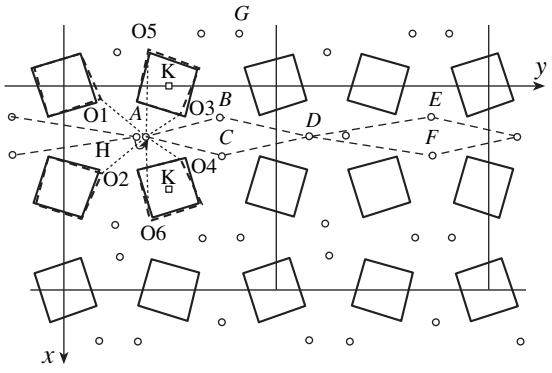

Fig. 1. "Chains" of geometrically favorable cavities and the defect region formed by an isolated Fe^{II} ion in the position (0.25 0.44 0.125): □ are potassium-ion vacancies; the ideal structure is shown by solid lines; the deformed structure is shown by dashed lines; the atomic displacements are indicated by arrows.

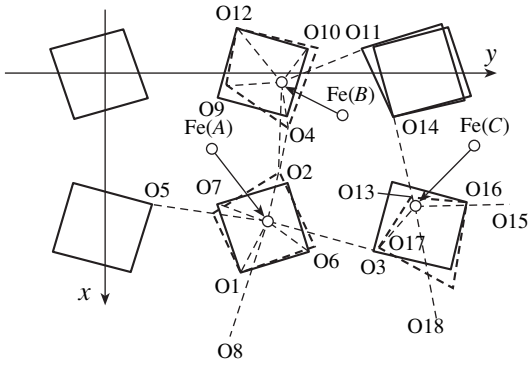

Fig. 2. Defect formed due a cluster consisting of three Fe^{II} ions; the ideal structure is shown by solid lines; the deformed structure is shown by dashed lines; iron displacements are indicated by arrows.

too large potassium cavities, the interaction potential should be added a new term which would take into account the partly covalent character of F–O bonding. Thus, the data on the migration of Fe^{II} impurities into potassium cavities cannot be considered as quite reliable.

Unlike a monatomic defect center where the structure distortion manifests itself mainly in the rotation of PO_4 tetrahedra, the formation of a cluster defect results in the distortion of these tetrahedra. The detailed analysis of these distortions cannot give reliable results, even at the maximum possible dimensions of the region I (for the computer used), because considerable errors arise at its boundaries.

Therefore, an Fe^{II} impurity, irrespectively of its form (isolated ions or clusters), provides considerable stresses in the structure, much higher than those caused by Fe^{III}; therefore, Fe^{II} should influence the growth kinetics of KDP crystals much more pronouncedly [9].

Indeed, it has been experimentally established [10] that divalent metal impurities (Ni and Co), whose effect on the KDP structure should be similar to that of Fe^{II} ions, suppress the "catalytic effect of impurities" typical of trivalent metals (Fe and Cr).

ACKNOWLEDGMENTS

We are grateful to J.D. Gale (the Royal Institution and Imperial College, London, UK) for supplying the GULP program package, A.B. Tovbis for adapting this program package to a personal computer, and V.A. Blatov for the search for crystal structures in which cations are displaced from the centers of the respective cavities by the TOPOS program.

This study was supported by the Russian Foundation for Basic Research, project no. 99-03-32557.

REFERENCES

1. T. A. Eremina, V. A. Kuznetsov, T. M. Okhrimenko, and N. G. Furmanova, Kristallografiya **41** (4), 717 (1996) [Crystallogr. Rep. **41**, 680 (1996)].
2. T. A. Eremina, V. A. Kuznetsov, T. M. Okhrimenko, *et al.*, Kristallografiya **43** (5), 906 (1998) [Crystallogr. Rep. **43**, 852 (1998)].
3. J. Foncuberta, R. Rodríguez, and J. Tejada, J. Cryst. Growth **44**, 593 (1978).
4. N. N. Barett, G. M. Lamble, K. J. Roberts, *et al.*, J. Cryst. Growth **94**, 689 (1989).
5. J. D. Gale, *GULP. User Manual* (Royal Institution and Imperial College, London, 1992–1994).
6. G. V. Lewis and C. R. A. Gatlow, J. Phys. C: Solid State Phys. **18**, 1149 (1985).
7. D. N. Olson, G. T. Kokotailo, and J. T. Chanell, J. Colloid Interface Sci. **28**, 305 (1968).
8. J. B. Paris, R. D. Shannon, E. Prince, and D. E. Cox, Z. Kristallogr. **165**, 175 (1983).
9. N. T. Barret, G. M. Hamble, K. J. Roberts, and J. M. Sherwood, J. Cryst. Growth **94**, 689 (1989).
10. V. A. Kuznetsov, T. A. Eremina, N. N. Eremin, *et al.*, Kristallografiya **45**, 1120 (2000) [Crystallogr. Rep. **45**, 1035 (2000)].
11. B. C. Frazer and R. Repinsky, Acta Crystallogr. **6**, 273 (1953).

Translated by T. Safonova

Crystallography Reports, Vol. 46, No. 1, 2001, pp. 81–87. Translated from Kristallografiya, Vol. 46, No. 1, 2001, pp. 88–94.

PHASE TRANSITIONS

Phase Transitions in Solid and Liquid Silicon

A. Ya. Gubenko

Moscow Institute of Electronics and Mathematics (Technical University), Bolshoĭ Trekhsvyatitel'skiĭ per. 1-3/12, Moscow, 109028 Russia

e-mail: root@onti.miem.msk.su

Received June 2, 1998

Abstract—It has been established that continuous variations of impurity concentration and temperature in silicon and other semiconductors give rise to phase transitions in the range of existence of solid and liquid solutions. The specific feature of these phase transformations is the occurrence of a phase transition proper in the range of the varying parameter of state, which is accompanied by a thermal effect. In such ranges, all the electrophysical and thermodynamic properties oscillate. It has also been shown that these oscillations result from the equilibrium self-organization of the material. The beginning of phase transitions with the change of the temperature depends on the concentration of defect in the initial material. The "driving force" of the phase transformations is the instability arising in the material with the variations in the temperature and the component concentrations. *© 2001 MAIK "Nauka/Interperiodica".*

INTRODUCTION

Earlier [1–4], we showed that melts and alloys and crystals formed from these melts undergo phase transitions within certain intervals of a variable parameter of the system (concentration, temperature, and pressure). In the range of the parameter variation, the properties of the liquid and solid phase oscillate. These oscillations consist of maxima and minima and are caused by the periodic changes of the structural state of the materials associated with its ordering and disordering processes accompanied by the changes in the character of atomic interactions. Thus, along with the statistical distribution of individual atoms in the melt, there exist some ordered groups of atoms with a certain short-range order structure. In this case, material disordering is accompanied by the reduction of the number of ordered groups of atoms, whereas ordering increases their number. Such periodic changes in the structural state of the material associated with ordering and disordering processes can also occur in the range of the parameter variation during the phase transitions in the solid phase [1–3]. The effect of ordering and disordering processes on the structural rearrangement and atomic interactions in the materials opens new possibilities for controlling the properties of growing crystals.

However, such control is impossible without a clear understanding of the nature of the phenomena occurring in the range of the parameter variation. The present study was undertaken with the aim to clarify these problems. We chose as an object of study a silicon semiconductor, the most important material in modern solid-state electronics.

EXPERIMENTAL

We studied phase transitions in the liquid and solid phases of P-, B-, and Sb-doped Czochralski-grown Si crystals. In addition to the traditional dopants, we also introduced into the melt the Ge, Sb, and Ti modifying impurities (MI), which, at a certain concentration, initiated a phase transition. As an example of the structurally sensitive properties, we studied the material density in the solid (d') and the liquid (d'') states by the contact-free radiation method with the use of penetrating gamma-radiation [5]. The density was determined within an error not exceeding 0.1% of the measured value in the absolute measurements and 0.05% in the relative measurements. The density was calculated using a specially written computer program. The points on the concentration curves of the density were averaged over three measurements. The differential thermal analysis (DTA) was performed on a DTA-5 setup designed and constructed in the Baĭkov Institute of Metallurgy of the Russian Academy of Sciences. The temperatures were measured by a tungsten–rhenium thermocouples, the crucibles were made of a fused quartz. Both heating and cooling rates were equal to 25°C/min. The setup was computer-controlled; the thermograms were calculated with the aid of specially designed software. The temperatures were measured with an accuracy of ±1 K. The DTA analysis was performed on single-crystal specimens cut out from the ingot parts having the diameter of 100 mm. Since melted silicon interacts, to a certain degree, with the crucible material, some experiments were made on Ge, whose melt did not interact with the walls of the quartz crucible.

1063-7745/01/4601-0081$21.00

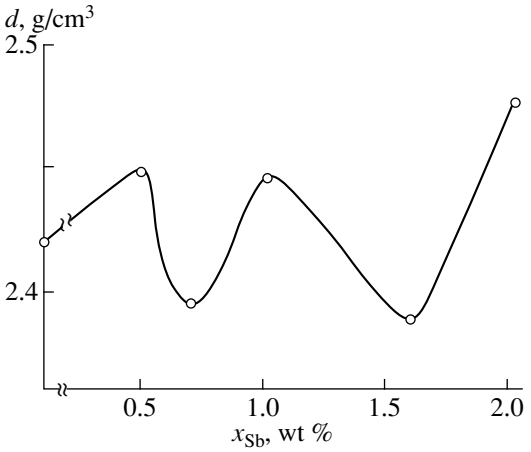

Fig. 1. Dependence of the density of the P-doped (5×10^{17} cm^{-3}) silicon on Sb concentration in the melt.

Phase transition in the liquid phase. It was shown [6] that the thermal effect accompanying a phase transition in the melt is more pronounced the higher the degree of order.

Therefore, we had to study the dependence of d'' on the concentration of the modifying impurity in the melt at temperatures close to the crystallization temperature, T_{cr}.

The dependences obtained had the form of oscillating curves (Fig. 1). This type of dependence was preserved up to T_{cr} + 100 K. With an increase of the temperature, the maximum and the minimum oscillation amplitudes decreased so that, at high temperatures, the curve was rather smooth and had a deflection point. The temperature dependence of d'' for the nigly Sb-doped (to a concentration of 2×10^{19} cm^{-3}) silicon melt containing the modifying titanium impurity differed from the previous dependence and was characterized by two extrema—a broad minimum and a sharp maximum. The curve shape did not depend on the mode of measurements (heating or cooling).

The thermograms of both solid and liquid phases showed, in addition to the thermal effects associated with melting and crystallization, some additional thermal effects occurring in the supercooled melt (Fig. 2a) prior to the thermal effect caused by crystallization (Fig. 2b). The thermal effects with an alternating sign were recorded at temperatures exceeding the melting point by 10–40°C (Fig. 2c). The existence of the sign-alternate additional thermal effects indicated the existence of alternating ordered and the disordered melt structures along the oscillation branches. Numerous measurements of d'' and kinematic viscosity ν in the vicinity of T_{cr} in the supercooled Si [7], Ge [8], and GaSb melts showed that their values drastically increase with a lowering of the temperature, whereas their temperature dependences have the oscillating character. The amplitudes of the maxima and the minima of d'' and ν oscillations in supercooled melts depend on the degree of their order. The higher the order degree, the more pronounced the oscillation maxima (minima) and the additional thermal effects [7]. In the experiments, the temperature curve of the melts with the disordered structure either showed the mini-

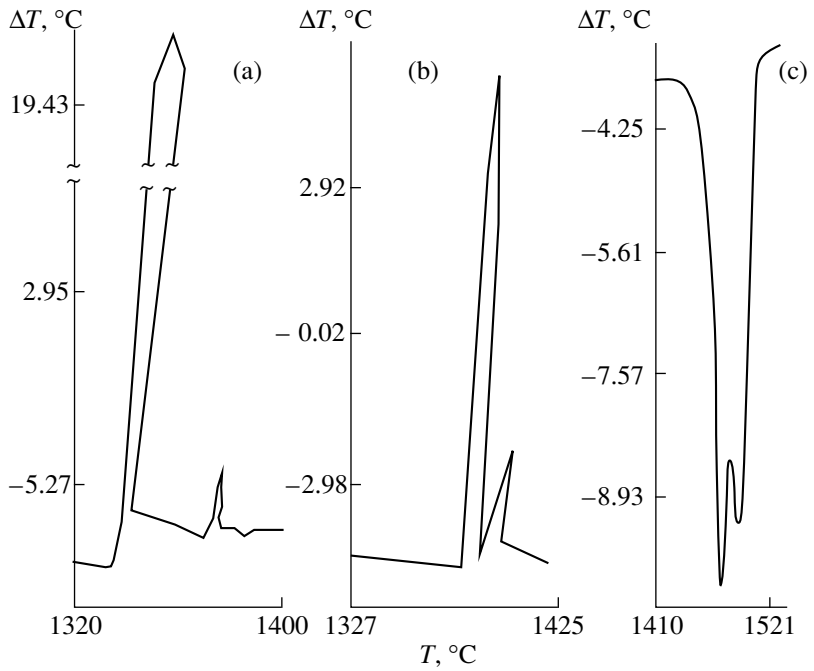

Fig. 2. Fragments of thermograms of (a) Ga(2×10^{19} cm^{-3})-, (b) B(6×10^{19} cm^{-3})-, and (c) Ga(2×10^{19} cm^{-3})- and Au(8×10^{15} cm^{-3})-doped silicon, respectively.

mum oscillations or had no oscillations at all. The dramatic increase of the melt density in the vicinity of T_{cr} and the X-ray data from metal melts [9] indicate that the structures of the supercooled melts differ from the structures of the melts overheated with respect to the melting point. The nonmonotonic changes in d'' with the temperature revealed in our studies considerably (by several times) exceed the error of the density measurements. The nonmonotonic changes in the properties observed in the vicinity of the melting point for Si melts and at higher temperatures were also observed in [10]. The effects associated with the structural rearrangements in the melts produce a considerable influence on the crystallization and the properties of the grown crystals [2, 3]. The introduction of a modifying impurity with the concentration at the extreme point x_{EP} into the melt results in the maximum degree of disorder in the melt possible for this modifying impurity. The concentration of the solid phase corresponding to the concentration x_{EP} of the modifying-impurity is referred to as x'_{EP}.

Phase transformations in the solid phase. The character of phase transformations occurring in the solid phase can be established from the character of d' variation and the existence or absence of additional thermal effects during the variations of the parameters of state of the system. The main task was to establish the range of the parameter variation. The d' and d'' values were measured every 30 s at a temperature variation rate of 10°C/min. As is seen from Fig. 3, the d' value of Ge-doped silicon (at the concentration higher than x_{EP}) is dramatically changed in the temperature ranges 600–750, 700–1000, and 1000–1100°C and also at temperatures higher than 1350°C, which indicates the occurrence of phase transitions accompanied by considerable changes in atomic interactions. The temporal intervals of d' measurements in Fig. 3 are marked with dots. Knowing the d'-values and the periodicity of its measurements, we could calculate the rate of d' variation. Usually it was equal to $(3–5) \times 10^{-4}$ g(cm^3 s)$^{-1}$, whereas within the above intervals it was 9×10^{-4}–3×10^{-3} g(cm^3 s)$^{-1}$. The location of the density peak at 650°C correlates with the position of the oscillation maximum of the integral reflection coefficient and the average dimensions of the regions of coherent X-ray scattering on the corresponding temperature dependences obtained for Ge-doped silicon with the similar Ge concentration [11]. It should be indicated that in crystals grown from the melt with the Ge concentration equal to x_{EP}, no drastic jumps in the temperature dependence of density was observed. At the same time, such jumps on the density polytherms obtained during growth of Ge-doped silicon at the concentration exceeding x_{EP} were always present. The halfwidth of the X-ray rocking curves for such crystals exceeded by a factor from 1.5 to 2 the halfwidth for crystals grown from melts at the Ge concentration x_{EP}, whereas the mechanical stresses determined by the X-ray method

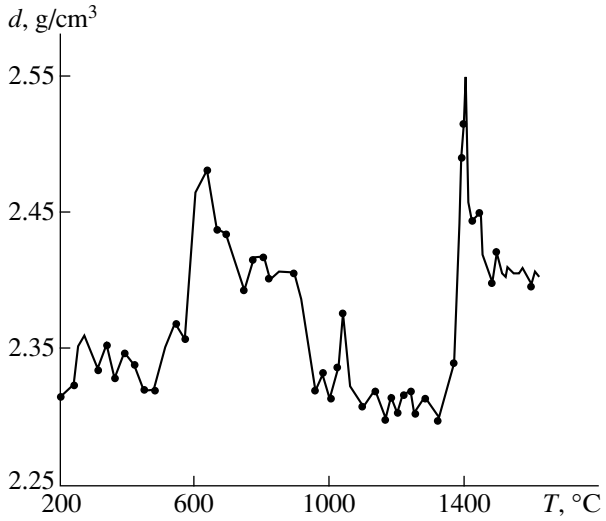

Fig. 3. Polytherm of density for Ge-doped *n*-type silicon.

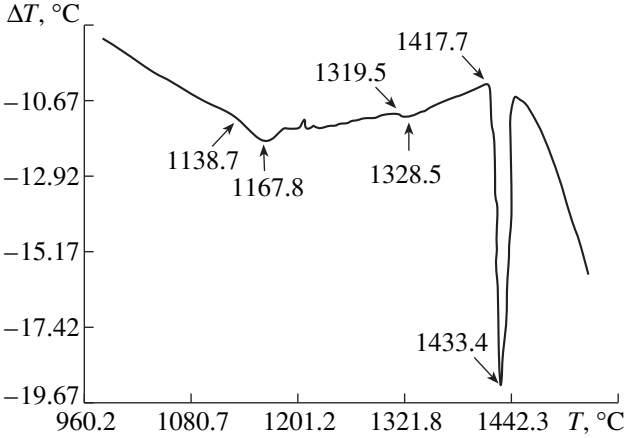

Fig. 4. Thermogram of polycrystal *n*-type silicon, ρ = 200 Ω cm.

were twice higher. The measurements of other properties showed [12] that crystals grown from melts with disordered structures had a much higher degree of structural perfection. At the same time, the experiments on crystals with elevated density of defects allowed one to reveal phase transitions from the jumps in d and the presence of additional thermal effects. In order to study the influence of the defect density on the detection of phase transitions, we obtained thermograms from *n*-type polycrystal silicon with the resistivity ρ = 200 Ω cm. The thermogram revealed two additional thermal effects (Fig. 4). The *n*-type silicon specimens with ρ = 90 Ω cm cut out from the grown crystals showed no additional thermal effects at all, whereas upon specimen quenching from 1100°C, such thermal effects were clearly seen. The rate of the temperature variation during the DTA was constant. Thus, the inertia of the thermal unit in the experiments was also constant. It was shown that silicon melts at a fixed temper-

ature. The comparison of the additional thermal effect and the thermal effect due to melting shows that the former (similar to the phase transition) is spread over a certain temperature interval. Such intervals coincide with the intervals of the jumpwise changes of the lattice parameter and other properties observed on silicon specimens [3, 13]. The change in the defect concentration in silicon with an increase of doping level influenced the number of the phase transitions revealed in the experiments in a similar way. The DTA curves from the P-doped silicon up to a resistivity value of $\rho = 0.03\ \Omega$ cm showed no additional thermal effects, whereas at $\rho = 0.005\ \Omega$ cm, the curves showed the occurrence of four additional thermal effects. The extreme points (EPs) were observed at 908, 1137, 1295, and 1365°C, respectively. The individual measurements of heat capacity for B-doped silicon specimens with the boron concentration 5×10^{19} cm^{-3} showed that the heat capacity oscillates in the temperature range from 400 to 450°C.

DISCUSSION

Earlier, it was shown that a change in the parameters of state can initiate phase transitions in silicon at high temperatures [14]. The data described above indicate that such transitions can take place over a wide temperature range and can be accompanied by additional thermal effects. The neighboring additional endo- and exothermic effects indicate the opposite directions of the changes of atomic interactions in the range of the parameter variation, which is confirmed by the correlated jumpwise change of the Debye temperature, Young's modulus, and equilibrium vapor pressure directly related to atomic interactions [15]. The temperature of the phase-transition beginning (the oscillating variation in a material property) depends on the initial state of the material. In particular, the structural and the chemical defects and various inhomogeneities give rise to stress fields in the crystal lattice of the material (in particular, in silicon), which, in turn, increases the free energy. With an increase of the temperature, the vibrations of numerous atoms about their equilibrium positions in the crystal lattice stop being consistent. Under these conditions, the anharmonicity of thermal vibrations and the change in the concentration of equilibrium thermal defects and also of the lattice parameter change the frequency and the amplitude spectra in the crystal. The material cannot exist in such a state any longer and becomes instable. Thus, the material should acquire a new state with a different atomic motion, which can be implemented only due to a phase transition. Therefore a phase transition can be considered as a reaction of the material which, during variation of its parameters of state, cannot exist in its initial state anymore. The instability can be interpreted as the difference between the free energies of an ideal (regular) solid solution and a real crystal. An increase of the number of defects in the material is accompanied by an increase of the free energy and, thus, promotes the attainment of the limiting instability sufficient for the transfer of its energy to fluctuations, which is necessary for an increase of the fluctuation scale. As a result, large-scale fluctuations are formed, which, in turn, provide the occurrence of a phase transition [2, 3]. Thus, if, e.g., either the number of defects in the material increases by some reasons or the material becomes unstable, the phase transition and the range of the parameter variation are shifted to the lower values of the varying parameter of state and the numbers and the amplitudes of the oscillation maxima and the minima would increase. Therefore, experimentally [13], the temperature of the beginning of the parameter-variation range is shifted, first, to the region of lower values in the solidified polycrystal Si specimen in comparison with its position in a single crystal with dislocations and in the crystal with dislocations, in comparison with its position in the dislocation-free single crystal. The same cause results in the shift of the phase-transition beginning to the high-temperature range in materials with the perfect crystal structures. Such a temperature shift of the range of the parameter variation and the extreme point and the appearance of property oscillations with time during isothermal annealing take place if silicon (or any other material) was preliminarily quenched from a high temperature or if these materials had the limiting instability sufficient (for some reasons) for the formation of large-scale fluctuations, such as the Curie temperature. Similar shifts were really observed in various materials.

The comparison of the liquidus and the solidus curves and surfaces of binary and multicomponent systems with the diagrams "composition–property of a liquid (solid) phase" showed that to the range of the parameter variation there correspond special segments of the curves and special surface regions of the phase diagrams [1–3]. Thus, a "fold" on the composition–property diagram of a solid phase in the range of the existence of solid solutions corresponds to the fold on the solidus surface, with the points in the regions of the phase diagrams being observed on the same conodes. This situation is consistent with the following relationship obtained for the binary system [4]:

$$\partial^2 G''/\partial x_i'' = k_i' G'/\partial x_i'', \quad (1)$$

where k_i is the equilibrium distribution coefficient, G is the molar free energy, and x_i is the concentration of the varying component. Hereafter, a prime and a double prime denote the quantities relating to the liquid and the solid phases, respectively. Hence, the oscillation maxima and minima are the sequence of equilibrium microstates of the material. Now, substitute $\partial^2 G''/\partial x_i^2$ in Eq. (1) by the equal ratio $RT/S_{cc}(x_i'', 0)$ [16], where $S_{cc}(x_i'', 0)$ is the structure factor in the long-wavelength limit. Thus we arrive at

$$\partial^2 G'/\partial x_i^2 = RT/k_i S_{cc}(x_1'', 0). \quad (2)$$

Now, represent k_i in the binary system in the form

$$\ln k_i = \ln a_i' - \ln a'', \quad (3)$$

where a_i is the activity of the ith component in the corresponding phase. According to [16], we have

$$S_{cc}(x_i'', 0) = (1 - x_i^n)(\partial \ln a''/\partial x_i'')^{-1}. \quad (4)$$

Differentiating Eq. (3) and substituting the value of $\partial \ln a_i''/\partial x_i''$ by its value from Eq. (4), we obtain

$$\partial \ln k_i/\partial x_i'' = \partial \ln a_i'/\partial x_i' - (1 - x_i'')/S_{cc}(x_i'', 0). \quad (5)$$

Using the well-known relationship between $\partial \ln a_i/\partial x_i$ and $\partial^2 G/\partial x_i^2$, taking into account Eq. (1), and performing the necessary transformations, we obtain

$$\partial \ln k_i/\partial x_i'' = 1/S_{cc}(x_i'', 0)[(1 - k_i)/k_i]. \quad (6)$$

It follows from Eq. (6) that nonmonotonic variations in k_i are caused by structural transformations occurring in the melt. Equation (6) can be represented as

$$S_{cc}(x_i'', 0) = [(1 - k_i)/k_i]/\partial \ln k_i/\partial x_i''. \quad (7)$$

Now, substituting $S_{cc}(x_i'', 0)$ in Eq. (4) by its value from Eq. (7), we obtain

$$\partial \ln a_i''/\partial x_i'' = (1 - x_i'')(\partial \ln k_i/\partial x_i''): [(1 - k_i)/k_i]. \quad (8)$$

Since in the range of the parameter variation, $\partial \ln k_i/\partial x_i''$ oscillates [1–3], then $\partial \ln a''/\partial x_i''$ and other thermodynamic quantities (entropy) also oscillate, which was confirmed experimentally [17].

Equation (7) can be represented in the form

$$\partial^2 G''/\partial x_i^2 = (\partial \ln k_i/\partial x_i'')RT/[(1 - k_i)/k_i]. \quad (9)$$

Calculating $\partial^2 G/\partial x_i^2 f(x_i)$ for the Si–Al, Ge–Sn, and Ge–Pb systems, we see that, in the range of concentrations variation, the $\partial^2 G/\partial x_i^2$ value also oscillates and, at x_{EP}, attains the zero value. Therefore, the mean-square concentration fluctuations at this concentration attain the maximum values in accordance with the well-known equation

$$\overline{(\Delta x_i)}^2 = RT/\partial^2 G/\partial x_i^2 N, \quad (10)$$

whereas inside range of the parameter variation, their amplitudes considerably exceed the amplitudes beyond this range. Thus, oscillations in the range of the parameter variation are caused by the development of nonattenuating large-scale fluctuations. This was confirmed by the well-known experimental data: the fluctuations drastically increased prior to the phase transition. It follows from Eqs. (7), (8), and (10) that

$$S_{cc}(x_i'', 0) = [(1 - k_i)/k_i]/\partial \ln k_i/\partial x_i'' = \overline{(\Delta x_i)}^2 N \quad (11)$$

or

$$(1 - x_i'')(\partial \ln a_i''/\partial x_i'')^{-1} = \overline{(\Delta x_i)}^2 N, \quad (11a)$$

where $S_{cc}(x_i'', 0)$ and $\partial^2 G''/\partial x_i^2$ also oscillate in the range of the parameter variation [1, 3]. According to Eqs. (9) and (10), $\overline{(\Delta x_i)}^2$ also varies within the whole range of the parameter variation. This conclusion is confirmed by the analysis of numerous experimental data on scattering of X-rays, light, and neutrons. The scattering intensities proportional to fluctuations can oscillate only in the range of the parameter variation. Since the fluctuations of various physical quantities are interrelated, they should oscillate in the whole range of variation of these parameters. Therefore, the interacting large-scale fluctuations should form a sequence of microstates characterized by different atomic interactions, which results in the appearance of additional thermal effects. It follows from Eqs. (1) and (10) that large-scale fluctuations, which form the states of the material in the liquid phase, should also form the states of the solid phase. It was shown [3] that oscillations of all the properties of the material in the range of the parameter variation are independent of the type of the varying parameter of state. Thus, one can assume that an instability formed in the vicinity of the range of the parameter variation should initiate the formation of nonattenuating interacting large-scale fluctuations. In this case, the energy of internal stresses in the crystal lattice is transferred into the energy of fluctuations, thus increasing the scale of these fluctuations. The amount of the transferred energy, together with the feedback (whose mechanism is determined by the nature of the formation of the large-scale fluctuations), provides the appearance of oscillations and the number of their maxima and minima and their amplitudes during the monotonic variation of the parameters of state. Experimentally, one can reveal one or several amplitudes depending on the sensitivity of the studied property to the changes occurring within the range of the parameter variation and the measuring method, with all the other conditions being the same. The similar character of the dependence of large-scale fluctuations and material properties in the range of the parameter variation indicates the cooperative character of the processes occurring in this range. Therefore, the nonattenuating interacting fluctuations developed in the whole condensed-phase volume and at the monotonic change of the parameter of state either continue growing or decrease to the extreme point, where the character of the fluctuation development is changed to the reversed one. Of course, the formation of fluctuations is of the probabilistic nature. Fluctuations can vary from point to point, which results in the formation of nonequilibrium states with the tendency of being transformed into the equilibrium ones. At the same time, between the neighboring extreme points, the fluctuations either increase of decrease. However, with due regard for the above and

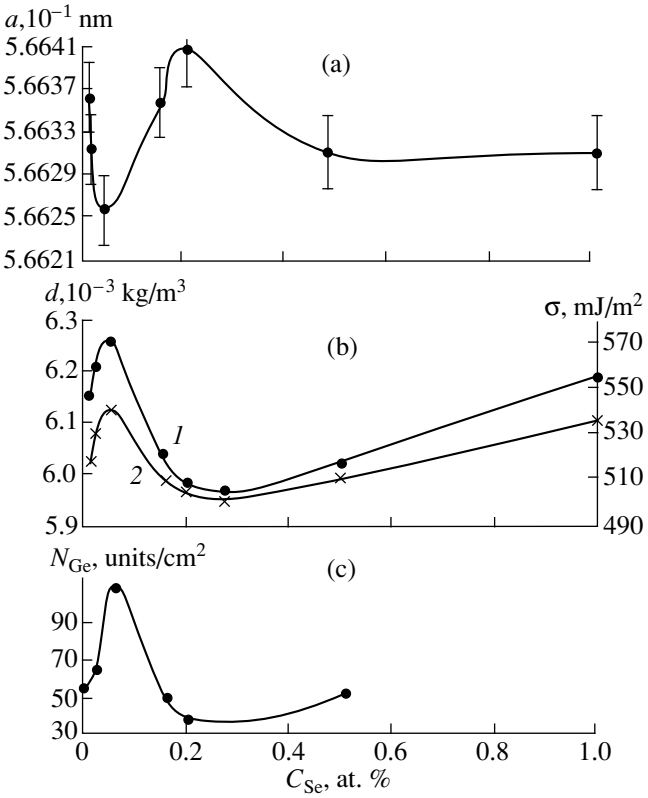

Fig. 5. Dependence of the lattice parameter of (a) Ge crystals (grains) in the two-phase Ge (80 at. %)–Sn (19–20 at. %) alloy; (b) the surface-tension (*2*) density (*1*) of the melts formed by these alloys, and (c) the number of Ge crystals in the alloy as a function of the Sb concentration in the melt.

the preserved tendency, the dependences of various properties can have some oscillating segments (Fig. 3). The sequence of microstates determines the formation of oscillating macroproperties in the system well reproducible from one experiment to another. Of course, each microstate has the corresponding macrostate. The process of the development of large-scale fluctuations and the formation of sequences of equilibrium microstates or microstates close to equilibrium ones in range of the parameter variation should be considered as an equilibrium self-organization process providing the transition of the material to a new phase with a lower free energy. The self-organization is implemented by large-scale fluctuations "seeking for a new state by trials and errors." Upon the attainment of such a state, the large-scale fluctuations attenuate. The process of self-organization results in the formation alternating ordered and disordered structures (with the maximum order at the extreme points). Such a development is characteristic of the dynamic self-organization and various evolutionary processes. The state of the material in the range of the parameter variation is limited by the structures formed at the given values of fluctuations. At the disordered segment of the range of the parameter variation, the fluctuations attain their maximum values. Therefore, on these segments, materials undergo the most pronounced changes. Thus, at the Curie point (which is an extreme point), the oscillations are maximal. At this point, one also observes the phase transition from the ferro- to the paramagnetic state [3]. The rate of property changing in the range of the parameter variation reflects the rate of the development of large-scale fluctuations and the phase transition itself. The above feature of the self-organization determines the appearance of such segments on the dependences which are impossible in terms of the classic thermodynamics. Thus, the derivative dp/dv takes the positive values, whereas d' and d'' (Figs. 1, 3) and the kinematic viscosity ν of the melts increase with the temperature rise. The latter dependence was repeatedly observed experimentally. Therefore, on some segments of the range of the parameter variation, the pressure derivative with respect to temperature can both increase or decrease with the temperature [3]. The oscillations of the surface tension also correlate with the bulk properties in the range of the parameter variation [18]. During crystallization of alloys, the large-scale fluctuations in the melt form the critical-size nuclei, which, when growing, form the grains or small crystals and the alloy itself. To each value of x_{MI} in the solid and liquid phases there corresponds a set of large-scale fluctuations, and also a certain number of nuclei and grains in the alloy and a certain set of their properties. Therefore, the dependence of the number of grains in the Ge (80 at.%)–Sn (19–20 at.%)–Sb alloy (where Sb is the modifying impurity) on x_{Sb} in the melt is also an oscillating dependence (Fig. 5) similar to that of the melt properties and the properties of the crystallized alloys. In other words, to each value of x_{MI} there corresponds an individual set of material properties. In the same manner, the critical supercooling also oscillates in the range of the parameter variation [19]. In the systems compared, the states thus formed are characterized by different atomic interactions, which provides the appearance of additional thermal effects. These results confirm once again the character of the variations in the size and the number of large-scale fluctuations and the fact that just these fluctuations are responsible for the formation of a set of microstates. The fluctuation nature of the material formation also takes place in the range of the parameter variation during directional crystallization. In the latter case, the properties of the solid phase in the range of the parameter variation correlate with the growth-rate oscillations. The experiment showed that in a liquid phase, additional thermal effects during the phase transitions can be recorded by the method of differential thermal analysis. In other words, the number and the size of the ordered groups of atoms are rather large. If the number of such groups becomes smaller irrespectively of the factors that influence the system, the probability of recording the phase transitions by the DTA method or by considering the oscillations of the structurally sensitive properties decreases. The experiment showed that in the melts with disor-

dered structures, the influence of impurities on the properties is only feebly marked, and it is hardly possible to record possible phase transitions caused by an increase of the temperature. The same factors result in the degeneration of the maxima (minima) of the oscillating properties with an increase of the melt temperature, which, in turn, results in the reduction of the number and dimensions of the ordered groups of atoms. In a similar way, numerous observations show that the extrema of the oscillations of the concentration dependences of various properties and light scattering by aqueous solutions and electrolytes also degenerate. These results indicate that the amplitude of large fluctuations in range of the parameter variation decrease with an increase of the temperature. Thus, we can assume that instability is formed just in the ordered groups of atoms and that this instability, similar to the case of the crystal lattice, predetermines the occurrence of phase transitions.

All the above data indicate that the impurities with the concentrations lying in the range of the parameter variation influence both the properties of silicon and other materials and the occurrence of phase transitions during temperature variation and can both reduce them or make them more pronounced. If the modifying impurity initiates the formation of the disordered structure in the melt and provides the formation of a more perfect crystal structure, it simultaneously suppresses the possible occurrence of phase transitions with increase of the temperature. In the case of formation of the ordered structure in the material, the impurity deteriorates the structure and increases the probability of a possible phase transition. The similar effects are also produced by the modifying impurity on the kinetics of various processes, e.g., the growth rate. In this case as well, there is a certain correlation between the oscillations of the growth rate, the properties of the melt, and the grown crystals [19]. All the above data show that in the range of the parameter variation, the Le Chatelier–Brown principle is invalid.

CONCLUSIONS

The changes in the concentration and the temperature in the solid and liquid silicon give rise to phase transitions accompanied by a thermal effect and occur due to nonattenuating large-scale fluctuations.

Phase transitions occur in the range of variation of the parameter of state, where atomic interactions and, therefore, also the whole set of properties of silicon (and other semiconductors) oscillate.

Phase transitions occur due to the equilibrium self-organization process providing the oscillating dependences of various properties on any parameter of state.

REFERENCES

1. A. Ya. Gubenko, Izv. Akad. Nauk, Met., No. 1, 206 (1992).
2. A. Ya. Gubenko, Vysokochist. Veshchestva, No. 4, 110 (1994).
3. A. Ya. Gubenko, Tsvetn. Met. (Moscow), No. 7, 44 (1994).
4. A. Ya. Gubenko, Tsvetn. Met. (Moscow), No. 8, 74 (1984).
5. O. B. Borovskiĭ, *Gamma-Method in Metallurgical Experiment* (Nauka, Novosibirsk, 1981), p. 22.
6. A. Ya. Gubenko and N. G. Stronina, Rasplavy, No. 5, 3 (1992).
7. A. Ya. Gubenko, Izv. Akad. Nauk, Met., No. 4, 99 (1997).
8. A. Ya. Gubenko, A. L. Anikin, and V. V. Zamyatin, *Collection of Scientific Works of the Moscow Institute of Electronic Engineering* (Mosk. Inst. Élektronnogo Mashinostroeniya, Moscow, 1990), p. 124.
9. H. Menke, Phys. Z. **33**, 593 (1932).
10. S. Kimura, K. Terashima, H. Sasaki, *et al.*, in *Proceedings of the IV Asian Conference on Thermophysical Properties, Tokyo, 1995*, p. 1.
11. A. I. Kurbakov, V. G. Mordkovich, *et al.*, Preprint No. 1125, Leningradskiĭ Inst. Yadernoĭ Fiziki im. B. N. Konstantinova (Konstantinov Institute of Nuclear Physics, Russian Academy of Sciences, Leningrad, 1985).
12. A. Ya. Gubenko, in *Proceedings of the 1st All-Russia Conference on Materials Science and Physicochemical Fundamental of Technology of Production of Doped Silicon Crystals, Moscow, 1996*, p. 196.
13. Yu. N. Taran, V. Z. Kutseva, K. P. Uzlov, and É. S. Fal'kevich, Izv. Akad. Nauk SSSR, Neorg. Mater. **27**, 2229 (1991).
14. A. Ya. Gubenko, in *Proceedings of the International Conference on Silicon, Roznov pod Radhostem, 1990*, Vol. 2, p. 11.
15. S. A. Zaĭtseva and Yu. A. Priselkov, Vestn. Mosk. Univ., Ser. 2: Khim., No. 6, 22 (1964).
16. A. B. Bhatia, in *Liquid Metals: Proceedings of the 3rd Int. Conference*, Ed. by R. Evans and D. A. Greenwood (Metallurgiya, Moscow, 1988), p. 27.
17. M. R. Madhava and G. A. Saurs, Philos. Mag. **38** (6), 576 (1978).
18. A. Ya. Gubenko, A. N. Shotaev, and V. A. Ermanchenkov, Adgez. Rasplavov Paĭka Mater., No. 9, 47 (1982).
19. A. Ya. Gubenko, *Growth of Semiconductor Crystals and Films* (Nauka, Novosibirsk, 1984), p. 34.

Translated by L. Man

Crystallography Reports, Vol. 46, No. 1, 2001, pp. 88–91. Translated from Kristallografiya, Vol. 46, No. 1, 2001, pp. 95–98.

Temperature-Induced Changes in Physical Properties and Lattice Symmetry of Nickel Crystals

Kh. Sh. Borlakov

Karachaevo-Cherkessk State Technological Institute, ul. Stavropol'skaya 36, Cherkessk, 357100 Russia
e-mail: 0801@00800000.mhs.rosmail.com or azamat@chen.elektra.ru

Received March 22, 1999

Abstract—It has been shown that the changes in some physical properties of nickel crystals can be explained on the assumption of the existence of an isotropic magnetic phase within the temperature range $470 < T < 631$ K, whose thermodynamic properties are determined by the exchange interaction alone. At $T_{is} \approx 470$ K, this phase should be transformed into an anisotropic magnetic phase because of the cooperative effect of relativistic interactions. This provides a consistent interpretation of the changes in the symmetry and the number of physical characteristics of the crystal in the framework of the Landau theory within the temperature range $273 < T < 650$ K.

INTRODUCTION

Although Ni crystals have been studied thoroughly, there are some inconsistent experimental data and commonly accepted theoretical concepts. Below, we discuss these inconsistencies and suggest a method of their elimination. The matter reduces to the following. At the Curie point $T_C = 631$ K, a nickel crystal is transformed into the ferromagnetic state. However, the constants of magnetic anisotropy have nonzero values only below $T = 570$ K [1]. In the range of $570 < T < 631$ K, there is not even one vanishing constant of magnetic anisotropy and, hence, there are neither hard nor easy magnetization axes. In other words, within this temperature range, an isotropic (absolutely magnetically soft) ferromagnetic phase should exist. It is shown that this isotropic magnetic phase can be logically described within the Landau thermodynamic theory of phase transition.

CHOICE OF SYMMETRY GROUP OF PARAMAGNETIC PHASE

In the paramagnetic phase, the nickel structure relates to the structural type of copper, *A*1, described by the sp. gr. O_h^5 [2]. The Ni atoms occupy the 1(a) positions (in Kovalev's notation [3]); these are cube vertices and face centers. The O_h^5 group is symmorphic, i.e., no screw axes and glide planes.

Thus, the space group of the paramagnetic phase can be chosen unambiguously. On the contrary, the magnetic symmetry group is chosen somewhat arbitrarily. It can be either the Shubnikov paramagnetic group $O_h^5 1'$ or the exchange paramagnetic group $O_h^5 \times O(3)$ [4], where 1' is the operation of spin inversion and $O(3)$ is the three-dimensional rotation group in the spin space. In the fist case, the existence of the isotropic phase cannot be described theoretically. Therefore, following Borlakov [5], we chose the sp. gr. $O_h^5 \times O(3)$ possessing magnetic subgroups which coincide with the sp. gr. O_h^5.

CHANGES IN MAGNETIC SYMMETRY IN TRANSITION TO THE ISOTROPIC MAGNETIC PHASE

In the Landau thermodynamic theory, the transition to a ferromagnetic phase is described by the magnetization vector **M**. This order parameter behaves as a scalar with respect to the space transformations and is transformed as a vector in the spin space. Therefore, the order parameter **M** is transformed by the irreducible representation $A_{1g} \times V$ of the exchange paramagnetic group, where A_{1g} is the unit irreducible representation of the group O_h^5 and V is the vector irreducible representation of the group $O(3)$. It should be indicated that the phase transitions occurring without the change of the translation symmetry can be described using, instead of the irreducible representation of the space group, the irreducible representation of the corresponding point group [6]. Since the symmetry of the crystal lattice and the ferromagnetic structure with respect to rotation about the direction of the magnetization vector **M** is preserved, the symmetry group of the isotropic phase is $O_h^5 \times O(1)$, where $O(1)$ is the one-parametric group of rotations about the vector **M**. Now, consider the transition from the isotropic to the anisotropic phase.

1063-7745/01/4601-0088$21.00 © 2001 MAIK "Nauka/Interperiodica"

SYMMETRY GROUPS OF ANISOTROPIC PHASES

To determine the symmetry groups of anisotropic phases within the Landau theory, one has to know the irreducible representation of the group O_h^5, according to which the order parameter describing the phase transition is transformed. The order parameter, which describes the transition at the Curie point is transformed according to the irreducible representation $A_{1g} \times V$ of the magnetic group $O_h^5 \times O(3)$. The irreducible representation of the group O_h^5 describes the transition to the anisotropic phase and should be related to $A_{1g} \times V$. There is a method of successive derivation of a subgroup from the irreducible representation of a certain group which extends the restrictions of the initial irreducible representation to the subgroup [4]. The restriction of irreducible representation $A_{1g} \times V$ calculated by formulas from [4] is equal to the irreducible representation F_{1g} of the group O_h^5. This agrees with [6], where the transition to the ferromagnetic phase in crystals of the class O_h is induced by the irreducible representation F_{1g}. The only difference in our case consists in the fact that this irreducible representation induces the transition from the isotropic to the anisotropic phase.

Denote the constraint imposed onto the irreducible representation of $A_{1g} \times V$ of the group $O_h \times O(3)$ by the same symbol but enclosed into brackets, $[A_{1g} \times V]$. Then, the result can be written in the form $[A_{1g} \times V] = F_{1g}$. This irreducible representation of O_h determines the lowering of the symmetry in the transition to the anisotropic ferromagnetic phase and is called critical [7].

Let the symmetry of a certain anisotropic phase be described by the point group $G_D \subset O_h$ and $T(g)$ be the matrices of the irreducible representation corresponding to the elements $g \in G_D$. Since the structure of the anisotropic phase is invariant with respect to the group G_D, the following algebraic equation is valid for every element $g \in G_D$:

$$T(g)\mathbf{c} = \mathbf{c}. \quad (1)$$

Equation (1) signifies that **c** is a stationary vector (S-vector) of the matrices of the irreducible representation. In other words, this vector is not changed by the matrices of the irreducible representation corresponding to the elements of the subgroup G_D. For each subgroup of the group O_h, there exists a specific S-vector; i.e., there is one-to-one correspondence between S-vectors of the irreducible representation and the subgroups of the initial group. The results of the calculations by Eq. (1) for various space groups are tabulated; thus, the necessary information can be taken, e.g., from Table 1. Obviously, the results of symmetry calculations for the star of the wave vector $k = 0$ are the same for all the space groups of a crystallographic class.

Table 1. Low-symmetric phases induced by irreducible representation F_{1g} of the group O_h

c	*ccc*	0*cc*	*c*00	$c_1c_2c_3$
G_D	$C_{3i}(C_3)$	$C_{2h}(C_2)$	$C_{4h}(C_4)$	$C_i(C_2)$
EA	[111]	[011]	[100]	[*lmn*]

Table 2. Complete condensate of stationary vectors of the critical irreducible representation F_{1g} of the group O_h^5

c	A_{1g}	A_{2g}	E_g	F_{2g}
ccc	*a*	*a*	–	*aaa*
0*cc*	*a*	–	*a*, 0	*aab*
*c*00	*a*	–	$a, -\sqrt{3a}$	–
$c_1c_2c_3$	*a*	*a*	*a*, *b*	*abc*

The notation of magnetic point groups in the table was taken from [9]; i.e., the symbol of a magnetic group consists of two symbols of ordinary point groups and has the meaning which can be understood from the following example. The notation of the magnetic group of the trigonal phase is $C_{3i}(C_3)$, where C_{3i} is the point group of the corresponding phase and C_3 is the subgroup of index 2 for the group C_{3i}. The black–white magnetic classes corresponding to the magnetically ordered states of a crystal should be designed just in this way [9]. The last row of table gives the symbols for easy-magnetization axes.

ACCOMPANYING DEFORMATIONS

The critical irreducible representation F_{1g} determines the possible lowering of the symmetry reduction at the point of a phase transition. However, in addition to symmetry lowering and the appearance of hard- and easy-magnetization axes, some other physical phenomena consistent with the symmetry of a new phase [7] can occur in each anisotropic phase. Among them, there are accompanying spontaneous deformations. Both critical and noncritical irreducible representations form the so-called complete condensate. Performing computations by the scheme [7], one can obtain the complete condensate of the critical irreducible representation F_{1g} of the group O_h (Table 2).

Discuss the physical meaning of individual degrees of freedom involved in the complete condensate. The unit irreducible representation A_{1g} describes the isotropic expansion or compression, accompanying the relativistic phase transition. The appropriate secondary order parameter is equal to the sum of the diagonal elements of deformation tensor [10]

$$a = u_{xx} + u_{yy} + u_{zz}. \quad (2)$$

The two-dimensional irreducible representation E_g describes the compression–extension deformations accompanying the relativistic phase transition. The components of the order parameter are expressed in terms of the deformation-tensor components as follows:

$$a_1 = (1/\sqrt{6})(2u_{zz} - u_{xx} - u_{yy}),$$
$$a_2 = (1/\sqrt{2})(u_{yy} - u_{xx}). \quad (3)$$

The three-dimensional irreducible representation F_{2g} with the components of the secondary-order parameter

$$a_1 = u_{yz}, \quad a_2 = u_{zx}, \quad a_3 = u_{xy} \quad (4)$$

describes the shear deformations accompanying the transition to the anisotropic phase. The correlation between the data in Table 2 and the data obtained by formulas (2)–(4) is obvious.

Now we can proceed to the discussion of the results obtained for nickel crystals.

DISCUSSION

At room temperature, nickel is a ferromagnetic with an easy-magnetization [111] axis. However, nickel cannot be directly transformed from the isotropic to the trigonal phase. The first magnetic-anisotropy constant K_1 changes the sign at a temperature of $T \simeq 380$ K [10]. Within the range of $380 < T < 570$ K, the constant $K_1 > 0$, whereas at $T < 380$ K, the constant $K_1 < 0$. It is known [9] that the change of the sign of K_1 leads to the spin-flip phase transition with the change of the direction of the easy-magnetization axis.

Thus, during cooling of a nickel crystal from the Curie point, $T_C = 631$ K, the following processes develop. At T_C, nickel is transformed to the isotropic ferromagnetic phase; i.e., the symmetry of crystal lattice remains the same, whereas the magnetization vector **M** can have an arbitrarily direction with respect to the crystallographic axes. At $T_{ls} \approx 570$ K, the crystal undergoes the transition to the anisotropic phase with the easy-magnetization axis along [100], because both magnetic-anisotropy constants are positive. The symmetry of crystal lattice is described by the sp. gr. C_{4h}^5. This phase transformation is a specific spin-flip transition from an arbitrarily directed easy-magnetization axis to the fourfold [100] axis. With the further lowering of the temperature down to 380 K, the constant K_1 becomes negative and the transition from tetragonal to rhombohedral phase with easy magnetization [111] axis occurs. The crystal-lattice symmetry of this phase is C_{3i}^2 and is preserved to room temperature and even lower.

Note that the sequence of phase transitions obtained in this article $O_h^5 \xrightarrow{631\text{ K}} O_h^5 \xrightarrow{570\text{ K (470 K ?)}} C_{4h}^5 \xrightarrow{380\text{ K}}$ C_{3i}^2 is inconsistent with the known data. According to [2, 11, 12], the tetragonal nickel phase is similar to the tetragonal indium phase (*A*6) described by the symmetry group D_{4h}^{17}. The rhombohedral phase also has a higher symmetry D_{3d}^5 typical of the crystal lattice of mercury (*A*10). Thus, we face a contradiction, which, at first glance, is difficult to eliminate. However, our scheme provides the interpretation of all the symmetry groups determined experimentally and following from the group–theoretical considerations. Indeed, the symmetry of possible low-symmetry phases is determined by the critical irreducible representation F_{1g} of the group O_h^5. However, all possible changes compatible with the symmetry of a newly formed phase can occur in a nickel crystal [7]. These additional changes are associated with accompanying effects, in particular, with deformation in the crystal.

The compression-extension deformation induced by the secondary irreducible representation E_g gives rise to displacements characterized by the symmetry group D_{4h}^{17}. These displacements are small in comparison with the critical ones occurring in the vicinity of the temperature $T_{ls} \approx 570$ K of the relativistic phase transition. However, with an increase of the distance of the transition point, the noncritical displacements associated with compression–extension deformations start exceeding the critical values. Then, the X-ray diffraction analysis yields the symmetry group D_{4h}^{17} corresponding to the secondary order parameter. This does not contradict the chain of transitions suggested in this study. Analogously, the trigonal displacements induced by the secondary irreducible representation F_{2g} below 380 K exceed the critical displacements, so that, instead of the true symmetry C_{3i}^2, the X-ray diffraction analysis yields a higher symmetry D_{3d}^5.

Note that the true temperature of the relativistic transition from the isotropic to the anisotropic phase seems to be lower than 570 K corresponding to the vanishing of the magnetic-anisotropy constants. The point is that the magnetic-anisotropy constants are measured in strong external magnetic fields, which fact, as is well known [13], shifts the transition point to higher temperatures. It is more probable that the point of relativistic phase transition has the temperature $T = T_{ls} \approx 470$ K at which the pronounced λ-peak is observed on the curve of initial magnetic permeability of nickel [14]. Within our model, the formation of this peak is quite clear. Indeed, according to Kersten, the initial permeability in the anisotrpic phase is inversely proportional to the square root of the magnetic-anisotropy constant [14]: $\chi_a = c\frac{M}{K_1^{1/2}}$. Magnetization M is determined mainly by the exchange interaction and does not exhibit any

anomalous changes near the relativistic transition. It should be noted that a small kink is formed on the dependence $M(T)$, which is explained by relativistic contribution to magnetization below the point T_{ls} [15]. However, the magnetic-anisotropy constant tends to zero with the temperature rises up to $T_{ls} \approx 470$ K [16]. Thus, the initial permeability shows an anomalous increase. Note that we observed a feebly marked λ-peak at a temperature about 470 K by the method of differential thermal analysis [16]. The temperature dependence of the lattice parameter, has a kink at the above temperature [14], indicating a second-order phase transition at this temperature.

Thus, the set of experimental data indicate that nickel crystals are likely to have an isotropic phase within a temperature range of $470 < T < 631$ K.

CONCLUSION

The changes in the magnetic symmetry, the temperature dependence of magnetic-anisotropy constants, magnetization, initial permeability, and some other physical characteristics of nickel crystals can be consistently interpreted on the basis of the Landau theory of phase transitions and the use of a postulate stating the existence of the isotropic phase from the temperature below the Curie point down to $T_{ls} \approx 470$ K. At this temperature, the transition to the anisotropic phase takes place which is caused by the cooperative effect of relativistic interactions. At the Curie point, only the magnetic symmetry is lowered, while the symmetry of crystal lattice is preserved so that the Landau–Lifshitz criterion holds for the symmetry group of the isotropic phase [4, 17].

Note that the above effects are more pronounced in crystals containing magnetic ions with triply degenerate orbital states [18]. In this instance, the relativistic interactions reduce to spin-orbit interactions. The cooperative effect of the relativistic interactions becomes much more pronounced than in pure 3*d*-metals. However, it is usually interpreted as the cooperative Jahn–Teller effect and is considered independently of magnetic phenomena in crystals [19].

REFERENCES

1. *Tables of Physical Quantities*, Ed. by I. K. Kikoin (Nauka, Moscow, 1976).
2. T. Penkala, *Foundations of Crystal Chemistry* (Pa'nstwowe Wydawn. Naukowe, Warszawa, 1972; Khimiya, Leningrad, 1974).
3. O. V. Kovalev, *Irreducible Representations of Space Groups* (Akad. Nauk Ukr. SSR, Kiev, 1961).
4. Yu. I. Izyumov, V. E. Naĭsh, and R. P. Ozerov, in *Neutron Diffraction of Magnetics* (Atomizdat, Moscow, 1981), Vol. 2.
5. Kh. Sh. Borlakov, Fiz. Met. Metalloved. **86** (2), 123 (1998).
6. V. L. Indenbom, Kristallografiya **5** (1), 115 (1960) [Sov. Phys. Crystallogr. **5**, 106 (1960)].
7. V. G. Bar'yakhtar and D. A. Yablonskiĭ, Fiz. Nizk. Temp. **6** (3), 345 (1980) [Sov. J. Low Temp. Phys. **6**, 164 (1980)].
8. V. P. Sakhnenko, V. M. Talanov, and G. M. Chechin, Fiz. Met. Metalloved. **62** (5), 847 (1986).
9. T. I. Ivanova, V. N. Kesoretskikh, V. P. Sakhnenko, *et al.*, Available from VINITI, No. 5263-V86, 1986.
10. L. D. Landau and E. M. Lifshitz, *Course of Theoretical Physics*, Vol. 8: *Electrodynamics of Continuous Media* (Nauka, Moscow, 1982; Pergamon, New York, 1984).
11. V. P. Sakhnenko and V. M. Talanov, Fiz. Tverd. Tela (Leningrad) **21** (8), 2435 (1979) [Sov. Phys. Solid State **21**, 1401 (1979)].
12. R. M. Bozorth, *Ferromagnetism* (Van Nostrand, New York, 1951; Inostrannaya Literatura, Moscow, 1951).
13. J. Donohue, *The Structures of the Elements* (Wiley, New York, 1974).
14. L. D. Landau and E. M. Lifshitz, *Statistical Physics* (Nauka, Moscow, 1976; Pergamon, Oxford, 1980), Part 1.
15. S. Tikazumi, *The Physics of Ferromagnetism: Magnetic Properties and Applications* (in Japanese) (Mir; Moscow, 1987).
16. *Landolt-Börnstein: Numerical Data and Functional Relationships in Science and Technology*, Group 3: Crystal and Solid State Physics (Springer-Verlag, Berlin, 1986), Vol. 19.
17. Kh. Sh. Borlakov and E. I. Nesis, Inzh.-Fiz. Zh. **59** (4), 671 (1990).
18. Kh. Sh. Borlakov, Fiz. Met. Metalloved. **86** (2), 120 (1998).
19. Kh. Sh. Borlakov, Preprint No. 116 T (1997), pp. 1–15.
20. M. Kataoka, J. Phys. Soc. Jpn. **36** (2), 456 (1974).

Translated by A. Darinskiĭ

Crystallography Reports, Vol. 46, No. 1, 2001, pp. 92–99. Translated from Kristallografiya, Vol. 46, No. 1, 2001, pp. 99–107.

Crystallographic Aspects of Macroinhomogeneous Plastic Flow in Single Crystals of Metals

L. B. Zuev*, V. I. Danilov*, S. A. Barannikova*, Yu. I. Chumlyakov, and N. V. Kartashova***

** Institute of Strength Physics and Materials Science, Siberian Division, Russian Academy of Sciences, Akademicheskiĭ pr. 8, Tomsk, 634055 Russia*

*** Siberian Physicotechnical Institute, Tomsk State University, Tomsk, Russia*

e-mail: lev@zuevs.tomsk.ru

Received June 7, 1999

Abstract—Various crystallographic aspects of the distribution of strain-localization zones have been studied in single crystals of metals subjected to tensile stresses at different orientations of the tension axes and characterized by different mechanisms of plastic flow (slip of dislocations and martensite transformations). It is shown that the crystallographic orientations of the strain-localization zones (interpreted as the patterns of plastic-flow self-organization) are preserved within the whole deformation process. Some characteristic features of the dynamics of the strain sites are considered. *© 2001 MAIK "Nauka/Interperiodica".*

INTRODUCTION

The detailed studies of localization of plastic deformation undertaken in recent years showed the universality of this phenomenon. It was established that, at the macroscopic level, plastic flow is always inhomogeneous: the deformed medium is stratified into zones of active plastic deformation and undeformable regions. Also, there exists a unique correspondence between the mode of plastic flow at the given stage of deformation [the corresponding segment on the stress-strain plastic-flow (or simply plastic-flow) curve $\sigma(\varepsilon)$] and the type of space–time evolution of strain localization. Experiments [1–3] show that the plateau on the stress–strain plastic-flow curve corresponding to the stage of easy slip is formed due to the motion of unit deformation fronts; in the course of linear hardening, one observes synchronously moving slip systems, whereas in the parabolic hardening, the stationary systems of several equidistantly located strain zones. Comparing the data on deformation of various poly- and single crystals, we established that the patterns of inhomogeneous plastic flow are almost independent of the type and the structure of a material and that they are associated with the shape of the dependence of the coefficient of the deformation hardening of a material $\theta = d\sigma/d\varepsilon$ on strain ε.

Unfortunately, in the studies performed earlier on single crystals [1–3], the crystallographic characterization of the strain-localization zones were almost ignored. However, this problem is essential for understanding the nature of deformation hardening, especially at the final plastic-flow stage because, as it has long been known [4], the crystallographic cause of shear characteristic of small strains can essentially differ from that of pronounced deformations, so that the process can often be completed by strain-localization, i.e., by formation of the fault regions [5]. Therefore, continuing our earlier studies of plastic deformation [1–3], we analyze in this article the crystallographic orientations of macroscopic strain-localization zones and the character of their evolution at all the stages of plastic flow.

MATERIALS AND EXPERIMENTAL METHODS

Materials and Specimens

The chemical composition of the alloys used in the study is given in the table. Solving the problem, we used the following Bridgman-grown crystals:

Single crystals of the quenched Cu–Ni–Sn alloy in the one-phase (quenched) state hardened by inclusions of dispersed particles of the $(Cu,Ni)_3Sn$ intermetallic compound;

Ni, Cr, Mn, and Mo-alloyed austenite *single crystals* additionally saturated with nitrogen up to concentrations of 0.35 or 0.5% (γ-Fe_I);

Mn-alloyed austenite *single crystals* (γ-Fe_{II});

Titanium nickelide (NiTi) *single crystals* with a composition close to equiatomic.

The above alloys were chosen because the mechanical tests of the corresponding alloy specimens provided the analysis of all the main characteristics of plastic flow, because the plastic deformation in γ-Fe and Cu–Ni–Sn single crystals (quenched and hardened by disperse particles) is attained via dislocation glide. In NiTi single crystals, the deformation is caused by the martensite phase transformation $B2 \longrightarrow B19'$ [6].

1063-7745/01/4601-0092$21.00 © 2001 MAIK "Nauka/Interperiodica"

Chemical composition (wt %) and crystallographic orientation of specimens

Chemical composition								Orientation	
matrix	Sn	Ni	Cr	Mn	Mo	C	N	tension axis	working plane
Cu	6.0	10.0	–	–	–	–	–	[111]	(123)
$(\gamma\text{-Fe})_I$	–	12.4	18.0	1.2	2.3	0.013	0.35	[001]	(110)
							0.50	[001]	(110)
							0.35	[111]	$(\bar{1}\,10)$
							0.50	[111]	$(\bar{1}\,10)$
$(\gamma\text{-Fe})_{II}$				13.0	–	<0.1	–	[012]	(110)
Ti		55.4	–	–	–	–	–	$[\bar{1}\,12]$	(110)

The diversity of the plastic flow curves was provided by the choice of appropriate orientations of the tension axis and, if necessary, also by thermal treatment (aging of the Cu–Ni–Sn alloy) or additional alloying (diffusion saturation of the $\gamma\text{-Fe}_I$ alloy with nitrogen). The specimens with the working volume of $25 \times 5 \times 1$ mm for mechanical tests were cut out from single-crystal ingots by electric erosion. The crystallographic indices of the tension axes and working surfaces (large faces of the specimens) are also indicated in the table. In all the above materials, where plastic flow at the microscopic level is implemented by dislocation-induced shear, the above orientations may provide the multiple slip. Thus, for the [001] orientation in $\gamma\text{-Fe}_I$, the Schmidt factor equals ~0.41 for the four-slip systems $[0\bar{1}1]$ (111), $[\bar{1}01]$ (111), $[\bar{1}01]$ $(\bar{1}11)$, and $[0\bar{1}1]$ $(\bar{1}11)$. On the (110) working surface, they should form the slip traces forming angles of 90° (the first two slip systems) and 35°16′ (the second slip systems) with the tension axis. If the longitudinal axis in $\gamma\text{-Fe}_{II}$ and the Cu–Ni–Sn alloy has the [111] orientation, equal values of the Schmidt factor (~0.27) are possessed by three $\langle 110\rangle\{111\}$ systems. The slip traces on the front surface of the specimen should form the angles equal to 19°28′, 35°16′, and 90° with the loading direction in $\gamma\text{-Fe}_I$ and 24°, 160°, and 68° in Cu–Ni–Sn. The high value of the Schmidt factor in $\gamma\text{-Fe}_{II}$ (~0.48) is characteristic of two-slip systems $[\bar{1}01]$ (111) and $[\bar{1}0\bar{1}]$ $(\bar{1}11)$. The slip traces on the working surface of the specimen for these two systems should form angles of 51° and 161°30′ with the tension axis.

Analysis of Strain Localization

Single crystal specimens were subjected to tensile stresses on an Instron-1185 machine at the constant velocity of a movable clamp 0.1 mm/min, ($d\varepsilon/dt = 6.6 \times 10^{-5}$ s^{-1}). During the extension process, we analyzed (at a 2% step) the inhomogeneous plastic-flow patterns corresponding to the stress–strain curve revealed by the method of two-exposure speckle-interferometry [7].

This procedure allowed us to determine the fields of the displacement vectors $\mathbf{r}(x, y)$ of the points on the surface of a flat specimen and their evolution with time. The local values of the components of the plastic-distortion tensor $\beta = \nabla\mathbf{r}(x, y)$ (elongation ε_{xx}, shear ε_{xy}, and rotation ω_z) were calculated by the numerical differentiation of these fields with respect to coordinates at all points of the front surface of the specimen within an accuracy of $\sim 10^{-4}$ (the orientations of the coordinate axes: the specimen was located in the $x0y$ plane, the z-axis was normal to the specimen plane, extension took place along the x-axis) [8]. The spatial $\varepsilon_{xx}(x, y)$ or spatial-temporal $\varepsilon_{xx}(x, t)$ patterns were constructed by the experimental data obtained to extract the information about the positions of the strain-localization zones and their motion. The orientation of the slip traces in the deformed specimens was analyzed on a Neophot-21 microscope. All the tests were made at 300 K.

EXPERIMENTAL RESULTS

Depending on the single crystal composition, the orientations of the tension axis and the total strain showed all the main types of the $\sigma(\varepsilon)$ dependences, namely: easy slip (NiTi; quenched Cu–Ni–Sn alloy, $\gamma\text{-Fe}_I$ 0.35% N, [111], $\gamma\text{-Fe}_{II}$); linear hardening ($\gamma\text{-Fe}_I$ with 0.35 and 0.5% N, [111], 0.35 and 0.5% N, [001]); quenched Cu–Ni–Sn alloy; and parabolic hardening (in all the specimens studied).

In what follows, the focus is made on the specific features of strain localization at different stages of the plastic flow (the corresponding segments on the plastic flow curves). The strain-localization zones are revealed as the maxima of the $\varepsilon_{xx}(x, y)$ distributions. Their positions correspond to $\varepsilon_{xy}(x, y)$ and $\omega_z(x, y)$, which facilitates the determination of such zones and the establishment of the characteristics of their spatial location and evolution with time.

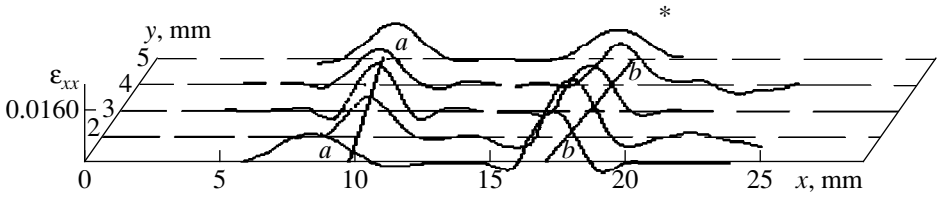

Fig. 1. Distribution of local strains (elongation) on the working plane of the nigh-nitrogen chrome–nickel γ-Fe_I specimen with nitrogen concentration 0.35% and the [111] tension axis during the process of deformation from 2.6 to 2.8% at the stage of easy slip (* is the moving strain site).

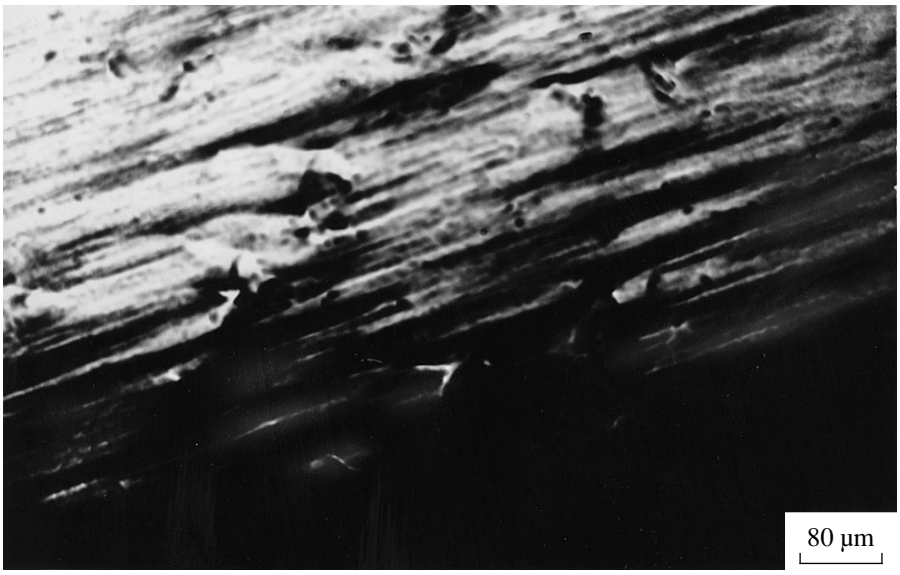

Fig. 2. Traces of slip system $(11\bar{1})$ [101] on the working surface of a deformed high-nitrogen (0.35%) chrome–nickel γ-Fe_I single crystal with the [111] strain axis at the stage of easy slip (ε_{tot} = 2.0%).

Localization at the Stage of Easy Slip

At the beginning of the easy-slip stage in γ-Fe_I with 0.35% N and the tension-axis orientation [111], the spatial pattern consisted of two strain-localization sites located at angles of 17° ± 4° and 30° ± 4° to the tension axis (Fig. 1, lines *a–a* and *b–b*, respectively). After a short time, one of these strain-localization sites stopped, whereas the other continued moving at a constant velocity until the completion of this stage. The deformation of such specimens was characterized by the action of three slip systems $(11\bar{1})[101]$, $(1\bar{1}1)[011]$, and $(\bar{1}11)$ $[\bar{1}0\bar{1}]$. As was already indicated, their slip traces should make angles of 19°28′, 35°16′, and 90° with the loading axis, respectively. However, the microscopic study showed that, at the stage of easy slip, most traces formed an angle of ~20° with the tension axis [111] (Fig. 2). This allows us to state that, at this stage, mainly the $(11\bar{1})$ [101] slip system is in action (the calculated angle formed by traces of this system at the stage of easy slip was equal to 19°28′).

At the stage of easy slip, loading of a NiTi specimen gave rise to the formation of a moving deformation front. The X-ray diffraction analysis showed that, prior to this stage, the material was in the austenite state (the *B*2-phase) and then in the martensite state (the *B*19-phase), i.e., the *B*2 ⟶ *B*19' phase transformation was observed [6]. Thus, the position of the deformation front and the kinetics of its motion reflected the localization and kinetics of the phase transformation. In the specimen volume, the strain-localization zone was located was at an angle of ~63° with respect to the tension axis (Fig. 3). It should be emphasized that at the titanium nickelide specimen orientations indicated above and the given tension axis, the most developed habit plane was (021), its trace made an angle of ~70° with the tension axis. In some cases, the front of the martensite transformation (the zone of deformation localization) was well seen on the photographs obtained by laser, because the surface distortion during deformation changed the scattering indicatrix (Fig. 4a). In the process of deformation, the front can change its orientation first to the wedgelike configuration and finally to the mirror-reflected one. The wedge sides and the tension axis formed angles ranging from 60° to 70° (Fig. 4b). Similar geometry of the front transformation was also observed in [9].

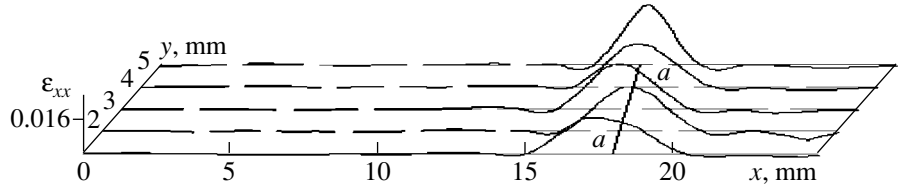

Fig. 3. Distribution of local strains (elongation) on the working plane of a NiTi single crystal deformed from 1.6 to 1.8% at the stage of easy slip.

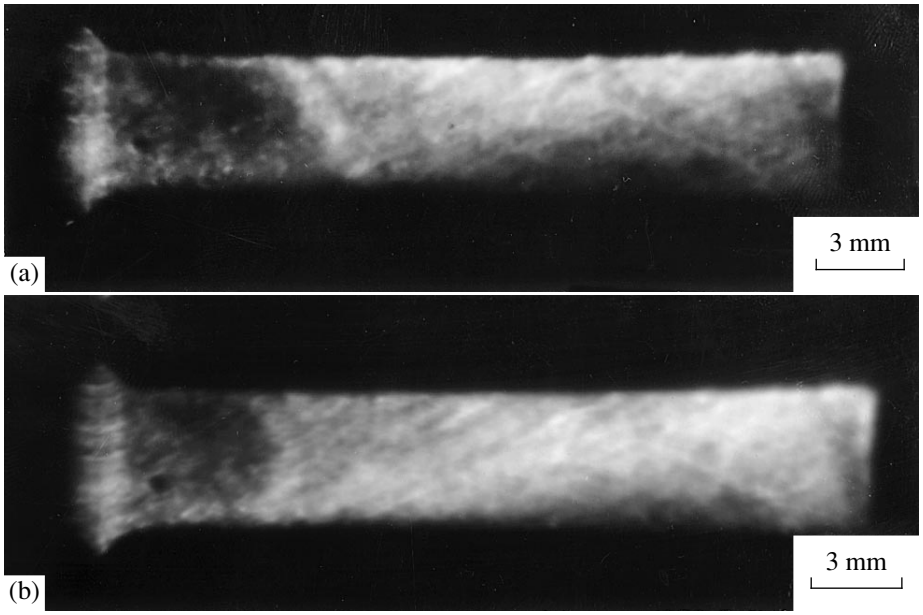

Fig. 4. The propagating strain-localization front in deformed NiTi single crystal at the stage of easy slip; (a) ε_{tot} = 2.6% and (b) ε_{tot} = 6.6%.

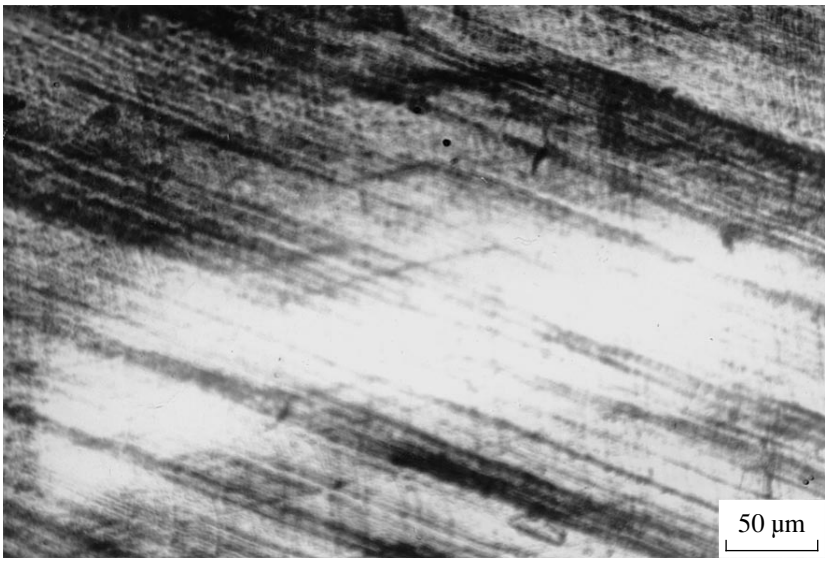

Fig. 5. Slip traces of the system (111) $[0\bar{1}1]$ on the working surface of a quenched Cu–Ni–Sn single crystal at the stage of linear hardening (ε_{tot} = 12.5%).

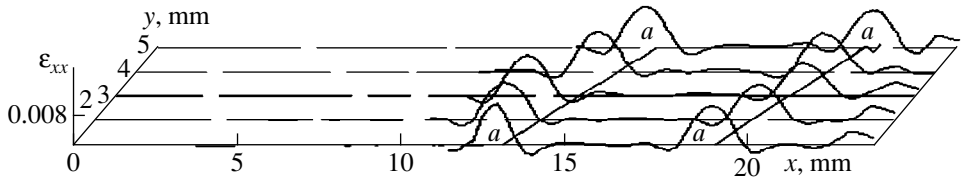

Fig. 6. Distribution of local strains (elongation) on the working plane of a quenched Cu–Ni–Sn single crystal deformed from 3.4 to 3.6% at the stage of linear hardening.

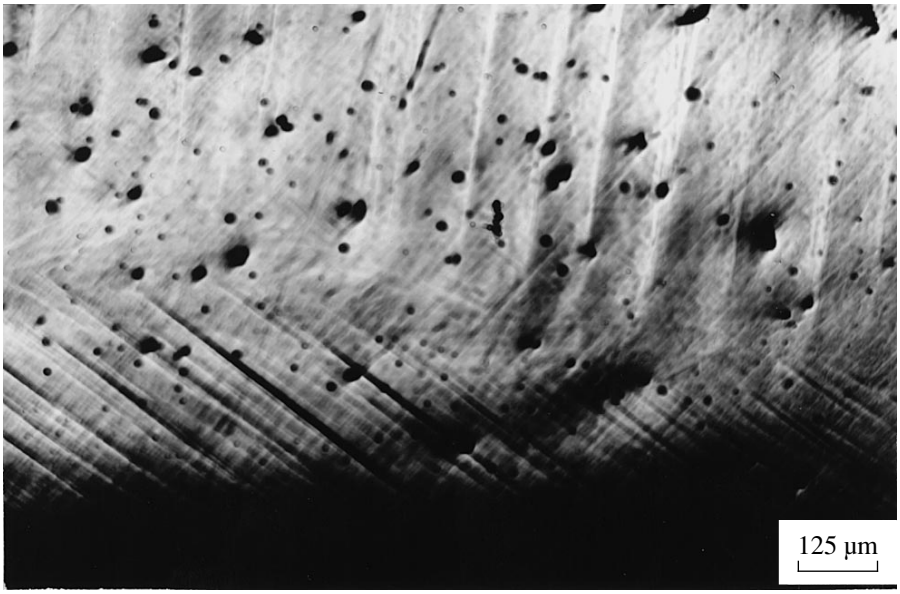

Fig. 7. Slip traces of the (111)[0$\bar{1}$1) and ($\bar{1}$11)[0$\bar{1}$1] systems on the working surface of a deformed high-nitrogen (0.35%) chrome–nickel γ-Fe_I specimen and the [001] tension axis at the stage of linear hardening (ε_{tot} = 4.0%).

Similar easy-slip stages were also observed in deformation of Cu–Ni–Sn single crystals and γ-Fe_{II}. It should be emphasized that all the four materials studied had a common feature in the distribution of the strain-localization zones at this stage—the motion of single deformation fronts at the same constant velocity of ~10^{-5}–10^{-4} m/s.

Linear Hardening

At these stages of the plastic flow, we observed the propagation of several regular local-deformation fronts. During deformation of quenched one-phase Cu–Ni–Sn single crystals, the propagation of these fronts is accompanied mainly by the formation of traces of only one-slip system [0$\bar{1}$1] (111), which forms an angle of ~20° with the tension axis (Fig. 5). The slip traces of other systems are rather weak. In this case, the maxima of the distribution of the distortion-tensor components in the range of total strains $0.2\% < \varepsilon_{tot} < 4\%$ are observed along the lines forming an angle of ~26° ± 4° with the tension axis. Thus, at the macroscopic level, the positions of the strain-localization zones are set by the crystallographic orientation of the slip planes. Moreover, the strain-localization zones are equally spaced from one another (~8 ± 0.5 mm) in the whole strain range studied. The positions of the maxima of the local-strain distribution in the specimen with only one acting slip system ($\bar{1}\bar{1}\bar{1}$)[0$\bar{1}$1] is shown in Fig. 6.

In γ-Fe_I specimens with the nitrogen concentration 0.35%, [001], the analysis of the arrangement of the slip traces on the working face upon the attainment of the total strain ε_{tot} = 3% showed that, in fact, all the four slip systems were active. However, one can see that the slip traces from the (111) [0$\bar{1}$1] system forming an angle of 88° with the tension axis and the ($\bar{1}$11) [0$\bar{1}$1] system forming an angle of 33° with this axis prevail (Fig. 7). It should be indicated that the deviation angles formed by slip traces with the tension axis and measured directly on the specimen from their calculated values (90° for the (111) [0$\bar{1}$1] system and 35°16′ for the ($\bar{1}$11) [0$\bar{1}$1] system) seem to be associated with the error in the specimen orientation in the clamps of the test machine. It should also be emphasized that the traces of the ($\bar{1}$11) [0$\bar{1}$1] system are more often seen close to the specimen edges, whereas the traces of the

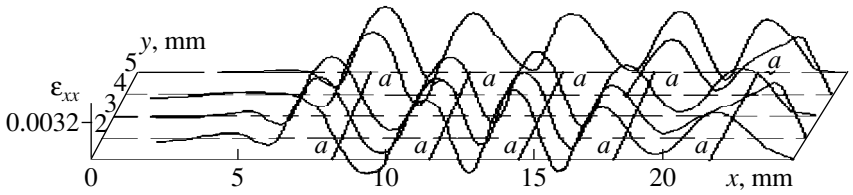

Fig. 8. Distribution of local strains (elongation) on the working plane of a high-nitrogen (0.35%) chrome-nickel γ-Fe_I single crystal and the [001] tension axis deformed from 4.2 to 4.4% at the stage of linear hardening.

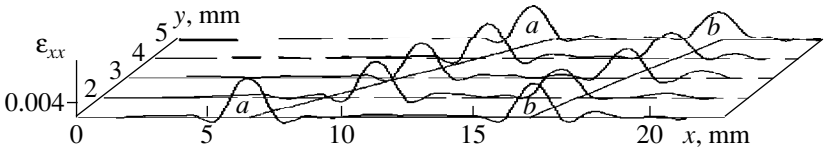

Fig. 9. Distribution of local strains elongation on the working plane of an aged Cu–Ni–Sn single crystal deformed from 6.0 to 6.2% at the parabolic hardening stage.

(111) [$0\bar{1}1$] and (111) [$\bar{1}01$] systems are seen over the whole working field of the specimen,

Evolution of the fields of local strain for γ-Fe_I single crystals with the nitrogen concentration 0.35% was studied by examining the segment of the stress-strain curve, which included the transition from elasticity to developed plastic flow and also, partly, the linear stage. Earlier, it was shown [1–3] that the distribution of the component $\varepsilon_{xx}(x)$ of the distortion tensor upon the attainment of the total strain $\varepsilon_{tot} = 4\%$ forms the pattern of moving equidistant local elongation maxima along the specimen axis. It was established that the strain zones are oriented normally to the tension axis of single crystals (Fig. 8).

Evolution of the patterns of the local-strain distribution in γ-Fe_I with 0.35% N and [111] orientation at the stage of linear hardening is also characterized by the motion of the equidistant system of strain sites. The arrangement of three such localized strain zones over the specimen volume is similar to that shown in Fig. 1 for the stage of easy slip.

In the specimen with 0.5% N, [111], the strain zones on the linear segment are oriented at the angles of 21° and 90°, with the latter angle becoming prevalent with an increase of the strain. The analysis of the slip traces on the metallographic section of the specimen indicated again the prevalent ($11\bar{1}$) [101] slip system (as in the case of lower nitrogen concentration at the same orientation), whose coarse slip traces form an angle of 20° with the tension axis. We also observed some traces from the ($1\bar{1}1$) [011] system forming an angle of 33° with the tension axis.

In specimens with the [001] orientation containing 0.5% N, the strain-stress curves also had a well-pronounced linear segment. In this case, we also recorded the action of the four slip systems indicated above. Upon the attainment of 4% total strain, the preferable systems were ($\bar{1}11$)[$\bar{1}01$] and ($\bar{1}11$) [$0\bar{1}1$] which, according to the data of the metallographic analysis, formed angles of 30° and 33° with the tension axis. Nevertheless, the characteristic feature of the arrangement of strain zones over the specimen was their normal orientation with respect to the tension axis.

At the linear stage of the process, the evolution of strain-localization patterns from all the single crystal specimens subjected to tensile stresses had one common feature: the maxima $\varepsilon_{xx}(x)$, $\varepsilon_{xy}(x)$, and $\omega_z(x)$ of the stress–strain curve equally spaced from one another move at constant velocities characteristic for each material, $V \approx (2.6–7.5) \times 10^{-5}$ m/s. For each degree of deformation, we observed from two to four strain-localization zones. During the time of the experiment, up to four localization zones have travelled through some specimen sections, which were located along the traces of the crystallographically set slip and revealed from the maxima of the distribution of the distortion-tensor components.

Localization in Parabolic Hardening

At the parabolic segments of the stress–strain curves, the stationary (immobile) localization zones were formed in all the materials. Thus, the study of aged Cu–Ni–Sn single crystals showed that immediately upon the attainment of the yield stress, the stable localization zones are formed in which the whole plastic deformation of the material is concentrated. In this case, the localization zones form angles of ~42° and ~30° with the tension axis (Fig. 9, lines *b–b* and *a–a*, respectively). For such an arrangement, the regions of action of two-slip systems do not intersect—they are located in different parts of the specimen. The analysis of the $\varepsilon_{xy}(x)$ distribution shows that these systems give rise to the corresponding maxima of the shear compo-

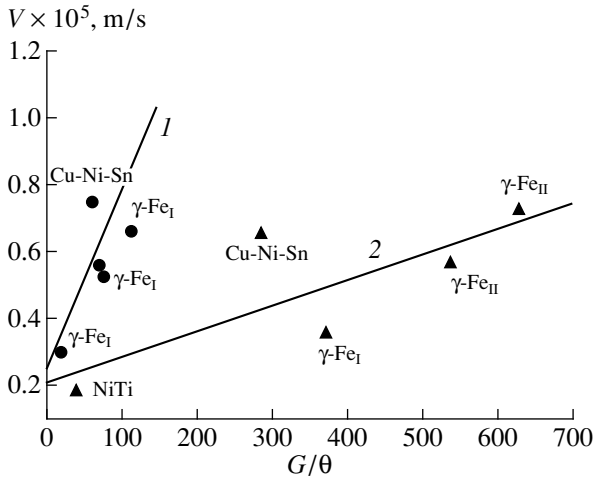

Fig. 10. Velocity of deformation-front propagation versus the coefficient of deformation hardening for single crystals studied: (*1*) linear hardening and (*2*) easy slip.

nent of the plastic-distortion tensor, which have the opposite signs.

An increase of the nitrogen concentration up to 0.5% in the specimens with the [001] orientation activated all the four above slip systems. Upon the attainment of 4% total strain, the $(\bar{1}11)$ $[\bar{1}01]$ and $(\bar{1}11)$ $[0\bar{1}1]$ systems prevailed, which, according to the metallographic data, formed angles of 30° and 33° with the tension axis. Nevertheless, the arrangement of the strain zones in the specimen during the deformation process remained the same. The zones of local elongation were distributed over the whole specimen normally to the tension axis.

DISCUSSION OF RESULTS

Generalizing the experimental data obtained, we should like to emphasize two important features of plastic flow in single crystals, namely:

In the course of plastic deformation, macroscopic systems of plastic-flow sites arise, whose type is fully determined by the nature of deformation hardening;

at the macroscopic level, the spatial positions of the strain-localization zones during plastic flow in single crystals is set by the orientation of acting slip planes.

Strain Localization and Deformation Hardening

The above characteristic features of plastic flow were ignored in all the known models of deformation hardening and interpretations of the multistage nature of plastic flow the revealed from the stress-strain curves. Beginning with the well known Seeger publication [10], all the theories of deformation hardening considered only the characteristics of elementary shear on the microscopic scale (Burgers vectors and dislocation paths [10, 11]), whereas the formation and evolution of the ordered systems of plasticity sites during plastic flow were almost totally ignored. This seems to be erroneous, because it has already become obvious that elementary shears are self-organizing during the deformation process, and, as follows from the experimental data, the structure formed is characterized by the macroscopic scale of ~1–5 mm. In order to describe the appearance and evolution of such ensembles, Nikocis and Prigogine [12] invoked the concepts of synergetics. Now, such attempts, based mainly on the autowave model [13] of plastic deformation [14–17], are widely used. The experimental data show that in the course of plastic flow, the plastic material is stratified into the active and passive layers regularly organized in space. The characteristic macroscale of such systems contradicts the ideas that plastic flow is caused by dislocations with their characteristic microscale—Burgers vectors $b \approx (3–5) \times 10^{-10}$ m.

The data obtained show that in each zone of localized plastic deformation, in addition to elongation and the shear component of the plastic-deformation tensor, the rotation mode is also formed [18], whose appearance can hardly be explained by slip along one system of planes characteristic of deformation in single crystals [5]. A large volume of the material is evolved into rotation, and the rotation region extends from the slip-zone axis to a distance considerably exceeding the shear-zone width. It was assumed [5, 8] that rotations are associated with the accumulation of immobile dislocations during deformation. As will be shown in the next section, this hinders the development of shears and limits the size of the active deformation site.

Mobility of Sites of Plastic-Flow Localization

The systems of moving equidistantly located plastic-flow sites observed at the stage of linear-deformation hardening form a specific wave. Some kinematic and dynamic characteristics of the propagation of this wave are known. Thus, the study of the dependence of the propagation velocity V of such a wave on the loading conditions showed that, at the stage of linear hardening, the wave velocity is inversely proportional to the coefficient of deformation hardening (Fig. 10) so that

$$V(\theta) = V_0 + \zeta\theta_*^{-1}, \quad (1)$$

where V_0 and ζ are certain constants. This dependence can describe the experimental data for all the single crystals studied if one uses the dimensionless coefficient of deformation hardening $\theta_* = \theta/G$ (where G is the shear modulus). For concrete material and the dimensional (in Pa) coefficient of deformation hardening θ, Eq. (1) acquires the form $V(\theta) = V_0 + J\theta^{-1}$, where the coefficient J has the dimension (Pa m)/s = J(m^2 s)$^{-1}$. This allows one to interpret J as a energy flow through the object deformed in a loading device. The form of Eq. (1), $V \sim \theta^{-1}$, shows the different natures of the peri-

odic processes observed and elastic and plastic waves propagating with the velocities $V_e \sim E^{1/2}$ and $V_p \sim \theta^{1/2}$, respectively. The sense of J and the essential difference in the functions $V(\theta)$ do not allow one to relate the spatial–temporal characteristics of inhomogeneous plastic flow either to elastic or to plastic waves. We are probably dealing with autowave phenomena [13], i.e., the processes of self-organization occurring in a deformable medium. It should be emphasized that the necessary condition for the occurrence of such processes is the flow of energy through the medium [12, 13].

At other values of constants V_0 and ζ, Eq. (1) is also valid for the easy-slip stage in single crystals, where the strain-localization zone propagates as a single front. In this case, the motion velocity of such a site and the coefficient of deformation hardening are inversely proportional (Fig. 10). This is quite consistent with the concept of autowave processes [13] which considers several variants of self-organization.

The physical sense of Eq. (1) becomes clear within the concept of the nature of θ suggested in [11]. In this case θ is proportional to energy $W \approx Gb^2\rho_s$ of immobile dislocations accumulated during plastic flow and is inversely proportional to the energy $Q \approx \sigma bL\rho_m$ scattered by mobile dislocations (per unit volume, where b is the Burgers vector of dislocations; ρ_s and ρ_m are the densities of the accumulated and mobile dislocations, respectively; L is the dislocation path; and G is the shear modulus). Thus, we have [11]

$$\theta/G \sim W/Q \sim Gb^2\rho_s/\sigma bL\rho_m \sim (b/\varepsilon_{el}L)(\rho_s/\rho_m). \quad (2)$$

At the steady-state plastic flow J = const. In this case, an increase in the density of the accumulated defects results in an increase in W, which, according to Eq. (1), results in a decrease of V. On the contrary, an increase of the fraction of energy transformed into heat Q in the specimen results in specimen heating, which increases the probability of elementary events of thermally activated plastic deformation and, thus, results in an increase of V.

CONCLUSIONS

The data obtained in the present study and the earlier results [1–3] show that an important feature of plastic flow in single crystals is the formation of large-scale strain-localization zones, whose positions correlate with one another and whose shapes depend on the type of deformation hardening characteristic of the given stage of the process. The spatial position of such macroscopic deformation sites is determined by the crystallography of the slip systems acting in single crystal specimens up to the attainment of the limiting values of the total strain. At the same time, during plastic flow, the transitions from one slip system to another are possible. This substantially hinders the crystallographic characterization of plastic flow at all its stages.

Interpreting the nature of deformation hardening and the different segments of the strain–stress curves for single crystals, one necessarily has to take into account not only the microscopic characteristics of the structure with defects, but also the existence and evolution of large-scale (macroscopic) correlations between the shear-zone positions. These correlations exist for both mobile and immobile systems of plastic-flow sites. It was shown that the velocity of site motion and the value of the coefficient of deformation hardening are inversely proportional.

REFERENCES

1. L. B. Zuev and V. I. Danilov, Fiz. Tverd. Tela (St. Petersburg) **39**, 1399 (1997) [Phys. Solid State **39**, 1241 (1997)].
2. L. D. Zuev and V. I. Danilov, Int. J. Solids Struct. **34**, 3795 (1997).
3. L. D. Zuev and V. I. Danilov, Philos. Mag. A **79**, 43 (1999).
4. M. V. Klassen-Neklyudova, *Plastic Properties and Strength of Crystals* (GTTI, Leningrad, 1933).
5. A. A. Urusovskaya, in *Some Problems of Physics of Crystal Plasticity* (Akad. Nauk SSSR, Moscow, 1960), p. 75.
6. V. S. Boĭko, R. I. Garber, and A. M. Kosevich, *Reversible Crystal Plasticity* (Nauka, Moscow, 1991).
7. R. Jones and C. M. Wykes, *Holographic and Speckle Interferometry* (Cambridge Univ. Press, Cambridge, 1983; Mir, Moscow, 1986).
8. V. L. Indenbom, V. I. Al'shits, and V. M. Chernov, in *Defects in Crystals and Their Computer Modeling* (Nauka, Leningrad, 1980), p. 23.
9. J. A. Shaw and S. Kyriakides, Acta Mater. **45**, 683 (1997).
10. A. Seeger, *Dislocations and Mechanical Properties of Crystals* (Wiley, New York 1957; Inostrannaya Literatura, Moscow, 1960), p. 179.
11. A. L. Roĭtburd, *Physics of Deformation Hardening of Single Crystals* (Naukova Dumka, Kiev, 1973), p. 5.
12. G. Nicolis and I. Prigogine, *Exploring Complexity* (Freeman, New York, 1989; Mir, Moscow, 1990).
13. A. V. Vasil'ev, Yu. M. Romanovskiĭ, and V. G. Yakhno, *Aufoware Processes* (Nauka, Moscow, 1987).
14. E. C. Aifantis, Int. J. Plast. **3**, 211 (1987).
15. E. C. Aifantis, Int. J. Eng. Sci. **30**, 1279 (1992).
16. G. A. Malygin, Fiz. Tverd. Tela (St. Petersburg) **37**, 3 (1995) [Phys. Solid State **37**, 1 (1995)].
17. Yu. Z. Estrin, B. Sluys, Y. Brechet, and A. Molinari, J. Phys. IV **8**, 135 (1998).
18. L. B. Zuev, T. M. Poletika, and B. S. Semukhin, Kristallografiya **40** (6), 1071 (1995) [Crystallogr. Rep. **40**, 996 (1995)].

Translated by L. Man